HIGH-ENERGY PARTICLE ACCELERATION FROM JETTED ACTIVE GALACTIC NUCLEI

By

Alina L. Kochocki

A DISSERTATION

Submitted to
Michigan State University
in partial fulfillment of the requirements
for the degree of

Physics—Doctor of Philosophy

2026

ABSTRACT

In the last century, the study of high-energy cosmic rays has opened a new window to the extreme, astrophysical universe. Accelerated particles originate from some of the most energetic environments, the accretion flows and jets driven by supermassive black holes at the centers of galaxies, active galactic nuclei (AGN). These jets and outflows are expected to impact galaxy and cluster formation, critical for modeling the structural development of the late universe. Studies of high-energy cosmic-rays, as well as neutrinos and multi-wavelength emission produced with the jet, may allow us to better understand the mechanisms of jet formation, jet feeding, particle acceleration and energy dissipation. In this work, we focus on a number of jetted, astrophysical sources relevant from the recent perspective of neutrino astrophysics. Such objects exhibit powerful jets, and may harbor substantial hadronic particle acceleration. Likelihood-based inference may be used to characterize these systems of high-energy particle interaction and evolution. We perform correlations of the time-dependent, multi-wavelength activity of these jetted objects with data from the IceCube South Pole Neutrino Observatory. We also focus on a selection of jetted AGN with substantial evidence for detectable neutrino production, and use methods of leptohadronic and radiative transport to model their dynamic and extended jets. Finally, we consider time correlations of such AGN activity, to more broadly understand the relation between radio and gamma-ray emission within a large population sample.

My dedication...

ACKNOWLEDGEMENTS

My acknowledgements...

TABLE OF CONTENTS

LIST OF TABLES

LIST OF FIGURES

CHAPTER 1

THE STRUCTURAL EVOLUTION OF THE UNIVERSE, ACTIVE GALACTIC NUCLEI

1.1 The Early Universe

1.1.1 Origins, The Big Bang

The current, favored model for the origin of the universe suggests an initial, spontaneous injection of energy into an infinitely small space, or singularity. This space would have had an instantaneous infinite temperature and energy density. It is unclear how the physical laws or symmetries of our modern universe might have existed in this earliest state.

At some point, this singularity would have begun to expand in a 'Big Bang'. As this volume increased, the energy density decreased, and spontaneous symmetry breaking might have allowed for the development of the fundamental laws and symmetries known today. While this initial state cannot be verified experimentally, and the development of laws or symmetries and energy during this period is largely uncertain, several observations support an origin similar to this model. First, the expansion of the universe as indicated by the measured rate of separation of astrophysical structures and its success in describing structural developments in the universe. Models of this evolving volume suggest that the universe was originally smaller, denser and hotter. Second, the observed cosmic microwave background (CMB), a thermal bath of photons observed from the very early universe, is an expected relic of the transition to optical transparency with expansion 380,000 years after the Big Bang. Third, the abundances of the lightest elements in the modern universe well match theoretical expectations for their nucleosynthesis in the first minutes [Huterer, 2023].

In general, owing to observations, there is substantial theoretical agreement about the state and development of the universe after the first 10^{12} seconds. Here, the forces and fundamental particles we know of today have emerged. Still, this initial, earliest state and the physical laws that might have been present is the focus of ongoing research.

1.1.2 Inflation

While the fundamental laws and symmetries of the earliest universe have some uncertainty, it also seems that an additional mechanism is required to explain structural imprints in the earliest universe. Specifically, the regular distribution of over- and under-densities of matter indicated in the observable universe requires an additional origin. This is often referred to as the 'horizon problem', as the apparent causal horizon of fluctuations in this otherwise relative homogeneity was much smaller then the observed volume. We note that the leading model for such a process is a period of Inflation. In the first 10^{-35} – 10^{-32} seconds, a more rapid period of volume expansion than that of today occurred. During this time, initial quantum fluctuations in the energy density of the universe might have expanded out to larger volumes, seeding the earliest gravitationally bound structures. Inflation is also expected to support the observed flatness of the universe and the lack of magnetic monopoles [Huterer, 2023].

1.2 Modeling the Evolving Universe

A number of observations provide direct evidence for an expanding universe. Light from physical processes in the distant universe is known to be redshifted, meaning the wavelength of emitted light, $\lambda_{\rm em}$ differs from the observed wavelength, $\lambda_{\rm ob}$, by an amount,

$$z \equiv \frac{\lambda_{\rm ob} - \lambda_{\rm em}}{\lambda_{\rm em}}. \tag{1.1}$$

Observed light which is redshifted to longer wavelengths suggests a relative velocity between the point of emission and observation. Early measurements at the start of the previous century indicated the majority of observable galaxies were receding from us at a distant-dependent velocity [Hubble, 1929]. This rate was parameterized with Hubble's law,

$$z = \frac{H_0}{c} r. \tag{1.2}$$

Here, H_0 is Hubble's constant, which is determined experimentally for a given time of observation (assumed to be the present day). r and c are distance and the speed of light,

respectively. More generally, we may express Hubble's parameter for a given time, t since the early universe (post-Inflation), as,

$$H(t) = \frac{\dot{a}(t)}{a(t)}. \tag{1.3}$$

Here, $a(t)$ is a time-dependent scale factor, describing the expansion or contraction of space from a time t to a present time, t_0,

$$r(t) = a(t)r(t_0). \tag{1.4}$$

The expanded universe following $a(t)$ is observed and experienced, though it can be also be useful to think of 'comoving distances' prior to the transform of expansion. Modeling or parameterizing this scale factor, $a(t)$, requires a knowledge of the geometry of the universe, its content, and how the content of the universe drives its evolution or changing state. $a(t)$ is set to be 1 in the present day, $a(t) < 1$ in the past and $a(t) > 1$ in the future (assuming an overall expansion).

We can assume a spontaneous energy injection into a closed system, and track this energy density as a function of time. As there is no heat flow into or out of the universe, the first law of thermodynamics (assuming a Newtonian space), follows as,

$$0 = dQ = dE + PdV. \tag{1.5}$$

Here, this adiabatic expansion occurs as an exchange between internal energy dE, pressure, P, and varying volume, dV. We may rewrite as, $\dot{E} + P\dot{V} = 0$. Assuming an expanding sphere (driven by a time-varying scale factor, $a(t)$), we have,

$$\dot{V} = \frac{4\pi}{3} r^3 3a^2\dot{a} = 3HV. \tag{1.6}$$

Assuming, $\rho(t)$ is the energy density of the system, $E(t) = \rho(t)V(t)$. We can then express the changing energy density, given the current energy density, pressure, and Hubble's parameter. This is the continuity equation, which also applies in a relativistic context as derived.

We can also define the time evolution of the scale factor or expansion of the universe in terms of the evolving energy density. This is referred to as the Friedmann I equation,

$$\left(\frac{\dot{a}}{a}\right)^2 = \frac{8\pi G}{3}\rho + \frac{\kappa}{R_0^2}\frac{1}{a^2}. \tag{1.7}$$

The notion of this expression can derived through considering Newtonian acceleration of a radial surface at time t, but is stated here for a relativistic context. Here, G, is the gravitational constant, R_0 is the radius of curvature, and κ is a curvature parameter determined by the assumption of a closed ($\kappa = +1$, spherical), flat ($\kappa = 0$, Euclidean), or open ($\kappa = -1$, hyperbolic) geometry. Given the measured Hubble parameter, we can also consider a critical density, ρ_{crit} such that the universe would be flat,

$$\rho_{\text{crit}} = \frac{3H^2}{8\pi G}. \tag{1.8}$$

Last, we can also introduce the Friedmann II equation, or acceleration equation, which relates acceleration to both pressure and energy density,

$$\frac{\ddot{a}}{a} = -\frac{4\pi G}{3}(\rho + 3P). \tag{1.9}$$

These three equations are not entirely independent – only two are required to describe the system. Solving these equations requires a specific description of the energy content, the pressure and energy density of each component. We can define an equation of state for each component, the relative pressure and energy density, ω,

$$\omega = \frac{P}{\rho}. \tag{1.10}$$

We treat the components of the universe as fluid-like or uniform in density. Based on their differing equations of state, we consider just three components – radiation, matter and dark energy. The density of each at a given time can be parametrized relative to the total

required critical density. For radiation, matter and dark energy, we have,

$$\Omega_R \equiv \frac{\rho_R(t_0)}{\rho_{\text{crit}}(t_0)}, \tag{1.11}$$

$$\Omega_M \equiv \frac{\rho_M(t_0)}{\rho_{\text{crit}}(t_0)}, \tag{1.12}$$

$$\Omega_\Lambda \equiv \frac{\rho_\Lambda(t_0)}{\rho_{\text{crit}}(t_0)}. \tag{1.13}$$

The density offset from flatness can be described as,

$$\Omega_k \equiv 1 - \Omega_M - \Omega_R - \Omega_\Lambda. \tag{1.14}$$

After considering the evolution of each component (dependence on scale factor), we can consider a relationship between these components, scale factor and time. We note that the value, ω, is here used only to describe the equation of state of dark energy,

$$\frac{da}{adt} = H_0\left(\Omega_M a^{-3} + \Omega_R a^{-4} + \Omega_\Lambda a^{-3(1+\omega)} + \Omega_k a^{-2}\right)^{1/2}. \tag{1.15}$$

Further explanations for the time-evolution of each component can be referenced in existing literature [Huterer, 2023]. With this review, we note that there is great interest in measuring these cosmological parameters, the relative densities of these different components. Experimental measurements suggest a nearly flat universe, though there is still substantial uncertainty, ultimately impacting our knowledge of the origin and fate of our universe [Planck Collaboration, 2020]. We expect there to have been three relevant epochs in the universe, an early radiation-dominated era, a matter-dominated era and most recently (and currently) a dark-energy-dominated era. In each period, the dominating component largely sets the rate of expansion and varying temperature, T of the system.

1.2.1 Fundamental Symmetries and the Standard Model

While the continued structural development of gravitationally bound systems largely depends on lower-energy, non-relativistic matter, fundamental particles and symmetries which are generally probed at the highest energies may provide some insight into the most energetically dense and dynamic regions in the universe. The Standard Model (SM) is a minimal

working representation of (almost) all known free parameters and symmetries governing the observed physical universe.

The Lagrangian satisfies three group symmetries [Peskin and Schroeder, 1995]:

$$SU(3)_C \times SU(2)_L \times U(1)_Y. \tag{1.16}$$

The special unitary group, $SU(3)_C$, describes the space of matrix transformations which preserve the unit normalization of three vectors. This symmetry describes the color space of the model – specifically the color mediated in strong force interactions. Only colorless particles are observed. This concept of color confinement is maintained with this symmetry.

The special unitary group, $SU(2)_L$ and unitary group $U(1)_Y$ describe other symmetries which do not involve color – left-handed Fermi interactions and hypercharge in the electroweak theory. The $SU(2)_L$ group represents the existence of left-handed fermion doublets (right-handed anti-fermion doublets). These particles are observed with nonzero, weak isospin, forming pairs. Right-handed fermions have no weak isospin, and exist individually in singlets. These relations pair generation members of charged leptons and neutrinos, and generation members of quarks. The hypercharge quantum number is then determined from this projected isospin and the electromagnetic charge via the Gell-Mann–Nishijima formula, $Y = 2(Q - I_3)$.

	I	II	III	I_3	Y	Q
Leptons	$\begin{pmatrix}\nu_e\\ e\end{pmatrix}_L$	$\begin{pmatrix}\nu_\mu\\ \mu\end{pmatrix}_L$	$\begin{pmatrix}\nu_\tau\\ \tau\end{pmatrix}_L$	$+1/2$ $-1/2$	-1 -1	0 -1
	e_R	μ_R	τ_R	0	-2	-1
Quarks	$\begin{pmatrix}u\\ d\end{pmatrix}_L$	$\begin{pmatrix}c\\ s\end{pmatrix}_L$	$\begin{pmatrix}t\\ b\end{pmatrix}_L$	$+1/2$ $-1/2$	$+1/3$ $+1/3$	$+2/3$ $-1/3$
	u_R	c_R	t_R	0	$+4/3$	$+2/3$
	d_R	s_R	b_R	0	$-2/3$	$-1/3$

Figure 1.1 Observed charge, weak isospin and hypercharge for quarks and leptons Grefe [2014].

The two special unitary symmetries introduce 8 and 3 force carriers to the theory, following the dimensionality of generators introduced with $SU(3)$ and $SU(2)$. These first eight

bosons represent the basis of color combinations which can be taken with a gluon. The following three bosons, W_1, W_2 and W_3 represent weak force carriers. Last, an additional neutral boson is introduced from the hypercharge symmetry, B.

The first two weak carriers rotate together to form the observed W^+, W^- mass eigenstates,

$$W^+ = \frac{W_1 - iW_2}{\sqrt{2}},\ W^- = \frac{W_1 + iW_2}{\sqrt{2}}. \tag{1.17}$$

The third weak carrier and neutral boson compose the photon and Z mass eigenstates:

$$\begin{bmatrix} \gamma \\ Z \end{bmatrix} = \begin{bmatrix} \cos(\theta_W) & \sin(\theta_W) \\ -\sin(\theta_W) & \cos(\theta_W) \end{bmatrix} \begin{bmatrix} B \\ W_3 \end{bmatrix}. \tag{1.18}$$

Here, θ_W is the Weinberg mixing angle.

Last, a final mechanism is needed to set the masses of particles. This symmetry breaking occurs through a phase shift in the Goldstone boson, ϕ, representing the vacuum,

$$\phi = \begin{bmatrix} (V + i\phi^o)/\sqrt{2} \\ \phi^o/\sqrt{2} \end{bmatrix} \rightarrow \begin{bmatrix} (V + h)/\sqrt{2} \\ 0 \end{bmatrix}. \tag{1.19}$$

Here, V is the vacuum expectation, and h is the Higgs expectation. Three free parameters, ϕ^o, ϕ^+ and ϕ^- can be considered. When symmetry is spontaneously broken, the parameter ϕ^o settles to a specific value, and the freedom of one Goldstone boson is lost. The action of the covariant derivative on this field,

$$D_\mu = \partial_\mu + ig_2 W_\mu^a \tau^a, \tag{1.20}$$

$$(D_\mu\phi)(D_\mu\phi) \rightarrow \left(\frac{g_2 V}{\sqrt{2}}\right)^2 W^+W^- = M_W^2 W^+W^-. \tag{1.21}$$

Here, g_2 is the gauge coupling, W_μ^a represents the weak boson fields, and τ^a is the set of Pauli matrices. The now specified Higgs boson sets the mass of the W bosons, M_W. A similar constraint sets the mass of the Z boson. The specification of the three parameters, ϕ^o, ϕ^+ and ϕ^-, removes longitudinal freedoms from the Goldstone field, and imparts masses to the

three weak bosons [Higgs, 1964, Englert and Brout, 1964, Guralnik et al., 1964]. In this way, the Higgs mass, W^+, W^- and Z masses are specified, while no such symmetry breaking is present to set the masses of the gluon and photon. This splitting of the electroweak forces is expected to have taken place approximately 10^{-11} seconds after the Big Bang.

In summary, the fermionic elementary particles, leptons and quarks, are observed to obey a number of symmetries in nature. Describing these symmetries and explicit freedoms introduces a number of communicative forces represented by bosons. The full Lagrangian can be written to express this content. We can first consider the covariant derivative which is used to express the kinetic terms of this system:

$$D_\mu = \partial_\mu - ig_1\frac{Y}{2}B_\mu - ig_2\frac{\tau^j}{2}W_\mu^j - ig_3\frac{\lambda^a}{2}G_\mu^a. \tag{1.22}$$

- The second term acts on all fields of hypercharge, including left-handed fermionic doublets, right-handed singlets, and bosons. g_1 is the gauge coupling, Y is the hypercharge quantum number and unit matrix used for the symmetry group $U(1)$, and B_μ is the vector potential of the neutral boson.

- The third term represents the action of the weak force, acting only on $SU(2)$ doublets. g_2 is the gauge coupling, τ^j are the Pauli matrices used as generators for $SU(2)$, and W_μ^j are the vector potentials of the three weak bosons.

- The last term represents the action of colored fermions, quarks, following $SU(3)$. g_3 is the gauge coupling, λ^a are the eight Gell-Mann matrices spanning the space of $SU(3)$, and G_μ^a are the vector potentials of the eight possible gluon color combinations.

The general Lagrangian will consist of kinetic terms for both fermions and bosons, $\mathscr{L}_{f,kin}$, $\mathscr{L}_{b,kin}$, interaction terms for electroweak and QCD processes, $\mathscr{L}_{f,int}$, terms for massive particle, $\mathscr{L}_{mass}$, and the energy associated with scalar fields, $\mathscr{L}_\phi$:

$$\mathscr{L}_{SM} = \mathscr{L}_{f,kin} + \mathscr{L}_{b,kin} + \mathscr{L}_{mass} + \mathscr{L}_{f,int} + \mathscr{L}_\phi. \tag{1.23}$$

While the Standard Model provides a description of action for three forces – the weak, strong and electromagnetic, the fourth known force, gravity, is not yet agreeably included within this model. A quantized model of gravity is not agreed upon. Ultimately, many hope for a unified model to describe the most fundamental symmetries of the earliest universe. As the electroweak forces were known to split through spontaneous symmetry breaking, it is attractive to consider that the strong force and gravity may have also emerged through similar mechanisms at an earlier point.

1.3 Structure Formation

After separation of the electromagnetic and weak forces, a hot plasma of quarks, gluons, charged and neutral leptons and photons was present. Only as the universe expanded was the relatively short-range interaction of the strong force insufficient to maintain the quark-gluon plasma, forcing a transition to bound hadrons around 10^6 seconds after the Big Bang [Huterer, 2023].

Subsequently, the high-energy density ($T \gg 10\text{MeV}$) at this time allowed for the pair production of electron-positron pairs via,

$$\gamma + \gamma \leftrightarrow e^- + e^+. \tag{1.24}$$

Weak-force interactions then allowed for transitions of the form,

$$n + \nu_e \leftrightarrow p + e^- \tag{1.25}$$

$$n + e^+ \leftrightarrow p + \bar{\nu}_e. \tag{1.26}$$

Protons and neutrons were then in thermodynamic equilibrium. Similarly, neutrinos were kept in equilibrium following the reaction,

$$\nu_e + \bar{\nu}_e \leftrightarrow e^- + e^+. \tag{1.27}$$

Neutrino scatterings depend on the weak cross section, σ_w, and the temperature, T. During this radiation dominated era, $T \propto a^{-1} \propto t^{-1/2}$. The result is a scattering rate decreasing

with time, becoming lower than the expansion rate and allowing for neutrino escape,

$$\Gamma = n_\nu c \sigma_w \propto a^{-3} T^2 \propto T^5 \propto t^{-5/2}. \tag{1.28}$$

After this transition, there was a decoupling between neutrons and protons. As neutrons are unstable and decay on the order of 15 minutes, this brief period in the early universe allowed for formation of lightest nuclei after hydrogen – deuterium, tritium, helium-4, beryllium and lithium. As the most favorable reactions proceeded first, neutrons, protons, and the produced elements were utilized in successive reactions forming heavier elements. A number of factors contribute to the slow or bottleneck of this early nucleosynthesis, meaning only the production of lighter elements were ultimately in this process.

Notably, these earliest nuclei were not necessarily neutral elements. At this time, equilibrium with an electron-photon plasma prevented stable neutral elements. Only ∼378,000 years after the Big Bang did this plasma decouple in a process known as reionization. Again, as cross section for photon-electron scattering depends on the expansion rate of the universe, continued expansion leads to a period in which photon escape is more probable than the expectation for a scatter. At this time, free-streaming photons exit the plasma and are observed as the relic CMB. The remaining electrons are now able to stably bind with present nuclei, less likely to be broken or excited by radiation.

This now matter-dominated universe then underwent a period of gravitational structure formation. On the largest scales, gravity competes with expansion and structure formation is largely linear. On smaller scales, structure formation is nonlinear and must be modeled through simulation. Structure formation is hierarchical. Stars and globular clusters developed first, leading to galaxies, groups and clusters. Only very recently (∼8 billion years after the Big Bang) has the universe transitioned to a phase dominated by dark-energy energy. Today, expansion of the universe accelerates, meaning the era of maximal structure formation has passed. Measurement of the distributions of gravitationally bound systems in both the early and late universe provides sensitivity to these cosmological components

and relevant parameters controlling expansion. In this era of precision cosmology, many are interested in systematics impacting structure formation at this late stage of the universe.

1.4 Active Galactic Nuclei

At the centers of modern spiral galaxies are supermassive black holes (SMBH), expected to reach up to tens of billions of solar masses. It is unclear how black holes (BHs) might have seeded galaxy formation in the early universe, whether they existed prior, formed along with the youngest stellar clusters, or had a later origination. It is clear that supermassive black holes have played a major role in regulating galaxy growth, especially for the oldest, most massive spiral galaxies. In the most extreme cases, this effect can also disrupt galaxy group and cluster formation. Feedback from the central, accreting black hole or active galactic nuclei (AGN) is responsible.

1.4.1 AGN Feedback

AGN generally consist of of a SMBH, an accretion flow of matter, and its surrounding non-vacuum environment. This accretion disk is unstable and will experience energy dissipation through a number of processes. The result is radiation and a flow of matter both to the black hole and towards the containing galaxy or structure [Fabian, 2012, Hardcastle and Croston, 2020]. This feedback from the AGN can take multiple forms depending on the conditions of turbulence present in the accretion disk and environment.

A quasar or "quasi-stellar radio source" is an AGN in which the accretion flow consists of approximately Keplerian orbits. Frictive interactions between concentric, quasi-stable accretion rings produces thermal emission, slowly lowering the overall energy of the flow with time. The result is a galactic center with high X-ray luminosity. In extreme cases, the outwards radiation pressure may exceed the gravitational force of the black hole, ceasing continued accretion. This maximal luminosity is known as the Eddington Luminosity, L_{Edd}. At the same time, the lower-energy matter will spiral inwards, tending to exhaust the material. Radiation and winds driven by this feedback tend to disrupt the inwards flow of material towards the galaxy and black hole, naturally linking the size of the black hole and

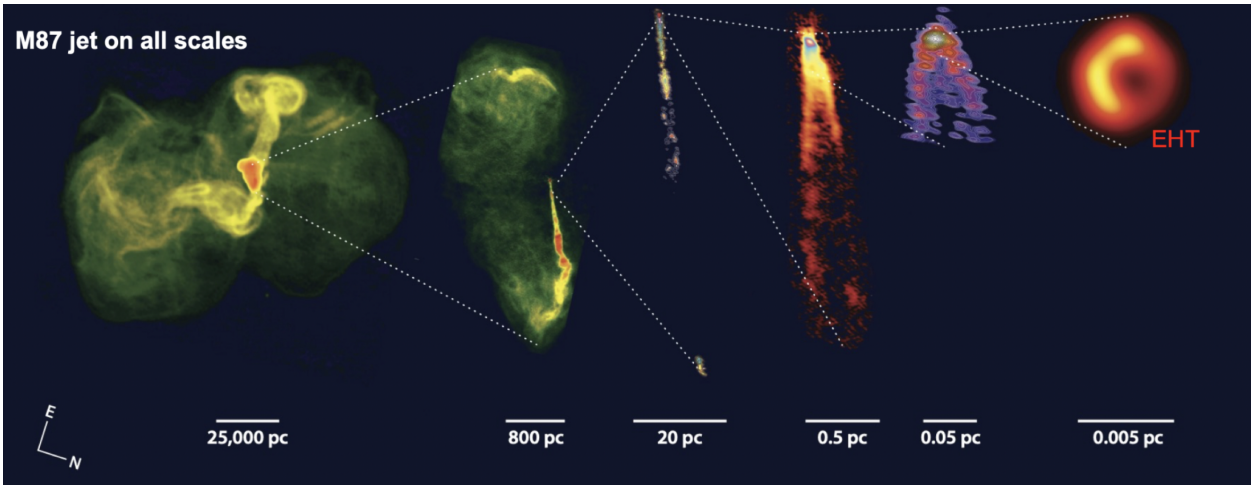

Figure 1.2 The M87 radio jet at multiple spatial scales [Blandford et al., 2019]. At the left, we have the galactic-scale radio lobes from the NRAO, 90-cm VLA. In order from left to right, the central three images correspond to the collimated jet structure at decreasing size scale, imaged by NRAO 20-cm VLA, 20-cm VLBA, and 7-mm VLBA, respectively. The fifth image from the left represents the radio jet base, or parabolic jet launching region, observed by the 3-mm global VLBI network. The right-most image is the central black hole and photon ring, taken by the 1.3-mm Event Horizon Telescope.

galaxy. The formation of stars and other structures within the galaxy is also perturbed.

If substantial turbulence is present within the accretion disk or environment, the formation of a bipolar jet also becomes possible. Jets form from electromagnetic perturbations relating the accretion flow and its environment. Material and energy is carried away from the galactic center. These jets may be sub-relativistic, taking the form of dispersive winds, or relativistic in the form of highly-directed jets. The exact properties of the jet relate to the form of impact on the galactic environment or larger structure. One of the most well-studied radio AGN, M87, exhibits highly-collimated dual jets. At largest scales, these jets interact with the gaseous environment of its host galaxy. The jet morphology is presented in Fig. 2.1. An understanding of jet formation, propagation and interaction has become increasingly important for models of cosmological evolution.

CHAPTER 2

MODELS OF JET PRODUCTION

2.1 Accretion and Angular Momentum Transport

The accretion material associated with any compact object has some relative angular momentum. To allow for accretion and inward flow, the outward transport of angular momentum is required. In the presence of magnetic fields, disks with differential rotation experience magnetorotational instability (MRI). Small perturbations couple neighboring fluid cells through magnetic tension. As inner fluid components orbit more rapidly, angular momentum is transferred outward. The perturbation tends to grow exponentially. This nonlinear evolution is a form of magnetohydrodynamic turbulence, allowing for the transport of angular momentum out of the central system and subsequent accretion inwards [Balbus and Hawley, 1991, 1998].

2.2 The Disk-Jet System

The connection between turbulence in the disk and properties of the jet is a active area of research [Miller et al., 2012]. We describe a simple model which allows for the formation of a bipolar jet. We consider a black hole of some mass M_{BH} and spin a. The Schwarzschild radius, characterizing the radius of the event horizon, is,

$$r_s = \frac{2GM}{c^2}. \tag{2.1}$$

An accretion disk with angular momentum L of size tens-hundreds of r_s is established around the black hole. As thermal forces produce a hot and ionized flow, currents, J are frozen into the accretion disk [Shakura and Sunyaev, 1973]. These currents establish a poloidal magnetic field structure, threading the black hole and accretion disk with vertical field lines. Due to these high temperatures and free charges, we can assume a an ideal, highly conducting fluid,

$$J = \sigma\left(\frac{\vec{v}}{c} \times \vec{B} + \vec{E}\right). \tag{2.2}$$

Here, $\vec{v}$ is the velocity of the current flow and σ is the electric conductivity. A Finite current implies,

$$\frac{\vec{v}}{c} \times \vec{B} + \vec{E} \approx 0. \tag{2.3}$$

If we solve for the electric field, take the curl, and apply the Maxwell-Faraday relation,

$$\nabla \times E = \nabla \times \frac{\vec{v} \times B}{c} = -\frac{1}{c}\frac{dB}{dt}. \tag{2.4}$$

This implies that a change in the magnetic field is sufficient to conserve the magnetic flux flowing along with the fluid. The magnetic field will follow perturbations to the fluid and likewise.

The Blandford-Znajek and Blandford-Payne (BZ and BP) processes describe two processes in which perturbations to the magnetic field (and to the magnetic flux and material) result in bipolar jets driven by the dissipation of energy stored in either the black hole spin or accretion disk angular momentum [Tchekhovskoy et al., 2012]. In both cases, the existence of free charges in the environment around the disk-jet system naturally disrupts the poloidal magnetic field and toroidal accretion flow. The result is a net current flow in the direction perpendicular to the plane of the accretion disk. Owing to the frozen magnetic flux, a component of the magnetic field now connects instead to the local environment. As the system (black hole or accretion disk) continues to rotate, this plasma flow is wound, representing a new toroidal magnetic flux component, synonymous with the jet.

In the case of a rotating, Kerr black hole, vertical magnetic field lines threading the frame of the black hole drive the jet [Tchekhovskoy et al., 2012]. The work performed to move charges away from the black hole acts to brake it. This is the Blandford-Znajek process, which is discussed in depth elsewhere [Blandford and Znajek, 1977].

The rotation of the accretion disk provides an additional opportunity to wind the field lines of a vertically threading magnetic field. Again, the work to produce wound magnetic field lines and to remove charges results in a braking of the disk. This is known as the Blandford-Payne process [Blandford and Payne, 1982]. If black holes do not have an intrinsic

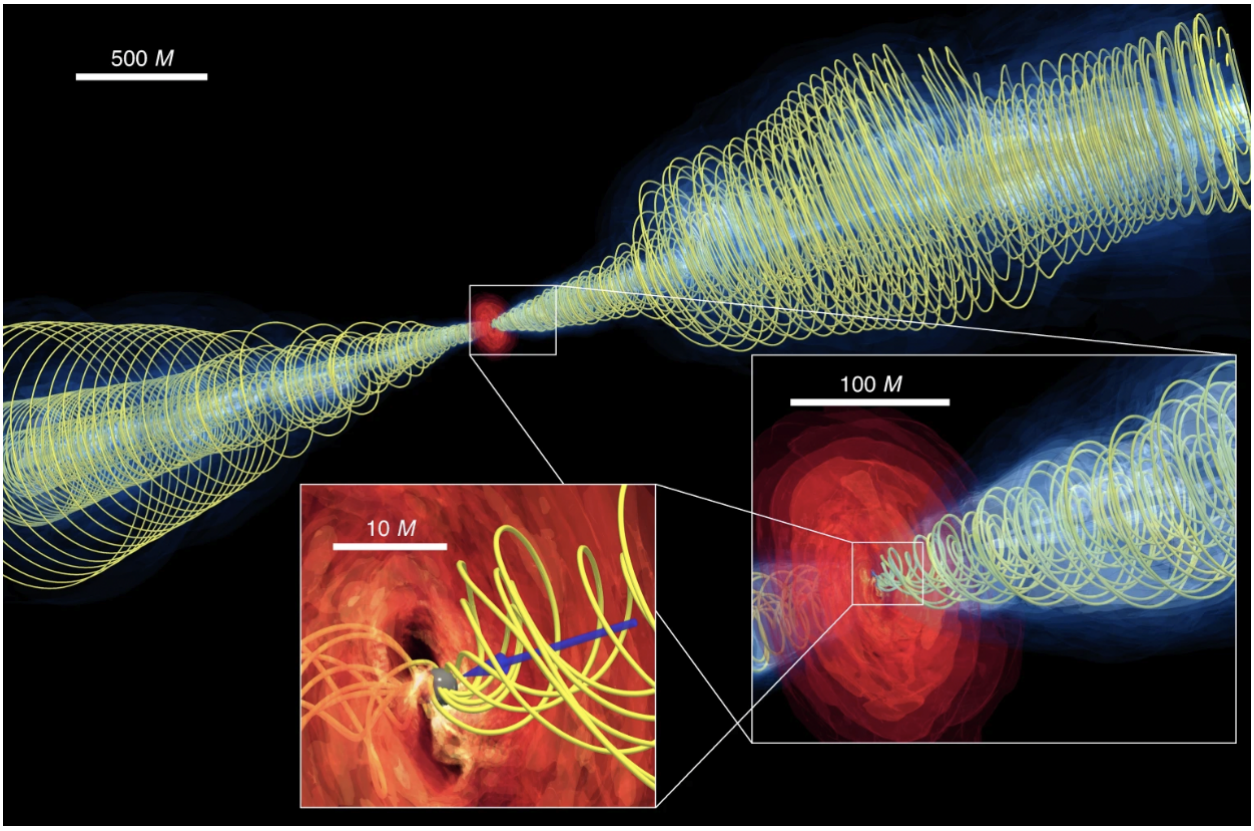

Figure 2.1 An image of simulated disk and jet magnetic field structure [Cruz-Osorio et al., 2021]. The structure reflects a 3D general-relativistic magneto-hydrodynamic (GRMHD) simulation for a rotating black hole with magnetic field structure and accretion fluid flow. The dense accretion material is shown in red, while dilute material within the jet is shown in blue. The yellow lines represent helical magnetic field structure. M is a gravitational length unit.

spin, as in the case of a Schwarzschild black hole, jets would need to be driven in this way. However, the power expected from this process is substantially less than what is observed from real jets, suggesting that the BP process is subdominant to BZ at least in the case of AGN jets. If both processes drive jet formation, we would also expect to see a 'spine-sheath' structure, an inner, more-powerful, relativistic and highly-collimated jet driven by BZ, surrounded at the base by a weaker, less-collimated jet driven by BP. Such a structure has been observed.

2.3 Energetics of the Jet

The acceleration of material in the jet is set by the supported magnetic field structure. As magnetic field lines are continually wound, the freshly wound lines carrying plasma exert

pressure on each other, tending to unwind at larger distances. This apparent collimation at the base of the jet sets the collimation angle, ϕ.

Plasma at the base of the jet is highly collimated and confined to a small region. In the frame of a test charge, q an outward magnetic force, $\vec{F_q}$, acts to counteract an apparent centrifugal force,

$$\vec{F_q} = q\left(\frac{\vec{v}}{c} \times \vec{B}_\perp\right). \tag{2.5}$$

Here, $\vec{B}_\perp$ is the component of the magnetic field along the edge of the cone of the jet and perpendicular to the charge velocity, $\vec{v}$. As the curvature and collimation of the jet changes at larger distances, this sets the maximal velocity achieved by the charge or plasma, the 'bulk Lorentz factor'. When the jet radius is effectively constant, F_q no longer has a component parallel to the jet, and acceleration ends [Blandford and Znajek, 1977].

It's also worth considering the maximal power of the jetted material. For a black hole of radius,

$$r_g = \frac{GM}{c^2}, \tag{2.6}$$

we can estimate a power of,

$$P_j \approx a^2 B^2 r_g^2 c \propto \Phi^2 \left(\frac{a}{r_g}\right)^2. \tag{2.7}$$

The maximal power is approximately the magnetic energy flux through an area spanned by the black hole modulated by the driving angular momentum or spin, per unit time. Here, the magnetic flux, $\Phi \approx B r_g^2$ [Tchekhovskoy et al., 2012]. In the case of active galactic nuclei, the black hole spin is not expected to vary dramatically on observable timescales. However, the magnetic flux or bulk amount of plasma will vary notably.

CHAPTER 3

THE SUB-KILOPARSEC BLAZAR JET

At the smallest jet scales, we have an opportunity to study jet formation, turbulence in the accretion disk and along the jet, the accelerated material driven into the jet, and thermal non-thermal processes occurring in this environment.

3.1 The Jet Environment, Atmosphere

The inner kiloparsec essentially hosts its own atmosphere relative to the quickly varying jet. At the very base of the jet, in the inner tens-hundreds of light days, the accretion disk is generally associated with a multicolor thermal blackbody spectrum. At different distances from the jet, frictive interactions allow for energy dissipation, generally ranging from optical to ultraviolet [Shakura and Sunyaev, 1973].

In the inner few-hundred light days, hot gas is photoionized, resulting in observable broad emission lines. This 'broad line region' (BLR) is commonly associated with H and He Lyman-alpha emission, which are often prominent. The BLR is optically thick, meaning ionizing gamma-ray radiation produced from within is not directly observable, obscuring the highest-energy base of the jet. The BLR may represent a wind driven by the central accretion disk.

Within the central light years, a region of dust known as the 'torus' is present. The torus is associated with infrared thermal emission. In cases where the jet is not aligned with the observer, this dust may act to obscure emission from the inner central bright AGN. The torus may represent a failed or extended accretion flow to the central accretion disk.

At further distances, within the inner kiloparsec, are additional filaments of cooled gas associated with narrow-line emission or forbidden lines. Examples include [OIII], [OII], [OI], [NeIII], [NeV], [NII], in addition to others.

Only beyond a few-hundred parsecs or kiloparsecs is there substantial interstellar medium, the gas commonly associated with the climate of the surrounding galaxy and star formation.

3.2 Particle Acceleration

While the bulk Lorentz factor of material within the jet is set by energetics of the BH, disk and surrounding environment, charged particles and nuclei are initially accelerated to a non-thermal energy spectrum. Processes of turbulence within the accretion disk or at the very base of the jet are expected to lift thermal distributions of particles to non-thermal distributions. These kinematically excited populations of particles are only then accelerated to a bulk velocity and Lorentz factor as they exit via the jet.

At the accretion disk, closest to the black hole, and kinks along the jet, magnetic reconnection is expected to play a role in the acceleration of charged particles [Lyubarsky, 2005, Sironi and Spitkovsky, 2014]. At a boundary, magnetic field lines pointing in opposite directions may come into near contact. If these magnetic field lines break and reconnect, a localized, strong electric field develops. This transient electric field will accelerate the local plasma of charged particles. The resulting energy distribution of particles moving through the reconnection zone is a power law,

$$\frac{dN(\epsilon)}{d\epsilon} \propto \epsilon^{-p}. \tag{3.1}$$

Here, ϵ is some energy of a particle species.

At the base and along the jet, Fermi acceleration is expected to dominate. In first-order Fermi acceleration, charged particles may be reflected back-and-forth over a shock front, potentially by scattered magnetic interactions [Fermi, 1949, Blandford and Ostriker, 1978]. The result is a successively increased velocity. The energy distribution of a number of particles potentially experiencing these kinematic boosts is a power law. In general, the index, $p \gtrsim 2$. In second-order Fermi acceleration, or diffusive shock acceleration, scattered magnetic fields again lead to successive velocity perturbations, resulting in a power-law energy distribution.

3.3 Non-Thermal Emission

Accelerated energy distributions of electrons and protons,

$$\frac{dN_e}{dE} \text{ and } \frac{dN_p}{dE}, \tag{3.2}$$

participate in high-energy inelastic collisions and scatters with each other, present radiation and other particles. Here, protons are taken to represent free protons as well as hydrogen nuclei, and are must abundant relative to the nuclei of heavier elements. The mass of the proton is related to the electron as, $m_p \approx 1836 m_e$. While the intensity and energy range of accelerated protons is less well known, electrons are expected to reach high energies.

Two primary processes driven by leptonic (electron) populations are regularly cited as likely explanations for the broadband continuum electromagnetic emission observed from AGN. First, in the presence of a magnetic field $\vec{B}$, electrons or other charged particles will move on a curved path, producing synchrotron radiation at a frequency related to this curvature [Rybicki and Lightman, 1986, Blumenthal and Gould, 1970]. While the general solution involves a full consideration for particle dynamics in response to the magnetic field, we can treat the approximation of an electron in circular orbit. Such a particle orbits at frequency,

$$\omega_B = \frac{\omega_G}{\gamma} = \frac{q_e B}{m_e \gamma c}. \tag{3.3}$$

Here, q_e, m_e and γ are the electron charge, mass and relativistic electron Lorentz factor. B is the component of magnetic field strength perpendicular to the plane of particle motion. ω_G is the non-relativistic gyroradius.

The power radiated by a single electron is,

$$P = \frac{2e^2}{3c^3}\gamma^2 \frac{e^2 B^2}{m_e^2 c^2}\nu^2 \sin^2\alpha. \tag{3.4}$$

This depends only on the electron kinetic energy, the pitch angle α between the electron's velocity and magnetic field, and the magnetic energy density, $U_B = B^2/(8\pi)$. The power as a function of frequency, ν, for a single electron is,

$$P(\nu) = \frac{\sqrt{3} e^3 B \sin\alpha}{m_e c^2}\left(\frac{\nu}{\nu_c}\right)\int_{\nu/\nu_c}^{\infty} K_{5/3}(\eta) d\eta. \tag{3.5}$$

Here, ν_c is the critical frequency, defined in terms of ν_G (in analog to ω_G),

$$\nu_c = \frac{3}{2}\gamma^2 \nu_G \sin\,\alpha. \tag{3.6}$$

The synchrotron emissivity is,

$$\left(\frac{dN}{dE_\gamma dt}\right)_{\rm syn} = \frac{\sqrt{3}}{2\pi}\frac{e^3 B\,\sin\,\alpha}{m_e c^2 \hbar E_\gamma}\int_{E_\gamma/E_c}^{\infty} K_{5/3}(\eta)d\eta. \tag{3.7}$$

$K_{5/3}$ is a modified Bessel function. The critical energy, E_c is defined in analog to the critical frequency, ν_c. E_γ represents the photon energy, such that $E_\gamma = h\nu$, where h is Planck's constant. As the emission is observed from a relativistic source in circular motion, electrons orbiting towards and away from the observer span a range of frequencies.

For a distribution, dN_e/dE, $dN_e = N_{\rm e}(\gamma)d\gamma$, the resulting spectrum of synchrotron radiation is,

$$\left(\frac{dN_{\rm tot}}{dE_\gamma dt}\right)_{\rm syn} = \int_{\gamma_{\rm min}}^{\gamma_{\rm max}} N_{\rm e}(\gamma)\frac{dN}{dE_\gamma dt}(\gamma)d\gamma \tag{3.8}$$

The result is a continuum spectrum of emission extending from radio to X-ray frequencies in AGN.

This produced radiation may scatter off the initial electron population in the process of synchrotron self-Compton [Rybicki and Lightman, 1986, Blumenthal and Gould, 1970]. More generally, background photon fields produced at the source (internal inverse-Compton) or from background starlight (external inverse-Compton), may contribute to this scattering process. If we have a photon field of differential density,

$$n(\varepsilon) = \frac{dn}{d\varepsilon dV}, \tag{3.9}$$

the general result for inverse-Compton emissivity is given by,

$$\left(\frac{dN}{dE_\gamma dt}\right)_{\rm IC} = \frac{2\pi r_e^2 m_e c^3}{\gamma}\frac{n(\varepsilon)d\varepsilon}{\varepsilon}\left[2q\ln q + (1+2q)(1-q) + \frac{1}{2}\frac{(\Gamma_e q)^2}{1+\Gamma_e q}(1-q)\right], \tag{3.10}$$

where, $\Gamma_e = 4\varepsilon\gamma/m_e c^2$, $q = E_1/\Gamma_e(1-E_1)$. The energy of the up-scattered photon, E_γ, is such that $E_\gamma = E_1\gamma m_e c^2$. This is the energy distribution of the resulting scattered photon

from a specific electron of energy, $\gamma m_e c^2$. The energy of up-scattered photon is defined in terms of this initial electron energy and a scale, $\epsilon_1 = \gamma m_e c^2 E_1$. In the Thomson limit, $\Gamma_e \ll 1$ and $E_1 \ll 1$, photon scatters result in only a small energy transfer. In the Klein-Nishina limit that $\Gamma_e \gg 1$, the electron energy losses of individual scatters becomes important. Large fractions of the initial electron energy are lost. This sets a natural limit on the energy of radiation produced through inverse-Compton processes. The resulting continuum spectrum spans from X-rays to gamma rays in AGN.

While less critical for the environments of AGN jets, annihilation is also expected in regions of high gamma-ray density,

$$\gamma + \gamma \rightarrow e^+ + e^-. \tag{3.11}$$

Here, the symbol, γ is used to represent to colliding photons [Gould and Schréder, 1967].

The role of accelerated hadronic populations or protons in the jets of AGN is less understood. While a similar number density of protons is expected relative to electrons in the accretion material, their substantially greater mass means they are less efficiently accelerated. It's unclear at what intensity and to what maximal energy are protons accelerated to in the vicinity of the accretion disk near the base of the jet. It is then also unclear the integral intensity of protons making it to the jet to be boosted or further accelerated. If high-energy protons are present in these regions, a number of additional processes become feasible, allowing for the production of additional particles and non-thermal radiation.

In the Bethe Heitler process, a photon scattered from a proton, p, produces an electron-positron pair,

$$p + \gamma \rightarrow p + e^+ + e^-. \tag{3.12}$$

The resulting leptons will participate in synchrotron and self-Compton processes as long as a magnetic field is present.

Similarly, scatters between protons and photons can indirectly lead to electron production through pion and muon decay,

$$p + \gamma \rightarrow \pi \rightarrow \mu \rightarrow e. \tag{3.13}$$

Again, this decay process offers a source of leptons for synchrotron and self-Compton processes.

3.4 Neutrino Production in the Jet

Notably, the presence of a hadronic population allows for neutrino production via two common channels [Murase and Stecker, 2023]. In the first, proton-proton collisions produce charged and neutral pions,

$$p + p \rightarrow \begin{cases} \pi^0 + X & 1/3 \text{ of time}, \\ \pi^+ + X & 1/3 \text{ of time}, \\ \pi^- + X & 1/3 \text{ of time}. \end{cases} \tag{3.14}$$

Here, X are additional products of the collision. While the neutral pion may decay further to gamma rays, the charged pions decay to neutrinos,

$$\pi^+ \rightarrow \mu^+ + \nu_\mu \rightarrow \bar{\nu}_\mu + e^+ + \nu_e + \nu_\mu, \tag{3.15}$$

$$\pi^- \rightarrow \mu^- + \bar{\nu}_\mu \rightarrow \nu_\mu + e^- + \bar{\nu}_e + \bar{\nu}_\mu. \tag{3.16}$$

pp neutrino production is feasible at any proton energy. It is most efficient in proton-dense regions. The resulting ratio of neutrino flavors at the source follows, $(\bar{\nu}_e, \bar{\nu}_\mu, \bar{\nu}_\tau) = (\nu_e, \nu_\mu, \nu_\tau) = (1 : 2 : 0)$.

At high enough center-of-mass energies, an additional channel for neutrino production from photon and nuclei collisions opens,

$$p + \gamma \rightarrow \Delta^+ \rightarrow \begin{cases} \pi^+ + n & 1/3 \text{ time}, \\ \pi^0 + p & 2/3 \text{ time}. \end{cases} \tag{3.17}$$

Such a process requires the intermediate production of the $\Delta(1232)$ or heavier resonances [Atoyan and Dermer, 2001]. Having a rest mass of 1.232 GeV, this center-of-mass energy is necessary in production of $\Delta(1232)$. In a relativistic inelastic collision between a photon of energy E_γ and proton of energy E_p, the resonance of mass m_Δ must have energy E_Δ,

$$m_\Delta^2 c^4 \lesssim E_\Delta^2 = m_{\rm p}^2 c^4 + 2E_\gamma E_{\rm p} + 2\vec{p}_\gamma \cdot \vec{p}_{\rm p} \approx m_{\rm p}^2 c^4 + 4E_\gamma E_{\rm p}. \tag{3.18}$$

As an example, a ∼20 TeV proton is required in a collision with a ∼10 keV X-ray photon. After pion decay, the exiting neutrinos leave with ∼10% of the initial proton energy. As only the π^+ is produced as a charged pion, the resulting neutrino flavor ratio at the source is, $(\bar{\nu}_e, \bar{\nu}_\mu, \bar{\nu}_\tau) = (0:1:0), (\nu_e, \nu_\mu, \nu_\tau) = (1:1:0)$.

3.5 Observational Effects

A number of effects impact the emission that actually escapes the immediate environment of the AGN accretion disk and jet base. The directed, relativistic nature of the jet also changes the intensity, frequency and timing of the observed emission. Last, the orientation of an AGN relative to an observer greatly impacts the appearance of the source [Urry and Padovani, 1995, Rybicki and Lightman, 1986]

3.5.1 Escaping Radio-Wavelength Radiation

Synchrotron radio emission is produced at high intensity at the jet base, where the magnetic field is largest. As the jet is also most collimated in this region, a relatively dense field of radio photons results along with the initial radiating population of electrons

Electrons of energy $E = \gamma m_e c^2$ primarily radiate near ν_c,

$$\nu_c \approx \frac{\gamma^2 eB}{2\pi m_e c}. \tag{3.19}$$

The Lorentz factor of the approximate corresponding electron is then,

$$\gamma = \left(\frac{2\pi m_e c\nu}{eB}\right)^{1/2}. \tag{3.20}$$

Here, we are assuming electrons of a specific energy emit at a specific frequency. If the resulting photon field at a given frequency is sufficiently dense, the source will become optically thick. The brightness temperature at a given frequency cannot exceed the temperature of the corresponding electron population. In a relativistic gas, we have,

$$T_e = \frac{E}{3k} = \frac{\gamma m_e c^2}{3k} \approx \left(\frac{2\pi m_e c\nu}{eB}\right)^{1/2} \frac{m_e c^2}{3k}. \tag{3.21}$$

Here, k is Boltzmann's constant. The photon intensity is found by equating T_e and the photon temperature in the Rayleigh–Jeans limit:

$$I_\nu \approx \frac{2kT_e\nu^2}{c^2} \propto \nu^{5/2}B^{-1/2}. \tag{3.22}$$

The result is that the synchrotron spectrum of a self-absorbed source follows an index of 5/2. As typical accelerated electron spectra are most intense in number at lower energy, lower-energy radio photons are generally absorbed first. The observed broadband spectrum will feature a break indicating the transition from absorbed to unabsorbed frequencies.

Synchrotron self-absorption also impacts the observed jet morphology and apparent size at a given frequency. If a region has the conditions for self-absorption (involving density and magnetic field), it is opaque to photon escape, and this free streaming will only occur at the edge of the region, which does not satisfy the absorption conditions. In the case of AGN jets, as the base of the jet is smallest in radius and only expands with distance, the base of the jet has the best conditions for self-absorption, and higher relative frequencies can be absorbed. Moving down the jet, this larger radius and lower magnetic field length suggests that only relatively lower frequencies are absorbed. The result is a frequency-dependent morphology. Lower-frequency, absorbed regions appear larger and more extended. The highest-absorbed frequencies, often at millimeter wavelengths, instead trace a smaller, compact region closest to the true jet base and accretion disk.

3.5.2 Escaping Gamma-Ray Radiation

The highest, gamma-ray wavelengths also experience attenuation. Gamma-ray photons produced near the jet base may interact with lower-energy photons in the broad line region, if present. The result is a cascade development, where lower-energy photons continue to interact until the region is effectively transparent or any potential interaction is below the pair production threshold in energy.

$$\gamma_{\text{low}} + \gamma_{\text{high}} \rightarrow e^+ + e^- \rightarrow \gamma + \gamma. \tag{3.23}$$

In this process, initial high-energy photons of energy ϵ are reprocessed to lower energies of $\approx \epsilon/2$. The intermediate electron-positron pair may also participate in synchrotron and inverse-Compton processes, experiencing further energy losses. When the optical depth for these photons, $\tau < 1$, escape is possible. Commonly, $10 - 100$ GeV gamma-rays are reprocessed to MeV-GeV energies [Dermer and Menon, 2009]. As there are only limited observations of extragalactic point sources in the MeV-energy range, the scale of this reprocessing as well as the nature of the initially produced > 10 GeV gamma-ray spectrum is poorly constrained.

3.5.3 Relativistic Effects

As the jet is relativistically beamed, this bulk flow of material experiences a number of relativistic effects in an observers frame [Dermer and Menon, 2009]. The bulk Lorentz factor, Γ, is related to the speed, $v = \beta c$,

$$\Gamma = \frac{1}{\sqrt{1-\beta^2}}. \tag{3.24}$$

If the jet is oriented at an angle, θ, relative to the observer, we define the Doppler factor,

$$\delta = \frac{1}{\Gamma(1-\beta\,\cos(\theta))}. \tag{3.25}$$

We can consider two events of times t_2 and t_1 in the frame of the jet or emission frame, such that $\Delta t_{\rm em} = t_2 - t_1$. Due to time dilation, in the observer frame,

$$\Delta_{\rm obs} - \delta^{-1} t_{\rm em}. \tag{3.26}$$

Similarly, the time between the transmission of successive wavelengths is impacted,

$$\nu_{\rm obs} = \delta \nu_{\rm em}. \tag{3.27}$$

Here, $\nu_{\rm obs}$ is the frequency of observed emission. $\nu_{\rm em}$ is the frequency of emission in the jet frame. The intensity or observed photon rate is also impacted. While radiation is emitted isotopically in the frame of the jet, relativistic aberration beams this radiation into a smaller solid angle, as seen by an observer. Additionally, as photons appear more rapidly due to time dilation in the observers frame, the overall intensity, $I_{\rm em}$ is scaled such that $I_{\rm obs}$,

$$I_{\rm obs} = \delta^3 I_{\rm em}. \tag{3.28}$$

If the energy flux is instead considered, an additional Doppler factor is included in the scaling due to the frequency and energy shift.

3.5.4 Orientation and Classification

Active galactic nuclei have traditionally been classified based on observed spectral properties, regarding both the continuum and line features. The environment of gas and accreting matter around the black hole and the development of jets may vary between sources. The orientation of the disk-jet symmetry axis relative to an observer also has a substantial impact on the observed emission and structure. The dusty torus sits in the plane of the accretion disk at a larger radius. If the observer is also in the plane of the torus, any bipolar jet is oriented perpendicular to this plane, minimally beamed. The torus will obscure emission from the potentially bright accretion disk and inner nucleus. Instead, emission from the galaxy itself will be dominant.

Radio-quiet and radio-loud AGN are essentially differentiated by the presence of the jet and intensity of synchrotron radiation. AGN may be further classified based on the presence of broad and narrow (forbidden) lines. These common types are named in Table 1.

Type Classification	Radio Quiet	Radio Loud
Type 1	Radio Quiet Quasar (RCC) - Possible Broad Absorption Lines Seyfert 1 (Possible Narrow Lines)	Radio Loud Quasar (RLQ) (Steep or Flat Spectrum) Broad Line Radio Galaxy
Type 2	Seyfert 2 (Possible Narrow Lines)	Narrow Line Radio Galaxy
Type 3	LINER	Weak Line Radio Galaxy
Type 0		Blazar: BL Lac/OVV

Table 3.1 Common Classifications Used for AGN. Both radio quiet and radio loud quasars are observed, related to the prominence of the synchrotron continuum spectrum. Type 1 AGN have broad emission lines observed at optical wavelengths. Type 2 AGN have only narrow emission lines. Sources with lower luminosity are described as Type 3. Last, sources with substantial variability at optical wavelengths are described as Type 0.

Early study of the varied spectra of AGN began with optical observations of local spiral galaxies in the 1940s Seyfert [1979]. AGN with visible broad, permitted lines were differentiated (Seyfert 1 galaxies) from those which lacked these lines (Seyfert 2 galaxies). Both

classes also showed selections of narrow, forbidden lines.

Low-luminosity AGN show evidence for activity around the central nucleus through observed emission lines. Such spectra are evidence of low ionization nuclear emission line regions (LINER AGN). These sources are otherwise quiet spiral galaxies. Some uncertainty exists as to whether these emission lines relate to the active nucleus or to starforming regions within the galaxy.

The same spectral lines observed in radio-quiet Type 1 and 2 Seyferts have also been observed from radio bright quasars, with broad-line radio galaxies (BLRG) and narrow-line radio galaxies (NLRG), respectively. Weak-line radio galaxies (WLRG) are also observed, comparable to the radio-quiet LINERs. Blazars are AGN which show substantial optical variability, including BL Lacertae Objects (no notable emission lines), and optically violently variable quasars (OVV) Tadhunter [2008].

Generally, these classifications are not discrete, and these features may be present or feasible in most AGN environments on a continuous scale. However, such prominent spectral and morphological properties can help to reveal the physical nature of the source.

Early attempts at categorical unification suggested the difference between radio-bright and radio-quiet AGN lied in the orientation of the jet relative to the line of sight [Urry and Padovani, 1995]. Jets lying at small angles were observed with superluminous motion, the relativistic aberration effect causing anisotropic emission, beaming. While the jet would appear differently based on this angle, this positioning was not sufficient to explain the presence or total lack of synchrotron continuum spectra between different sources. This orientation was successfully used to explain the existence of radio halos around nuclei, the end-on view of jet lobes.

Alternately, interest in optical and X-ray observations has contributed to unification. It was noted that Seyfert 2 galaxies experience increased extinction relative to Seyfert 1 galaxies, likely related to gas and dust in the regions surrounding the central black hole. Insight into the geometric shapes of these obscuring regions came based on studies of radio

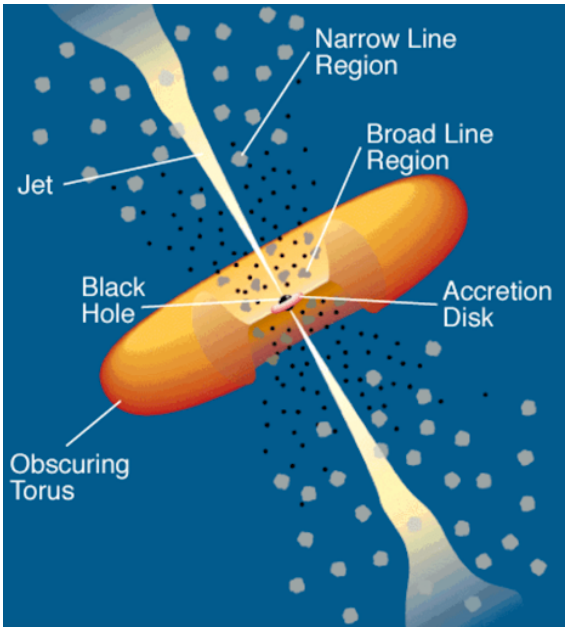

Figure 3.1 The classic schematic AGN. This figure shows the traditional AGN structure assumed in the unified scheme [Urry and Padovani, 1995]. The accretion disk is the small, center-most region around the black hole. The radiative broad line region and obscuring torus are pictured. Dual jets are pictured. The narrow line region is denoted at a distance beyond the torus. While many exceptions exist, AGN classification roughly reflects the viewing angle, obscuration, and beaming of this structure.

galaxies. Narrow line radio galaxies (NLRG) were observed with polarization perpendicular to the radio axis and broad line radio galaxies (BLRG) were found with parallel polarization. This former case was associated with polar scattering on material within an accretion disk facing Earth. In the latter case, equatorial scattering is viewed from the accretion disk viewed on its edge. NGC 1068 was detected with broad, polarized permitted line emission, evidence of an obscured Seyfert 1 nucleus beyond its optically thick accretion torus. This obscuration was the difference between Seyfert 1 and 2 classes.

Relativistic beaming and anisotropic obscuration are considered together in the unified picture. When the radio jet sits at a large angle relative to the observer, the nuclei is obscured, and the source is observed as a NLRG. At less extreme angles, the source is observed as a quasar or BRLG, where the AGN dominates or competes with the luminosity of the host galaxy. When the beaming is most direct, the source is classified as an FSRQ or blazar, where the synchrotron of the jet dominates. In this sense, AGN of identical

power, age, spectral, jet and torus properties can be largely identified with the inclusion of orientation. We describe this structure further in Fig. 3.1.

To verify this unified model, a number of tests have been applied to consider the spectral, morphological and polarization features, the extent of the lobes, core dominance and line spectra Seyfert [1979]. These tests trace properties which are expected to vary based on or regardless of orientation.

CHAPTER 4

MODEL SYSTEM: GALACTIC X-RAY BINARIES

In the effort to understand accretion and jet production in AGN, galactic X-ray binaries (XRBs), or microquasars, offer a model test system. X-ray binaries are binary systems consisting of a compact object and late-stage stellar companion in close orbit. The compact object may be a few-solar mass black hole or neutron star. The stellar companion is generally associated with strong winds and has expanded to a large radius. The outer gaseous shells of the companion are easily accreted by the compact object. The result is the production of an accretion disk and jet.

4.1 Observations

Observations over the last few decades have revealed the cyclic nature of the emission of X-ray binaries [Remillard and McClintock, 2006]. As such objects were initially recognized as X-ray bright, early studies focused on characterization of their varying X-ray spectra. Four characteristic phases are commonly identified in relation to observed activity:

- **A Luminous, Thermal Spectrum.** In this state, a bright, thermal spectrum dominates observations.
- **A Dim, Soft Power-Law Spectrum.** The overall intensity dims. The thermal spectrum begins to become sub-dominant to a growing non-thermal, power-law component. This may present a softer power law index ($\sim$2.5).
- **A Hard Power Law Spectrum.** A hard power law is observed. High-energy X-ray photons are increased in intensity relative to the thermal state, and the intensity of low-energy X-ray photons may decrease. Jets are often observed during this phase.
- **A Bright, Soft Power Law Spectrum.** A soft power-law is again observed, now at higher intensities. Jets may be observed during this state. The system would then return to a state of thermal emission.

These four phases might repeat many times in the observation of a single source, commonly on the time scale of several months to years [Remillard and McClintock, 2006]. The phases could be identified with a hysteresis cycle in the plane of spectral index and flux intensity.

4.2 X-ray Binary Hysteresis

The phases observed have been widely accepted as related to the underlying disk-jet system. In general, the bulk of X-ray emission is related to the accretion disk. The intensity and observed spectral properties reflect the physical state of the underlying accretion flow. In turn, this accretion flow is intrinsically linked to jet production. We describe physical expectations for each phase of the disk-jet system below.

- **A Luminous, Thermal Spectrum.** The accretion flow is well described by a geometrically thin disk. Turbulent angular momentum transport is present, allowing for the inward accretion flow. However, radiative output is dominated by thermal emission from frictive interactions between Keplerian flows of the disk. The jet is inactive.

- **A Dim, Soft Power-Law Spectrum.** Turbulence begins to develop within the accretion disk. A fraction of the electron and nuclei plasma is lifted to higher energies via acceleration processes. The disk increases in temperature, and expands in vertical width or height.

- **A Hard Power Law Spectrum.** The inner flow becomes hot and geometrically thick. These accelerated electrons and protons contribute to the inverse-Compton scatter of lower-energy photons, forming the corona around the disk. Specifically, a hard X-ray power law forms. Material exits along magnetic field lines threading the disk, forming the jet.

- **A Bright, Soft Power Law Spectrum.** Turbulence within the accretion flow decreases. Some sporadic jets may be observed as the system relaxes back to a thermal disk.

While the general connection between turbulence and jet production in X-ray binaries is largely accepted, the mechanism driving turbulence, and relationship with magnetic flux, accretion and jet production, has been an active topic of research over the last two decades [Petrucci and et al., 2008, Balbus and Hawley, 1998, Nixon and Salvesen, 2014, Scepi et al., 2024, Huang et al., 2025, Raha et al., 2026]. In all cases, particle acceleration is modulated on the scale of the hysteresis cycle. We highlight one model.

Magnetically Arrested Disks As material is accreted, magnetic flux threading the plasma is also drawn inward. Magnetic pressure builds around this inner accretion region, until gravitational forces are balanced. This accretion state is described as a magnetically arrested disk (MAD), and provides conditions for maximally efficient jet production and outflows [Begelman and Armitage, 2014, Narayan et al., 2003]. This magnetic accumulation is related to the hysteresis cycle in Fig. 4.1.

4.3 A Comment on AGN Jet Feeding

The hysteresis cycle of X-ray binaries provides an opportunity to characterize accretion and jet evolution on observable time scales. These system physics are widely applicable to AGN, when scaled appropriately for their much larger mass. We note that the sporadic nature and variability associated with powerful AGN or blazar jets is generally not related to accretion hysteresis. These are smaller scale, sporadic fluctuations in the accreted plasma. Instead, the time scale for accretion phase transitions may extend to 10^4–10^6 years, given a simple mass-scaling argument.

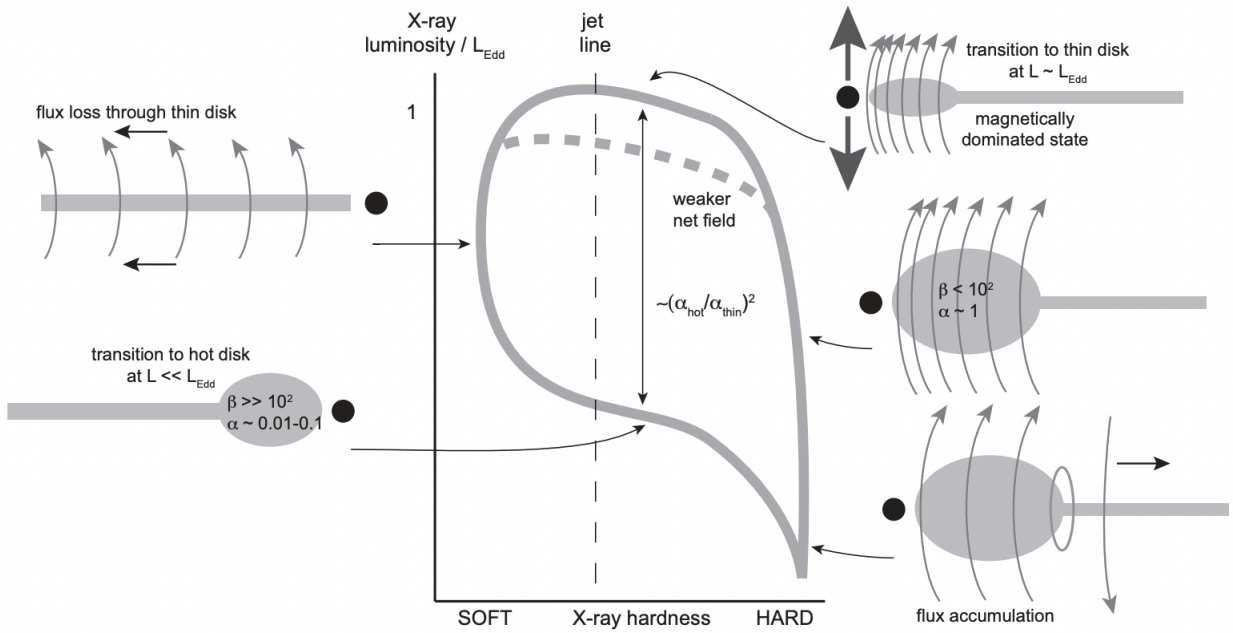

Figure 4.1 A representation of the X-ray binary accretion hysteresis cycle [Begelman and Armitage, 2014] We show a widely accepted model of physical transitions in the magneto-hydrodynamic state of the accretion disk. The X-ray flux follows a cycle in a plane of spectral hardness and luminosity. Recent work has commonly identified these transitions with magnetic flux accumulation from the accreted material. α is a viscosity parameter which may correspond to either a thin, thermal disk, or a thick, hot disk. β represents the ratio between gas and magnetic pressure. L represents luminosity, where $L_{\rm edd}$ is the Eddington luminosity.

CHAPTER 5

A DISCUSSION OF ASTROPHYSICAL MESSENGERS

5.1 A History of Multimessenger Detection

Multimessenger astrophysics has developed rapidly over the last several decades. In addition to photons, cosmic rays, neutrinos and gravitational waves offer additional channels to study the most extreme source environments. In each case, there are both unique benefits and drawbacks, corresponding to a new discovery space for each channel [Halzen and Klein, 2010, Mészáros et al., 2019]. We provide a brief historical discussion of the field, with emphasis on cosmic rays, gamma rays and neutrinos of astrophysical origin.

1957, 1958: Early High-Altitude and Space-Based Measurements of CRs The first substantial measurement of primary cosmic ray intensity at high altitude and high latitude was performed by a series of balloon-launched rocket missions carried out by the State University of Iowa in 1957 [Van Allen et al., 1958]. In the next year, data from the first U.S. satellite, Explorer 1, was used to discover primary cosmic ray electrons and light nuclei trapped within Earth's magnetic fields. This experiment was lead by the same group. These regions of high electron and proton cosmic ray intensity became known as the Van Allen Belts [Kraushaar et al., 1965].

1961: First Space-Based Gamma-ray Measurements The Explorer 11 satellite mission carried out the first space-based gamma-ray measurement. This telescope had a large angular resolution of several degrees, but was able to establish the existence of an extraterrestrial gamma-ray background.

1962: Volcano Ranch The Volcano Ranch experiment was one of the first successful demonstrations of ultra-high-energy cosmic ray detection through measurements of their extensive air showers. Cosmic rays in excess of 10^{15}–10^{16} eV were too low in flux intensity to detect through ballon or satellite experiments. John Linsley deployed an initial array

of scintillation detectors over a square kilometer. As primary cosmic rays interact in the upper atmosphere, their secondary products produce particle showers with projected size at Earth's surface dependent on energy and species. This experiment was the first successful reconstruction of primary properties from ground-level observational data. These studies also resulted in the observation of a single primary of estimated energy of 10^{20} eV [Linsley, 1963]. These high energies raised interest in relation the particle's origin, acceleration mechanism and propagation which remain central to the field today [Nagano and Watson, 2000].

1968: Homestake Experiment The Homestake experiment used approximately 615 tonnes of shielded, chlorine-rich perchloroethylene to search for the interaction of solar electron neutrinos. An electron neutrino interacts with a chlorine nuclei producing an electron and radioactive argon. The resulting argon was counted. The experiment successfully detected a flux of solar electron neutrinos from the sun, but measured approximately one third the predicted intensity. This initiated the field of extraterrestrial neutrino detection and astronomy. Additionally, the result provided the first evidence for neutrino oscillations [Davis, 1994].

1990s–1990s: Proton Decay Experiments In the 1980s and 1990s, motivated to understand proton stability, a number of groups instrumented multi-tonne water tanks as active volumes to constrain decay [Perkins, 1984]. These experiments were deployed at sites several kilometers underground to substantially reduce background from secondary cosmic rays. In the early 1980s, anomalous event rate excesses from the direction of an astrophysical source, the X-ray binary, Cygnus X-3, were claimed by several groups [Lamb et al., 1982, Samorski and Stamm, 1983]. While these initial results were not later corroborated, intrigue of the non-standard particle emission proposed from such a source garnered substantial interest from the community, setting the stage for modern cosmic-ray and neutrino astroparticle physics [Kochocki et al., 1990].

1987: Supernova (SN) 1987A Deep underground detectors used for studies of proton decay also played a substantial role in the observation of neutrinos from SN 1987A. A star in the Large Magellanic Cloud underwent a supernova, emitting neutrinos from core collapse several hours prior to the emission of visible light. Across three sites, 25 likely neutrino events were observed, establishing the start of extragalactic neutrino astrophysics [Hirata et al., 1987, Haines et al., 1988, Alekseev et al., 1987].

1989: The Whipple Observatory The Fred Lawrence Whipple Observatory in Arizona pioneered ground-based, very-high-energy gamma-ray astronomy. The Whipple 10-meter telescope used photomultiplier tubes to detect Cherenkov radiation from charged particles in air showers induced by primary gamma-ray photons. This demonstrated the technique of ground-based gamma-ray detection, and also established the field of TeV-energy gamma-ray astronomy [Weekes et al., 1989].

Modern Air Shower Arrays and CR Experiments Modern study of cosmic rays continues to focus both on primary, space-based detections, as well as ground-level measurements of the secondary air shower from branching secondary products of the initial primary cosmic ray. In the former case, the Alpha Magnetic Spectrometer Experiment AMS-02, is a space-based spectrometry experiment onboard the International Space Station (ISS). AMS-02 performs precision measurements and identification of charged cosmic rays from hundreds of MeV to the TeV scale [AMS Collaboration, 2013]. Main science goals include characterization of electron, positron, proton, antiproton and light nuclei such as helium spectra, study of galactic cosmic-ray transport, as well as indirect searches for dark matter and antimatter.

Indirect characterization of primary cosmic ray nuclei also proceeds through large-scale ground-based experiments. In particular, the Pierre Auger Observatory in Argentina and the Telescope Array Project in the U.S. are two several-thousand square kilometer air shower arrays [Pierre Auger Collaboration, 2015, IceCube Collaboration, 2012]. Their large foot-

prints allow for both a large detection area as well as coverage to individual ultra-high-energy showers of large spatial scale. Both experiments roughly provide sensitivity to showers from primary particles in the energy range of $10^{17.5}$–10^{20+} eV, characterizing the highest energy tail of the cosmic-ray spectrum. These observatories use a combination detection technique of both surface detector arrays, as well as stereoscopic fluorescence telescopes able to observe nitrogen fluorescence emitted by the air shower. This combination allows for the reconstruction of primary energy, arrival detection, and composition or species-specific observables. Modern science continues to focuses on the astrophysical origin sources of these events, as well as a finer characterization of the spectral energy structure and mass composition. The composition of cosmic rays at the highest energies, between light nuclei like proton and helium, as opposed to heavier nuclei like iron, is still being determined.

Modern Gamma-ray Observatories Gamma-ray astronomy continues to employ both space-based detection techniques as well as new ground-based methods. In the former, the U.S. Fermi Large Area Telescope is a satellite observatory capable of indirect gamma-ray detection [Atwood et al., 2009]. High-energy photons enter the silicon-tungsten tracking calorimeter system. If the gamma-ray interacts, electron-positron pairs are produced and recorded. The tracker system has sub-degree angular resolution above 1 GeV in energy, allowing for directional gamma-ray astronomy. The calorimeter determines event energy, with sensitivity to primary gamma rays between 20 MeV and 500 GeV. As the observatory orbits Earth, full-sky cadence is achieved every several hours.

Very-high-energy gamma-ray astronomy has also continued to develop through ground-based imaging atmospheric telescope arrays. Three major sites have pushed forward gamma-ray astronomy in the past fifteen years – the High-Energy Stereoscopic System (HESS) in Namibia [Hinton, 2004], the Major Gamma-ray Imaging Cherenkov Telescopes (MAGIC) in the Canary Islands and the Very Energetic Radiation Imaging Telescope Array System (VERITAS) at the Fred Lawrence Whipple Observatory [MAGIC Collaboration, 2016, VER-

ITAS Collaboration, 2006]. All arrays consist of multiple, reflective imaging telescopes with cameras composed of a grid of photomultiplier tubes. The result is sub-degree scale angular resolution for gamma rays and energy sensitivity between several hundred GeV and several TeV. In conjunction with space-based observations, measurements have made substantial contributions to high-energy, galactic astrophysical sources, as well as extragalactic sources such as blazar AGN.

A more recent gamma-ray detection technique utilizes methods traditionally used for the highest-energy nuclei cosmic rays. The High-Altitude Water Cherenkov Observatory (HAWC) in Mexico and the Large High Altitude Air Shower Observatory (LHAASO) in China use large arrays of instrumented water tanks to detect Cherenkov radiation from the secondary particles of gamma-ray air showers [HAWC Collaboration, 2017, LHAASO Collaboration, 2021]. In the last years, this technique has opened gamma-ray astronomy up to few-hundred TeV energies, and in some cases PeV-energy events. Current results are especially promising, and continued operation is expected to contribute to our understanding of the highest-energy astrophysical sources and acceleration mechanisms. There is also some possibility that these measurements will closely relate to the source of the highest-energy nuclei cosmic rays, ultimately providing a unified, multimessenger picture of these extreme environments.

Modern Astrophysical Neutrino Observatories Some of the most substantial advancements in astrophysics have arguably been made in the domain of neutrino astronomy in the last two decades. A large volume of ice or water can be instrumented with photosensitive detectors. When a neutrino interacts with nuclei in this target volume, the products produce radiation from Cherenkov and other stochastic losses. These photons are detected by a lattice of photosensors, allowing for three-dimensional reconstruction of the interaction. This method was first successfully pioneered in the 1990s and early 2000s by the Antarctic Muon and Neutrino Detector Array (AMANDA) at the South Pole [Andrés and et al., 1999].

Hot water drilling was used to instrument strings of sensors at depths between 1500 and 1750 meters. The final detector consisted of 19 vertical strings of several hundred photosensors, with sensitivity between several hundred GeV and a PeV. The configuration achieved an angular resolution of several degrees. AMANDA successfully detected muons and neutrinos as secondary products in atmospheric air showers, and provided a proof-of-concept for TeV-PeV neutrino detection in natural target volumes.

The IceCube South Pole Neutrino Observatory was constructed at the same site as AMANDA. The same technique of hot water drilling was used between 2004 and 2011. The final configuration consisted of 86 strings for a total of 5160 photosensors. IceCube is sensitive from several GeV to tens of PeV. Angular resolution is dependent on energy and the type of interaction. In the case of muon neutrinos, an uncertainty of a few tenths of a degree is achieved for events in excess of tens of TeV in energy. IceCube is designed to observe both potential astrophysical neutrino interactions from galactic and extragalactic sources, as well as the interactions of penetrating cosmic-ray air showers within the ice [IceCube Collaboration, 2017].

After an excess of high-energy neutrinos was measured relative to atmospheric backgrounds around 2013 and 2014, this was identified as a diffuse, near-isotropic flux of astrophysical neutrinos [Aartsen et al., 2013]. Given the high energy of the spectrum, this marked the birth of modern galactic and extragalactic neutrino astronomy. In 2017, the first neutrino point source was discovered, the blazar AGN TXS 0506+056 [Tanaka et al., 2017, IceCube Collaboration, 2018a]. In 2021, a second point source, the Seyfert AGN, NGC 1068, was announced [IceCube Collaboration, 2022b]. More recently, an excess of neutrinos was also associated with the galactic plane, indicating the existence of galactic, hadronic cosmic-ray sources [IceCube Collaboration, 2023].

IceCube has also made contributions to the study of nuclei cosmic-ray air showers. In particular, IceTop is a square-kilometer scale array of ground-level ice tanks [IceCube Collaboration, 2013a]. Each tank is instrumented with photomultipliers for the detection of

Cherenkov radiation. This allows for ground-level air shower measurements for primaries of energy between 10^{14} and 10^{18} eV. In combination with in-ice observations, IceCube has contributed to characterization of the cosmic-ray energy spectrum and composition. IceCube's unique ability to image the muonic shower development in high resolution has also contributed to our understanding of the secondary shower evolution.

Presently, a number of additional experimental collaborations are actively developing additional natural-volume neutrino observatories. Notably, these sites may offer superior coverage to the southern hemisphere, coverage to extended energy ranges, or improved angular resolution [Twagirayezu et al., 2024, Adrián-Martínez et al., 2016].

5.2 Messengers in the Universe

This work utilizes neutrinos, radiative emission, and cosmic rays to study some of the most extreme acceleration environments from jetted, astrophysical sources. We discuss and compare the unique propagation of each messenger, assuming an extragalactic origin.

5.2.1 Cosmic-Ray Transport

The vast majority of cosmic rays exiting astrophysical sources are charged, allowing for their acceleration via electromagnetic interactions. Neutral cosmic rays which may be produced after acceleration are unstable, decaying well before detection would become relevant. Charged nuclei experience the galactic magnetic fields of their origin galaxy, weak extragalactic fields along long intermediate distances, and the magnetic fields of our own galaxy. Nuclei follow curved trajectories with Larmor radius dependent on their rigidity, Z, momentum, p, and magnetic field strength, B,

$$r_L = \frac{pc}{ZeB}. \tag{5.1}$$

Highest-energy cosmic rays are least deflected. Nuclei with larger charge experience a greater deflection. Galactic magnetic fields of order μG and extragalactic magnetic fields of order nG substantially impact the directions of charged cosmic rays, especially at energies below the EeV scale.

Cosmic rays also interact with extragalactic photon backgrounds. In particular, CMB

photons and extragalactic background light (EBL) provide targets. In the case of protons,

$$p + \gamma \rightarrow \Delta^{+}. \tag{5.2}$$

In the case of heavier nuclei, photon interactions lead to photodisintegration. As the cross section for interaction generally increases with energy, cosmic ray propagation at the highest energies is naturally limited to a certain characteristic distance by these interactions, known as the GZK horizon.

In summary, the highest-energy cosmic rays retain some directional information over long distances, but are ultimately attenuated in energy by line-of-site interactions [Kotera and Olinto, 2011]. Lower-energy cosmic rays are highly deflected, and typically studied as a composite flux.

5.2.2 Gamma-Ray Transport

Gamma rays are uncharged and travel on straight line trajectories. However, gamma ray photons experience substantial attenuation at the highest energies from CMB and EBL interactions via,

$$\gamma + \gamma = e^{+} + e^{-}. \tag{5.3}$$

The result is an observable horizon dependent on energy. Attenuation becomes relevant at few-hundred GeV or TeV energies. Sources of hundreds of TeV in energy have very limited horizons, essentially limiting observation to our own galaxy and local extragalactic objects [Dwek and Krennrich, 2013].

5.2.3 Neutrino Transport

Neutrinos are uncharged, near massless particles. Only weak interactions become relevant for propagation. The result is a long mean free path, leaving a full view of the Universe essentially accessible. As neutrinos also travel in straight trajectories, they are the only high-energy particle messenger capable of resolved point-source astronomy for distant, extragalactic objects [Ahlers and Halzen, 2018].

5.3 Messengers at Earth

5.3.1 Atmospheric Shower Tree Evolution

At Earth, nuclei cosmic rays and gamma rays interact in the upper atmosphere, producing secondary products through a series of branching interactions and decays. The result is an air shower of secondary, atmospheric cosmic rays. This shower evolution forms a stochastic, branching tree [Engel et al., 2011].

Interactions with atmospheric nuclei commonly produce neutral pions, leading to the following interaction chain,

$$\pi^0 \rightarrow \gamma + \gamma, \tag{5.4}$$

$$\gamma \rightarrow e^+ + e^-, \tag{5.5}$$

$$e^\pm \rightarrow e^\pm + \gamma. \tag{5.6}$$

These processes are associated with the 'electromagnetic branch' of the shower, in which a large fraction of energy is ultimately dissipated through low-energy photons.

Alternately, the 'hadronic branch' is initiated nuclei interactions and produces hadrons of lowered energy,

$$p + N \rightarrow \pi^\pm, \pi^0, K^\pm, \ldots \tag{5.7}$$

Pions and kaons are available at low energies, and dominate the mesonic content of the shower for primaries of energy less than 100 TeV. Either meson may decay through a leptonic channel. Pions decay almost exclusively to muons and muon neutrinos owing to helicity suppression,

$$\pi^\pm \rightarrow \mu^\pm + \nu_\mu, \tag{5.8}$$

$$K^\pm \rightarrow \mu^\pm + \nu_\mu, \tag{5.9}$$

$$\mu^- \rightarrow e^- + \overline{\nu}_e + \nu_\mu. \tag{5.10}$$

These decays occur over relatively long time scales, allowing for intermediate meson interactions and energy loss prior to decay. The resulting atmospheric neutrino spectrum is softened

in spectral index relative to the primary cosmic-ray energy spectrum, presenting an index of $\gamma \approx 3.7$. As electron neutrinos are primarily produced through muon decay, they are outnumbered by muon neutrinos by a factor of two with some energy dependence. As these atmospheric neutrinos from lightest mesons are most common and dominate the shower, they are described as conventional atmospheric neutrinos.

At higher primary energies, additional hadrons formed from heavier quarks become available. In particular, charmed mesons and baryons are produced from hadronic interactions,

$$p + N \to D^{\pm}, D^{0}, D_{s}, \Lambda_{c}, \ldots \tag{5.11}$$

As such particles are relatively unstable, they decay before additional interactions and energy losses can occur. This prompt atmospheric neutrino spectrum exhibits a harder spectral index of $\gamma \approx 2.7$. Additionally, as neutrino production relies on semileptonic decays, electron and muon neutrinos are equally represented in intensity. We provide a schematic illustration of both prompt and conventional air showers in Fig. 5.1.

Air-shower development is naturally described by a branching process. Interactions and decay events act as branching vertices, while particle transport through the atmosphere determines spatial evolution. Each particle state may be characterized by species, A, energy, E, direction, Ω and atmospheric depth, X,

$$\varepsilon = (A, E, \Omega, X). \tag{5.12}$$

Evolution of the process may induce a random branching transition:

$$\Delta X \sim \exp(\lambda_{A}(E)), \quad \varepsilon \longrightarrow \{\varepsilon\}_{i=1}^{N}. \tag{5.13}$$

Here, λ_A is a species-specific interaction length. Branching vertices are determined by hadronic and electromagnetic generators [Riehn et al., 2020], determining,

- daughter multiplicity,
- particle species,

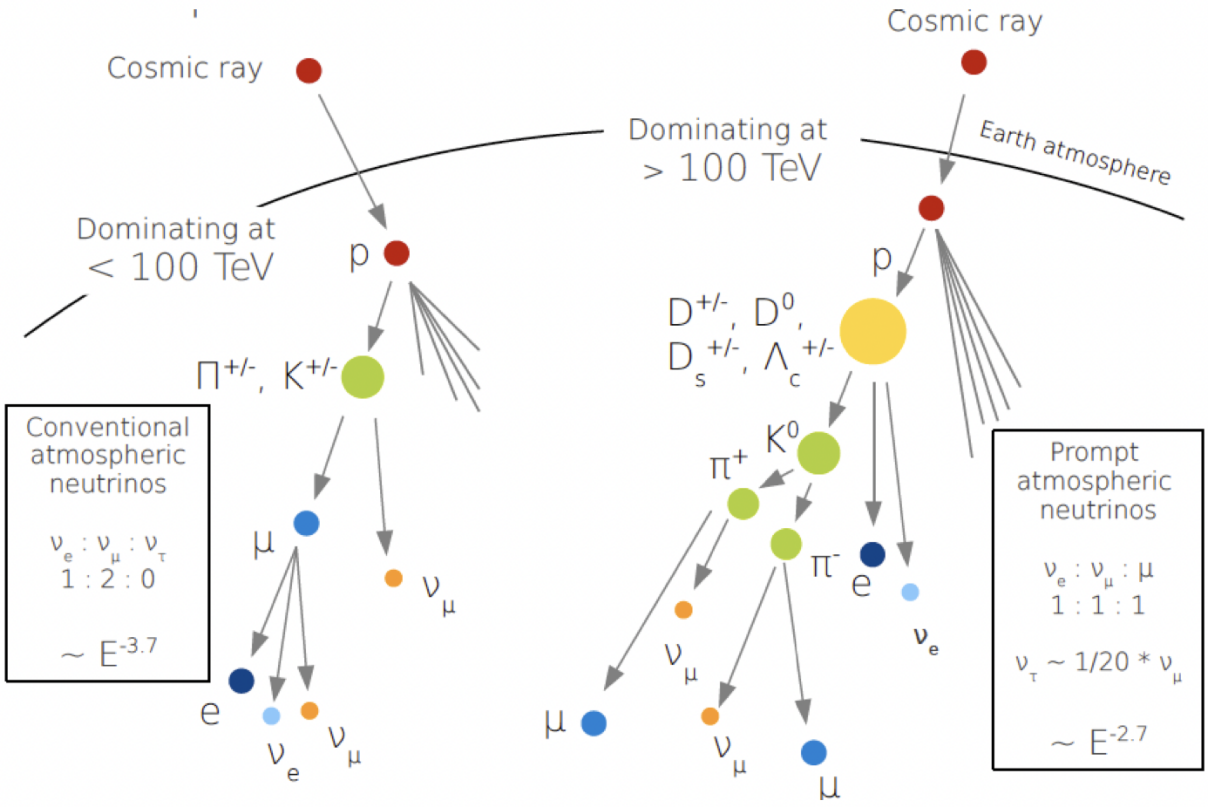

Figure 5.1 An example of conventional atmospheric neutrinos and prompt atmospheric neutrinos. The figure is credited to Anne Schukraft. We provide two examples of air shower development. On the left-hand side, a conventional air shower is indicated with the corresponding flavor ratio and soft spectral index. On the right-hand side, an example air shower containing neutrinos from charmed hadron decay is presented. This latter shower has a differing flavor ratio and expected spectral index.

- energy partition,
- angular deflection.

A single shower is a realization of a measure-valued process,

$$Z_X(\omega) = \sum_i \delta_{\varepsilon_i}(X). \tag{5.14}$$

Modern simulation frameworks like CORSIKA generate explicit realizations of these branching trees through Monte Carlo sampling of interaction and decay probabilities [Huege, 2022].

5.3.2 Shower Cascade Transport Approximations

We also highlight that shower evolution for multiple species is commonly modeled through coupled transport equations. Primary cosmic ray spectra are evolved through atmospheric interactions, particle decays, and continuous energy losses. The solution gives altitude-dependent or ground-level energy spectra. From a probabilistic perspective, cascade equations may be viewed as moment or mean-field descriptions of an underlying stochastic branching transport process [Fedynitch et al., 2015, Fedynitch, 2015].

If Φ_i represents an energy flux of a species, the spectrum with atmospheric depth can be represented as,

$$\frac{d\Phi_i(E,X)}{dX} = -\frac{\Phi_i(E,X)}{\lambda_{\mathrm{int},i}(E)} \tag{5.15}$$

$$-\frac{\Phi_i(E,X)}{\lambda_{\mathrm{dec},i}(E,X)} \tag{5.16}$$

$$-\frac{\partial}{\partial E}(\mu(E)\Phi_i(E,X)) \tag{5.17}$$

$$+\sum_k \int_E^\infty dE_k \frac{dN_{k(E_k)\to i(E)}}{dE}\frac{\Phi_k(E_k,X)}{\lambda_{\mathrm{int},k}(E_k)} \tag{5.18}$$

$$+\sum_k \int_E^\infty dE_k \frac{dN^{\mathrm{dec}}_{k(E_k)\to i(E)}}{dE}\frac{\Phi_k(E_k,X)}{\lambda_{\mathrm{dec},k}(E_k)}. \tag{5.19}$$

$$\tag{5.20}$$

In order, we have sink terms or flux losses for the species i from atmospheric interactions, decays, and continuous losses. We then have source terms for all other particle interactions and decays in which species i is produced, respectively.

Spectra representing reasonable primary cosmic-ray fluxes are commonly used as atmospheric neutrino and muon expectations in neutrino astronomy. These predictions represent ensemble means across many shower realizations and conditional shower structure is not retained. Example spectra for muons and neutrinos is presented in Fig. 5.2.

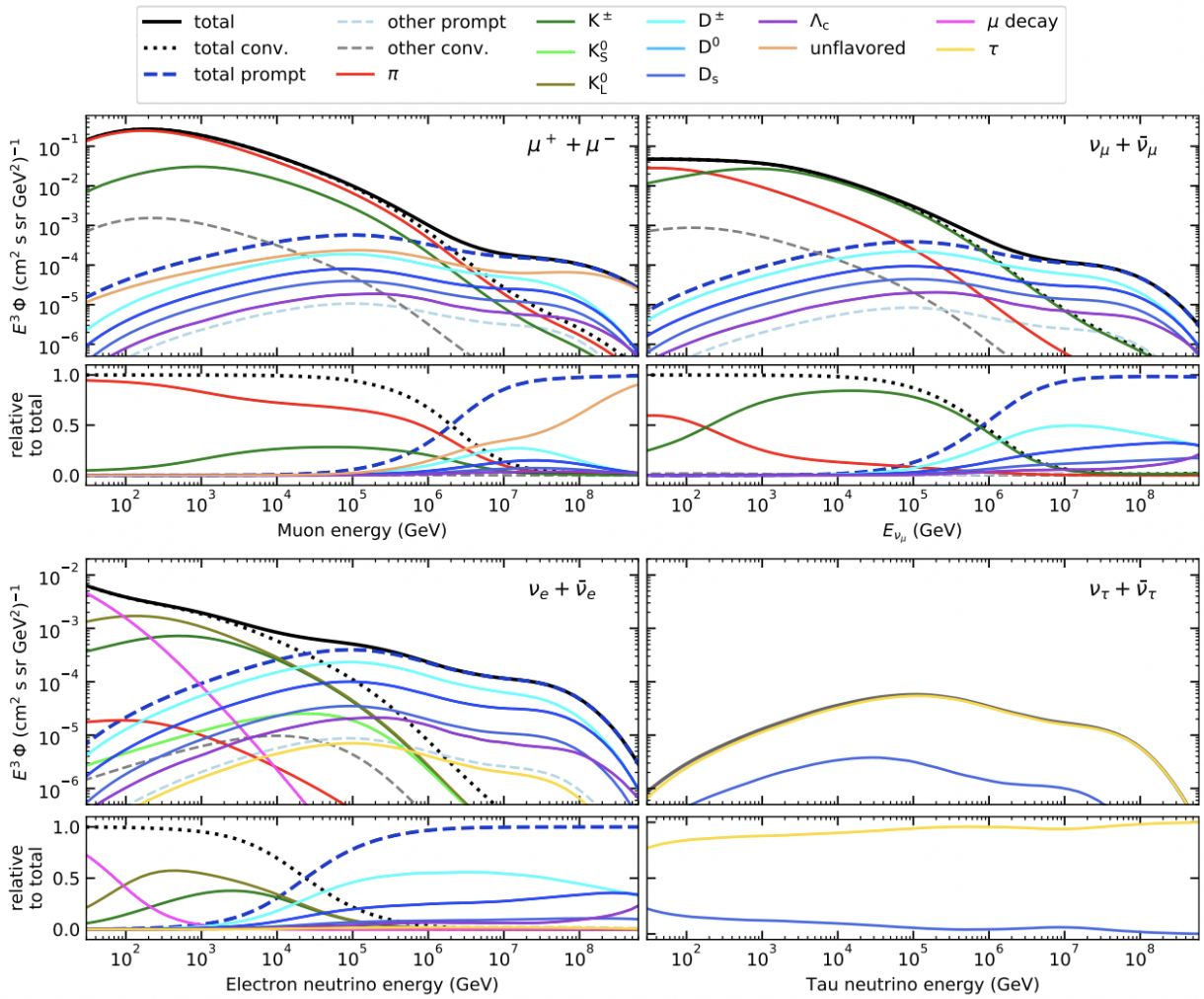

Figure 5.2 Example spectra for atmospheric muons and neutrinos assuming the hadronic generator model, Sibyll-2.3c, and the primary cosmic-ray spectral parameterization, $H3a$ [Fedynitch et al., 2015]. We note that muon neutrinos attributed to charm hadron decay only exceed conventionally produced neutrinos near an energy, $E_\nu \approx 10^{15}$ TeV. Prompt electron neutrinos dominate their respective flavor channel earlier, closer to $E_\nu \approx 10^{13}$ TeV.

5.3.3 Muon Matter Interactions

Within the Earth, muons experience a number of matter interactions, impacting their energy and observability. These effects are highly relevant to neutrino astronomy, which relies on shower predictions from the full sky and all possible intersections with the Earth.

Energy Losses Muons traveling through matter interact with the surrounding nuclei. With propagation through a distance, x, a muon experiences both ionization losses, $a(E)$, and radiative losses, $b(e)E$, dependent on energy,

$$\frac{dE}{dx} = a(E) + b(E)E. \tag{5.21}$$

Below roughly a TeV in energy, ionization commonly described by the Bethe-Bloch formula dominates the total energy losses of the particle. Ionization losses occur through atomic excitation of the surrounding matter and result in a nearly continuous energy loss along the muon trajectory.

Beyond this energy range, radiative losses from a number of processes contribute. Bremsstrahlung first contributes, in which a charged muon interacts with and accelerates local nuclei, exciting the medium initiating an electromagnetic cascade,

$$\mu + N \rightarrow \mu + N + \gamma. \tag{5.22}$$

At higher energies, pair production also becomes relevant. A muon again interacts with surrounding nuclei, leading to a pair production event and electromagnetic cascade,

$$\mu + N \rightarrow \mu + N + e^+ + e^-. \tag{5.23}$$

At highest energies, deep photonuclear interactions begin to dominate. The muon interacts with a nearby nuclei, resulting in a new hadronic final state,

$$\mu + N \rightarrow \mu + X. \tag{5.24}$$

The result is a hadronic shower.

In summary, TeV-PeV radiative losses occur as discrete, stochastic interactions, as opposed to a continuous energy loss process. As a result, muons of identical energy and path may produce varied patterns of localized energy deposition along their trajectory [Lipari and Stanev, 1991, Groom et al., 2001]. Accurate modeling of these losses is critical for describing expected event rates and interactions at a detector.

5.3.4 Neutrino Propagation and Earth Interactions

While neutrino weak interactions have a low cross section, propagation and matter interactions still impact the flavor composition and energy spectrum of observed neutrinos. This is relevant both for atmospheric neutrinos and neutrinos of astrophysical origin.

Flavor Oscillations Neutrinos are observed as their flavor eigenstates. However, these flavor states resulting from weak interactions are superpositions of different, distinct mass eigenstates. An observed flavor state is represented as,

$$|\nu_\alpha\rangle, \quad \alpha = e, \mu, \tau. \tag{5.25}$$

An observed mass eigenstate takes the form,

$$|\nu_i\rangle, \quad i = 1, 2, 3. \tag{5.26}$$

Evolution is governed by the Pontecorvo–Maki–Nakagawa–Sakata (PMNS) matrix, an extension of the Standard Model [Maki et al., 1962, Gonzalez-Garcia and Maltoni, 2008]. This is a unitary mixing matrix which represents the relation between flavor and mass eigenstates. The matrix is specified by three mixing angles, θ_{12}, θ_{23} and θ_{13}, determining the proportion of each mass eigenstate represented by each flavor eigenstate. An additional phase, δ_{CP}, determines whether neutrinos and antineutrinos behave identically. Two additional Majorana phases may be included, though this parameterization does not impact oscillation. We can

express the matrix as three rotations,

$$U = \begin{pmatrix} 1 & 0 & 0 \\ 0 & c_{23} & s_{23} \\ 0 & -s_{23} & c_{23} \end{pmatrix} \begin{pmatrix} c_{13} & 0 & s_{13}e^{-i\delta_{\rm CP}} \\ 0 & 1 & 0 \\ -s_{13}e^{i\delta_{\rm CP}} & 0 & c_{13} \end{pmatrix} \begin{pmatrix} c_{12} & s_{12} & 0 \\ -s_{12} & c_{12} & 0 \\ 0 & 0 & 1 \end{pmatrix}. \tag{5.27}$$

Here,

$$c_{ij} = \cos\theta_{ij} \quad \text{and} \quad s_{ij} = \sin\theta_{ij}. \tag{5.28}$$

$c_{ij} = \cos\theta_{ij}$ and $s_{ij} = \sin\theta_{ij}$.

At any time, an observed state may be represented as,

$$|\nu_\alpha\rangle = \sum_i U_{\alpha i}|\nu_i\rangle. \tag{5.29}$$

Mass eigenstates evolve with propagation,

$$|\nu_i(t)\rangle = e^{iE_i t}|\nu_i(0)\rangle. \tag{5.30}$$

In the case of relativistic neutrinos,

$$E_i \simeq p + \frac{m_i^2}{2E}. \tag{5.31}$$

The evolved flavor state can then be expressed as,

$$|\nu_\alpha(L)\rangle = \sum_i U_{\alpha i}e^{-im_i^2 L/(2E)}|\nu_i\rangle. \tag{5.32}$$

Projecting onto a selected flavor state, β, gives the probability of observation,

$$P_{\alpha\to\beta} = \left|\sum_i U^*_{\beta i}U_{\alpha i}e^{-im_i^2 L/(2E)}\right|^2. \tag{5.33}$$

An equivalent description is obtained by considering the evolution of the flavor state vector. In the flavor basis,

$$i\frac{d}{dt}\begin{pmatrix} \nu_e \\ \nu_\mu \\ \nu_\tau \end{pmatrix} = H_{vac}\begin{pmatrix} \nu_e \\ \nu_\mu \\ \nu_\tau \end{pmatrix}. \tag{5.34}$$

The vacuum Hamiltonian,

$$H_{vac} = \frac{1}{2E} U \begin{pmatrix} m_1^2 & 0 & 0 \\ 0 & m_2^2 & 0 \\ 0 & 0 & m_3^2 \end{pmatrix} U^\dagger. \tag{5.35}$$

Neutrinos oscillations can be viewed as unitary evolution generated by a non-diagonal Hamiltonian in flavor space.

Matter Effects In matter, electrons experience coherent forward scattering. This is the Mikheyev-Smirnov-Wolfenstein (MSW) effect [Wolfenstein, 1978, Mikheyev and Smirnov, 1985]. This may be represented as an effective potential in the evolution Hamiltonian,

$$H = H_{vac} + \begin{pmatrix} V_e & 0 & 0 \\ 0 & 0 & 0 \\ 0 & 0 & 0 \end{pmatrix}. \tag{5.36}$$

Here,

$$V_e = \sqrt{2} G_F n_e. \tag{5.37}$$

The value G_F is the Fermi constant, and n_e is the electron number density. This effect is most relevant for neutrinos of energy 1–100 GeV.

Tau Neutrino Regeneration Tau neutrinos may interact weakly with nuclei when passing through large depths of matter. We consider the following interaction, which is described in more generality later in this text,

$$\nu_\tau + N \to \tau^- + X. \tag{5.38}$$

The tau is unstable and decays quickly, as opposed to muons and electrons. Through flavor conservation, one of the products is another tau neutrino,

$$\tau^- \to \nu_\tau + X. \tag{5.39}$$

This process of regeneration lowers the energy of the initial tau neutrino over successive increments. The result is substantial for tau neutrinos observed closest to Earth's center [Halzen and Saltzberg, 1998, Argüelles et al., 2022].

Muon and Electron Neutrino Attenuation Muon and electron neutrinos of high energy also interact when passing through large depths of matter. As regeneration through decay is minimal for muon neutrinos and and negligible for electron neutrinos, the result is an attenuation of these neutrino spectra at high energies [Argüelles et al., 2022]. Again, this effect is most notable for neutrinos passing closest to Earth's center.

CHAPTER 6

ASTROPHYSICAL NEUTRINO DETECTION

6.1 The South Pole IceCube Neutrino Observatory

The South Pole IceCube Neutrino Observatory is a volumetric neutrino telescope, a cubic kilometer of instrumented, natural ice at the geographic South Pole [IceCube Collaboration, 2017]. The current experimental collaboration is represented by approximately 450 members across 58 institutions in 14 countries. Funding is contributed by multiple international agencies. The majority of funding, core infrastructure at the South Pole Amundsen-Scott South Pole Station, is contributed and managed by the United States' National Science Foundation.

The configuration consists of 86 vertical strings of digital optical modules (DOMs). Each DOM contains a downward-facing 10-inch photomultiplier tube, digitizing electronics, calibration systems, and communication hardware enclosed within a pressure-resistant glass sphere. Each string carries 60 DOMs, for a total of 5,160 sensors. Sensors generally have an approximate 17-meter vertical spacing and 125-meter horizontal spacing. Eight strings in the center of the detector footprint have a more compact configuration, with 7 and 70-meter vertical and horizontal spacings, respectively. These inner strings are known as IceCube-DeepCore. The overall footprint is approximately hexagonal. Sensors are placed between a depth of 1450 and 2450 meters, reflecting depth-dependent ice properties and bedrock location.

Each string carries both power and communications. Above ice, strings collect at the nearby IceCube Laboratory (ICL). Here, power is also provided. Detector triggering, calibration and initial event reconstruction are performed. Due to limited satellite bandwidth, only selected data products are transferred north in near real time. The full data set is archived and transported in the following Austral summer.

An additional surface array, IceTop, is centered on the IceCube sensor configuration. 81 ice tanks are placed in close proximity to a string below [IceCube Collaboration, 2013a].

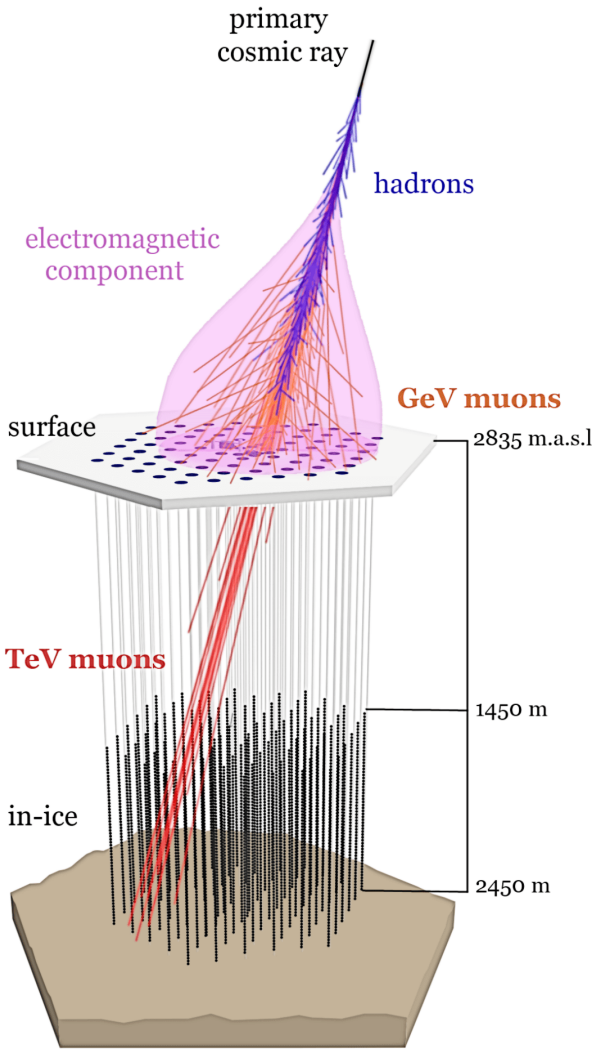

Figure 6.1 A diagram of the in-ice IceCube optical lattice and above-ice IceTop surface array. A cosmic ray air shower from the south is pictured. The high-energy muonic component of the shower reaches the optical sensors. Only a small fraction of air showers can be vetoed by the surface array.

The array spans a square kilometer. IceTop is sensitive to the electromagnetic and muonic components of air showers. In addition to cosmic-ray science goals, IceTop may also be used as a veto for cosmic ray air showers in southern event selections. A schematic of the IceCube and IceTop configuration is shown in Fig. 6.1.

IceCube detects the Cherenkov emission and radiative losses of products produced through interactions with local nuclei. Neutrinos and muons which interact within or near the detector produce observable photons.

6.2 Cherenkov Radiation

Cherenkov radiation is produced when charged particles travel at a velocity, v, in excess of the phase velocity of light in that medium, c/n. Here n is the refractive index.

As a charged particle moves through a medium, it polarizes the surrounding particles. Upon exit, the particles will release the energy given to them in this excitation, and return to their ground state. In the case $v > c/n$, polarized nuclei are not able to return to their ground state at the same rate at which they are disturbed. This asymmetric excitation front results in constructive interference and a high-intensity of radiation at a characteristic angle, θ_c.

The frequency spectrum of Cherenkov radiation is continuous, dependent on the medium's permeability, μ, index of refraction, and particle charge, q. As a function of frequency, ω, the Frank-Tamm formula describes this continuum,

$$\frac{d^2E}{dxd\omega} = \frac{q^2}{4\pi}\mu(\omega)\omega\left(1 - \frac{c^2}{v^2n^2(\omega)}\right). \tag{6.1}$$

Cherenkov radiation peaks in intensity around ultraviolet wavelengths [Frank and Tamm, 1937].

6.3 Charged and Neutral Current Interactions by Flavor

Two types of interactions with nuclei are most common for neutrinos [Navas et al., 2024, Formaggio and Zeller, 2012]. Dependent on this type of interaction, and the flavor of the products, different radiative event signatures or topologies appear within the detector.

6.3.1 Neutral Current Interactions

In the first interaction channel, a neutrino may exchange a neutral Z boson with a neighboring nuclei. This exchange of energy probes the hadronic structure, producing a hadronic shower of products. A neutrino of the same flavor exits the interaction with lowered energy.

For all flavors, the interaction topology appears the same. Photons produced from the hadronic shower create a near-spherical photon source. The slight directionality of the pho-

ton shower development indicates the direction of the initial neutrino, but depends on the interaction kinematics.

6.3.2 Charged Current Interactions

Within a charged current interaction, a neutrino may exchange a W^+ or W^- boson with nearby nuclei. This exchange of energy again probes the hadronic structure, producing a hadronic shower. Additionally, the exchange of charge means that the outgoing lepton exits as its charged partner of the same flavor.

The charged lepton provides an additional source of photons, dependent on flavor. In the case of electrons, the charged lepton produces an additional electromagnentic cascade. As the electron interacts quickly, this cascade may occur within a few meters of the initial hadronic cascade. The result is a near-spherical photon source of increased intensity.

In the case of muon neutrino charged current interactions, a produced muon of high energy will travel long distances without decaying and maintaining a minimum ionizing energy. The muon produces radiation along its straight-line trajectory. At energies below 1 TeV, Cherenkov emission dominates the photon intensity from such interactions. Beyond 1 TeV, additional radiative losses contribute with increasing relevance. This signature allows for improved estimation of the initial neutrino's direction.

Tau neutrino charged current interactions are associated with multiple radiative topologies [IceCube Collaboration, 2022c, IceCube Collaborarion, 2024]. In general, the tau lifetime is short,

$$\tau_\tau \simeq 2.9 \times 10^{-13} \text{ s}. \tag{6.2}$$

However, relativistic time dilation gives an energy dependent decay length,

$$L_\tau \simeq \gamma c \tau_\tau \approx 50 \text{ m} \left(\frac{E_\tau}{1 \text{ PeV}} \right). \tag{6.3}$$

Here, γ is the Lorentz factor of the tau, and E_τ is the particle energy. This length scale determines the observed event topology. Additionally, taus commonly decay via three chan-

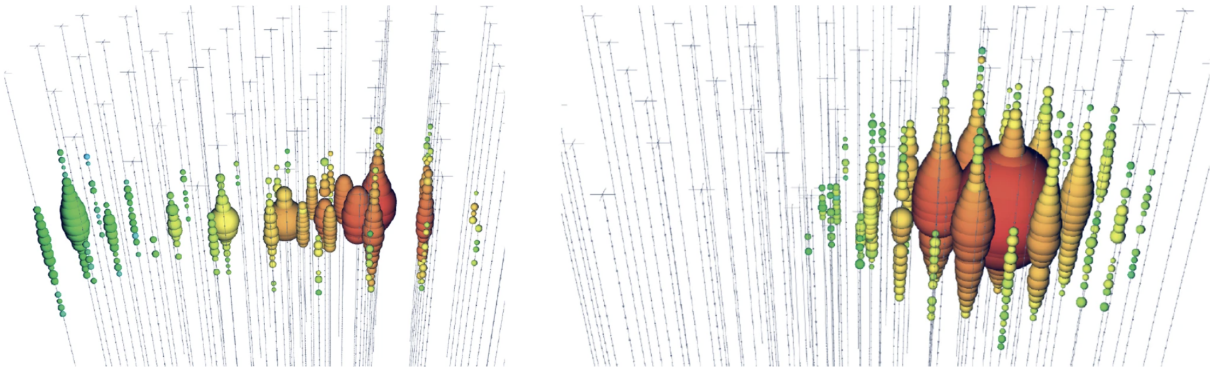

Figure 6.2 Two example event views of particle interactions within IceCube [Ahlers et al., 2018]. On the left, we show an example track topology produced from a traversing muon. On the right, we show a cascade produced by a potential neutral current interaction, or electron or tau charged current interaction.

nels,

$$\nu_\tau + N \to \tau + X, \tag{6.4}$$

$$\tau^- \to \mu^- + \bar{\nu}_\mu + \nu_\tau \qquad (17.4\%), \tag{6.5}$$

$$\tau^- \to e^- + \bar{\nu}_e + \nu_\tau \qquad (17.8\%), \tag{6.6}$$

$$\tau^- \to \text{hadrons} + \nu_\tau \qquad (64.8\%). \tag{6.7}$$

At $E_\tau \lesssim 100$ TeV, the tau decay length is on the order of several meters. The majority of events will appear as blob-like cascades, except in the case that a muon is produced. In the regime, $E_\tau \gtrsim 100$ TeV, there are three generally visible topologies. Depending on where a hadronic shower or electromagnetic cascade is produced relative to the initial interaction site, the event may again appear as a cascade. If the tau travels for a longer distance and then decays, a 'double-bang' topology is instead observed. Two distinct cascades with spatial separation are measured by the detector. Last, in the case that a muon is produced, a track-like topology is also possible.

We note that in all interactions, the number of produced photons is approximately linear with deposited energy. We provide event views of an example track and cascade interaction topology in Fig. 6.2.

6.4 Cosmic-Ray Muon Interactions

Cosmic-ray air showers form a dominating background for astrophysical neutrino events. The penetrating, interacting air shower is composed primarily of high-energy muons. As this component of the shower is relativistic, this muon bundle appears highly collimated. The interaction topology of such events appears as an approximate superposition of many interacting muons. This track-like signature has lower stochasticity relative to individual muons, as the discrete energy losses of all particles contribute in summation [Gaisser et al., 2016].

6.5 Radiative Propagation in Ice

The natural Antarctic ice sheet provides the detector medium and target volume for neutrino interactions. IceCube sensors are deployed within glacial ice that accumulated over tens of thousands of years through continual snowfall and compression.

The optical properties of the ice vary substantially with depth. Several periods of increased volcanic activity and atmospheric dust resulted in ice layers enriched in ash and particulates. These impurities increase both photon scattering and absorption, tending to dim and diffuse potential particle interaction signals. In contrast, purer ice layers exhibit longer scattering and absorption lengths, allowing longer photon propagation before attenuation [IceCube Collaboration, 2013b, Chirkin, 2013].

In addition to vertical dependence, the ice exhibits anisotropic optical properties. The ice sheet slowly flows over the underlying bedrock at rates on the order of several meters per year. The bedrock is inclined, with a varied tomography. Over glaciological timescales, this directional flow orients and deforms the crystal structure of the ice. The result is increased scattering in directions perpendicular to the flow, and a slight transmission asymmetry with the forward flow direction [Abbasi et al., 2024].

Photon transport is characterized by both position and direction-dependent scattering and absorption coefficients. This optical heterogeneity impacts the timing and spatial diffusion of emitted photons. Event simulation and modern reconstruction must account for

these depth-dependent and anisotropic optical properties.

6.6 Detection and Initial Processing

Data Acquisition Photons that reach a photomultiplier tube (PMT) are converted to photoelectrons. This initial charge signal is amplified through a series of dynodes, producing a cascade of electrons with intensity approximately proportionate to the initial number of photons. Electronic onboard the DOM continuously monitor PMT output and digitize electron pulses. The recorded waveform carries both timing and charge information.

Digitized waveforms are time-stamped and transmitted through the string cabling to the ICL. At this location, data from all sensors are assembled for triggering and storage [IceCube Collaboration, 2017].

Triggering and Online Filtering The majority of photon signals originate from low-energy atmospheric muons and sources of in-ice and detector noise. To reduce this data volume, IceCube employs a hierarchy or trigger algorithms that identify spatially and temporally correlated activity across multiple DOMs. The primary trigger and data used in this work rely on a minimum multiplicity of eight sensors with photon hits within a predefined time window.

Events satisfying trigger criteria are readout. Fast reconstruction algorithms are applied at the South Pole to identify a selection of interesting or notable events. This smaller subset of events can be transmitted for remote analysis in real time.

Calibration and Pulse Extraction The recorded waveforms are then calibrated. Calibration account for PMT gain variations, electronics response, timing offsets, and baseline fluctuations. Detector status information is used to identify malfunctioning or unstable optical modules, which are removed from further analysis.

The calibrated waveforms are decomposed into a series of reconstructed pulses. This process estimates the arrival time and charge of individual photon signals by deconvolving the waveform with templates describing the PMT and detector response.

Additional cleaning algorithms remove isolated noise hits and retain pulses causally consistent with particle propagation. These cleaned pulse series are then reconstructed.

6.7 Event Reconstruction

IceCube utilizes a number of event reconstruction algorithms of varying complexity. In general, IceCube reconstructs events on a feature space,

$$\mathcal{X} = \mathcal{E} \times \mathcal{P} \times \mathcal{S}^2 \times \mathcal{T} \times \mathcal{Z}.$$

Here, $\mathcal{E}$ represents a space of energies, $\mathcal{P}$ represents a space of positions, $\mathcal{S}^2$ represents a space of directions, and $\mathcal{T}$ represents time. The last common observable space, $\mathcal{Z}$, indicates the event signature or topology.

We highlight the Millipede reconstruction algorithm, which was designed to reconstruct series of stochastic energy losses along straight-line trajectories, utilizing a near-complete ice model [IceCUbe Collaboration, 2014]. This is one of the most physically-realistic reconstruction algorithms available. The model has been applied with success to all-flavor neutrino interaction topologies, as well as cosmic-ray muon bundles.

As the photon intensity of a point-like stochastic loss or shower scales linearly with energy, Millipede relies on detector response expectations dependent only on sensor position and angle as well as the loss interaction vertex and direction. We describe a coordinate in this sensor and interaction-dependent space as θ. The expected detector response, $\mathbf{B}(\theta)$, reflects the expected spatiotemporal evolution of the radiative cascade, independent of energy.

Given a position and direction hypothesis for a track trajectory, Millipede places m discrete, stochastic losses at equally placed increments along this track. Commonly, this hypothesis is seeded by simpler, faster reconstruction algorithms. We can consider n detector observables, which may correspond to time-integrated sensor photon counts, or to sensor-specific counts within specified time bins. We also propose a hypothesis vector, $\mathbf{E}$, of energies corresponding to each loss. The expected number of photons, $\mathbf{N}$, is described by,

$$\begin{pmatrix} N_1 \\ N_2 \\ \vdots \\ N_n \end{pmatrix} = \begin{pmatrix} B(\theta_{11}) & B(\theta_{12}) & \cdots & B(\theta_{1m}) \\ B(\theta_{21}) & B(\theta_{22}) & \cdots & B(\theta_{2m}) \\ \vdots & \vdots & \ddots & \vdots \\ B(\theta_{n1}) & B(\theta_{n2}) & \cdots & B(\theta_{nm}) \end{pmatrix} \begin{pmatrix} E_1 \\ E_2 \\ \vdots \\ E_m \end{pmatrix}. \tag{6.8}$$

This may be compactly expressed as,

$$\mathbf{N} = \mathbf{BE}. \tag{6.9}$$

Determining the optimal loss energies, $\mathbf{E}$, for a given observed set of detector responses, $\mathbf{N}_{\text{obs}}$, constitutes an inverse problem. Additionally, detector noise and background contributions, b_i, must be accounted for at each sensor. In principle, one may seek a solution for the unknown energy vector $\mathbf{E}$,

$$\mu_i = (\mathbf{BE})_i + b_i. \tag{6.10}$$

However, the detector response matrix $\mathbf{B}$ is generally non-square, sparse, and ill-conditioned. The observed detector counts arise from a stochastic counting process and fluctuate about their expectation values. Consequently, direct matrix inversion is neither possible nor statistically appropriate.

The detector observables are instead modeled as independent Poisson random variables with expected means. The probability of observing a set of counts $\mathbf{N}_{\text{obs}}$ is then,

$$P(N_{\text{obs}}|\theta) = \prod_{i=1}^{n} \frac{\mu_i^{N_i}}{N_i!} e^{-\mu_i}. \tag{6.11}$$

Maximum-likelihood reconstruction is equivalent to solving for μ_i, where deposited energies are constrained to be positive.

For a fixed track geometry, the negative log-likelihood is convex in the amplitudes $\mathbf{E}$, ensuring the existence of a unique global optimum. In practice, Millipede exploits this structure through constrained sparse optimization techniques related to non-negative least-squares and expectation-maximization methods. The resulting reconstruction may be interpreted as an unfolding of the longitudinal energy-loss profile of the charged particle trajectory. Rather

than assigning a single energy to the event, the algorithm estimates a discretized approximation to the energy-loss density along the track, resolving localized stochastic losses from bremsstrahlung, pair production, and photonuclear interactions.

The Millipede response matrix, $\mathbf{B}$, has tradiitonally been based on high-statistics detector cascade simulation. The observation at each sensor as a function of cascade properties is determined from interpolation.

6.8 Generative Stochastic Losses

CHAPTER 7

DIFFUSE FLUXES

7.1 Atmospheric Muons and Neutrinos

IceCube experiences a substantial flux of cosmic-ray air showers. These events create a substantial background for astrophysical track selections at all energies, and can mimic cascade topologies at low energies. As cosmic-ray air showers originate from all directions, both northern and southern events are relevant for the construction of targeted data selections.

In northern selections, the muons of cosmic ray air showers are attenuated within the Earth. Many air showers are entirely reduced below the minimum ionizing level prior to reaching the South Pole. This substantially reduces the detected rate of air shower events.

In southern selections, muons are attenuated with only an approximate kilometer of ice before reaching the detector. This leaves the south exposed to a high flux muonic cosmic rays.

7.2 The Astrophysical Neutrino Flux

In the last decade, many studies have focused on characterization of the diffuse astrophysical neutrino flux. In particular, the energy spectrum, spatial anisotropy, and flavor composition, may indicate the underlying astrophysical source populations. We provide a summary of current knowledge of this diffuse flux.

Spectral Structure Initial studies focused on power-law descriptions of the astrophysical neutrino flux,

$$\Phi_{\nu,\bar{\nu}} \;=\; \Phi \;\times\; \left(\frac{E}{100\ \mathrm{TeV}}\right)^{-\alpha} \times\; 10^{-18}\ \mathrm{GeV}^{-1}\ \mathrm{cm}^{-2}\ \mathrm{s}^{-1}\ \mathrm{sr}^{-1}. \tag{7.1}$$

Here, $\Phi_{\nu,\bar{\nu}}$ describes the astrophysical flux from both neutrinos and antineutrinos of a given flavor and energy, E. Recent studies have found an approximate spectral index, $\gamma \simeq 2.3$ – 2.5, and normalization $\Phi \simeq 1.3$ – 1.4. This index and normalization vary depending on the analyzed energy range, zenith range, and topology selection, suggesting likely degeneracies in the underlying model parameterization [Stettner, 2019].

Recent results provide evidence for additional energy-dependent structure. Combined fits to multiple data selections have identified possible deviations from a single power law near a few TeV and around 100 TeV [IceCube Collaboration, 2026a,b]. A distribution of events at these highest energies has previously been speculated to relate to an underlying blazar source class. The statistical significance of these features remains under active investigation, though they may indicate the presence of multiple source populations, Galactic contributions, or transitions between atmospheric and astrophysical components.

Galactic Excess and Anisotropy Early studies were consistent with an isotropic flux, supporting a large population of unresolved extragalactic sources as a possible origin. More recently, IceCube has reported evidence for diffuse neutrino emission associated with the Galactic Plane [IceCube Collaboration, 2023]. Although this Galactic component constitutes only a minority of the total astrophysical flux, it introduces measurable anisotropy and is now routinely incorporated into precision diffuse-flux analyses. The observed flux is often modeled as the sum of isotropic extragalactic and structured Galactic components.

Flavor Composition Neutrino oscillations occur over astrophysical baselines. Over these long propagation distances, the flavor composition evolves towards approximate equipartition. Assuming neutrinos are initially produced through conventional pion decay, we expect an approximate flavor ratio at the source,

$$(\nu_e : \nu_\mu : \nu_\tau) \approx (1 : 2 : 0). \tag{7.2}$$

At Earth, we would then observe,

$$(\nu_e : \nu_\mu : \nu_\tau) \approx (1 : 1 : 1). \tag{7.3}$$

Current measurements are consistent with this composition, given substantial, remaining uncertainties.

7.3 Forward-Folding and Inverse Problems

Diffuse IceCube analyses are typically formulated as forward-folding inference problems. Rather than attempting to directly invert detector effects and reconstruct the underlying neutrino flux, a physical model for the contributing particle populations and detector effects is assumed. Monte Carlo simulation for each channel and detector response is produced. Primary particles or neutrinos are generated according to an assumed flux model, propagate through the Earth, undergo interactions, propagate through the glacial ice, and are finally transformed into detector readout and reconstructed quantities. The resulting Monte Carlo events therefore live in the same observable space as the experimental data. Several event classes contribute to the observed data,

- astrophysical neutrinos,
- conventional atmospheric neutrinos,
- prompt atmospheric neutrinos,
- atmospheric cosmic-ray muon bundles.

Let $x \in \mathcal{X}$ denote a reconstructed event in the observable space. The expected detector-level event intensity is modeled as,

$$\lambda(x) = \sum_k \alpha_k \lambda_k(x; \theta_k), \tag{7.4}$$

where λ_k denotes the detector-level prediction for a component, k. θ_k are component-specific physical parameters, and α_k are normalizations. Parameter estimation proceeds by comparing the observed event distribution to the predicted detector-level intensity. If the observable space is partitioned into bins indexed by i, the expected counts is,

$$\mu_i(\Theta) = \int_{\text{bin } i} \lambda(x; \Theta)\, dx. \tag{7.5}$$

Assuming independent Poisson fluctuations in each bin, the likelihood of the observed counts $\{n_i\}$ is,

$$\mathcal{L}(\Theta) = \prod_i \frac{\mu_i(\Theta)^{n_i} e^{-\mu_i(\Theta)}}{n_i!}. \tag{7.6}$$

Θ denotes the collection of physical and nuisance parameters. The expected counts, μ_i, are obtained directly from the forward model. This approach differs from classical unfolding methods, which seek an estimate of the underlying flux by approximately inverting the detector response operator. Such inverse problems are typically ill-conditioned and require regularization. Forward-folding avoids this inversion by embedding detector effects directly into the statistical model, at the cost of substantial simulation requirements.

7.4 Atmospheric Neutrinos and Muon Bundles as Separate Components

Although atmospheric neutrinos and atmospheric muon bundles originate from the same cosmic-ray air showers, they are usually treated as distinct event classes in diffuse analyses. A full description would require simulation of the joint bundle and neutrino interaction. Sampling the possible, accompanying neutrinos produced within the shower and their potential interactions is resource intensive, and not traditionally performed.

Instead, atmospheric neutrino and atmospheric muon backgrounds are generally simulated independently. As atmospheric neutrinos are produced within the shower tree, they are associated with some probability of an accompanying, unattenuated muon. If one or more shower muons reaches the detector, the event can be rejected as atmospheric background. The relevant quantity parameterizing this probabilty is the neutrino passing fraction,

$$P_{\text{pass}}(E_\nu, \theta_z) = P(\text{no detectable accompanying muons}), \tag{7.7}$$

Here, θ_z is the event zenith angle. This probability depends on the shower composition and energy, shower development, and muon propagation to detector depth.

The resulting atmospheric neutrino intensity may be written schematically as,

$$\Phi_\nu^{\text{eff}}(E_\nu, \theta_z) = P_{\text{pass}}(E_\nu, \theta_z)\Phi_\nu(E_\nu, \theta_z). \tag{7.8}$$

This treatment correctly reproduces the leading-order reduction in atmospheric neutrino rate [Gaisser et al., 2014, Argüelles et al., 2018]. However, the joint topology of the neutrino interaction and its accompanying shower is not retained. Correlations between neutrino energy, muon multiplicity, shower fluctuations, and detector observables are neglected. For most diffuse analyses these effects are small compared to statistical and systematic uncertainties, but they become increasingly relevant for studies of rare atmospheric branches, including prompt neutrinos produced through charm hadron decay.

7.5 A Study of Atmospheric Event Topology in Analysis

7.6 Event Selections

Last, we provide a summary of event selections typically used in analyses. As neutrinos can generally be differentiated from cosmic ray muon bundles on the basis of their radiative signature, we consider both track and cascade selections.

In this work, we utilize the Point Source Tracks dataset from the IceCube Neutrino Observatory [IceCube Collaboration, 2021a]. This selection focuses on topologies consistent with a single muon track. In the north, muon bundles are naturally shielded, and the selection achieves a high signal-to-background ratio in this hemisphere. Astrophysical events outnumber atmospheric events in excess of approximately 100 TeV. In the south, harsh cuts are used to remove likely muon bundles. Still, the result is a low signal-to-background ratio.

The Point Source Tracks selection offers ideal angular resolution. As many tracks intersect and extend through the detector, their is a maximal, observable lever arm available. Directional reconstruction yields a resolution of $\delta \approx 0.1 - 0.3$ for energies in excess of 100 TeV. These events are ideal for spatial localization of point sources. The differential energy losses associated with a muon track also depend on muon energy. This allows for an approximate reconstruction of the track energy. However, this resolution is lower, and energies are generally constrained within an order of magnitude of their true value.

Cascade interactions can also be usefully incorporated within analyses. As this interaction signature is clearly distinct from a cosmic-ray muon bundle, the dominating background is

instead atmospheric neutrinos. Similar signal-to-background ratios are achieved in both the northern and southern hemispheres.

Cascades have sphere-like interaction signatures. Still, some directionality is represented through their slight asymmetry and propagation from their initial interaction location. In general, events in excess of 100 TeV may have an angular resolution on the order of a few degrees. At lower energies, events may be constrained within tens of degrees of their neutrino origin direction. However, cascades have calorimetric energy deposition. In the case of charged current interactions, the number of produced photons closely reflects neutrino energy. This makes cascades an ideal channel for constraining structure in energy spectra. In this work, we focus on the DNNCascades selection, which utilizes a neural network for cascade angular reconstruction [IceCube Collaboration, 2021b].

CHAPTER 8

KNOWN ASTROPHYSICAL NEUTRINO SOURCES

Since the discovery of the astrophysical diffuse flux, a central objective of neutrino astronomy has ben the identification of its sources. These associations would allow for direct study of sites of hadronic particle acceleration. In this section, we provide an overview of current results in neutrino astrophysics.

8.1 Blazars

Blazars are active galactic nuclei with relativistic, beamed jets. They have historically been viewed as a favorable candidate class for high-energy neutrino production.

TXS 0506+056 Some of the strongest evidence linking an individual blazar to neutrino emission originates from TXS 0506+056. In September 2017, IceCube detected the high-energy track event, IceCube-170922A, from a direction consistent with this source [IceCube Collaboration, 2018b]. The alert triggered an extensive multi-wavelength observing campaign that identified contemporaneous gamma-ray activity [Tanaka et al., 2017].

Subsequent analyses of archival data revealed an earlier neutrino flare between 2014 and 2015 from the source [IceCube Collaboration, 2018c]. This emission was consistent with a neutrino spectral index of $\gamma \approx 2$. These observations, established TXS 0506+056 as the first, likely astrophysical neutrino candidate source.

Additionally, further radio monitoring and very-long-baseline interferometry identified long-time scale radio activity from the parsec-scale core region of the jet. A radio flare was seen to build from 2016 or 2017, ultimately peaking in 2020. This activity is suggestive of a causal connection between the earlier gamma-ray activity and hadronic acceleration events, and development of the blazar jet.

PKS 1424+240 In recent years, an additional blazar has emerged as a likely source of neutrinos, PKS 1424+240. This object was associated with a notable, local significance in

2020 [IceCube Collaboration, 2020a]. In subsequent analyses, the source has persisted as a likely neutrino source. Multi-wavelength observations reveal strong gamma-ray variability and delayed radio activity similar to that observed in TXS 0506+056.

Although the statistical significance remains below the threshold required for an individual source discovery, the similarities between these objects suggest that neutrino production may be associated with a particular subclass of blazars exhibiting prolonged high-energy activity and complex jet evolution.

Recent Blazar Analyses A number of analyses have searched for a neutrino excess associated with physically motivated selections of blazars [Huber, 2019, IceCube Collaboration, 2022d]. In particular, gamma-ray and radio-bright blazars have been exhaustively studied. As this time, significant or notable aggregate emission from any selection of blazars has not been identified.

8.2 Seyfert and X-ray Bright AGN

While early neutrino searches focused primarily on blazars, recent observations have highlighted the potential importance of other active galactic nuclei. In particular, Seyfert galaxies and X-ray bright AGN possess dense nuclear environments that may efficiently convert accelerated hadrons into neutrinos. These same coronal environments would absorb a significant fraction of the accompanying gamma-ray emission.

NGC 1068 NGC 1068 is one of the most significant neutrino candidate sources identified by IceCube [IceCube Collaboration, 2022b]. This nearby Seyfert II galaxy exhibits a relatively persistent excess of neutrino events. The source is soft, with a spectral index, $\gamma \approx 3.2$.

An accompanying gamma-ray flux is not observed. These observed properties are consistent with neutrinos originating deep within the accretion region, close to the central black hole. In such an environment, gamma rays are absorbed before escaping the source [Murase and Stecker, 2023].

A Seyfert Population More recently, studies have provided significant evidence for a population of multiple X-ray bright Seyfert galaxies as astrophysical neutrino sources [IceCube Collaboration, 2026c]. These results motivate interests in obsucred AGN as potential sites of efficient hadronic acceleration and neutrino production. Additionally, this production scenario differs substantially from that initially expected for blazars, suggesting multiple classes of environments conducive to high-energy neutrino production.

8.3 The Galactic Plane

Astrophysical neutrinos may also originate from within our galaxy. In 2023, a selection of cascades was used to search for an excess along the Galactic Plane. A significant signal was established, though its driving components remain the focus of active study [IceCube Collaboration, 2023].

Galactic Diffuse Emission Galactic hadronic accelerators act as local sources of hadronic cosmic rays. These cosmic ray nuclei may interact with interstellar gas and radiation fields within the Galactic Plane. The result is a diffuse neutrino flux, reflecting both magnetic deflection and scattering within the galaxy. Depending on the model assumed for neutrino production, a template for topographic neutrino intensity from the galaxy can be determined. Such templates were used in the 2023 result.

Galactic Point Sources It is also possible that individual galactic sources may produce neutrinos within their source environments. Potential source candidates include X-ray binaries, supernova remnants, massive stellar clusters, and regions of intense star formation.

At present, no individual galactic source has been observed with sufficiently high significance to establish a galactic neutrino source class. However, as such point sources exist along the Galactic Plane, it is not presently possible to discount individual source contributions to the measured diffuse galactic excess. The existence of high-energy galactic hadronic accelerators has been confirmed, not the mechanism responsible for neutrino production.

CHAPTER 9

LIKELIHOOD METHODS AND STATISTICAL DISTINGUISHABILITY

The two subsequent sections of this work focus on the incorporation of additional temporal information within point-source analysis likelihood formulations. The result is an improved distinguishability between signal and background resulting from the refined measure space. In this section, we describe this likelihood development, inference process, and interpretation.

9.1 Traditional IceCube Point-Source Likelihood

The two subsequent chapters of this work focus on the incorporation of temporal information into IceCube point-source analyses. The central idea is that additional astrophysical information may improve the distinguishability of signal and background hypotheses. In particular, multi-wavelength observations provide information about periods during which neutrino production may be enhanced, allowing the construction of refined likelihood models. In this section, we review the traditional IceCube point-source likelihood, discuss its interpretation in terms of probability measures, and describe how temporal information may be incorporated into the inference procedure.

9.2 Traditional IceCube Point-Source Likelihood

The traditional IceCube point-source search may be viewed as a likelihood-ratio test between a background-only hypothesis and a hypothesis incorporating an additional signal component. Let,

$$x_i \in \mathcal{X}, \tag{9.1}$$

$$\mathcal{X} = \mathcal{E} \times \mathcal{S}^2 \times \mathcal{Z}. \tag{9.2}$$

In particular, the reconstructed event realization x_i is a coordinate in a space of energy, direction, topology and quality observables. We denote this reconstructed energy as E_i, right ascension and declination as δ_i and R.A.$_i$, and directional uncertainty as σ_i.

For a source at a known spatial location, $\vec{x}_s(\delta, \text{R.A.})$, the spatial probability density

function (PDF), is a 2D Gaussian on a sphere,

$$S_{\rm spat}(\delta_i, \text{R.A.}_i|\sigma_i) = \frac{1}{2\pi\sigma_i^2}\exp\left(-\frac{1}{2}\left(\frac{\vec{x}_i - \vec{x}_s}{\sigma_i}\right)^2\right). \tag{9.3}$$

Similarly, we assume a power-law neutrino energy spectrum of hypothesis index γ from the source. To determine the observed energy distribution, Monte Carlo simulation is used to represent the effects of Earth propagation and reconstruction. The resulting spectrum depends on the source's assumed declination, δ. The result is an assumed probability density function for the source signal energy spectrum, $S_{\rm ener}(E_i|\delta,\gamma)$.

Complementary background probability density function are also defined. $B_{\rm dec}(\delta_i)$ assumes a varying profile of atmospheric background with declination or zenith. The background rate is assumed constant with right ascension, and a factor of $1/(2\pi)$ is used to normalize the considered solid angle. The energy probability density function, $B_{\rm ener}(E_i|\delta_i)$, represents the expected atmospheric spectral shape for a given event declination.

Given a sample of N observed events, the likelihood of n_s signal events from a source of spectral index, γ, is, γ, is,

$$\begin{aligned}\mathcal{L}(n_s,\gamma) = \prod_{i=1}^{N}\Bigg[&\frac{n_s}{N}\cdot S_{\rm spat}(\delta_i, \text{RA}_i \mid \sigma_i)\cdot S_{\rm ener}(E_i \mid \delta,\gamma) \\ &+ \left(1-\frac{n_s}{N}\right)\cdot\frac{1}{2\pi}\cdot B_{\rm dec}(\delta_i)\cdot B_{\rm ener}(E_i \mid \delta_i)\Bigg].\end{aligned} \tag{9.4}$$

The likelihood represents a mixture model of signal and background event populations.

9.3 Hypothesis Testing

Parameter estimation proceeds through maximization of the likelihood with respect to the unknown signal strength n_s and spectral index γ. The resulting maximum-likelihood estimates are denoted

$$\hat{n}_s \quad \text{and} \quad \hat{\gamma}.$$

Evidence for a source is quantified through the likelihood-ratio test statistic

$$\mathrm{TS} = 2\left[\ln \mathcal{L}(\hat{n}_s, \hat{\gamma}) - \ln \mathcal{L}(n_s = 0)\right].$$

This statistic compares the best-fitting signal-plus-background model to the null hypothesis of pure background. Large values indicate that the observed events are more consistent with the presence of a localized astrophysical source.

9.4 Event Intensities as Measures

A useful mathematical interpretation is obtained by viewing the observable space

$$\mathcal{X} = \mathcal{E} \times \mathcal{S}^2 \times \mathcal{Z},$$

as a measurable space equipped with signal and background measures,

$$\mu_S \quad \text{and} \quad \mu_B.$$

The corresponding probability densities may be expressed as Radon–Nikodym derivatives with respect to a common reference measure ν,

$$s(x) = \frac{d\mu_S}{d\nu}(x), \qquad b(x) = \frac{d\mu_B}{d\nu}(x).$$

The likelihood then corresponds to inference on a mixture measure,

$$\mu = \frac{n_s}{N}\mu_S + \left(1 - \frac{n_s}{N}\right)\mu_B.$$

Under this interpretation, detector reconstruction and event selection determine the measure on observable space, while statistical inference seeks to determine the relative contribution of the signal and background components.

9.5 Incorporation of Temporal Information

Many candidate neutrino sources exhibit substantial variability across the electromagnetic spectrum. Multi-wavelength observations can provide additional information related to periods of enhanced neutrino production.

To incorporate this information, the observable space is extended to include event time,

$$\mathcal{X} = \mathcal{E} \times \mathcal{S}^2 \times \mathcal{Z} \times \mathcal{T}.$$

The signal density becomes,

$$S(x_i) = S_{\text{spat}}(\delta_i, \text{RA}_i|\sigma_i) \times S_{\text{ener}}(E_i|\delta, \gamma) \times S_{\text{temp}}(t_i).$$

The background density becomes,

$$B(x_i) = \frac{1}{2\pi} B_{\text{dec}}(\delta_i) \times B_{\text{ener}}(E_i|\delta_i) \times B_{\text{temp}}(t_i).$$

The resulting likelihood is,

$$\begin{aligned} \mathcal{L}(n_s, \gamma) = \prod_{i=1}^{N} \Bigg[& \frac{n_s}{N} S_{\text{temp}}(t_i)\, S_{\text{spat}}(\delta_i, \text{RA}_i \mid \sigma_i)\, S_{\text{ener}}(E_i \mid \delta, \gamma) \\ & + \left(1 - \frac{n_s}{N}\right) \frac{1}{2\pi} B_{\text{temp}}(t_i)\, B_{\text{dec}}(\delta_i)\, B_{\text{ener}}(E_i \mid \delta_i) \Bigg]. \end{aligned} \tag{9.5}$$

The temporal density S_{temp} may be derived from external observations such as radio or gamma-ray light curves, incorporating astrophysical information unavailable to a purely time-integrated analysis.

9.6 Refinement of the Signal Measure

The inclusion of temporal information may be interpreted as replacing the original signal measure by a refined measure on the enlarged space,

$$\mathcal{X} = \mathcal{E} \times \mathcal{S}^2 \times \mathcal{Z} \times \mathcal{T}.$$

For a time-integrated search, the signal density is effectively uniform in time,

$$S_{\text{temp}}(t) = \frac{1}{T},$$

where T denotes the observation duration. Multi-wavelength observations instead motivate a non-uniform temporal density,

$$S_{\text{temp}}(t) = \frac{f(t)}{\int_T f(t')\, dt'}.$$

Here, $f(t)$ may represent a radio, millimeter, or gamma-ray light curve. The modified signal measure satisfies,

$$d\widetilde{\mu}_S = S_{\text{temp}}(t)\, d\mu_S.$$

This operation concentrates probability mass into periods of elevated source activity while preserving normalization. Events occurring during these periods contribute more strongly to the likelihood ratio than events occurring during quiescent intervals.

9.7 Distinguishability

The purpose of incorporating additional observables is to increase the distinguishability of the signal and background measures. In general, hypothesis testing becomes easier when the signal and background densities differ substantially across observable space. The addition of temporal information introduces a new dimension in which the two populations may be separated. While the background rate is approximately stationary, the signal density may become strongly concentrated around periods of enhanced activity. Consequently, events occurring during these intervals carry greater weight.

One way to quantify this separation is through the Kullback–Leibler divergence,

$$D_{\text{KL}}(\mu_S \| \mu_B) = \int \log\left(\frac{d\mu_S}{d\mu_B}\right) d\mu_S.$$

This represents the expected information gained when distinguishing signal events from background events. Incorporating temporal information modifies the signal measure and may increase this divergence, improving the sensitivity of the likelihood-ratio test.

CHAPTER 10

MILLIMETER-BRIGHT BLAZARS

In the last few years, several studies have suggested a potential excess associated with radio-bright blazars. Many of these studies have utilized lists of high-energy events with a high-likelihood of astrophysical origin released by IceCube for a correlation with a catalogue of known radio sources. Some analyses have also incorporated temporal information through radio light curves within correlation studies. In general, a mild significance was reported across these works [Plavin et al., 2020, Plavin et al., 2021, Hovatta et al., 2021, Aublin and Plavin, 2021, Illuminati and Plavin, 2021, Plavin et al., 2023].

A recent IceCube analysis focused on 15 GHz data from the Monitoring of Jets in Active Galactic Nuclei with VLBA Experiments (MOJAVE) campaign. This study found a small excess from the source population at the level of 1.9σ [IceCube Collaboration, 2024]. This result corresponded to a potential contribution on the order of 10% of the diffuse flux.

Previous work has also established a correlation between high-energy particle acceleration and radio activity [Fuhrmann et al., 2014]. In particular, gamma rays were temporally associated with radio activity. The strength of correlation was found to increase with radio frequency. These higher frequencies are generally less self-absorbed, probing the central-most regions of the AGN and jet base. If neutrino production occurs from sites that are gamma-ray opaque, millimeter wavelength emission may instead provide a superior tracer of particle acceleration and neutrino production.

In the following sections, we describe a search for astrophysical neutrinos with the IceCube Point Source Tracks dataset. We use a new catalogue of millimeter-wavelength blazar light curves from the Atacama Cosmology Telescope (ACT). We search for temporal correlations with physically motivated temporal models determined from this millimeter-wavelength data. These sections were previously published and are reproduced in part here [IceCube Collaboration and Atacama Cosmology Telescope Collaboration, 2025].

10.1 A First Catalog of ACT Millimeter-Wavelength Blazar Light Curves

ACT was a six meter telescope in the Atacama Desert of northern Chile built to image the CMB with ∼arcminute resolution. Over its 15 year lifetime, it observed a number of fields spanning declinations from $-62°$ to $+22°$. The first two generations of receiver—the Millimeter Bolometric Array Camera (MBAC, 2008–2010; [Atacama Cosmology Telescope Collaboration, 2011]) and ACTPol (2013–2016; [Atacama Cosmology Telescope Collaboration, 2016a])—observed eight fields ranging from hundreds to thousands of square degrees. In 2016, a year before the third generation receiver, Advanced ACTPol (AdvACT, 2017–22; [Atacama Cosmology Telescope Collaboration, 2016b]), was installed, a wide, ∼18,000 $\deg^2$ survey was undertaken, covering the full declination range and a wide range of right ascensions that avoided the Galactic plane [Atacama Cosmology Telescope Collaboration, 2020a]. The survey lasted until the observatory was decommissioned in September 2022 and was carried out in three principal frequency bands: 77–112 GHz (95.0 GHz), 124–172 GHz (146.9 GHz) and 182–277 GHz (225.0 GHz), where the values in parentheses are band centers appropriate for synchrotron radiation with spectral index, $\alpha = 0.7$ (assuming a flux density, $S_\nu \propto \nu^{-\alpha}$). [A comparison of source spectral indices at two frequency bands, constructed from synchronous 95 and 147 GHz light curve measurements and from 147 and 225 light curves, is provided in the published work.] Throughout, we refer to these bands by their central values of 95, 147 and 225 GHz. Two low frequency bands, 21–32 GHz and 29–48 GHz, were added in 2020; these centimeter wavelength observations are still being characterized and are not included in this paper.

The ACT Collaboration has produced a first catalog of 95, 147 and 225 GHz light curves for the brightest mm point sources in the ACTPol and AdvACT surveys. A paper describing the catalog in detail is in preparation (Ma et al.) and the light curves will be publicly released. Here, we summarize some of the basic properties of the data. The catalog consists of 205 radio sources with mean fluxes above 500 mJy in the 95 GHz band. This flux density threshold results in high signal-to-noise light curves. We primarily focus in this analysis

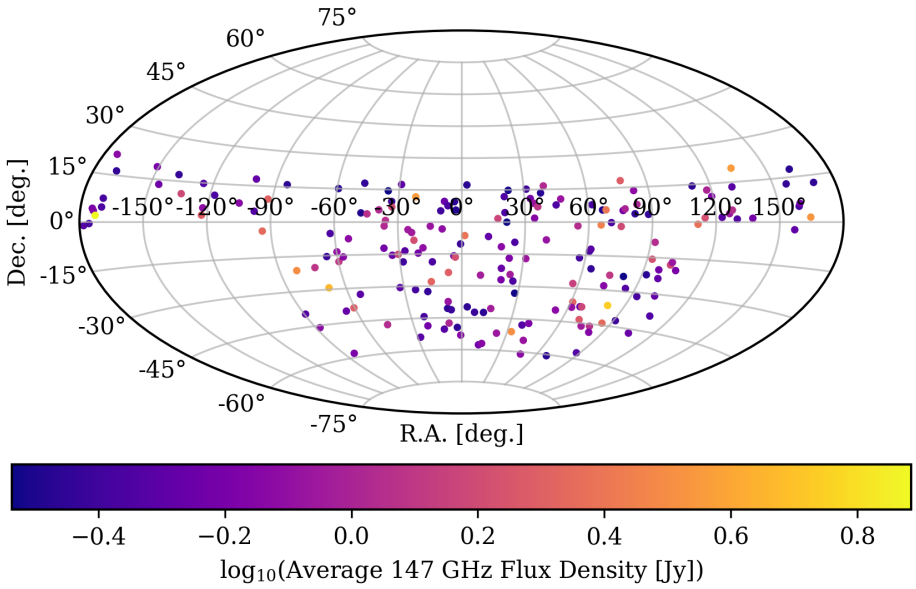

Figure 10.1 Map showing the spatial distribution in equatorial coordinates of the 195 blazars in the ACT catalog of mm-bright AGN. The average 147 GHz flux over the observing period is indicated by the marker color. ACT surveyed from $+22°$ in the north to $-62°$ in the southern hemisphere.

on the 95 and 147 GHz light curves as these bands have significantly lower uncertainties. Some sources are observed from 2013 onwards, but data for most sources date from 2016 when the wide-area survey began. This first catalog also excludes observations made during the daylight hours due to the more complex beam and calibration properties of these data. The beam size is approximately 1.4 arcminutes at 147 GHz and the point-source positional uncertainty is on the order of 3 arcseconds [Atacama Cosmology Telescope Collaboration, 2020b]. All sources have been cross-matched in the VizieR database, the NVSS databases, or the AT20G Australia Telescope 20 GHz survey catalog, and 195 of them are confirmed blazars [Ochsenbein et al., 2000, Condon, J. J. and others, 1998, Murphy et al., 2010]. The positions from these external catalogs are adopted throughout this work because of their much smaller uncertainties. Fig. 10.1 shows a map of source position and average mm flux density.

Sources were observed on a near-daily basis, but there are gaps of up to a few months due to only night-time data being included, as well as because of inclement weather, tele-

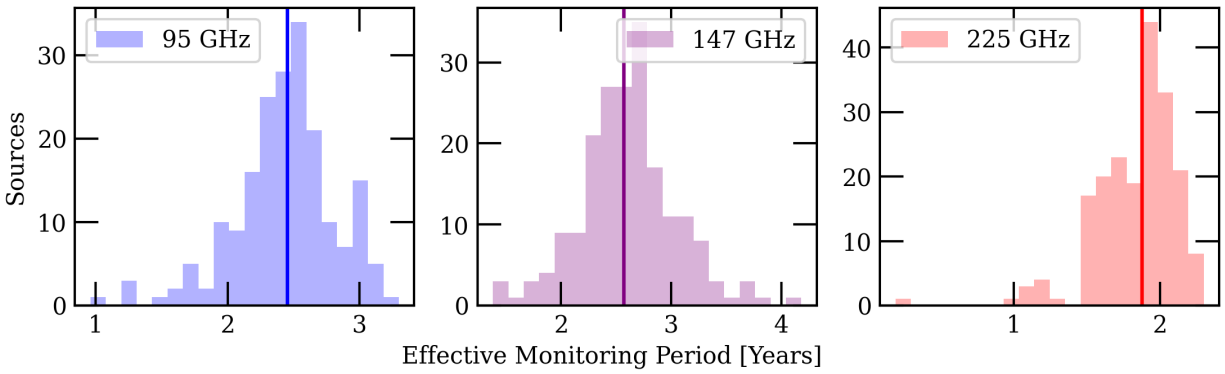

Figure 10.2 Histograms showing the amount of time each of the 195 blazars in the sample was observed, for the 95, 147 and 225 GHz bands. In each case, a vertical line representing the median of the distribution is plotted. Each data point in a source's light curve is assumed to represent its flux for fourteen days surrounding the date it was made on. The union of this set is expressed as its effective monitoring period. We do not expect substantial mm jet variability at this or shorter time scales. ACT takes few-month pauses for seasonal weather conditions or other telescope maintenance. We also note that there is some spread in the total effective monitoring period of each source. Still, these linearly-interpolated light curves provide a useful characterization of source activity. The majority of sources at 147 GHz built up this effective monitoring period over 5–7 years.

scope maintenance, hardware upgrades and seasonal visibility. As mm blazar jets exhibit strong variations on timescales of several months to years, this sampling cadence provides an excellent view of jet flaring activity. Distributions of source effective monitoring periods, after binning the data by 14 days, are shown in Figure 10.2. This 14-day timescale is used later on in this work as a constant bin size to construct temporal neutrino expectations from measurement and from interpolation.

The ACT light curves used in this paper use preliminary flux values that have continued to be improved, including while this paper was in review; as such, the light curves used here are not expected to match the final published ACT light curves. The primary updates have been to the matched filter used on the ACT maps, which we anticipate will create a $\sim \mathcal{O}(5\%)$ difference between the final light curves and those used in this paper. Since our analysis fits a neutrino/mm flux ratio and so relies on the relative fluxes between sources as a function of time rather than the absolute flux values (see Sec. 10.3, below), we have proceeded here with preliminary values and do not expect the final results to change what is reported here.

We estimate the flux completeness of the ACT AGN catalog relative to the expected distribution of blazar sources using the Harding–Abazajian luminosity-dependent blazar evolutionary model [Abazajian et al., 2011, Harding and Abazajian, 2012]. The fluxes of simulated source populations are generated as a function of redshift with FIRESONG [Tung et al., 2021]. Because our analysis assumes a constant of proportionality between average flux density and neutrino intensity, the predicted distribution of arbitrary-unit source fluxes in the Harding–Abazajian model can be linearly scaled to match the measured ACT flux densities. The ACT AGN catalog was extracted from a footprint covering 40% of the full sky. Thus, to allow for comparison with the ACT flux distribution, the predicted, full-sky population distribution is scaled by a factor of 0.40. This reduces the expected source number as a function of flux to reflect the limited solid angle viewed by ACT. Additionally, it is found that the resulting source number density as a function of flux is lower than that observed by ACT. The original Harding–Abazajian flux distribution is then scaled up by a factor of 2.4 to match the observed ACT blazar population. This discrepancy may owe to assumptions in construction of the original Harding–Abazajian model. This final flux distribution is shown in solid red in Fig. 10.3. The distribution of 195 sources used from the ACT catalog are also shown in blue for comparison. The flux completeness of the ACT catalog specific to its surveyed solid angle is the integrated or summed flux of the AGN in the catalog (the blue distribution of Fig. 10.3) relative to the summed flux expected from the entire population (the red distribution). Relative to the full-sky, we find a final flux completeness of 29%. Sources of the ACT catalog represent this fraction of the total flux expected from a comparable, complete, all-sky population.

10.1.1 TXS 0506+056 as a Millimeter Source

TXS 0506+056 is a relatively bright mm-wavelength source with an average 147 GHz flux density of $\sim$1 Jy, in the top 27% of the considered set of blazars. ACT observations of this source began in 2016, and include time periods prior to and during the 2017 IceCube alert event, IceCube-170922A [Tanaka et al., 2017]. A mm flare is observed between 2019

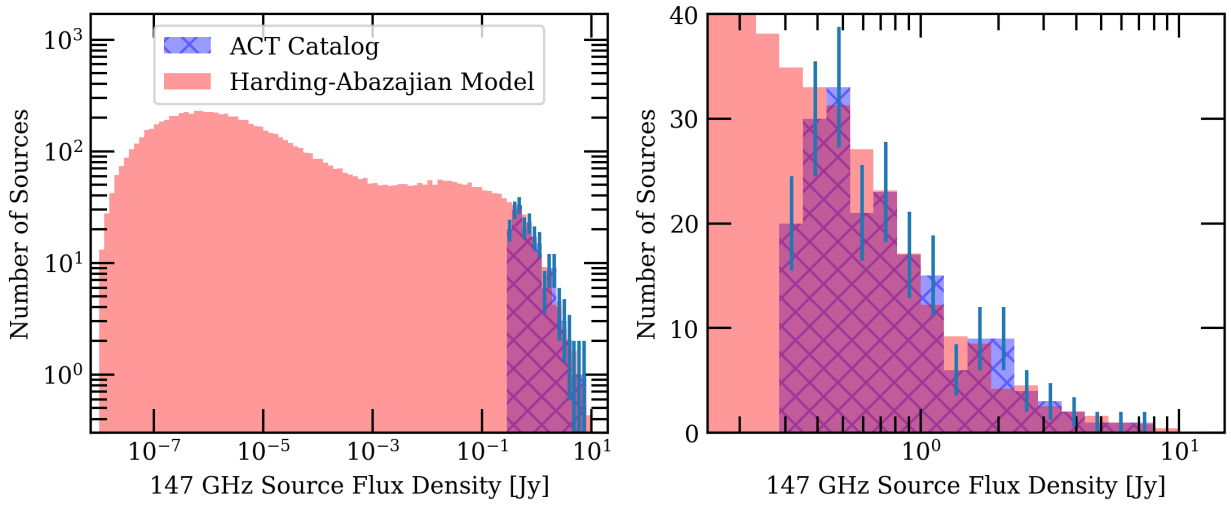

Figure 10.3 Distributions indicating completeness of the ACT catalog relative to the scaled Harding–Abazajian evolutionary model. The left panel shows the entire distribution of the model, while the right panel shows the flux range in the ACT catalog. The distribution of average ACT blazar 147 GHz flux densities is plotted on top of the source distribution predicted by the Harding–Abazajian model, after scaling for a mm-to-neutrino flux proportionality, as well as adjusting for the incomplete sky coverage of ACT (0.4) and for source number density as a function of flux; see text for details. The ACT catalog is flux-limited by the threshold of 500 mJy at 95 GHz that was used to select sources. While there is some slight bias in the catalog selection towards flaring, temporarily bright sources, the majority of blazar activity occurs on few-month-to-year timescales, so a representative description of average source brightness can still be provided with ACT's effective monitoring period. The fraction of predicted flux from sources in the ACT catalog relative to the entire mm population is derived from this comparison. Accounting for sources outside of ACT's surveyed field, the final flux fraction or completeness associated with the ACT catalog is 29%.

and 2022. The light curves in the three mm bands are shown in Fig. 10.4. While TXS 0506+056 does not peak in flux density in 2017, a spectral hardening was noted, as seen in the 'spectral index curve' of Fig. 10.4. Here, 'hardening' describes a relative increase in the intensity of higher-energy radiation. The spectral index is calculated assuming a power law between the 95 and 147 GHz flux densities.

We hypothesize that the spectrally hardened state observed around the time of IceCube-170922A represents a relative increase in higher-energy particle acceleration that is associated with neutrino production. We also note the average mm spectral index of the source is exceptionally hard, lying in the top ∼5% of the spectral indices of all sources within the catalog. Considering the per-source, time-averaged catalog spectral indices determined from

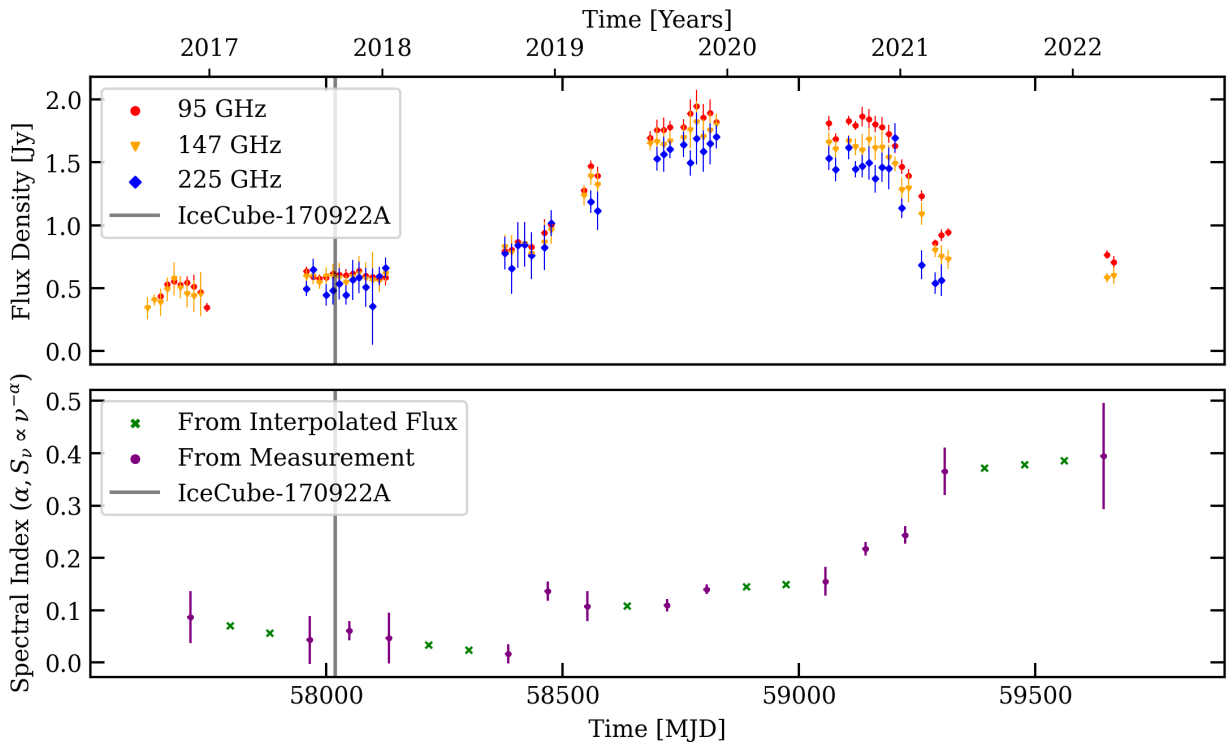

Figure 10.4 Millimeter light curves and spectral index curve for TXS 0506+056. On top, the red, orange and blue data correspond to 95, 147 and 225 GHz measurements averaged within 14-day bins. A substantial mm flare is observed between 2019 and 2021. On the bottom, a spectral index curve is determined from the interpolated 95 and 147 GHz light curves with 84-day bins. A power-law relation is assumed between 95 and 147 GHz flux densities. TXS 0506+056 shows a hardened state in the years surrounding the time of the IceCube ∼300 TeV track event. The power-law spectral index is at an absolute value near zero during this period, and slowly tapers off towards a value of 0.5. A spectral index of 0.5 to 0.7 is typical of optically-thin synchrotron spectra. The timescale of this variation is similar to that of the contemporaneous gamma-ray flare observed from the source [Tanaka et al., 2017]. The cadence of observations is representative of other sources within the catalog.

comparing 95 and 147 GHz light curves, the mean index and central 68% percentile is $0.41^{+0.13}_{-0.30}$. With the construction of a time-binned light curve for each source, we consider whether both 95 and 147 GHz flux density measurements are present in a given bin, and if so, we compute the spectral index for this time period. The average of these measurements for each source is then compared. If such emission is unabsorbed, the harder synchrotron spectrum would trace a steep underlying distribution of accelerated electrons. While a direct link between the underlying leptonic and hadronic populations would require further simulation, efficient high-energy particle acceleration is conducive to neutrino production.

10.1.2 Potential Neutrino-Millimeter Temporal Correlations

We consider three temporal models for a time-dependent correlation between mm and neutrino emission. In the first model, we assume a direct correlation between the neutrino intensity and the 147 GHz flux density. Such a model suggests that neutrino production is always possible in mm-bright sources, but is modulated by mm-flaring activity. In this case, emission from the jet or particle loading site dominates our mm observations. The 147 GHz band has the best livetime coverage and lowest uncertainty of the three bands included within the ACT catalog. These measurements are further binned into 14-day bins and averaged to minimize uncertainty. This timescale reflects a minimum expected period for major variations in source intensity. We also note that the 147 GHz band is less likely to trace self-absorbed regions than the 95 GHz band, which also has relatively low flux uncertainties.

The second model is motivated by the expectation that non-variable mm emission from regions around the AGN may contribute to the observed mm flux density without tracing neutrino production. Specifically, cooled populations of electrons further down the jet may radiate and produce a steady-state SED for the source. Extended emission from the galaxy would also contribute to this quiescent baseline. These components would not trace particle loading at the base of the jet. It is therefore possible that the conditions required for neutrino production are not available in these regions. To trace only flaring activity from the jet base or other variable regions, our second model consists of correlating with the 147 GHz mm light curve from which its minimum value has been subtracted, thereby assuming that there is no quiescent neutrino emission. The minimum used for the subtraction is obtained from the binned light curve described above. In general, the average flux density after subtracting the flux density minimum is roughly half that prior to the subtraction.

Finally, for the third model, we note that while TXS 0506+056 did not show an apparent correlation between mm emission and the high-energy event IceCube-170922A, the source was in a significantly hardened state. This spectral trend was also present during the 2014-2015 neutrino flare. RATAN-600 observations at 4.7, 8.2, 11.2 and 22.3 GHz between 2012

and 2017 suggest a relatively flat spectral state [Baikal-GVD Collaboration]. We consider that this spectral hardening of the synchrotron spectrum may trace high-energy particle injection and neutrino production. For all sources, a similar spectral index curve is determined from interpolated 95 and 147 GHz light curves. For each source, the top 32% of time in which the source is in its hardest state is chosen as a filter for the original 147 GHz light curve. This threshold is phenomenologically motivated: it roughly selects the gamma-ray flaring period coincident with IceCube-170922A for TXS 0506+056. Neutrino emission is assumed here to correlate with the observed flux density only during these periods. We refer to this temporal model as the 'index-filtered' model throughout this work.

10.2 An All-Sky Selection of IceCube Events

We consider a selection of track-like events from the full sky. Data from April 2008 through May 2022 are used in the selection. Twelve years of these data were taken with the full detector array, and the initial two years were taken with the partially completed detector. In the south, a set of selections are used to remove likely atmospheric cosmic rays [IceCube Collaboration, 2021c]. While this helps to improve sensitivity, a substantial background of atmospheric muons and neutrinos remains.

10.3 Methodology and Results

In this section, we discuss the specific methodology and search performed in this work. The text is heavily adapted from the original publication and references the likelihood formulation discussed in the previous section.

10.3.1 A Search for Neutrino Emission from Individual ACT Blazars

To test the three temporal models described in Sec. 10.1.2, direct correlation with the 147 GHz light curve, the baseline-subtracted light curve, and periods filtered by spectral hardness, we first utilize spatial, energy and temporal information to search for neutrino emission from individual sources. We assume a likelihood of the form of Eq. (9.5).

For each temporal model, we determine a temporal signal PDF using ACT data binned into equal periods, averaged and normalized. This temporal signal PDF, $S_{\mathrm{temp}}(t_i)$ is a func-

tion of event time, t_i. We note that in the linearly-interpolated and baseline-subtracted models, for time periods prior to the initial ACT observation and for periods after the last ACT observation, a constant value is assumed. Specifically, the average source flux density or average baseline-subtracted flux density is used for extrapolation. This assumption is equivalent to performing a joint time-independent analysis for these periods, where the observed duration provides an accurate representation of average mm intensity. The temporal background PDF represents an assumption of constant intensity.

Evaluation of this unbinned likelihood follows from previous work [Braun et al., 2008]. As event rates are essentially constant as a function of right ascension, randomizing data in this dimension allows us to characterize search sensitivity subject to the dominating background component. We determine best-fit signal values for an ensemble of such event realizations. In practice, we optimize n_s over a range of sampled γ values. As a final step, the L-BFGS-B optimization routine is used for a multi-dimensional fit [Byrd et al., 1995, Zhu et al., 1997, Morales and Nocedal, 2011].

We inject signals of varied strength from simulations to determine search sensitivity and discovery potential flux. Given an astrophysical neutrino spectrum of specific spectral shape, the 90% sensitivity flux indicates the signal intensity at which the test-statistic distribution of an injected signal exceeds the median of the background test-statistic distribution 90% of the time. Similarly, the 5σ discovery potential corresponds to the intensity at which the test-statistic distribution exceeds five standard deviations of the background test statistic distribution 50% of the time. Lastly, 90% confidence-limit upper limits may also be set by determining the flux intensity at which the test-statistic distribution exceeds the best-fit test statistic 90% of the time. In this work, we characterize our search sensitivities, discovery potentials and upper limits by the corresponding flux level at 100 TeV, $\Phi_{\nu_l+\overline{\nu}_l}$, assuming a specific spectral index, γ. In order to simplify the calculation of confidence intervals (as shown in Fig. 10.7) we assume that the background test-statistic distribution is chi-squared distributed based on Wilks' theorem [Wilks, 1938].

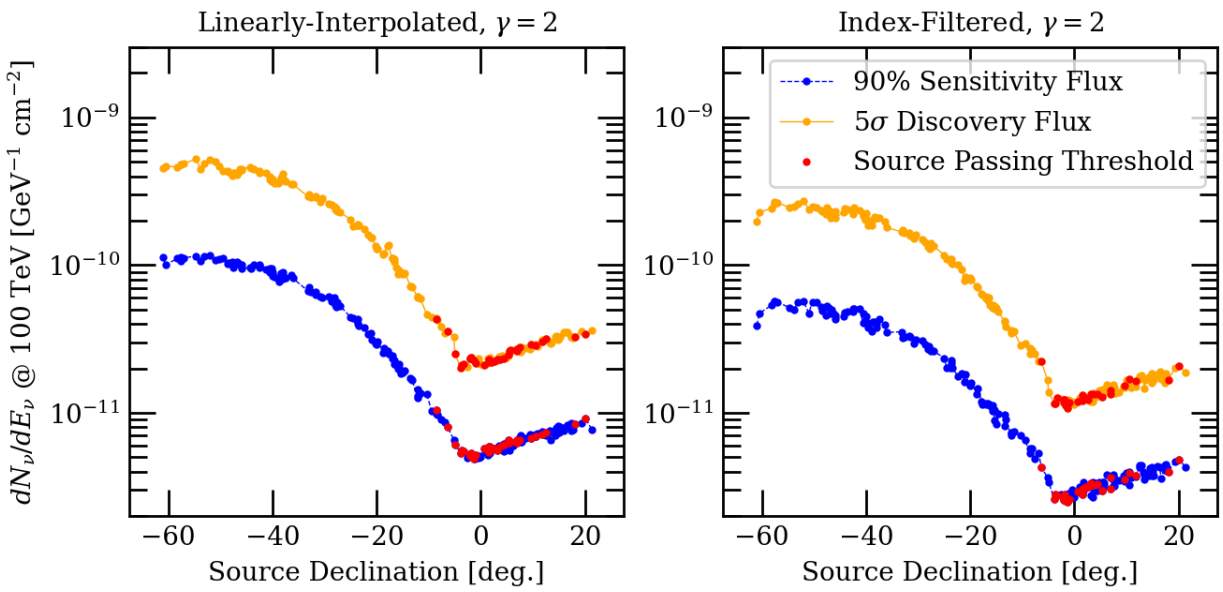

Figure 10.5 The sensitivity and discovery potential fluxes of IceCube searches for individual ACT blazars. Here, we show search sensitivity fluxes and 5σ discovery potential fluxes for each individual source under two temporal model assumptions, a linear-interpolation of the light curve and a spectral-index-based filtering. The plotted flux level represents a single-flavor contribution from both neutrinos and antineutrinos. An injected power-law signal following an index of 2.0 is used. The stronger background rejection associated with index filtering corresponds to lower sensitivity and discovery potential fluxes. Sources indicated in red pass the criteria for analysis. At negative declinations, events originating from the southern sky have poorer sensitivity due to the large background of atmospheric cosmic-ray muons. Sensitivity also worsens with increasing declination in the north, where attenuation within the Earth diminishes the number of observed events, especially for neutrino energies beyond 100 TeV.

In our analysis of individual sources, we focus on only a subset of the most promising objects in order not to dilute a potential significant result with additional trials, as explained further in this section. We first compare the relative expected neutrino fluence to the sensitivity flux for all 195 sources for each of the three temporal models. This fluence is proportional to the expected, model-dependent mm-fluence, equivalent to the time-integrated mm-flux density. An astrophysical neutrino spectrum of $\gamma = 2.0$ is assumed in all cases. This choice reflects the hard spectrum of candidate neutrino source, TXS 0506+056.

While an exact neutrino flux is not predicted for individual sources, we assume that the integrated mm fluence gives a description of relative neutrino intensity between different

sources under a specific model. In this way, the ratio between the integrated mm model fluence and the required astrophysical neutrino flux for sensitivity can act as a statistic to rank the relevancy of each source. This statistic is expressed as:

$$\text{Effective Weight} = \frac{\text{Model Dependent Average Flux}}{\text{Source Sensitivity}}. \tag{10.1}$$

After ranking the sources under each model assumption, we select the set of sources with at least 10% the weight of the most highly-ranked source for analysis. The sensitivities of all individual and selected sources are shown for a correlation with the linearly-interpolated 147 GHz light curve and with the index-filtered light curve in Fig. 10.5. This selection reduces the ultimate trials factor associated with the search. The final set of 45 sources selected for analysis based on any temporal model, their mm fluences and sky coordinates are listed in Table .1 within the Appendix. A total of 33, 42 and 27 sources are selected for the linearly-interpolated, baseline-subtracted and index-filtered models, respectively. Results particular to each temporal model are described in the following section.

10.3.2 Neutrino Emission from Individual ACT Blazars

The results of the analysis for each temporal model are reported within the Appendix in Tables .2, .3 and .4. Sources with excesses corresponding to a minimum 2σ local significance are highlighted in Table 10.1. The final trials-corrected p-value, taking into account all sources and all tested models, is provided for the most significant excess. The best-fit signal parameters for each source and temporal model are presented along with upper limits. There is a substantial correlation between the results of the linearly-interpolated and baseline-subtracted models.

In all searches, TXS 0506+056 is the most significant source. We note that this result is likely driven by correlation with the known neutrino flare in 2014. In our analysis, this flare would have occurred during an earlier period prior to ACT observations, where an average flux density was assumed. This neutrino flare is actually known to have taken place during a radio quiet state, as established by observations from RATAN-600 [Baikal-

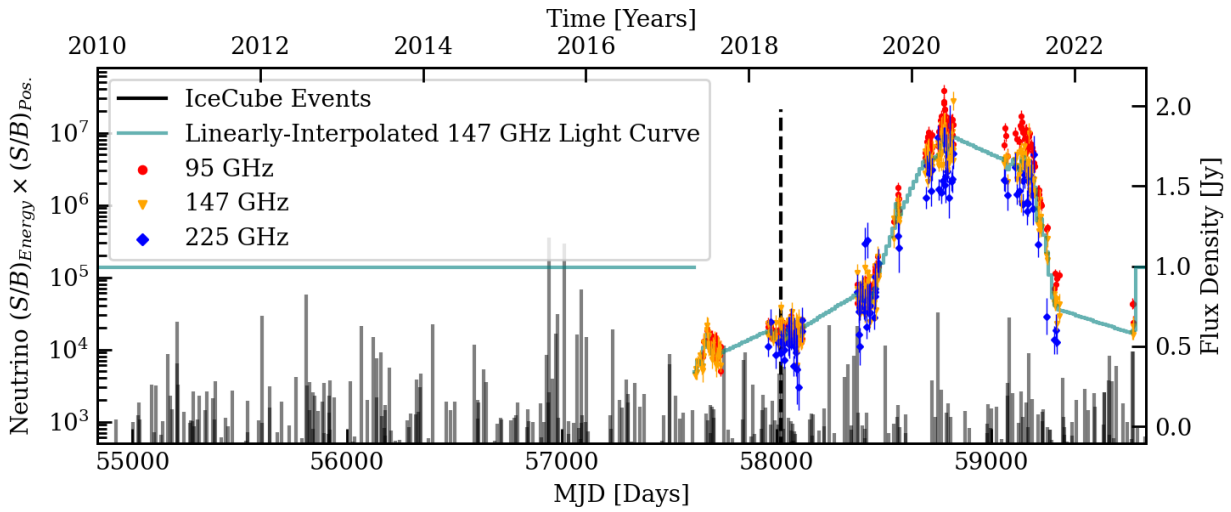

Figure 10.6 Events contributing to the TXS 0506+056 excess. Here, we provide neutrino event energy and spatial weight in black as a function of time for events within 1.5 degrees of TXS 0506+056. Correlation with the linearly-interpolated 147 GHz light curve (green line) is assumed. Prior to ACT observations, we extrapolate the mean 147 GHz flux. The raw ACT data for 95, 147 and 225 GHz are plotted for reference. The linearly-interpolated 147 GHz light curve is also plotted with extrapolated coverage extended to periods before and after ACT observation. The alert event, IC-170922A, is indicated with a dashed line. An excess of events around 57000 MJD is also visible, corresponding to the 2014-2015 flare. There is not an obvious correlation between the mm flux density flare from 2019 to 2021 and any neutrino activity.

GVD Collaboration]. Additionally, the TXS 0506+056 alert event, IceCube-170922A, arrived during the mm-quiet state observed by ACT. We provide in Fig. 10.6 a comparison of spatial and energy neutrino event weights with the ACT mm light curves. It is worth noting that there is no clear increase in neutrino emission correlated with the observed mm flare between 2019 and 2021. We include likelihood scans of the spatial excess and spectral parameters of the source under the linearly-interpolated and baseline-subtracted temporal models in Fig. 10.7.

Two other sources are observed in excess of a 2σ local significance. The first, J1415+1320, is a BL Lacertae object (BL Lac) with potential evidence for gravitational lensing of the jet [Vedantham et al., 2017a,b]. The second, 5BZB J0006-0623, is a low-synchrotron-peaked BL Lac [Kapanadze et al., 2020]. We note that such excesses are neither significant nor unexpected given the number of trials performed in this analysis. After a correction for the

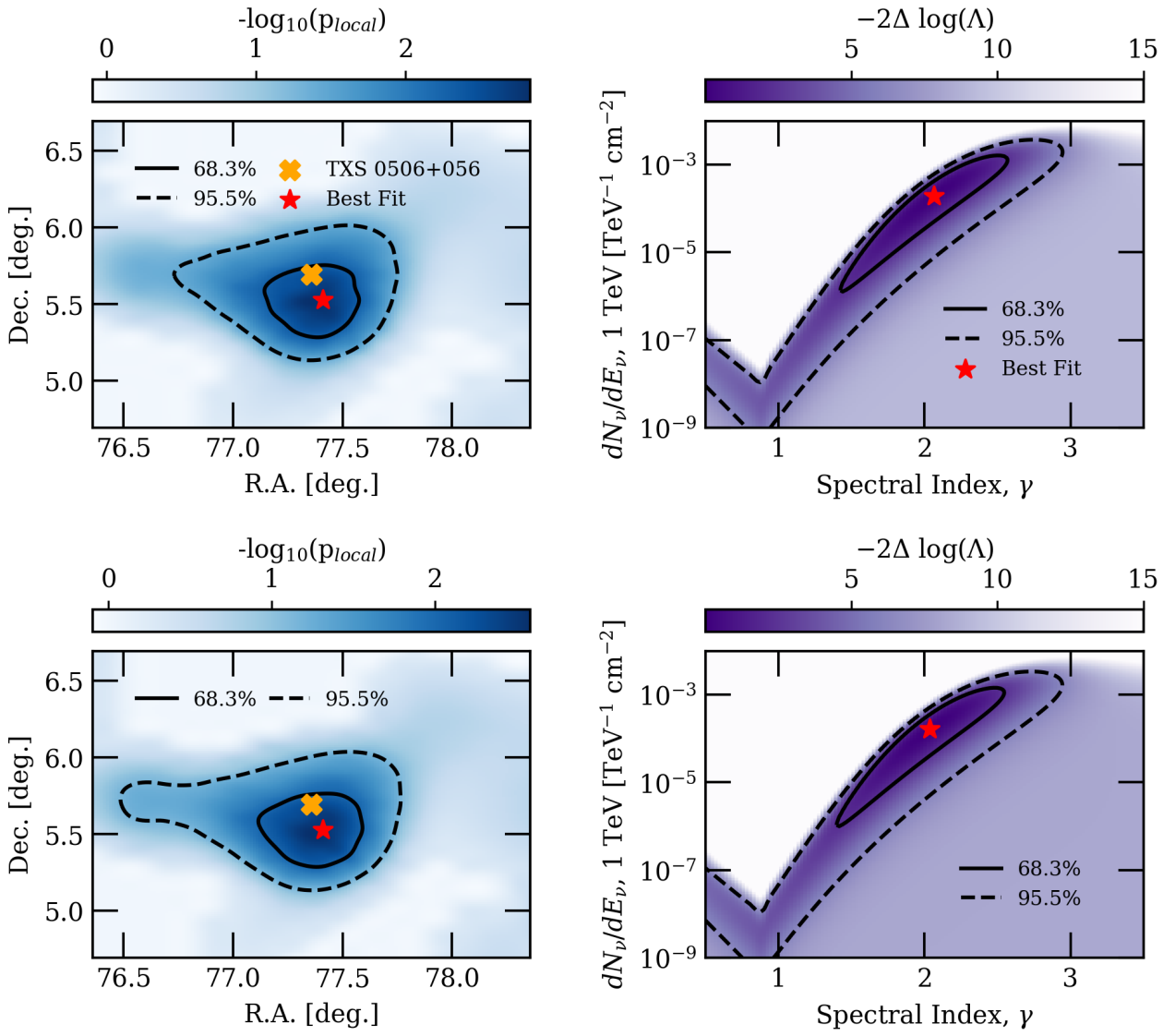

Figure 10.7 Positional and spectral scans of the IceCube TXS 0506+056 excess. Here, a positional and spectral scan of the TXS 0506+056 source location is shown in the top row assuming correlation with the linearly-interpolated 147 GHz light curve and in the bottom row for the baseline-subtracted 147 GHz light curve. On the left, the source likelihood is maximized as a function of assumed source right ascension and declination. The negative logarithm of the local p-value is plotted for each point. The known location of TXS 0506+056 is shown as an orange cross. On the right, the source likelihood is profiled as a function of signal intensity and power-law spectral index, γ. The logarithmic ratio between the best-fit likelihood and the likelihood of the selected signal parameters, Λ, is plotted. The best-fit locations for these spatial and energy signal parameters are pictured with a red star. The $\sim$0.25 deg. offset between the location of TXS 0506+056 and the best fit is comparable to the level of uncertainty expected for our highest-energy track events. 95.5% and 68.3% confidence regions are also shown, drawn from Wilks' theorem assuming two degrees of freedom.

number of trials, the global significance of the individual-source search is reduced to 0.8σ.

Search	Source Name	Z_{loc}	Z_{post}	$\hat{n}_s$	$\hat{\gamma}$	$\phi_{90\%,\gamma=2.0}$	$\phi_{90\%,\gamma=2.5}$
Linear-Interp.	**TXS 0506+056**	$\mathbf{2.56\sigma}$	0.8σ	**9.94**	**2.06**	**20.08**	**50.13**
Linear-Interp.	5BZB J0006-0623	2.07σ	–	11.29	4.00	21.84	44.72
Shifted	**TXS 0506+056**	$\mathbf{2.42\sigma}$	–	**9.35**	**2.04**	**18.85**	**46.56**
Shifted	5BZU J1415+1320	2.38σ	–	20.76	2.44	20.64	50.60

Table 10.1 Summary of results from the individual source searches. Here, we provide best-fit results for sources of significance in excess of 2σ from the three catalog searches performed. Only under the linearly-interpolated and baseline-subtracted models are such signals found. Results of the most significant source of each temporal model are bolded. The local significance and post-trials significance are presented as Z_{loc} and Z_{post}. The best-fit results are provided for these sources with upper limits for power-law spectral indices of 2.0 and 2.5, as well as the local significance, and a final post-trials significance reflecting all sources tested under all temporal hypotheses. Upper limits are presented in the form, $dN_\nu/dE_\nu(100\,\text{TeV}) = \phi_{90\%} \times 10^{-12}\,\text{GeV}^{-1}\,\text{cm}^{-2}$. The rate of a single-flavor flux, including both neutrinos and antineutrinos, is represented.

10.3.3 A Search for Neutrino Emission from the ACT Blazar Population

We also search for a combined signal from the entire population of ACT blazar AGN. In the event that individual sources are too faint to be observed, the cumulative emission may form a significant signal. A relative neutrino intensity is assumed between all sources, proportional to the integrated fluence expected for a specific temporal model. Additionally, a global neutrino spectrum is assumed for all sources, consisting of a power law following an index of γ.

For a source population of size, N_{src}, we generalize an event's signal PDF to allow associations with all locations:

$$\mathrm{S_{pop}}(\delta_i, \mathrm{R.A.}_i, E_i, t_i) = \frac{\sum_{j=1}^{N_{\text{src}}} w_j \cdot R(\delta_j, \gamma) \cdot S_{\text{temp},j}(t_i) \cdot S_{\text{spat},j}(\delta_i, \mathrm{R.A.}_i, \sigma_i) \cdot S_{\text{ener},j}(E_i|\delta_j, \gamma)}{\sum_{j=1}^{N_{\text{src}}} w_j \cdot R(\delta_j, \gamma)}. \tag{10.2}$$

Here, $S_{\text{spat},j}$ and $S_{\text{ener},j}$ are the spatial signal and energy PDFs of the jth source and w_j is a physically motivated weight controlling the relative amount of signal expected from a given source; in this case, w_j is the time-integrated fluence from a specific temporal model. As

detector effective area also varies as a function of source declination and neutrino energy, an additional weight is required to express this varying source acceptance, $R(\delta_j, \gamma)$.

The log-likelihood may then take the modified form,

$$\ln(\mathcal{L}_{\rm pop}(n_s, \gamma)) = \sum_{i=1}^{N} \ln \left[\frac{n_s}{N} S_{\rm pop}(\delta_i, {\rm RA}_i, E_i, t_i) + \left(1 - \frac{n_s}{N}\right) B_{\rm temp}(t_i) \frac{1}{2\pi} B_{\rm dec}(\delta_i) B_{\rm ener}(E_i \mid \delta_i) \right]. \tag{10.3}$$

10.3.4 Neutrino Emission from the ACT Blazar Population

We test each of three temporal models to search for emission from the set of 195 mm blazars. No significant signal is found under any model assumption, and we place upper limits. The best-fit results, local and trials-corrected significances are reported in Table 10.2. After correcting for our three trials, the global significance of the test is 0.25σ. Fluxes and upper limits determined from this stacked analysis reflect only the combined contributions of sources within the ACT catalog. As the ACT catalog flux completeness has been determined, dividing such results by this factor will provide corresponding fluxes and limits from a complete, all-sky population of comparable blazars. These quantities are shown for comparison with previous measurements of the all-sky astrophysical diffuse neutrino flux in Fig. 10.8. Including this correction for the geometric and redshift completeness of the ACT catalog, such a completeness-corrected population of blazars is constrained to around 5% of the diffuse flux under the models assumed in this work.

Energy ranges shown in Fig. 10.8 represent the 90% sensitive energy range of each presented temporal model and spectral index combination. A typical sensitive energy range for this analysis extends from 1 TeV to 10 PeV. The sensitivity depends on the energy spectra of the source population, source locations and time variability, among other characteristics, and we determine this sensitivity using simulations. To understand the dependence on energy, we adjust the lower or upper energy bound of injected source events upwards or downwards, respectively. When a 5% increase to the model sensitivity is determined for both the incre-

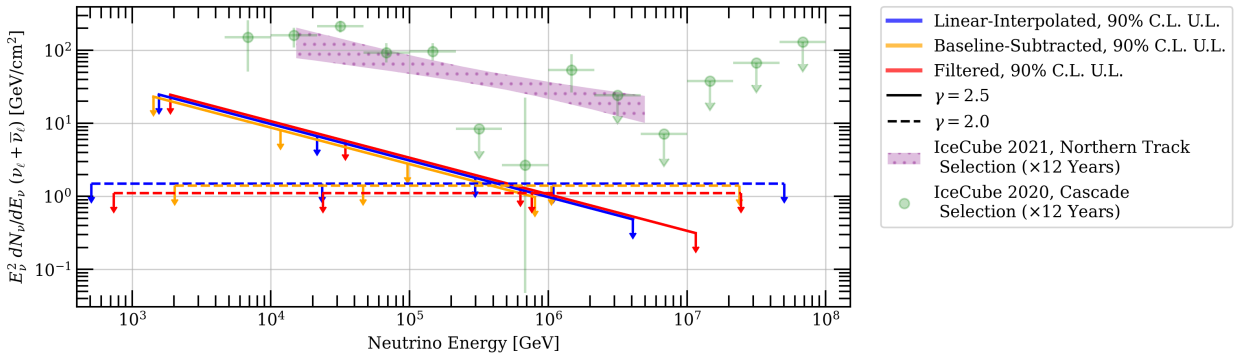

Figure 10.8 Upper limits on a neutrino flux from the stacked population of 195 ACT blazars, corrected for completeness of the population and shown for comparison with the observed high-energy diffuse neutrino flux. Here, we show upper limits from the three stacked analyses performed, assuming neutrino spectra of indices 2.0 and 2.5. It should be noted that the upper limits for the linearly-interpolated and baseline-subtracted models for a spectral index of 2.0 are nearly overlapping. The flux intensity represents the cumulative flux from the stacked population, corrected to represent a complete set of sources. 90% sensitive energy ranges are shown. The purple butterfly band is taken from a recent measurement of the all-sky diffuse tau and electron flux and is shown for comparison [IceCube Collaboration, 2020]. Similarly, green data points are taken from an analysis of track-like events originating from the northern hemisphere [IceCube Collaboration, 2022a]. All pictured fluxes represent a single-flavor flux including both neutrinos and antineutrinos.

Search	TS	Pre-Trials p-value	Post-Trials p-value	$\phi_{90\%,\gamma=2.0}$	$\phi_{90\%,\gamma=2.5}$
Linear-Interp.	0.01	0.64	–	4.41	9.10
Shifted	0.00	1.0	–	4.13	8.13
Index-Filtered	**2.16**	**0.14**	**0.25**	3.26	9.94

Table 10.2 Summary of results from the stacked population searches. In this table, we summarize the analysis results and significances for the three tested temporal models. Upper limits are presented in the form, $dN_\nu/dE_\nu(100\,\text{TeV}) = \phi_{90\%} \times 10^{-11}\,\text{GeV}^{-1}\,\text{cm}^{-2}$. The most significant result comes from the index-filtered search. However, this mild excess is in-part related to the TXS 0506+056 alert event, which was included within the search. A significant result is not found from this stacked population of mm-bright blazars.

mented lower and upper energy limits, this range is adopted as the sensitive energy range. Notably, these limits are fully derived from simulation, and the quoted energy ranges do not conflict with or relate to those resulting from recent analyses of the diffuse neutrino flux [IceCube Collaboration, 2020, 2022a].

10.4 Discussion and Conclusions

10.4.1 A Millimeter-Correlated Neutrino Flux

Our analysis of individual mm-bright blazars and of the stacked population has not revealed a significant signal from the source class. While three sources, TXS 0506+056, 5BZB J0006-0623, and 5BZU J1415+1320, exceed a local significance of 2σ, after a trials correction the result of this individual-source search is only significant at a level of 0.8σ. Considering the entire population, neutrino production among blazars following a spectral index of 2.5 is not correlated with mm-synchrotron activity at a level of $\sim$5% of the all-sky astrophysical neutrino flux. We note that previous analyses of public data conflict with this result. Specifically, a correlation with radio-bright blazar cores has been suggested [Plavin et al., 2020, Plavin et al., 2021, Hovatta et al., 2021, Plavin et al., 2023]. These analyses have generally focused on correlations with available, longer-wavelength radio emission, and have proposed that a superior tracer of time-dependent neutrino production would come from the unabsorbed mm wavelengths [Plavin et al., 2020]. The ACT mm-blazar catalog allows for this improved analysis of less-absorbed mm activity. The increased IceCube data livetime and the improved analysis methods of this work utilize event observables (reconstructed energy, direction and time) to provide a maximally sensitive search. As these millimeter wavelengths are generally accepted as a preferred tracer of radio–mm synchrotron activity from the blazar core, it is more likely that radio–mm blazar emission is not an important tracer of neutrino production.

A neutrino cascade interaction of $\sim$225 TeV in energy was observed by the Baikal Gigaton Volume Detector (Baikal-GVD) from the vicinity of TXS 0506+056 in April 2021. Due to large spatial uncertainties, the event was not significantly correlated. However, the arrival of the event during a radio flare from TXS 0506+056 was noted as potential evidence in favor of radio-correlated neutrino production [Baikal-GVD Collaboration]. We do not see any indication of new neutrino emission from the source during its observed mm flare from 2019 to 2021. Neutrino emission from TXS 0506+056 does not appear to trace its synchrotron

intensity.

While this work has constrained a general contribution from synchrotron-bright blazars, such synchrotron flares may trace or even facilitate neutrino production for a subset of sources. This relationship depends highly on the injected electron and proton populations, Compton-dominance of the injection zone, and whether the region is sufficiently magnetically dominated such that the energy output in synchrotron is significantly detected over the steady-state SED. Modeling of these flares may require treatment of each individual blazar and its unique jet and loading conditions. Based on this work, we can only infer that the general synchrotron-bright flare is either proton-light or does not offer conditions for efficient neutrino production. We have also placed upper limits on some of the brightest individual mm blazars, like 3C 273 (5BZQ J1229+0203). Future follow-ups will benefit greatly from the continued monitoring of blazar mm light curves with the Simons Observatory [Simons Observatory Collaboration, 2019, 2025].

10.4.2 Blazars as Neutrino Sources

While we find no evidence for a neutrino correlation with blazar-synchrotron activity, blazars are still expected to contribute as an astrophysical neutrino source class. Blazars offer some of the most powerful jets in the universe, sources of accelerated electrons and protons, and fields of target photons [Hovatta and Lindfors, 2019].

The sources TXS 0506+056, PKS 1424+240 and GB6 J1542+6129 have been associated with excesses of astrophysical neutrinos and share similar radiative spectral features. Specifically, they have hard, bright synchrotron spectra with a high peak in the optical or UV range. While traditionally classified as BL Lac objects, recent work has suggested broad line regions, emitting regions within one parsec of the central black hole, may be present. The broad optical emission lines expected from these zones would be subdominant to the bright synchrotron spectra. These photon and gas fields appear boosted in the frame of the jet, creating targets for potential p-gamma and p-p collisions. The combination of high acceleration powers for both electrons and protons and these boosted photon populations might make

this specific class of "masquerading BL Lacs" efficient neutrino emitters [Padovani et al., 2022, 2019].

Alternate modeling has also proposed a supermassive black hole binary system as an explanation for the TXS 0506+056 jet activity [de Bruijn et al., 2020, Tjus et al., 2022]. A precessing jet can be linked to the binary motion, ultimately modulating the intensity of observed neutrinos. If this model correctly explained neutrino emission in 2014–2015 and in 2017, a new flare would have been expected between 2019 and 2021, when the mm brightness increases (see Fig. 10.4). Such activity is not observed in the most recent IceCube data.

More specialized modeling and selections may be required to detect neutrino emission from blazars and to probe specific production scenarios. The presence of a coronal target photon field, high-peaked synchrotron spectra, broad lines, or other sources of target photons may indicate an efficient production environment. Selections based on these observable properties of the jet may have sensitivity to emission from a subset of blazars and are still viable. Alternatively, an excess of gamma rays from the Bethe Heitler process or pion decay may indicate the presence of proton populations. In general, difficulty in forming these selections comes from either a lack of knowledge about relative proton and electron distributions or about target photon fields. Still, it is this model development and testing which will help to constrain these physical quantities like proton luminosity in future work.

CHAPTER 11

MULTIWAVELENGTH X-RAY BINARIES

X-ray binaries are historically regarded as sites of high-energy particle acceleration. As the Galactic Plane neutrino excess may be partially driven by point sources, analysis of X-ray binaries as a potential, contributing source class is well motivated. In the following sections, we reproduce several sections from a recent analysis planned for publication.

11.1 Source Selection

Recently, leptohadronic modeling has been applied to describe the multiwavelength emission of a selection of black-hole X-ray binaries [Kantzas and et al., 2020, 2023]. A linkage between the observed X-ray intensity and the loaded material within the jet is assumed based on previous studies [Markoff et al., 2005]. These models provide predictions for the expected neutrino fluence during the jet active state. Assuming a 10% jet duty cycle, and comparing to IceCube search sensitivity for a synthetic light curve with a comparable neutrino-active state, we find only five sources have neutrino flux predictions within four orders of magnitude of IceCube's search sensitivity. This selection is largely sensitive to the distance and power of each source, and otherwise assumes that neutrino production is closely correlated with gamma-rays (production of the jet), or is closely coupled with the accretion timescale and variation traced by X-rays. We list these sources with relevant properties in Table 11.1.

Source Name	Dec. [°]	R.A. [°]	Binary Period	$M_\odot$	Long-Term Monitoring
MWC 656	44.72	340.73	60.4 days	3.8-6.9	Fermi
Cygnus X-3	40.95	308.11	4.8 hours	8-14	Fermi, MAXI, Swift
Cygnus X-1	35.20	299.59	5.6 days	21 ± 2.0	Fermi, MAXI, Swift
MAXI J1836-194	-19.32	278.93	< 4.9 days	7.5-11	Fermi, MAXI, Swift
V4641 Sagittarii	-25.43	274.84	2.8 days	6.4 ± 0.6	Fermi, MAXI, Swift

Table 11.1 We provide positions, binary system periods, compact object masses in terms of the solar mass, $M_\odot$, and the general public availability of light curves from several monitoring satellites. This information for MWC 656 [Grudzinska and et al., 2015], Cygnus X-3 [Kallman and et al., 2019, Stepanian, 1982], Cygnus X-1 [Jiang, 2024, Poutanen and et al., 2008], MAXI J1836-194 [Jana and et al., 2016] and V4641 Sagittarii [Orosz and et al., 2001] have been referenced from the literature.

As large uncertainties may be associated with the hadronic energy spectra present or best fit in modeling, we view these five sources as target-of-opportunity X-ray binaries. We collect MAXI 2–10 keV soft X-ray data [Mihara and et al., 2022], Swift 15–50 keV hard X-ray data [Krimm et al., 2013], and available Fermi-LAT light curves between for the low-energy 0.1–0.8 GeV and high-energy 0.8–10 GeV bands [Abdollahi and et al., 2023], for all sources where available. While 2–10 keV data are available for MWC 656, it was noted that in the absence of detailed background modeling, the raw light curve includes detector artifacts rendering it unsuitable for this analysis [Mihara et al., 2022]. Therefore, we do not consider a soft X-ray correlation for MWC 656. In essentially all cases, we note a characteristic timescale for the modulation of X-ray data. We estimate this time range for each source as the scale of one accretion cycle.

11.2 Multi-Wavelength Analyses

With each light curve, we use equal time bins to create time-averaged bin measurements. If data is not present during a time period, linear interpolation is performed. The resulting temporal distribution for each light curve is then used in a separate individual source analysis for each of the five sources, as outlined in Section 4.1. Here, the bounds of the free parameter $T_{\rm lag}$ are set either by the assumed scale of the accretion cycle for X-ray light curves or to a smaller range of ± 50 days for gamma-ray data. In the latter case, we assume that gamma-ray emission is likely to trace jet formation, and do not expect a large delay between this event and neutrino production. The parameter $f_{\rm threshold}$ is not fit and instead fixed to zero. We describe this temporal model as the 'linear interpolation' model.

In a second set of analyses, we examine each light curve, and note that both X-ray and gamma-ray data exhibit both high and low-intensity states. While it is possible that neutrino production directly correlates with and is attenuated by this variability, it is also possible that neutrinos are only produced during threshold processes (e.g. the production of a jet, a transition in the type of turbulence present in the accretion flow). To correlate only with the flux associated with these high-state periods, we select a flux threshold for each light curve,

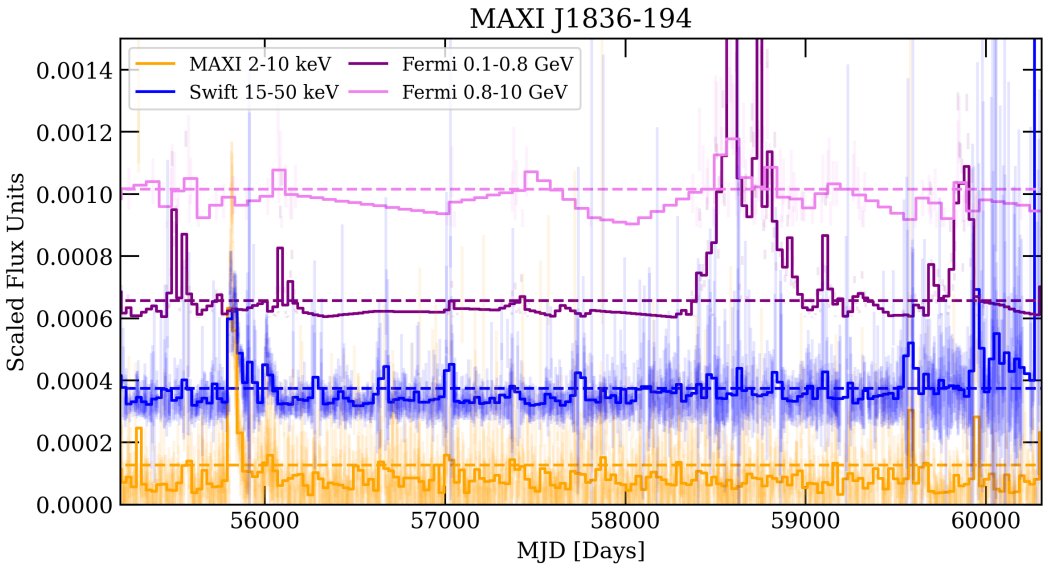

Figure 11.1 Scaled temporal PDFs for MAXI J1836-194. In this plot, we provide normalized temporal PDFs constructed from MAXI, Swift and Fermi-LAT public light curves. The original data and flux uncertainties are scaled by the normalization constant and plotted in the same color with a higher transparency as each PDF. We also plot a line indicating the relative threshold value assumed in the construction of each baseline-shifted temporal PDF. To allow for comparison, each subsequent PDF, data set and threshold is offset by a constant amount.

$f_{\text{threshold}}$, to distinguish low-state or quiescent emission from high-state or flaring emission. We again assume the bounds on T_{lag} described previously. We describe this temporal model as the 'baseline-shifted' model.

We provide an example of the constructed temporal PDFs for MAXI J1836-194 in Figure 11.1. The temporal models used for our four other sources are provided in the Appendix with Figure .1. The parameters relevant to each search and temporal PDF are described in Table .1 within the Appendix.

11.3 Periodic Analyses

Each of our five selected sources also has a well-characterized orbital period. In the systems of this study, binary activity modulates the multi-wavelength emission on timescales shorter than the accretion timescale, typically of order days. We therefore perform time-dependent analyses testing for neutrino emission modulated at the orbital period of each system. For this search, we construct a periodic temporal PDF consisting of two flux states

per orbit with a 50% duty cycle, corresponding to alternating high- and low-emission phases represented by a repeating square-wave template. The relative phase between the template and the data is scanned over a lag range spanning one half-period, which fully samples the unique phase space of the adopted symmetric template.

11.4 Results

We find that our most significant result across all analyses comes from the baseline-shifted multi-wavelength analysis with MAXI data, for MAXI J1836-194, with a local p-value of 0.04 (1.82σ significance). After accounting for the look-elsewhere effect from all multi-wavelength and periodic analyses for each source, the global p-value is 0.63. This result is summarized in Table 11.2. We provide the full best-fit results and upper limits for all multi-wavelength analyses in Table .3 and for all periodic analyses in Table .2, both found within the Appendix.

Temporal Model	Source Name	Instrument	TS	n_s	γ	$T_{\rm lag}$	p_{loc} (Z_{loc})	p_{post}
Baseline-Shifted	MAXI J1836-194	MAXI	13.33	9.81	2.03	-80.0	0.04 (1.82σ)	0.63

Table 11.2 Here, we provide the best-fit parameters, n_s, γ and $T_{\rm lag}$ for the baseline-shifted multi-wavelength analysis for MAXI J1836-194 using MAXI data. The excess is not significant after accounting for all analyses performed during the model-motivated search.

To further examine the time-dependence of this best-fit result, we compare our temporal model, MAXI data, and the relative signal weight to background weight of observed IceCube events in Figure 11.2.

11.5 Conclusion

While this source class may not explain the galactic neutrino flux, future work may probe alternate source classes as potential contributors. Additionally, further modeling and tests of the diffuse galactic flux produced from cosmic-ray interactions will also help to unfold the origins of galactic neutrinos.

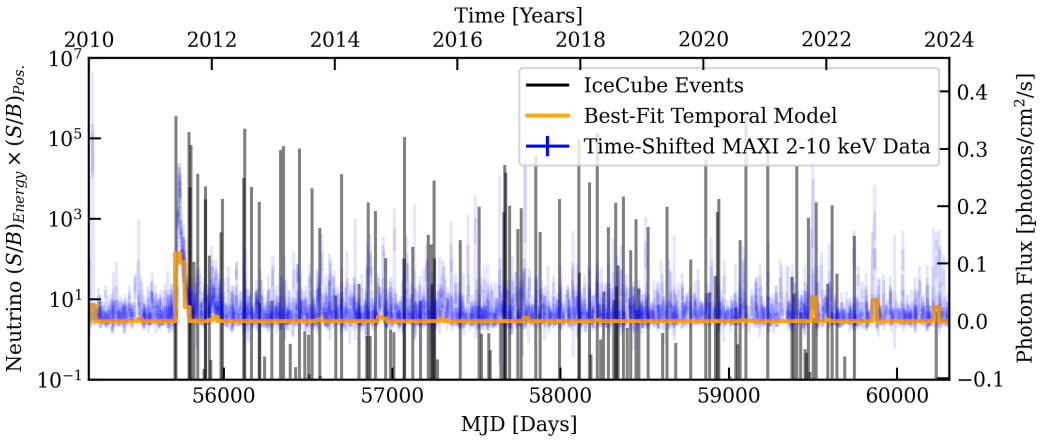

Figure 11.2 A comparison of the temporal model tested for MAXI J1836-194 and MAXI 2-10 keV data with the relative signal weight of IceCube events. In this plot, we provide the MAXI 2-10 keV data with flux uncertainties in blue along with the baseline-shifted temporal model constructed from this data in orange. In both cases, these time series are shifted by the best-fit lag, T_{lag}. In black, we plot the product of spatial and energy relative signal-to-background probability weights.

CHAPTER 12

LEPTOHADRONIC MODELING OF BLAZAR NEUTRINO SOURCES

While jetted astrophysical sources may commonly be too faint for a significant, individual signal, we can continue to learn about the environments of neutrino production through study of known candidate sources. In particular, we may learn about the connection between neutrino production and jet feeding by relating the high-energy emission of TXS 0506+056 to its subsequent radio evolution. This 'delayed radio flare' may provide insight into the inner parsecs of the AGN.

In the following sections, we describe high-energy and radio-wavelength observations of two candidate neutrino blazars – TXS 0506+056 and PKS 1420+240. We develop an exploratory, multi-zone, time-dependent radiative model to explain both gamma-ray emission and the subsequent radio flare. The sections are partially taken from text currently in preparation for submission.

12.0.1 Flaring Activity in Neutrino Blazar Candidates

In 2017, a muon neutrino with a probable energy in excess of ∼300 TeV was observed from the direction of the blazar TXS 0506+056 [Tanaka et al., 2017]. Blazars are AGN with active jets oriented within ∼15 degrees of Earth, leading to the relativistic boost of the observed frequency and intensity of the emission. The high energy of the event, well above that expected for terrestrial backgrounds, suggested an astrophysical origin, triggering a global multi-wavelength follow-up response [IceCube Collaboration, 2018d]. A gamma-ray flare also began in the months prior, increasing the source's luminosity by almost an order of magnitude before decaying over the following two years. During this flare, the spectrum had a power-law index of ∼2 over an energy range of 100 MeV to 100 GeV, before cutting off at the highest energies [Aartsen et al., 2018]. Potential flaring activity was also observed in the X-ray band [Acciari et al., 2022].

A slow flare was also observed in the radio, consistent with synchrotron radiation emit-

ted over a longer timescale, with onset during the gamma-ray flare and peaking three years after the IceCube event [Chang et al., 2022]. This radio activity was observed at multiple frequencies by the RATAN-600 telescope, and showed an evolving spectral shape initially consistent with strong synchrotron self-absorption (SSA) Baikal-GVD Collaboration. Similarly, a frequency-structured flare was observed at millimeter wavelengths by the Atacama Cosmology Telescope [IceCube Collaboration and Atacama Cosmology Telescope Collaboration, 2026]. Very long-baseline interferometry (VLBI) was used to study the varying morphology of the jet during this radio increase. The actual emission was found to originate from the radio core, often associated with the jet base [Kun et al., 2018]. This region was consistent with a projected size of several parsecs. We show a compilation of these multi-wavelength light curves in Figure 12.1.

To analyze the data, we have binned the available RATAN data of TXS 0506+056 into equal-sized time bins and fit a power-law energy spectrum to the mean measurements of each period. Given frequency, ν, we assume a power-law form of $F_\nu = \nu^\alpha$. We find that the source was optically thin prior to the start of the radio flare, corresponding to $\alpha < 0$. The source's spectral index becomes positive during the rise of the flare, and later becomes negative for the tail of the decreasing flare. We interpret this change in radio spectral index as driven primarily by partially absorbed radiative regions. If a combination of regions with varying density contributes, the index may temporarily become positive without reaching the classic value $\alpha_{\rm SSC} = 5/2$ corresponding to an optically thick emitting zone for SSA. Instead, sources will often display a value $0 < \alpha < 1$, as the total emission has contributions from multiple zones of different optical thickness along the jet.

Similarly, the blazar PKS 1424+240, also associated with an excess of neutrino emission [IceCube Collaboration, 2020a], underwent a substantial gamma-ray flare between 100 MeV and 300 GeV from 2010 through 2014, followed by a significant radio flare from the core, starting in 2013 and peaking years later [Kun and Medveczky, 2023]. For this source, however, there is no clear temporal association between neutrino and gamma-ray emission.

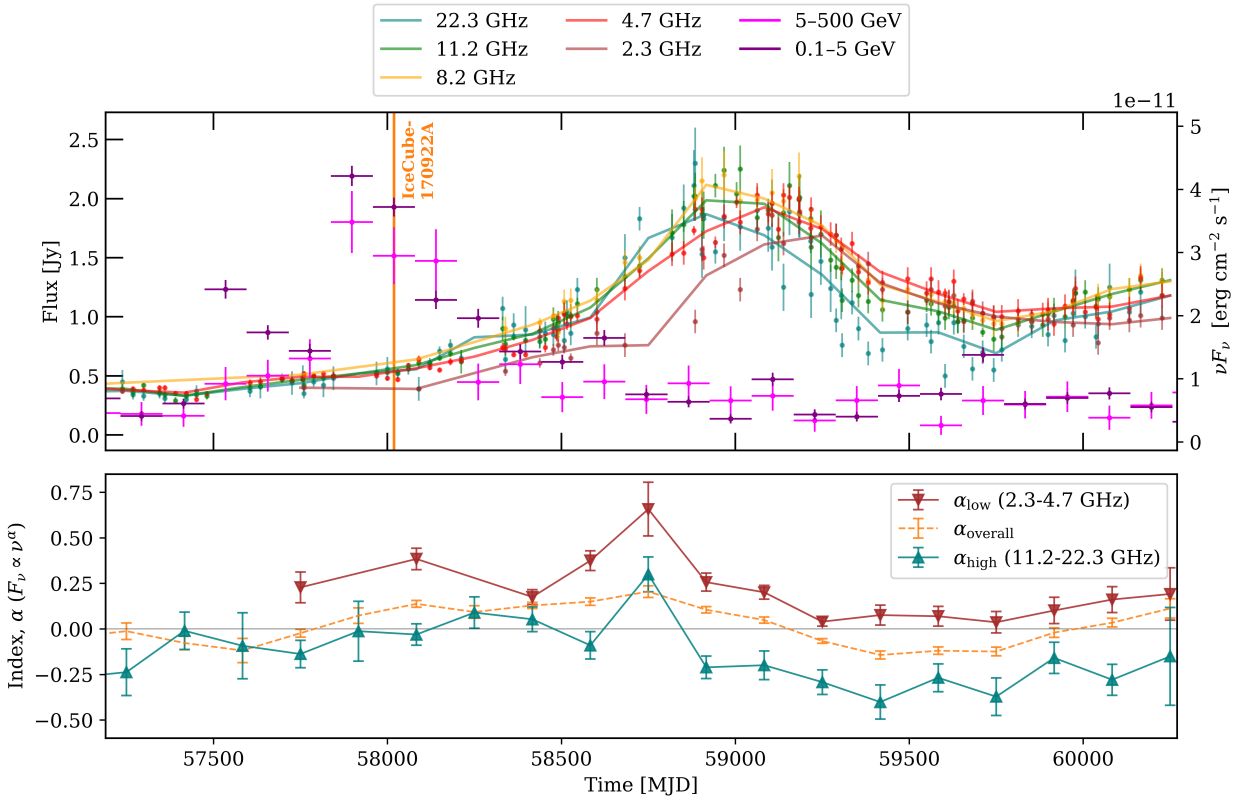

Figure 12.1 Multi-frequency light curves from TXS 0506+056. *Upper plot:* in purple and magenta, we show the Fermi light curves analyzed in this work in two energy bands. The uncertainties represent symmetrized 68% confidence intervals. The gray vertical line shows the time of the IceCube alert event of 2017. In other colors, we show time-domain RATAN-600 data at several wavelengths [Sotnikova et al., 2022]. For each frequency band, the respective solid curve shows the light curve obtained by interpolating from mean RATAN measurements over 30 larger aggregate time bins of 167 days in size. From visual inspection of these curves, we can see some variation in flare shape dependent on frequency. *Lower plot:* best-fit spectral index of the radio data within each time bin, using the same binning scheme, calculated between the two lowest frequencies (brown), the two highest frequencies (teal), and the overall index obtained when fitting a single power law across all frequencies (orange). At the lowest frequencies, the index becomes positive-valued during the flare's rising period, which our model describes as a sum of contributions from regions with different degrees of opaqueness.

More recently, a characterization of the prominence of these gamma-radio delayed flares in a larger sample of blazars has also been performed [Kochocki et al., 2026]. However, a comprehensive understanding of their origin is still developing.

High-energy neutrinos are produced in inelastic proton-photon (p-gamma) and proton-proton (pp) interactions as sub-products of the hadronic decay of charged secondaries, such

as pions. Simultaneously, these processes also emit gamma rays through the electromagnetic decay of the neutral pion, as well as photons at other frequencies from secondary electron-positron pairs. These interactions are typically efficient in compact regions with high target density. The same target photons also enable efficient inverse Compton scattering by primary electrons. For this reason, there is often a degeneracy between purely leptonic models, where the high-energy emission originates only in inverse Compton, and leptohadronic ones, where the emission has additional contributions from hadronic processes [Boettcher et al., 2013].

A basic jet structure appears collimated closest to the black hole, with cone-like or parabolic shape. Accelerated leptons and hadrons are loaded into the jet stream. Emission at the smallest, densest point at the base is expected to be Compton-dominated. Further along the jet, the observed spectrum is synchrotron dominated, where the traveling plasma has expanded. This exact transition in relative energy density depends on the distance-dependent magnetic field strength and jet geometry. The extended jet is often characterized by synchrotron 'lanterns', low-density regions of cooling electrons.

More complicated jet structures have been observed. Curved jets have been observed in a number of sources. Jets do not always form along the axis perpendicular to the accretion disk. In the case of TXS 0506+056, some evidence exists for a curved jet, or dual jet structure [Kun et al., 2018, Britzen et al., 2019]. The movement of structures away from the black hole indicates two directions of separated flow. This structure may represent an active jet, with most recent particle injection, as well as the synchrotron emission of a historical jet, originating from a previous magnetic field line orientation.

12.0.2 A Model for Delayed Radio Flares

General radio flares may show a delay relative to gamma-ray emission for a variety of reasons. If gamma-ray and radio emission were linked to a single evolving blob of particles in the case of TXS 0506+056 and PKS 1420+240, a multi-year delay in the observer frame must be explained. An evolving self-absorption break from expansion may cause delayed radio flares on similar timescales Potter [2017]. The delayed flare in TXS 0506+056 is

initially observed as self-absorbed, suggesting that this suppression alone does not explain the delay. Alternately, as the blob expands, a general transition from Compton dominance to synchrotron dominance is expected with decreased density [Boula et al., 2018]. Although, such an explanation depends on the geometry, kinematics and magnetic field evolution of the source, and does not seem applicable in these cases. A softening spectral index or decreasing break energy may also be chosen to match the radio evolution, though such a variation will impact the spectrum of the gamma-ray flare, leaving unobserved spectral signatures.

In this work, we explore a possible causal relation between the 2017 gamma-ray flare and the delayed radio flare of TXS 0506+056. We consider a multi-zone scenario that can describe an initial high-energy flare from an inner compact zone, followed by a delayed radio flare in less compact, downstream regions. We apply the model to the 2017 flare of blazar TXS 0506+056, fitting the parameters to the time-domain multiwavelength emission. We show that the data are well described by a shock front associated with propagation of the initially loaded jet material which interacts with cooled electron populations downstream at a distance of several parsecs. As the particle density determines the optical thickness in the radio band, the time-domain features in the multi-frequency light curves can constrain the particle density evolution along the jet.

We limit the radiative model to purely leptonic processes, motivated by two observations: (1) in most single-zone leptohadronic models in the literature, where protons are typically accelerated up to sub-PeV energies, the contribution from hadronic processes to the multi-wavelength emission is negligible because of suppression of synchrotron emission relative to electrons by the large proton/electron mass ratio [Acciari et al., 2022, Keivani et al., 2018, Gao et al., 2019, Cerruti et al., 2019, Petropoulou et al., 2020]; (2) even if protons contribute significantly to the high-energy emission [as predicted, for instance, by proton synchrotron models applied to this and other blazars Rodrigues et al., 2026, Cerruti et al., 2015], the radio emission coming from the parsec-scale jet is still likely to originate in synchrotron radiation by primary electrons, which is well captured by a purely leptonic framework. Thus, although our

model neglects direct emission from protons and other nuclei co-accelerated with electrons, the results can constrain the evolution of the proton-laden jet dynamics and geometry, which are key elements for building a consistent picture of neutrino production in blazar flares.

12.1 Multiwavelength Data

12.1.1 Radio Light Curves from RATAN-600

In this work, we consider the temporal evolution of multi-frequency radio data from the RATAN-600 telescope, located at the Special Astrophysical Observatory (SAO) in Russia. The telescope utilizes a 576-meter diameter reflective ring with adjustable declination orientation. A secondary reflective system focuses to an array of receivers spanning 1-30 GHz in frequency. RATAN-600 has operated for several decades, with several campaigns focused on high cadence observations of radio bright AGN.

Light curves of 2.3, 4.7, 8.2, 11.2, and 22.3 GHz frequency are available for TXS 0506+056 [Sotnikova et al., 2022]. Measurements are regularly taken on weekly or month-scale intervals. We focus on modeling the evolution of these light curves in this work.

12.1.2 Fermi-LAT Gamma-ray Light Curves

We present two light curves based on publicly available data from the Fermi-LAT gamma-ray telescope, in instrument with near-continuous cadence, sub-degree angular resolution between 1 GeV and 300 GeV, and degree-scale resolution between 20 MeV and 1 GeV. Owing to the high photon intensity, we perform a binned likelihood analysis, modeling TXS 0506+056 as a point source. We consider 45 equally spaced time intervals between December 11, 2009 and November 5, 2024, corresponding to 121-day bins. In each bin, we fit a power-law energy spectrum with free index and normalization to two energy ranges between 100 MeV and 5 GeV, and 5 GeV and 500 GeV.

We follow the standard analysis procedure outlined by Fermi. We download the relevant photon data, spacecraft data and supplemental data products. We filter our data, selecting events of class '128' and type '3' which have a high probability of being either front or back converting photons. To remove photons from Earth's limb, we use a maximum zenith cut

of 90 degrees. Further, only events with reconstructed energies between 100 MeV and 500 GeV are selected for the analysis.

As a function of space and energy, the event counts map, livetime and exposure map are determined. We assume an instrument response function based on the first eight years of observation, Pass 8 P9R3 [Atwood, 2012]. A model for galactic emission is used as well as an isotropic model for diffuse extragalactic emission. We use the Python package LATSourceModel to construct a list of contributing sources based on the LAT 14-year source catalog. If a source within 5 degrees of the target object exceeds a 5σ significance threshold, these sources are fit with free spectral parameters. We construct our binned likelihood analysis based on these expectations.

Here we use a test statistic in analysis defined as the ratio between the null-result likelihood, L_0, and the best-fit likelihood, L, $TS = 2\ln(L/L_0)$. If a binned measurement had a test statistic less than 4, a 95% upper limit on the flux was placed. Otherwise, the symmetrized 68% confidence interval was reported. The results of this analysis are shown in Figure 12.1.

We note that another nearby gamma-ray source in our search area, PKS 0502+049, was known to flare at energies below 1 GeV prior to 2016 Padovani et al. [2018], raising the possibility of source confusion. However, as our analysis focuses on the region after 2016, we do not expect this source to contribute substantially to our flux measurements.

12.2 A Time-Dependent Model for Blazar Flares

12.2.1 The Central Jet Environment of AGN

Blazars are broadly classified based on the visibility of line signals in their broadband emission spectra. Narrow and broad lines indicate the presence of ionized elemental populations along the line of sight of the blazar. Hydrogren and Helium are most abundant, leaving prominent Lyman alpha Hydrogen and Helium lines in the source spectrum. Such fields are largely expected to lie in the inner radius, extending tens of light days from the black hole—the broad line region (BLR) [Ghisellini et al., 2009]. These fields may be related

to outflows from turbulent disks, excited with randomized velocities by radiation from the hot, central accretion flow.

AGN are also known to have approximate torus-shaped regions of dusty material in the planes of their accretion disks Elitzur and Shlosman [2006]. Observations of off-axis AGN show that these regions surround the inner accretion disk, and effectively obscure the black hole and jet base. This material may extend for a thousand light days from the central black hole, radiating with an infrared-peaked black body distribution. The cooler torus may also represent material from outflows around the central accretion region or BH, as well as extended accretion flow which has yet to collapse into the accretion disk.

12.2.2 Flares Within the Radio Core

In this work, a model for particle injection at the jet base is developed to study a potential causal relation with a delayed radio flare. We limit our model to leptonic processes, as they are expected to sufficiently explain the bulk of observed emission. Our goal is to constrain some key properties of the jet and the non-thermal electron population by fitting the model to time-domain gamma-ray and radio data.

We assume that electrons are freshly accelerated at a few hundred light days from the black hole, an order of magnitude beyond the edge of the BLR region. This location allows for an observable gamma-ray flare from the loading position, and does not exceed the size of the observed radio core.

A second population of electrons is invoked to account for the delayed radio flare. The initial gamma-ray flare is attributed to particle injection at the dense jet base. The blob evolves down the jet as a function of time, with environmental parameters related to structure of the jet, surrounding photon fields and electromagnetic fields. The front of the jet impacts onto cooled, historically-emitted electrons downstream in the jet. These electrons are thus shocked, and then visibly contribute to the observed radiative emission. We provide a toy representation of this model in Figure 12.2. The larger radius of the jet as it opens downstream suggests a lower density of electrons within this region, feasible conditions for

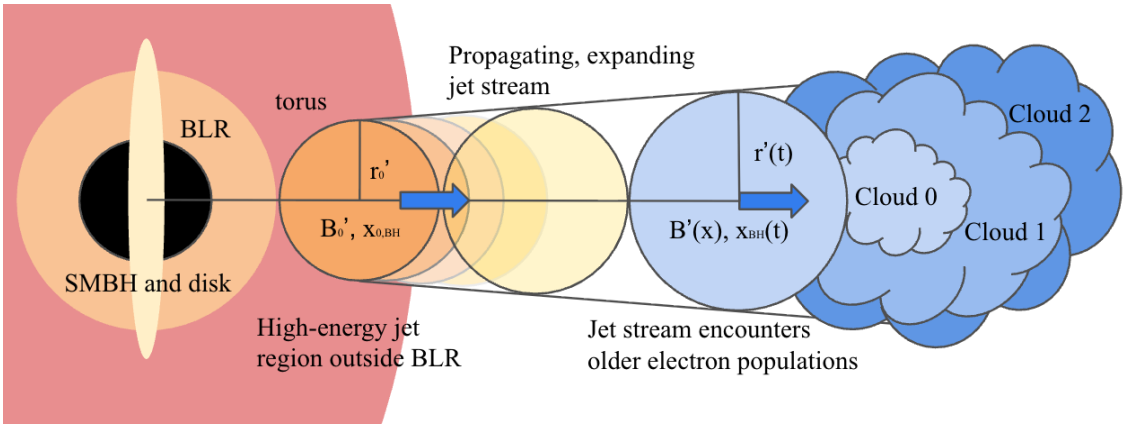

Figure 12.2 A cartoon representation of our model. We provide a cartoon diagram of our propagating, expanding and interacting jet. The initial emissive zone originates just outside the broad line region. Blobs of initial radius r'_0 and distance to the black hole $x_{0,\mathrm{BH}}$ travel along the jet and expand at a constant rate. The magnetic field strength decreases with this distance, following expectations from MHD modeling. The intensity of background photon fields from the accretion disk, broad line region, and torus also decrease. At a certain distance, corresponding to the observed radio flare, we assume that the leading blob interacts with a region of older, cooled electrons. We model this as three clouds centered on the jet axis of varying density and luminosity peak distance, where the maximal size of the 'shocked', interacting region is equivalent to the leading blob radius at that distance, $r'(t)$. The best-fit parameters characterizing the cloud luminosity profiles are provided in Fig. .3. As we evolve regions of uniform density and spherical geometry, we determine the instantaneous, relevant volumes resulting from the overlap of these three axial clouds (sees Appendix .2 for further details).

synchrotron dominance. All of this would take place within the observed radio core.

12.2.3 A Multizone Model of Blazar Flares

We now describe the details of our time-domain, multi-zone leptonic blazar model, applied to the multi-year flare of TXS 0506+056 that began in 2017. The model complexity required for dynamic, multiwavelength emission is large. We then fit our model with Markov chain Monte Carlo (MCMC) sampling in a small parameter range around a parameter vector seed motivated by similar physical systems.

Numerical Radiative Framework We model the interactions and radiative cooling of the electrons accelerated along the jet using the publicly available, time-dependent numerical code AM^3 [Klinger et al., 2024a]. The code treats all particle species and magnetic fields as homogeneously and isotropically distributed in the plasma rest frame, and solves the

time- and energy-dependent equations describing their cooling and respective electromagnetic emission, including non-linear cascades triggered by pair production. For a particle species i, the respective equation reads (in the local rest frame of the jet, as denoted by the primed symbols):

$$\partial_t n_i(E',t') = -\partial_{E'}\left[\dot{E}'_i(E',t')n_i(E',t')\right] - \alpha'_i(E',t')n_i(E',t') + Q'_i(E',t'). \quad (12.1)$$

Here, $n_i(E',t')$ is the time-dependent number density for particles of species i of energy E', $\dot{E}'(E',t')$ represents continuous energy losses, $\alpha'_i(E',t')$ represents losses particle losses through escape and interactions, and $Q'_i(E',t')$ represents particle injection. As we neglect interactions of protons and other nuclei, our species are limited to electrons and photons (as well as positrons from pair-production processes, subject to the same escape and loss terms as electrons). The electron injection term $Q'_{\rm e}$ includes pair production from photon annihilation, as well as the manual injection of a power-law spectrum with an exponential cut-off, representing the acceleration of fresh electrons: $Q'_{\rm e} \propto E'^{2-\gamma}_{\rm e}, E'_{\rm min} \leq E'_{\rm e} < E'_{\rm max}$ (cf. Eq. 12.1). The electron spectrum is normalized as a function of the total electron luminosity parameter: $L_{\rm e} = \Gamma^2 \int Q'_{\rm e} dE'$. As we describe in the following section, we modeled the electron luminosity as a time-dependent variable, in order to describe the time-domain flare.

The cooling term $\dot{E}'_{\rm e}$ accounts for synchrotron radiation, inverse-Compton scattering, and adiabatic losses from the time-dependent expansion of the region, as described in the following sub-section. The sink term $\alpha'_{\rm e}$ includes only physical escape from the region. We assume escape to be energy-independent, representing advective escape from the region at near-light speed.

For photons, the injection term Q'_γ includes photon emission from synchrotron, inverse Compton, and pair production, as well as external photon fields from the BLR and the dust torus (introduced manually as an additional injection term). The sink term α'_γ includes

photon-photon annihilation and synchrotron self-absorption (SSA) by electrons. As we discuss later on, inclusion of the SSA process is essential to capture the radio spectrum at the lowest frequencies, yielding additional constraints to the source geometry.

Time-dependent emission model We assume that the flaring event is initiated by electron acceleration in a compact region of the jet lying at a distance $x_{0,\mathrm{BH}}$ from the BH, leading to a prompt gamma-ray flare. As TXS 0506+056 has been shown to host a broad line region [BLR Padovani et al., 2022, 2019], the observed gamma-ray emission must be located beyond the BLR radius, R_{BLR}. Values of $x_{0,\mathrm{BH}}$ of tens to hundreds of light days are consistent with surveys of AGN jet formation and with radiative source models [Boettcher et al., 2013, Ghisellini et al., 2009, Jorstad et al., 2001, Kovalev et al., 2009, Lister et al., 2016].

The zone where non-thermal electrons are originally injected has an initial radius r'_0 and magnetic field strength B'_0 and moves along the jet with a bulk Lorentz factor Γ. To emulate the acceleration process, we inject electrons in this zone as a power law in energy $Q_{\mathrm{e}} \propto E^{-\gamma}$ (cf. Eq. 12.1), normalized in function of the total electron luminosity parameter: $L_{\mathrm{e}} = \Gamma^2 \int Q'_{\mathrm{e}} dE'$. We inject electrons at a constant rate for a period of three times the blob light-crossing time, $\tau'_{\mathrm{steady}} = 3 \times r'_0/c$. This timescale ensures that all relevant processes are represented, and the particle densities have reached a steady-state and no longer vary in time Klinger et al. [2024a].

We then simulate the downstream propagation of the blob from its original position. During this propagation, the blob expands at speed ηc, resulting in a reduction in the particle density and to the adiabatic cooling of the charged species, in this case electrons and positrons [the implementation of the blob expansion is detailed in Klinger et al., 2024b, particularly appendix A.7.]. In terms of the time t' in the rest frame of the blob (which is the relevant time measurement driving the radiative simulation), the size of the jet and distance

to the BH are given by

$$r'(t) = r'_0 + t'\eta c, \tag{12.2}$$

$$x_{\rm BH}(t) = x_{0,\rm BH} + t\Gamma\beta c. \tag{12.3}$$

At each point in time t', the density of background photon fields from the BLR and dusty torus is determined as a function of the distance of the blob to the BH, $x_{\rm BH}$, following previous approaches [Ghisellini et al., 2009, Rodrigues et al., 2024]. The magnetic field strength is assumed to evolve as a simple power-law in x:

$$B'(x) = B'_0 \times \left(\frac{x}{x_0}\right)^{-p}. \tag{12.4}$$

For a scenario lying between a purely poloidal and toroidal field, the spectral index lies in the range $1 \leq p \leq 2$ [McKinney, 2006]. As the results will show, our best-fit scenario favors a value closer to $p \gtrsim 1$ [cf. also Ref. Rodrigues et al., 2026, where a similar value of p was also obtained in a proton synchrotron scenario].

At each time step we update the magnetic field strength and the escape and expansion timescales as the blob propagates outward, and we call AM^3 to evolve the leptonic distribution and the emitted photon spectrum forward in time. In the observer's frame, the relativistic jet is angled at θ relative to Earth, so observed quantities from the jet are impacted by the Doppler boosting of the jet beam. For observed time intervals, we have $t' = t_{\rm obs}\,\delta/(1+z)$, where $\delta\,(\Gamma, \theta)$ is the Doppler factor of the jet, z is the source's redshift, and $t_{\rm obs}$ is the corresponding time in the Earth frame. Observed energies are given by, $E_{\rm obs} = E'\delta/(1+z)$; and energy fluxes by $E_{\rm obs}F_{\rm obs} = F'E'\delta^4/(1+z)$.

The parameters describing the source characteristics and the general jet structure are summarized in Tab. 12.1. In those cases where a parameter value is listed, we have fixed the parameter to that value based on the available source information, as described above. For those parameters that are not constrained *a priori*, we fit their values to the time-domain data, as described later on in this section, within the range of values given in Tab. 12.1.

Parameter	Value	Description
$M_{\rm BH}/M_\odot$	$3 \times 10^8\ M_\odot$	BH mass [Padovani et al., 2019]
z	0.3365	Redshift [Paiano et al., 2018]
θ	5 deg	Jet viewing angle [Kun et al., 2018]
$x_{0,\rm BH}$	3.5×10^{17} cm	Injection distance to the BH
$L_{\rm disk}$	8×10^{44} erg/s	Accretion disk luminosity [Padovani et al., 2019]
$L_{\rm BLR}$	8×10^{43} erg/s	BLR luminosity
$r_{\rm BLR}$	7×10^{16} cm	BLR radius
$r_{\rm torus}$	2.5×10^{18} cm	Torus radius
$T_{\rm torus}$	500 K	Torus temperature
$\alpha_{\rm BLR}$	0.1	BLR covering
$\alpha_{\rm torus}$	0.3	Torus covering
Γ	$[1, 10]$	Jet bulk Lorentz factor
r_0	$[0.1, 5] \times 10^{15}$ cm	Initial zone radius
η	$[0.05, 0.3]$	Expansion scale factor
B_0	$[0.1, 10]$ G	Initial magnetic field strength
p	$[0.85, 2.1]$	Magnetic field variation index

Table 12.1 Model parameters describing the jet and the core AGN environment. Note: for the parameters listed in the upper section of the table, we use values based on previous literature; for the parameters in the lower section, we fit their value to data together with the remaining model parameters, as described in the main text, searching within the range of values provided.

Since we wish to describe a temporally extended flare, we model the jet as a stream of contiguously placed blobs, separated from each other by one blob diameter, $2r_0$. Since simulating the downstream propagation of all of these blobs throughout the entire duration of the flare would be computationally prohibitive, we simulate only a small number of representative blobs, and assume that neighboring blobs emit identically to their representative.

For our $\sim$3.4 year injection period (as measured in the observer's frame), we found that seven representative blobs, launched in equally spaced time frames over this period provide sufficient temporal resolution to adequately sample the flare profile and rate of variation. To estimate the total light curves in the observer's frame, we add the contributions of all the blobs (the representative ones as well as the copies separated by $2r_0$). The total light curve in the observer's frame is obtained by adding the emission from each individual blob, shifted by an interval $\Delta t_{\rm obs} = \Delta x/(1+z)$, where their position x along the jet is defined in Eq. 12.3, thus capturing their sequential launching.

In each blob, we assume that the total electron luminosity $L'_{\rm e}(t)$ follows an asymmetric, double exponential distribution as a function of time, which we found to be the simplest time evolution function that can adequately describe the observed gamma-ray light curves:

$$L'_{\rm e}(t) = \begin{cases} L'_0 \exp\left(\dfrac{t' - T'_{\rm peak}}{\lambda\,\sigma}\right), & t \leq T'_{\rm peak}, \\ L'_0 \exp\left(-\dfrac{t' - T'_{\rm peak}}{\sigma}\right), & t' > T'_{\rm peak}, \end{cases} \tag{12.5}$$

where $T'_{\rm peak}$ is the time of the flare peak in the jet frame, and L'_0, σ and λ represent the luminosity amplitude, flare width, and asymmetry scale, respectively.

Describing the delayed radio flare requires additional particle injection. In our model, as the first emitted blob reaches the parsec-scale jet, it runs into higher-density regions, or 'clouds', stationary in the BH frame (cf. Fig. 12.2). The collision accelerates a fraction of the electrons in these clouds, which we model by injecting an additional population of electrons. To reflect the spatial extension of the clouds, we model the particle injection normalization as a time-dependent function in the jet frame $L'_{\rm e,\,cloud}(t')$. We detail this parameterization in Appendix .2.

We found empirically that reproducing the complex structure of the multi-frequency radio light curves requires contributions from multiple zones of varying levels of self-absorption. Specifically, during the rise of the radio flare, we can see in Fig. 12.1 it appears partly self-absorbed, while the tail is unabsorbed. As radio opacity and self-absorption are dependent on the particle and photon density of the emitting region, we expect the electron populations encountered earliest to be most dense, and the latter populations to be more diffuse. Motivated by the axial symmetry and conical structure of the jet, we assume three particle populations or clouds of differing density and temporal luminosity peaks (corresponding to distance along the jet stream) contribute in superposition on the jet axis.

We found a minimum of three blobs is necessary to well capture the multiwavelength peaks and evolution. The earliest-peaked population is smallest, a fraction of the expanding volume of the first blob representing the jet front. The second-peaking population is slightly

larger in volume, while the latest-peaking and least dense population is equivalent in volume to the jet front. These scales, ξ_0 and ξ_1 set the corresponding volumes of these particle populations as, $\xi_1 r(t) < \xi_0 r(t) < r(t)$. Here, $r(t)$ is the size of the first blob forming the jet front. Each cloud corresponds to a separate luminosity normalization. In increasing order of the time of the luminosity peak, each cloud has luminosity $L_{e,\mathrm{cloud},0}(t)$, $L_{e,\mathrm{cloud},1}(t)$, $L_{e,\mathrm{cloud},2}(t)$, respectively.

Asymmetric Gaussians allow for an improved description of the flare shape. The three luminosity profiles are parameterized as

$$L_{\mathrm{e,\ cloud},i}(t) = \begin{cases} L_{0,\mathrm{cloud},i} \exp\left[\frac{1}{2}\left(\frac{x - x_{c,i}}{\omega_{l,i}\rho}\right)^2\right], \\ \qquad x \leq x_{c,i}, \\ L_{0,\mathrm{cloud},i} \exp\left[-\frac{1}{2}\left(\frac{x - x_{c,i}}{\omega_{r,i}\rho}\right)^2\right], \\ \qquad x > x_{c,i}. \end{cases} \tag{12.6}$$

Here, $x(t)$, is the current position of the jet front and $x_{c,i}$ is the center of electron intensity of the ith zone used to model the cloud. Specifically, these positions correspond to a time $\epsilon T_{c,i}$, in the observer frame. ϵ is a nuisance parameter used within the model to shift the spatial location or effective temporal luminosity peak of the radio flare. $L_{0,\mathrm{cloud},i}$, $\omega_{r,i}$, and $\omega_{l,i}$, are the cloud electron luminosity amplitudes, width and asymmetry scales. Each electron energy spectrum follows the same spectral index and minimum and maximum energy,

$$n_{e,\mathrm{cloud}} \propto E_e^{2-\gamma_{\mathrm{cloud}}}, E_{\mathrm{min,\ cloud}} \leq E_e < E_{\mathrm{max,\ cloud}}. \tag{12.7}$$

As our simulation solves the evolution of particle populations of uniform density, in practice we determine the overlapping regions of our axially symmetric populations, and evolve the the relevant equivalent contributions. While the spatial luminosity profile is extended down the jet with conical symmetry, the instantaneous emissive zones are treated as spherical. This is described in Appendix B.

We summarize the parameters of the jet stream particle population, and the separate population of electrons in the jet path in Table 12.2. While these additional zones add substantial freedom within the model, we find that they are necessary to account for the frequency-dependent features of the radio flare.

We refer to the photon flux evaluated from the jet as $dN_{\rm jet}(t)/dE_\gamma dt$. The total flux from the three evaluated volumes is,

$$\frac{dN_{\rm cloud}(t)}{dE_\gamma dt} = \frac{dN_{\rm a}(t)}{dE_\gamma dt} + \frac{dN_{\rm b}(t)}{dE_\gamma dt} + \frac{dN_{\rm c}(t)}{dE_\gamma dt}. \tag{12.8}$$

12.2.4 A Model for Steady-State Emission

Emission from any blazar is often partially composed of slow time-varying or steady-state components. These are generally attributed to older jet activity. Electron populations have propagated over large distances, expanded and cooled. To provide this steady-state flux baseline within our model, we adopt a leptohadronic fit performed previously for archival TXS 0506+056 broadband data [Rodrigues et al., 2026]. To better describe the observed radio data, we add an additional electron population. This archival data, previous result, added synchrotron emission, and total spectrum are pictured in Figure .1.

As some archival flux measurements are taken over long periods, flaring or high states may be included. This is most notable when comparing our highest energy band Fermi light curve to the average archival flux measurement. Otherwise, we find that the archival fit gives a relatively close prediction to the steady-state flux levels observed in our light curves. As this work is primarily concerned with exploring the dynamic behavior of this source, we use this model as a sufficient baseline flux prediction.

We will refer to this steady-state component as $dN_{\rm steady}/dE_\gamma dt$ in this text.

Parameter	Value	Description
$\log_{10}\left(L_{0,\mathrm{jet}}/(\mathrm{erg\,s^{-1}})\right)$	$[41, 45]$	Jet stream luminosity
E_{min}	$[10, 2\times10^3]\times m_e c^2$ eV	Minimum injected electron energy
E_{max}	$[2\times10^3, 5\times10^8]\times m_e c^2$ eV	Maximum injected electron energy
γ	[1.7, 2.3]	Injected electron spectral index
T_{peak}	1.35 years	Jet flare peak, observer frame
σ	$[0.2, 1.0]$ years	Exponential flare scale, observer frame
λ	$[0.05, 0.7]$	Exponential flare asymmetry scale
$\log_{10}\left(L_{0,\mathrm{cloud},0}/(\mathrm{erg\,s^{-1}})\right)$	$[42, 45.5]$	Luminosity of cloud 0
$\log_{10}\left(L_{0,\mathrm{cloud},1}/(\mathrm{erg\,s^{-1}})\right)$	$[42, 45.5]$	Luminosity of cloud 1
$\log_{10}\left(L_{0,\mathrm{cloud},2}/(\mathrm{erg\,s^{-1}})\right)$	$[42, 45.5]$	Luminosity of cloud 2
γ_{cld}	[1.0, 1.65]	Electron spectral index for clouds
$E_{\mathrm{min,\ cloud}}$	$10\times m_e c^2$ eV	Minimum injected cloud electron energy
$E_{\mathrm{max,\ cloud}}$	$10^3\times m_e c^2$ eV	Maximum injected cloud electron energy
$T_{c,0}$	1400 days	Observer time of cloud center 0
$T_{c,1}$	1525 days	Observer time of cloud center 1
$T_{c,2}$	1600 days	Observer time of cloud center 2
ϵ	$[0.7, 1.3]$	Cloud timing scale
ρ	$[224, 416]$ days	Cloud width scale
ξ_0	$[0.25, 1.0]$	Size scale of cloud 1
ξ_1	$[0.1, 0.35]$	Size scale of cloud 2
$\omega_{l,0}$	1.11	Left side symmetry scale of cloud 0
$\omega_{l,1}$	0.77	Left side Asymmetry scale of cloud 1
$\omega_{l,2}$	0.2	Left side Asymmetry scale of cloud 2
$\omega_{r,0}$	0.2	Right side symmetry scale of cloud 0
$\omega_{r,1}$	0.3	Right side Asymmetry scale of cloud 1
$\omega_{r,2}$	0.2	Right side Asymmetry scale of cloud 2

Table 12.2 Parameter values and ranges used to parameterize the jet and cloud electron spectra and luminosity profiles. We present the list of values used to describe the modeled jet stream and three electron clouds. We assume two additional constraints in our model, $E_{\mathrm{min}} < E_{\mathrm{max}}$ and $\xi_1 < \xi_0$. Parameters with values listed as ranges are sampled within this work. All energy spectra are modeled as power laws. The jet luminosity varies as a function of time. Similarly, the luminosity of the electron clouds varies as a function of distance, with values tuned to match the observed radio flare peak and timescale.

12.2.5 Monte Carlo Model Evaluation

We compare the following total photon flux against RATAN-600 and Fermi-LAT light curves for TXS 0506+056,

$$\frac{dN_{\rm total}(t)}{dE_\gamma dt} = \frac{dN_{\rm steady}(t)}{dE_\gamma dt} + \frac{dN_{\rm jet}(t)}{dE_\gamma dt} + \frac{dN_{\rm cloud}(t)}{dE_\gamma dt}. \tag{12.9}$$

The steady-state component is assumed constant as a function of time. The results are compared both in the space of time and photon frequency.

We perform MCMC sampling seeded from a small parameter range around a model with parameters selected by an eye fit. Specifically, we use 500 independent sampler chains evolved with the Metropolis-Hastings algorithm. Each chain takes 80 steps. We evaluate approximately ∼40,000 model realizations. We treat the first 30% of steps as a burn-in and parameter exploration. Due to the high computational cost in evaluating the model, the entire physical parameter space is too large to sample completely. We perform a local exploration of the model space to determine the likelihood structure in the vicinity of a high-likelihood solution. The result is intended to reflect the spread of sampled values within this region as opposed to Bayesian credible intervals.

Our seed fit is selected in part by physical priors on the bulk Lorentz factor, Γ, and the magnetic field strength and variation index, B_0 and p. We assume a bulk Lorentz factor $\Gamma \approx 5$, as determined from previous studies of radio morphology [Kun et al., 2018, Li et al., 2020]. We also assume $p \gtrsim 1$ and a magnetic field strength on the order of 1 Gauss at the jet base. The eye fit used to seed our Monte Carlo sampling satisfies these rough parameter constraints.

We assume measurement uncertainties are Gaussian and independent. The measurement, $y_{i,j}$, and uncertainty, $\sigma_{i,j}$, correspond to the ith photon energy E and jth observation time t. Comparing the prediction, $f(\vec{\theta})$, of a sampled set of model parameters, $\vec{\theta}$, at a given time and photon energy, t and E, we can evaluate the quality of the prediction through maximum

Parameter	Highest-Likelihood Value
Γ	4.54
r_0	0.35×10^{15} cm
η	0.14
B_0	1.15 G
p	1.01
$\log_{10}\left(L_{0,\mathrm{jet}}/(\mathrm{erg\,s^{-1}})\right)$	1.30×10^{43} erg/s
$E_{\min}$	$263.63 \times m_e c^2$ eV
$E_{\max}$	$1.06 \times 10^7 \times m_e c^2$ eV
γ	1.94
σ	0.77 years
λ	0.21
$\log_{10}\left(L_{0,\mathrm{cloud},0}/(\mathrm{erg\,s^{-1}})\right)$	1.92×10^{44} erg/s
$\log_{10}\left(L_{0,\mathrm{cloud},1}/(\mathrm{erg\,s^{-1}})\right)$	2.41×10^{44} erg/s
$\log_{10}\left(L_{0,\mathrm{cloud},2}/(\mathrm{erg\,s^{-1}})\right)$	2.00×10^{44} erg/s
γ_{cld}	1.11
ϵ	1.01
ρ	281.56 days
ξ_0	0.34
ξ_1	0.21

Table 12.3 Maximum-likelihood results from MCMC sampling. We present the parameter values corresponding to the highest-likelihood model determined from our Monte Carlo sampling.

likelihood estimation. We seek to optimize the following likelihood,

$$\ln \mathcal{L} = -\frac{1}{2} \sum_{i=1}^{N_E} \sum_{j=1}^{N_t(i)} \left[\frac{y_{ij} - f_{ij}(\vec{\theta})}{\sigma_{ij}} \right]^2 . \tag{12.10}$$

12.2.6 Maximum-Likelihood Result

The nineteen parameters introduced with ranges in the previous section are sampled with the corresponding uniform priors. The maximal likelihood parameter set of our search is provided in Table 12.3. The light curves corresponding to this result are plotted in Figure 12.3. The sampled distributions of the parameter space relevant to the modeled jet stream are plotted in Figure 12.4. Additional distributions describing the sampled parameters sampled for the radio cloud, as well as a plot of the best-fit cloud luminosity profiles are provided within the Appendix D and Appendix E.

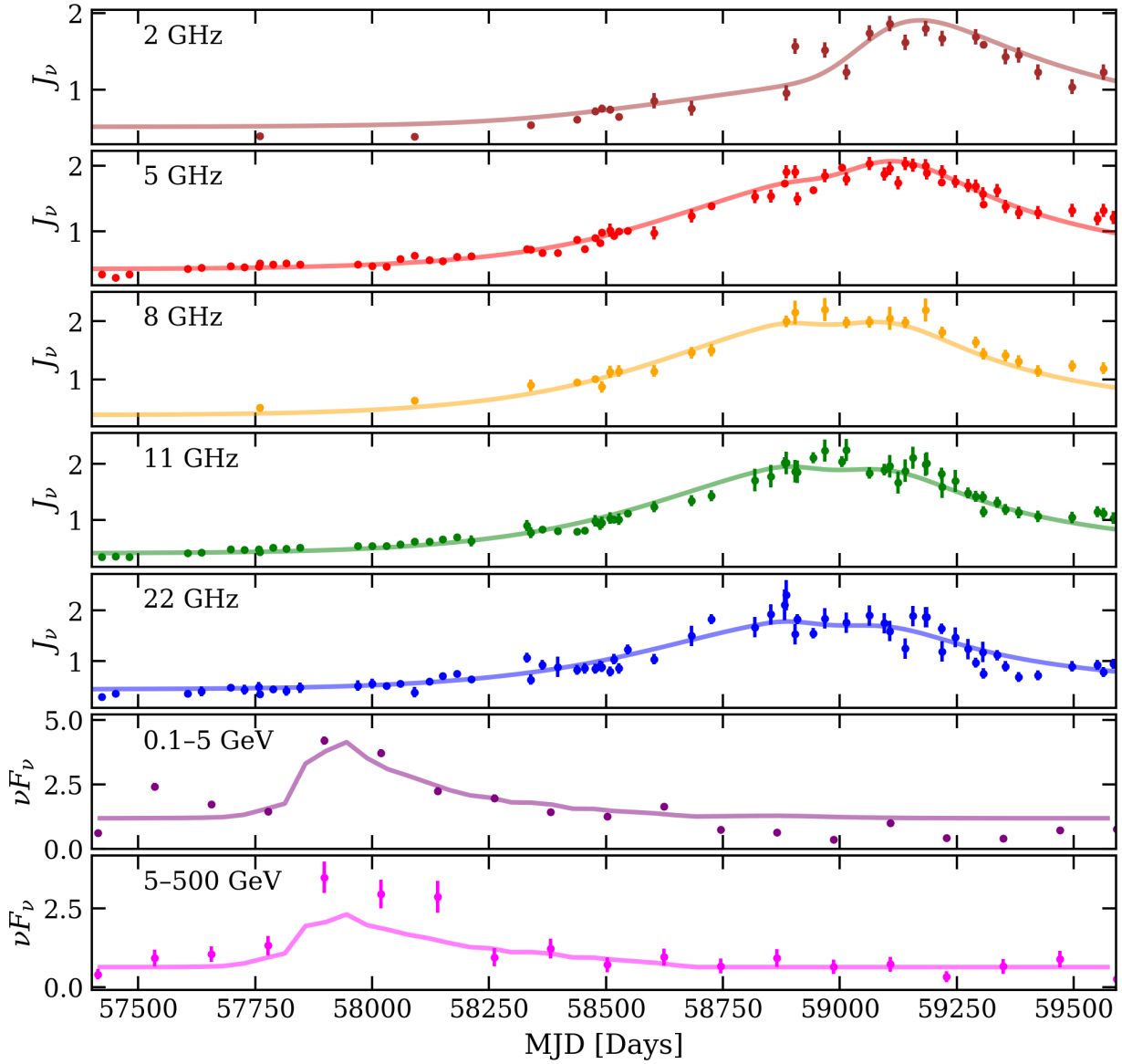

Figure 12.3 Light curves of the highest-likelihood jet model explored in Monte Carlo sampling. We provide a comparison of our Fermi-LAT light curves in two energy bands and public RATAN-600 data across several frequencies with our highest-likelihood model result. We find good agreement for both the initial gamma-ray flare and later radio activity. Importantly, the frequency-dependent evolution of the radio flare is well described with our multiple zone parameterization.

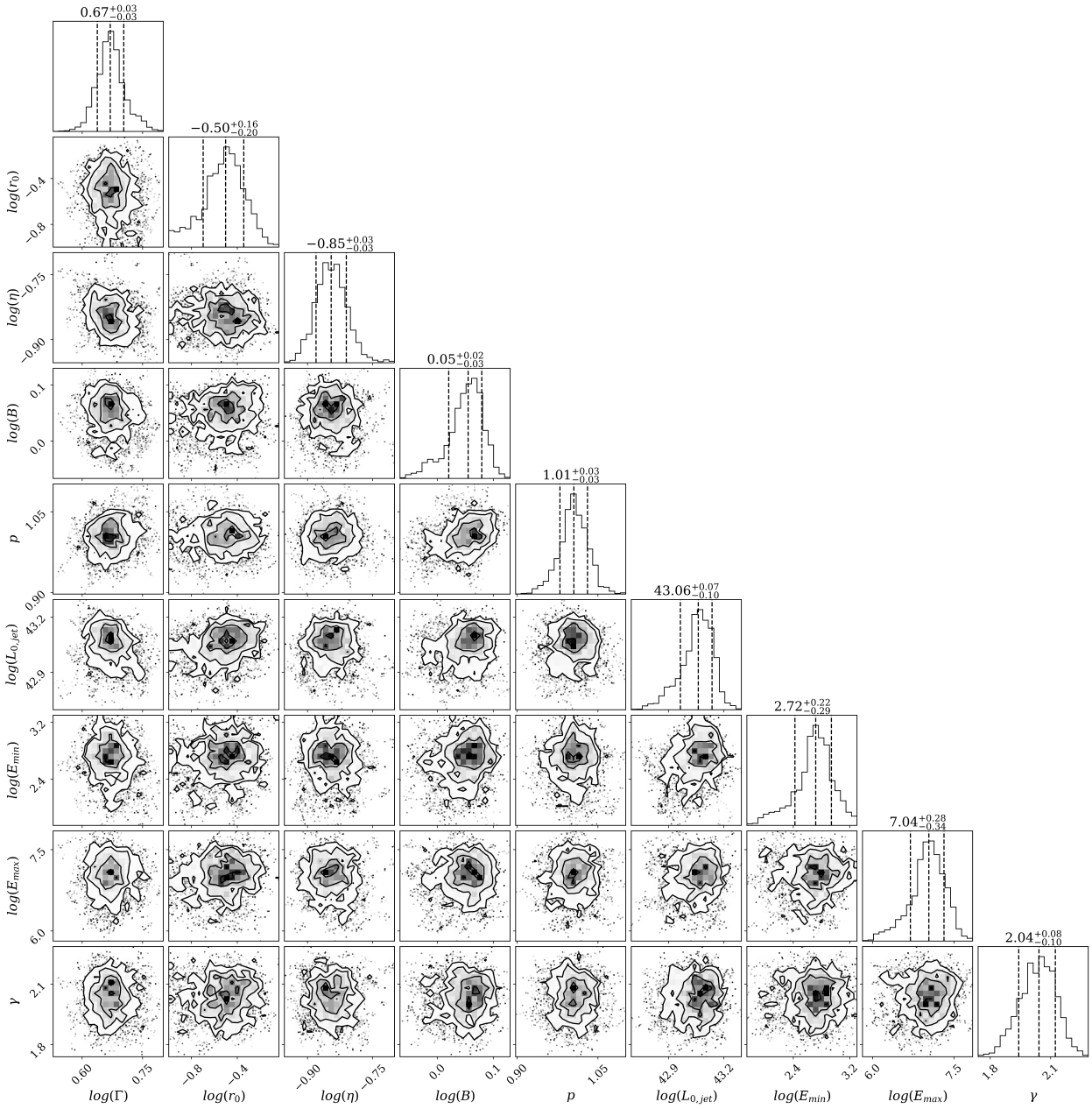

Figure 12.4 Parameter values relevant to the jet stream explored through MCMC sampling. We plot the distributions of parameter values sampled through our MCMC study. As our model has a high computational cost, we evaluate approximately ∼10,000 samples. The result is intended to represent exploration of the parameter space near a local, high-likelihood solution, as opposed to fully converged or globally representative Bayesian credible intervals.

12.3 Conclusion

In this work, we presented a first model of a causal relation between the 2017 gamma-ray flare from TXS 0506+056 and the subsequent radio flare. We considered a case in which a propagating and expanding jet stream interacts with older, cooled electrons at a distance from the black hole. We used publicly available data from Fermi-LAT and RATAN-600 to characterize the evolution of the system. As radio emission and gamma rays are often expected to be largely driven by leptonic populations, we have begun with a fully leptonic model to explore the dynamics of the jet and environment. With physically motivated model parameters, priors and seed parameter set, we were able to determine a high-likelihood model in agreement with our observations. Our results support a structured environment of electron populations as a cause for the varied frequency-dependent flare shape.

We note that, while this paper was in the final stages preparation, we also became aware of the submission of [Stathopoulos et al., 2026]. The results presented in this current work were shared via private communication with a member of this separate group in the year prior. This alternate work has also focused on an explanation for the delayed radio flare of TXS 0506+056 from downstream jet dissipation, but focuses on jet deceleration to explain the timescale of flare decay. Our model depends on the superposition of multiple electron populations to model the time and frequency-dependent impact of synchrotron self-absorption in the observed spectra. We have modeled an assumed variation in light curve shape as a function of frequency, which is not a strong focus in this alternate work.

12.3.1 Difficulties and Areas for Improvement

Evaluating a multiwavelength model from evolving particle populations over several years in an observer frame is resource intensive. This constrains the size of the parameter space and duration of the MCMC sampling which can be performed. To select initial seeds for our search and reduce the requirement for resources, we first optimized by-eye around several physically motivated parameter choices, then sampled in a small parameter space around that model selection to demonstrate the local likelihood structure.

The bulk Lorentz factor, Γ, magnetic field strength, B_0, index of magnetic field strength variation, p, and the initial blob size and expansion rate are partially degenerate with each other and with the electron luminosity of the population. While our best-fit result reflects existing knowledge about these values in blazar jet systems, previous studies have also found other solutions for similar objects with large variation in these parameters. An independent consensus on the environment of particle acceleration and emission within blazar jets is still developing, reflecting our uncertain knowledge and idealized modeling of these evolving, jetted regions. Our work represents one of the first studies modeling multiwavelength emission over long observer timescales, incorporating an extended, multizone, evolving jetted model. In this sense, our model may be more constraining than previous works, which commonly rely only on mean flux measurements or archival data independent of time. Our ability to describe the time evolution assuming a physically motivated model for the jet supports the parameter space sampled in our study. Whether other local minima from vast, order of magnitude changes, to the parameter set exist, would need to be studied in further work.

Our model tracks only the radiative emission from leptonic populations. In most standard models of blazar jets, leptonic and hadronic populations are expected together. Leptonic populations are likely to explain the majority of lower-energy radiative emission through synchrotron, while also accounting for a bulk of the observed gamma-ray emission. Hadronic populations may also contribute gamma rays as well as neutrinos. As we were primarily interested in introducing an exploratory model for the jet evolution, modeling the leptonic population alone allowed us to constrain the dynamics of the jet without greatly expanding the model space and complexity to account for hadrons. Future work would be required to incorporate hadrons, allowing for estimates of neutrino production during 2017. The result may also be more constraining, reflecting a comprehensive multimessenger model of several years of jet evolution.

12.3.2 Implications for Neutrino Astrophysics

In this work, we presented a first model offering a causal relationship between the gamma-ray flare observed from TXS 0506+056 in 2017 and the radio flare observed to develop over the following several years. Our model was constrained by both the frequency and time dependence of our data. The front of the propagating and expanding jet stream interacts with older leptonic populations at a certain distance, causing the observed, delayed radio flare. The relative delay of this radio flare, concurrent evolution of the jet size, magnetic field strength, and background photon fields, constrain the environment in which this radio flare and synchrotron processes occur. The resulting relative radio and gamma-ray intensity of either component and self-absorption are properly described.

Both TXS 0506+056 and PKS 1424+240 exhibit similar intermediate-peaked synchrotron spectra, high neutrino fluxes, and delayed radio flares. Numerous works have speculated on the conditions resulting in neutrino intensities observed from these sources. Further, searches for neutrinos from populations of both gamma-ray bright and radio-bright neutrino sources have placed strong constraints on these general source classes. It is worth considering that the unique conditions allowing for sufficient hadron populations for intense neutrino production may only be achieved in a smaller subset of sources. One possibility is that certain blazars may present atypical jet structures or disrupted disk-jet systems, as explored in recent MHD simulations. The behavior and characteristics of these systems may differ greatly from standard blazars. Both sources discussed in this work present some evidence for dual or twisted jet structures. In this sense, the spectra of leptons and hadrons within the environments of these systems may differ from typical sources, as well as the spatial distribution of plasma, resulting in older leptonic populations near the radio core. The existence of these target particle regions is especially relevant for neutrino production, potentially conducive to collisional interactions.

In future studies of blazars, it could become important to consider more varied models of disk-jet activity. These extreme conditions may allow for increased neutrino production.

The multimessenger perspective will continue to provide insight into the inner structure and dynamics of the jet, in conjunction with fluid simulations and models of particle acceleration. Communication between these perspectives will only become more important as future experiments provide new views of particle acceleration, transport and interaction at the most extreme energies.

CHAPTER 13

CORRELATIONS BETWEEN RADIO- AND GAMMA-RAY BLAZAR ACTIVITY

In general, delayed radio flares may represent twisted or messy jet evolution. These conditions may be conducive to neutrino production, providing gaseous target regions for interaction with the jet. In these next sections, we outline a correlation study between high-energy particle acceleration and radio jet activity. In particular, we describe a correlation between gamma-ray data and radio intensity and morphological observations. These sections are partially reproduced from a text previously submitted and in review [Kochocki et al., 2026].

13.1 Introduction

13.1.1 Blazar Jet Structure and Activity

Blazars, active galactic nuclei (AGN) with jets oriented within ∼15 degrees of earth, are especially bright due to their relativistically beamed emission. This orientation allows for observation and characterization of their inner-most parsecs. While the longer, extended jet is typically associated with galaxy interaction, these shorter scales allow for study of material loading at the jet base, particle acceleration, and potential radiative or neutrino production [Hovatta and Lindfors, 2019].

Typical models of blazar jet emission assume a compact, collimated jet base where freshly accelerated hadrons and leptons are additionally boosted [Blandford and Znajek, 1977]. A strong magnetic field is expected closest to the black hole, decreasing at larger distances. As leptons are accelerated in these magnetic fields, some portion of this energy is dissipated at radio–X-ray energies through synchrotron radiative emission. At higher gamma-ray energies, photons from synchrotron or external photons scatter off the leptonic population through the inverse-Compton process. The distance of material loading, magnetic field strength and material density, largely sets the relative intensity between gamma-ray and radio emission [Blumenthal and Gould, 1970, Cerruti, 2020, Petropoulou and Mastichiadis, 2014].

Several observational effects may impact the observed gamma-ray and radio intensities.

As the jet base is smallest in volume, produced photons from synchrotron emission may become self-absorbed, limiting the observable radiation [Potter and Cotter, 2012, 2013, 2015]. Additionally, the inner-parsec is commonly associated with the broad line region, a field of UV photons that may partially absorb gamma-ray emission from certain energy bands [Araudo et al., 2010, Liu and Bai, 2006].

Previous modeling work has proposed quasi-simultaneous flares between gamma-ray and radio data, with potential few-month lags [Boula et al., 2018, Wang et al., 2022]. A number of studies have searched for such correlations, assuming this rough time period as a prior, and found some evidence for this behavior in stacked populations of blazars [Fuhrmann et al., 2014, Kramarenko et al., 2021]. As the exact loading or injection point determines the relative radio or gamma-ray intensity, some sources may present weak or non-detectable flares, adding some complication.

13.1.2 Neutrino-Associated Blazars

In recent studies performed by the IceCube Neutrino Observatory, several blazars with similar spectral and flaring features have emerged as likely neutrino-bright sources. Specifically, the objects TXS 0506+056, PKS 1424+240 and GB6 J1542+6129 have been associated with local (pre-trial) $\sim 3\sigma$ significances in a time-integrated analysis [IceCube Collaboration, 2020a]. We list properties of these sources in Table 13.1. All sources present similar synchrotron spectral characteristics, with the distribution peaks of the former two cases in the optical to UV range [Padovani et al., 2022, 2019]. These two sources also show unique flaring signatures where an initial gamma-ray flare coincides with a multi-year delayed radio flare [Kun et al., 2018, Kun and Medveczky, 2023]. With either source, this previous work has also localized the radio flare to lie within several parsecs of the core region, as opposed to substantially longer distances along the jet. The initial gamma-ray flare for TXS 0506+056 corresponds to the period that the high-energy IceCube alert event, IceCube-170922A, was observed. In both cases, the slow rise of the radio flare begins around the time of the gamma-ray flare, peaking only years later. This suggests a causal relation between an initial

jet loading (gamma-ray activity) and later radio activity. While this could be related to observational effects, this may also be caused by the interaction of multiple particle populations or zones. As an example, the propagating material of the jet could interact with older electron populations further along the jet stream, causing a delayed increase in synchrotron radiation.

Source Name	R.A. [°]	Dec. [°]	Redshift (z)
TXS 0506+056	77.35	5.69	0.34
PKS 1424+240	216.76	23.80	0.61
GB6 J1542+6129	235.75	61.50	$0.34 \leq z \leq 1.76$

Table 13.1 Selected, significant IceCube blazars. We provide the right ascension (R.A.) and declination (Dec.) in degrees for the three blazars historically associated with potential neutrino excesses. The redshift of each source is also provided [Paiano et al., 2018, Sahu et al., 2024, Padovani et al., 2022]. Notably, all blazars have been traditionally characterized as BL Lac objects, but were more recently found to show substantial evidence for a broad line region [Padovani et al., 2022, 2019].

In Figure 13.1, we provide a comparison of archival gamma-ray data and radio data for the two sources, TXS 0506+056 and PKS 1424+240. While the third source, GB6 J1542+6129, shows some potential for a delay in radio emission, these light curves are more variable, potentially presenting emission from multiple zones.

13.1.3 A Search for Delayed Radio Flares

In this work, we investigate the general existence of this flaring behavior in a wider selection of ∼100 blazars. We focus on a correlation between Fermi-LAT gamma-ray data and RATAN-600 radio data with a -0.5 to 3.5 year relative lag. We consider correlations with two separate gamma-ray bands, 100 MeV–1 GeV and 1 GeV–500 GeV, as well as the integral band, to better compare the significance of any correlation between potentially gamma-ray opaque and transparent regions. We also utilize MOJAVE [Lister et al., 2018] morphological radio data to form an additional sub-selection of core-flaring blazars, where we are more sensitive to particle injection localized to the jet base.

Our source selection is based on the availability of high-cadence, long–duration RATAN–600 blazar light curves exhibiting some evidence of variability. We use this selection to perform

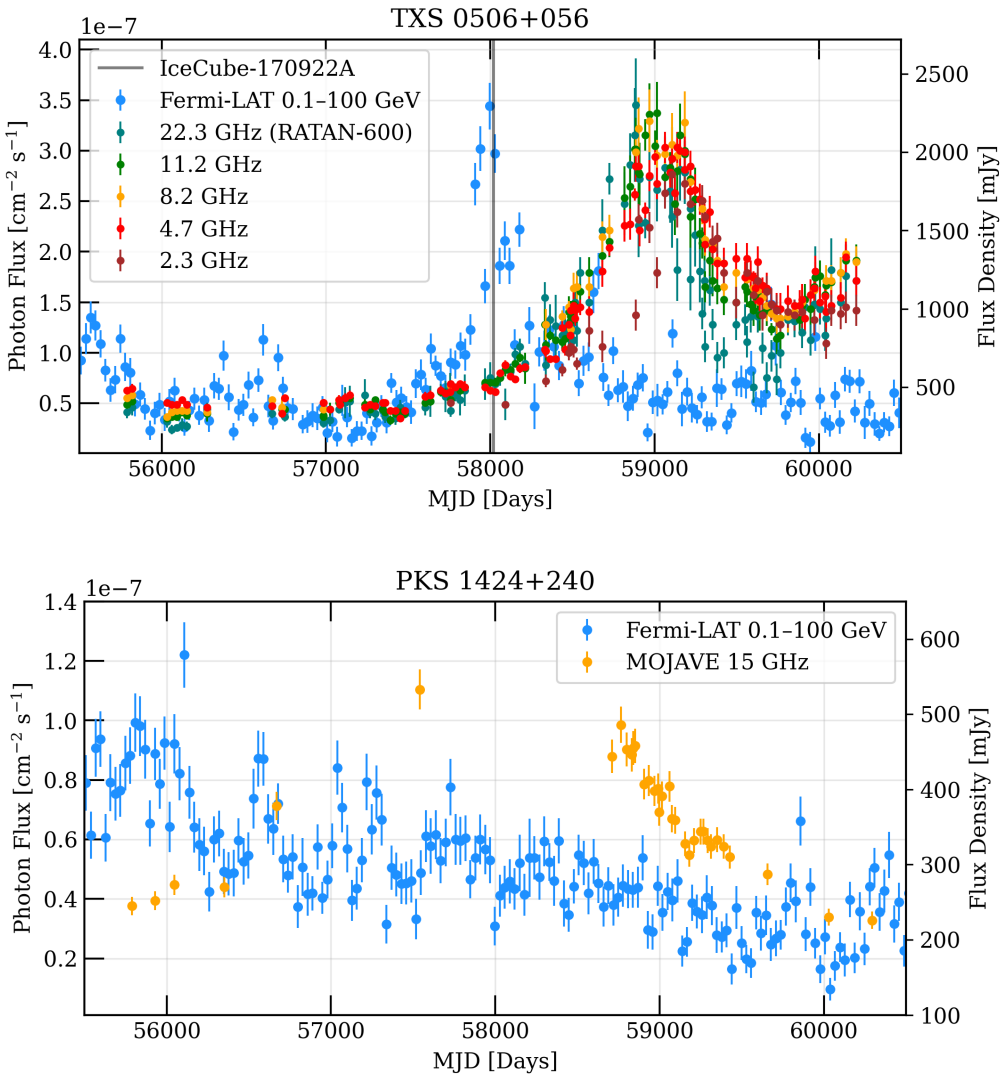

Figure 13.1 Light curves for TXS 0506+056 and PKS 1424+240. In the top plot, we present available RATAN-600 light curves at several frequencies as well as Fermi-LAT data for TXS 0506+056 [Sotnikova et al., 2022, Fermi-LAT Collaboration, 2023]. In the bottom plot, we provide MOJAVE and Fermi-LAT observations for PKS 1424+240 [Fermi-LAT Collaboration, 2023, Lister et al., 2018]. The left axis corresponds to the photon flux of the gamma-ray data, while the right axis represents the flux density of the radio data. In either case, a substantial radio flare follows a period of gamma-ray activity on a delay timescale of a few years. The radio intensity appears to begin to increase after the end of the gamma-ray-active period.

new Fermi–LAT light curve analyses at the relevant source locations for the described energy bands. While these data form the basis of our correlation analyses, we further analyze available MOJAVE morphological data to form an additional sub-selection of core–flaring blazars. We consider time-dependent correlations for individual sources as well as for aggregate, stacked blazar populations.

While this analysis is largely motivated by the phenomenology of neutrino-flaring blazars, we generally expect our study to better illustrate the multi-zone morphology of sub-hundred parsec AGN jets. If a substantial delayed correlation was observed, this might indicate a more complex density of particle populations along the jet stream.

CHAPTER 14

SOURCE SELECTION AND MULTIWAVELENGTH SURVEYS

14.0.1 RATAN-600 Radio Light-Curve Data

The RATAN–600 telescope is a centimeter–meter wavelength telescope located at the Special Astrophysical Observatory (SAO) in Russia. The telescope features a 576-meter diameter reflective ring, capable of adjusting to a range of declinations. A secondary reflective system also houses multiple receivers spanning roughly 1–30 GHz in frequency. The telescope has operated for several decades, providing exhaustive, long–term monitoring of radio-bright blazars at multiple wavelengths and declinations.

In this work, we consider available public blazar light curves for a range of observing wavelengths [Sotnikova et al., 2022]. As observing cadence varies substantially for different wavelengths between sources, we consider 7.7, 8.2, 11.2, 14.4, and 21.7 GHz data. While the level of self-absorption between these different wavelengths may very slightly, if a stacked set of light curves is tested, we generally expect this variation to be a sub-dominant effect in any result. The variation in absorption between these frequencies may lead to a shifted lag on the order of a few months as opposed to years.

We consider three selection criteria for a source's set of light curves, ℓ_f, of frequency, $f_j \in \{7.7, 8.2, 11.2, 14.4, 21.7\}$ GHz, where j indexes the available frequencies. Given N times, $t_{j,i}$, corresponding flux densities, $S_{j,i}$, and flux density uncertainties, $\sigma_{j,i}$, we select such that,

1. $\max_i(t_{j,i}) - \min_i(t_{j,i}) > 8$ years. Given the jth light curve for a specific flux density, this ensures a long enough observing period to examine multiple phases of radio activity.

2. Given all adjacent pairs of observations, $t_{j,i+1} - t_{j,i} < 1$ year. This ensures timing resolution at least on the order of one year for our light curves.

3. We choose the final light curve for a source, $\ell_{f_{\Delta\min}}$, such that $f_{\Delta\min}$ corresponds to $t_{\Delta\min} = \min_j(\max_i(t_{j,i+1} - t_{j,i}))$. The frequency selected is the light curve whose

sampling gap, or largest period between subsequent measurements, is minimal across frequencies.

If no light curve of any frequency satisfies these selection criteria, the source is not considered further. The result is 231 objects. We also make a selection based on the fractional excess variance of each light curve, and whether the RATAN object location is spatially coincident with a known Fermi–LAT source.

1. We define the mean flux, $\bar{S}$, sample variance of the fluxes, s^2, and measurement error, σ^2, as the following,

$$\bar{S} = \frac{1}{N}\sum_{i=1}^{N} S_i, \tag{14.1}$$

$$s^2 = \frac{1}{N-1}\sum_{i=1}^{N}(S_i - \bar{S})^2, \tag{14.2}$$

$$\sigma^2 = \frac{1}{N}\sum_{i=1}^{N}\sigma_i^2. \tag{14.3}$$

   The fractional excess variance is then,

$$F_{\text{var.}} = \frac{\sqrt{|s^2 - \sigma^2|}}{\bar{S}}. \tag{14.4}$$

   We select sources such that $F_{\text{var.}}(\ell_{f_{\Delta\text{min}}}) > 0.1$. Each chosen light curve then exhibits some evidence of variability or flaring over the observed period, with respect to the flux density measurement uncertainties.

2. We also compare the location of each source to objects within the Fermi 4LAC catalog. If the closest object exists with an angular separation less than 0.008 degrees, we retain the object.

We find that 104 sources pass these selection criteria.

14.0.2 Fermi-LAT Gamma-ray Light-Curve Data

The Fermi Large Area Telescope (Fermi–LAT) is a satellite observatory capable of indirect gamma-ray detection [Atwood et al., 2009]. High-energy photons that interact within the

silicon–tungsten tracking-calorimeter system produce electron–positron pairs. The tracker system is capable of reconstructing event angular uncertainty with sub-degree resolution above 1 GeV. A calorimeter measurement determines energy for the particle interaction. In general, Fermi–LAT provides sensitivity to an energy range between 20 MeV and 300 GeV. As the survey view is partially obstructed by the Earth, full-sky cadence is achieved only every several hours.

In this work, we perform binned likelihood analyses with roughly fifteen years of Fermi–LAT data for our selection of $\sim$100 blazars. The data selection spans the period between December 11, 2009 and November 5, 2024. We consider three energy bands for each source, 100 MeV–1 GeV, 1 GeV–500 GeV, and 100 MeV–500 GeV. As certain sources are relatively dim gamma-ray objects, we consider a conservative time binning scheme with a resolution of 22 bins over the observing period. In each bin, we fit the spectral parameterization suggested by the LAT 14-year source catalog, generally a power-law energy spectrum with free index and normalization.

Following the standard data analysis procedure recommended by Fermi, we download the relevant observational data, spacecraft data and supplemental data products. We first filter our data. We assume an event class of '128' and event type of '3' to select only events with a high probability of being a photon interaction that may be either front or back converting. This is the standard event quality cut used for Fermi point sources. We use a maximum zenith cut of 90 degrees with our event filter to remove photons from Earth's limb. Events with reconstructed energies between 100 MeV and 500 GeV are used for the general analysis.

Observed counts, the livetime and exposure map are determined as a function of space and energy. We use instrument response functions based on the first eight years of observation, Pass 8 P9R3. Standard models provided by Fermi are used for the expected, isotropic extragalactic emission and galactic emission. Basic settings follow previous, generic Fermi light curve tutorials. We use the Python package, LATSourceModel, to construct a source list referencing the LAT 14-year source catalog. Sources within 5 degrees of the target location

are fit with free spectral parameters if above a 5σ significance threshold. Flux expectations are generated for the selection of sources. Finally, we construct our binned observation and analysis objects based on these results, and perform our binned likelihood analyses for the described energy ranges.

The test statistic (TS) represents the relative likelihood ratio between the best-fit result, L, and null result, L_0, such that $TS = 2\ln(L/L_0)$. With each binned measurement, if a test statistic value > 4 was found, the symmetrized 68% confidence interval was determined. Otherwise, a 95% upper limit on the photon flux was instead placed. Given that a faint source may be dominated by upper limits, we further consider only gamma-ray light curves with at least 7 significant measurements (non upper limit). We used the determined photon fluxes within our correlation analyses.

14.0.3 MOJAVE Radio Morphology Data

14.0.4 VLBI core flux extraction for RATAN blazars with MOJAVE coverage

To quantify what fraction of the parsec-scale 15 GHz radio emission originates from the compact VLBI core, we analyzed those RATAN-monitored blazars that have Very Long Baseline Array (VLBA) coverage within the MOJAVE program at 15 GHz [Lister et al., 2018]. The calibrated complex visibilities were obtained from the public MOJAVE archive. The data reduction and model-fitting strategy follow the procedure described in [Kun et al., 2014, 2015].

For each observing epoch, the calibrated visibility data were imaged and self-calibrated in `DIFMAP` [Shepherd, 1997]. After standard phase and amplitude self-calibration cycles, we produced naturally weighted CLEAN maps with typical image sizes of 1024×1024 pixels and a pixel scale of 0.04 mas. The residual rms noise from the map and the restoring beam parameters were recorded for each epoch. The brightness distribution was parameterized by fitting circular Gaussian components directly to the visibility data. The first component of the model, located at the brightness peak and fixed to the center of the map, was identified as the VLBI core. Additional components were iteratively added to describe downstream jet

features until no significant residual structure remained above a predefined signal-to-noise threshold ($\sim 6\sigma$). This procedure yields, for each epoch, the flux density, size, and position of all fitted components.

The VLBI core flux density $S_{\rm core}$ was extracted as the flux of the first Gaussian component in the final model. The associated uncertainty was estimated from the image rms noise $\sigma_{\rm rms}$, the restoring beam size, and the fit component size, accounting for both thermal noise and the signal-to-noise ratio of the component. For each source, this resulted in a time series of 15 GHz core flux densities at the MOJAVE observing epochs.

The core dominance parameter was then defined as

$$f_{\rm core} = \frac{S_{\rm core}^{\rm VLBI}}{S_{\rm tot}^{\rm VLBI}}, \tag{14.5}$$

where $S_{\rm tot}^{\rm VLBI}$ is the quasi-simultaneous single-dish flux density at the closest available frequency to 15 GHz.

This approach allows us to quantify the fraction of the total radio emission that arises from the unresolved parsec-scale core, and to investigate whether major flares in the RATAN light curves are dominated by the compact core or by more extended jet components. The analysis provides a direct link between single-dish variability and structural changes on milliarcsecond scales.

We defined a conservative VLBI core-dominated subsample by requiring both a high maximum core fraction, $\max(S_{\rm core}/S_{\rm tot}) > 0.7$, and a strong correlation between the core-flux and total-flux VLBI light curves, quantified by a Pearson correlation coefficient $r > 0.8$. These thresholds were chosen pragmatically to isolate sources whose parsec-scale 15 GHz emission is clearly dominated by the compact core, rather than to define a unique physical boundary. This selection yielded 51 sources.

14.1 Correlation and Gaussian Process Modeling

Our correlation analysis uses Gaussian process modeling for smooth light curve construction. As our selection includes several gamma-ray-dim sources, several Fermi–LAT light curves result in only $\sim$10 high-significance data values. This low number of measurements

is not ideal for common correlation schemes (e.g. a z–transformed discrete correlation function). Instead, we use a Gaussian process model to infer a smooth underlying light curve consistent with the observed data and measurement uncertainties.

We use the Python package, celerite2, for Gaussian process (GP) modeling [Foreman-Mackey, 2018]. We assume each light curve can be described by the covariance of a stochastically driven, damped harmonic oscillator. This kernel allows for modeling of generally quasi-periodic, damped or noisy data. We can consider the form,

$$\ddot{x}(t) + \frac{\omega_0}{Q}\dot{x}(t) + \omega_0^2 x(t) = \sqrt{S_0}\xi(t). \tag{14.6}$$

Here, ω_0 determines the angular frequency, Q determines the relative damping rate, and S_0 is the amplitude of stochastic driving energy. $\xi(t)$ is the unit-variance Gaussian driving function or white noise. We can also relate these values to the parameterization $\{\rho, \sigma, Q\}$,

$$\rho = \frac{2Q}{\omega_0}, \tag{14.7}$$

$$\sigma^2 = \frac{S_0}{2\omega_0 Q}. \tag{14.8}$$

Here, ρ acts as the characteristic damping timescale and σ is the root mean square (RMS) amplitude of the oscillator. Gaussian process modeling assumes our input data or time series is jointly Gaussian with covariance determined by our kernel assumption. We define a model object as a function of ρ, σ, and Q, as well as the data uncertainties and times. We are then able to evaluate the likelihood of our observed data points given this constructed model.

In each case, we scale the input flux (density) values and flux (density) uncertainties relative to the mean flux (density). We assume $Q = 0.5$, $\sigma < 1$, and $\rho < 3000$ days. We optimize the kernel hyperparameters, σ and ρ by maximizing the GP log-likelihood. Finally, we compute the GP posterior predictive distribution at the desired evaluation times. This determines the posterior mean and covariance as our predicted function or smooth light curve and uncertainties.

We determine the predicted light curve for the radio and gamma-ray photon data of each source and Fermi–LAT analysis configuration. We provide examples for four sources in

Figure 14.1. We then test a range of sampled lag values, $T \in [-0.5, 3.5]$ years. If the light curve overlap is insufficient to consider the entire lag range, we discard the source. Given a lag value, our smooth gamma-ray light curve is shifted forward in time. The shifted gamma-ray curve is evaluated at the radio observation times for comparison. We then determine the Pearson product-moment correlation coefficient, between the two time series, $R \in [-1, 1]$, for the tested lag. We are able to determine the lag value, $T_{\rm best}$, in this range with the highest correlation coefficient.

To estimate an uncertainty range for this lag value, we generate 30 realizations of each data time series with additive perturbations. These perturbations are sampled from a Gaussian distribution with standard deviation determined from the original measurement uncertainty. We again determine the predicted smooth light curve for the synthetic data given our highest-likelihood Gaussian process model parameterization. We scan the same range of lag values and determine the maximal correlation coefficient and corresponding lag. Finally, we take the standard deviation of this selected lag distribution as the lag uncertainty, $\Delta T_{\rm best}$.

In this study, it is also relevant to consider the strength of temporal correlation within a stacked population. If we are generally insensitive to a potential significant correlation with an individual source, but the underlying trend is present within a larger population, considering this larger statistical population may allow for detection. With M sources, we construct stacked time series by appending each smooth, predicted curve, and properly incrementing each time value. This is done in such a way that flux measurements for a given source retain their time separation and ordering, and the time delay between sources within the stacked time series is sufficient to prevent overlap of any time series between different sources for the test range of lags. The lag value corresponding to the highest correlation coefficient is determined. We again use the perturbed synthetic data realizations to estimate the lag uncertainty.

Given either an individual source or stacked analysis, we are also able to estimate the result significance. In the case of of the individual source analysis, we perform additional

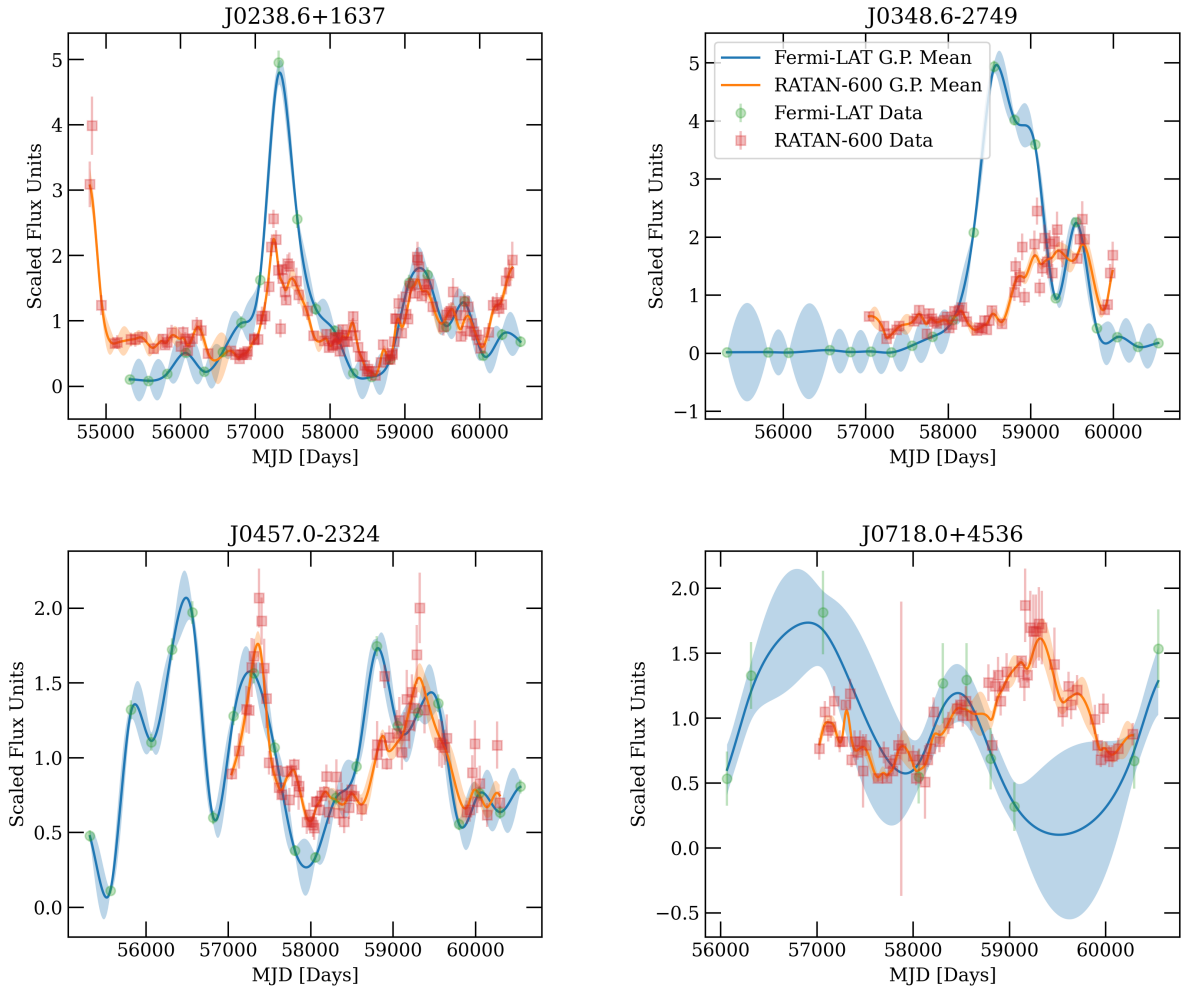

Figure 14.1 Representative light curves and uncertainties predicted through Gaussian process modeling. Here, we provide several light curve examples produced from Gaussian process modeling along with the underlying data. The name of the source is provided as the title in each case. The predicted means are plotted, as well as the 1σ posterior predictive uncertainties as shaded regions. The Fermi photon flux high-energy band is used for all examples. This selection is chosen to be generally representative of the light curve measurement quality observed within the ensemble of $\sim$100 sources. Upper limits are not used in our Gaussian process modeling, and the sparsity of pictured, significant measurements generally represents the number of measurements made per source.

correlations between the radio light curve and mismatched gamma-ray light curves. For a larger statistical sample, we also shift the selected gamma-ray light curve in time by a random value within the range of a year. These trials allow us to construct central 68% and 95% containment regions for our correlation coefficients as a function of lag. In the case of the stacked light curve, we again select a randomized order of gamma-ray light curves to construct the gamma-ray time series.

14.2 Individual-Source Correlations

We present the correlation results for our individual source studies at low and high gamma-ray energy bands in Table 14.1. Additional results for the integral energy band are listed with Figure .1 within the Appendix. Several sources show some evidence for best-fit correlations within a delayed window of 0.5 to 3.5 years.

Table 14.1 Correlation results for a radio-delayed flare. Given our search window of -0.5 to 3.5 years (-182.5 to 1277.5 days), we provide the tested lag and uncertainty, $T_{\rm delay}$ and $\Delta T_{\rm delay}$ in units of days, corresponding to the highest correlation coefficient $R_{\rm delay}$. Results for both the low-energy and high-energy gamma-ray band are provided. If one of the energy-band light curves did not pass our selection criteria for a given source, the results are not listed.

Source Name	R.A. [°]	Dec. [°]	$T_{\rm delay,\ low}$	$\Delta T_{\rm delay,\ low}$	$R_{\rm delay,\ low}$	$T_{\rm delay,\ high}$	$\Delta T_{\rm delay,\ high}$	$R_{\rm delay,\ high}$
J0018.8+2611	4.91	26.05	725.12	120.0	0.8	–	–	–
J0112.8+3208	18.21	32.14	625.05	163.87	0.13	578.02	130.49	0.22
J0118.9-2141	19.74	-21.69	619.05	16.35	0.68	252.8	158.54	0.74
J0132.7-1654	23.18	-16.91	534.99	15.81	0.81	523.98	13.63	0.71
J0144.6+2705	26.14	27.08	311.84	187.68	0.36	144.72	111.83	0.6
J0152.2+2206	28.07	22.12	319.84	383.57	0.6	-182.5	264.96	0.45
J0238.6+1637	39.66	16.62	-0.38	12.46	0.79	-0.38	10.87	0.78
J0239.7+0415	39.96	4.27	685.09	102.74	0.85	611.04	167.06	0.84
J0312.8+0134	48.18	1.55	–	–	–	319.84	501.43	0.5
J0336.4+3224	54.12	32.31	664.08	375.03	0.93	–	–	–
J0343.4+3621	55.87	36.37	–	–	–	1229.47	482.01	0.68
J0348.6-2749	57.16	-27.82	578.02	22.65	0.96	588.03	20.48	0.95
J0405.6-1308	61.39	-13.14	141.72	58.35	0.75	253.8	96.73	0.88
J0416.5-1852	64.15	-18.85	50.66	376.33	0.79	-182.5	714.01	0.4
J0423.3-0120	65.81	-1.34	269.81	90.9	0.79	-182.5	165.93	0.75

Source Name	R.A. [°]	Dec. [°]	$T_{\text{delay, low}}$	$\Delta T_{\text{delay, low}}$	$R_{\text{delay, low}}$	$T_{\text{delay, high}}$	$\Delta T_{\text{delay, high}}$	$R_{\text{delay, high}}$
J0423.9+4150	65.98	41.83	-128.46	562.18	0.65	-156.48	570.1	0.59
J0434.1-2014	68.53	-20.25	–	–	–	-182.5	635.09	-0.01
J0442.6-0017	70.66	-0.3	-182.5	285.3	0.45	-182.5	264.73	0.47
J0449.1+1121	72.28	11.36	30.65	19.16	0.91	30.65	153.51	0.83
J0453.1-2806	73.31	-28.13	910.25	53.14	0.44	79.68	211.4	0.49
J0457.0-2324	74.26	-23.41	125.71	25.29	0.59	72.67	20.92	0.77
J0502.5+1340	75.64	13.64	–	–	–	-182.5	311.7	0.95
J0510.0+1800	77.51	18.01	-65.42	11.95	0.56	-56.41	11.27	0.55
J0532.6+0732	83.16	7.55	1159.42	491.19	0.6	1138.4	504.63	0.5
J0533.3+4823	83.31	48.38	383.89	25.36	0.91	349.86	103.39	0.72
J0539.9-2839	84.97	-28.67	293.83	33.9	0.43	220.78	43.69	0.53
J0654.4+4514	103.6	45.24	-120.46	574.37	0.65	88.69	337.78	0.56
J0656.3-0322	104.05	-3.38	1277.5	638.35	0.05	40.65	450.3	0.34
J0659.6-2742	104.95	-27.75	450.93	257.19	0.62	214.77	211.75	0.63
J0718.0+4536	109.46	45.63	743.13	104.98	0.34	632.06	356.28	-0.22
J0725.2+1425	111.32	14.42	539.99	105.75	0.27	676.09	179.75	0.21
J0748.6+2400	117.15	24.01	753.14	149.33	0.74	-182.5	235.54	0.42
J0754.4-1148	118.61	-11.79	-74.43	129.46	0.83	-85.43	144.68	0.29
J0808.2-0751	122.06	-7.85	78.68	26.95	0.86	78.68	19.21	0.83
J0809.3+4053	122.23	40.88	735.13	99.6	0.5	599.04	256.56	-0.09
J0829.0+1755	127.27	17.9	-141.47	385.24	0.37	409.91	351.76	0.31
J0830.8+2410	127.72	24.18	262.81	114.63	0.5	206.77	83.09	0.61
J0850.0+5108	132.49	51.14	-84.43	355.44	0.23	98.69	162.47	0.34
J0920.9+4441	140.24	44.7	46.66	57.77	0.72	62.67	46.16	0.83
J0921.6+6216	140.4	62.26	-2.38	119.62	0.64	259.8	77.15	0.66
J0923.5+4125	140.88	41.42	81.68	20.26	0.23	948.27	315.44	-0.41

Source Name	R.A. [°]	Dec. [°]	$T_{\text{delay, low}}$	$\Delta T_{\text{delay, low}}$	$R_{\text{delay, low}}$	$T_{\text{delay, high}}$	$\Delta T_{\text{delay, high}}$	$R_{\text{delay, high}}$
J1006.7-2159	151.69	-21.99	1045.34	207.93	0.27	594.03	176.04	0.31
J1114.5-0819	168.63	-8.28	85.68	432.82	0.39	732.13	571.84	0.13
J1118.6-1235	169.57	-12.55	630.06	94.38	0.87	1237.47	478.42	0.79
J1127.0-1857	171.77	-18.95	1030.33	8.06	0.93	1029.33	11.75	0.94
J1129.8-1447	172.53	-14.82	939.27	20.75	0.8	995.31	154.75	0.81
J1135.7-0427	173.99	-4.47	1131.4	589.78	0.22	–	–	–
J1345.8+0706	206.45	7.11	817.18	296.4	0.25	745.14	347.01	0.26
J1357.1+1921	209.27	19.32	809.18	361.73	0.66	–	–	–
J1613.6+3411	243.42	34.21	725.12	30.81	0.74	511.98	209.64	0.89
J1616.7+4107	244.27	41.11	412.91	312.17	0.46	-182.5	678.96	-0.16
J1631.2+4926	247.82	49.46	964.29	377.93	0.85	1277.5	667.89	-0.02
J1635.2+3808	248.81	38.13	85.68	6.67	0.73	89.69	8.09	0.72
J1642.9+3948	250.74	39.81	-106.45	37.99	0.71	1063.35	405.52	0.67
J1728.4+0427	262.1	4.45	1277.5	370.66	0.25	1277.5	585.81	0.22
J1733.0-1305	263.26	-13.08	1277.5	75.94	0.4	1277.5	0.62	0.43
J1734.3+3858	263.58	38.96	669.08	14.25	0.45	690.1	129.14	0.37
J1740.5+5211	265.15	52.2	276.81	20.82	0.7	224.78	25.02	0.64
J1814.4+2953	273.4	29.88	849.21	127.05	0.27	–	–	–
J2136.2+0032	324.16	0.7	1277.5	90.46	0.44	–	–	–
J2146.4-1528	326.59	-15.43	117.71	612.94	0.88	–	–	–
J2147.1+0931	326.79	9.5	1277.5	137.62	0.21	92.69	533.38	0.28
J2158.1-1501	329.52	-15.02	309.84	275.21	0.25	392.89	347.83	-0.03
J2219.2-0342	334.72	-3.59	1277.5	548.17	0.44	254.8	96.22	0.87
J2219.2+1806	334.81	18.11	-35.4	9.17	0.72	451.93	218.21	0.47
J2225.6+2120	336.41	21.3	176.75	278.68	0.48	–	–	–
J2229.7-0832	337.42	-8.55	-13.38	12.16	0.84	-31.4	35.37	0.84

Source Name	R.A. [°]	Dec. [°]	$T_{\text{delay, low}}$	$\Delta T_{\text{delay, low}}$	$R_{\text{delay, low}}$	$T_{\text{delay, high}}$	$\Delta T_{\text{delay, high}}$	$R_{\text{delay, high}}$
J2232.6+1143	338.15	11.73	27.64	57.73	-0.09	236.79	200.42	-0.1
J2236.3+2828	339.09	28.48	60.67	24.52	0.56	81.68	21.45	0.51
J2243.9+2021	340.97	20.35	-66.42	413.31	-0.55	449.93	123.01	0.57
J2253.9+1609	343.49	16.15	478.95	14.7	0.84	457.94	17.66	0.82
J2311.0+3425	347.77	34.42	430.92	96.92	0.13	493.96	197.77	0.21
J2321.9+3204	350.47	32.07	10.63	252.95	0.35	523.98	91.59	0.36
J2321.9+2734	350.5	27.55	302.83	41.0	0.75	302.83	364.91	0.73
J2338.0-0230	354.49	-2.52	263.81	137.32	0.63	316.84	224.33	0.78
J2348.0-1630	357.01	-16.52	1277.5	0.72	0.48	1277.5	0.0	0.27

To compare the best-fit time lags, we provide a distribution of these values in Figure 14.2. The significances for each gamma-ray band are also compared in the same figure. While many sources show preference for a correlation with minimal relative time lag (on the order of a few months) between radio and gamma-ray emission, about half of the population has a highest-correlation time lag within the range of 0.5 to 3.5 years.

14.3 Stacked Correlations

We perform two sets of stacked correlations, considering both the selection of sources based on MOJAVE data and the set of all sources. As a majority of sources demonstrated a lag closer to zero within the individual source searches, we test this larger time window within the stacked correlation. Specifically, we have considered a range between -0.5 to 3.5 years. We provide the results of the stacked correlations for our different gamma-ray energy bands and selections in Table 14.2. We also plot the resulting correlation coefficient as a function of lag value for each case in Figure 14.3.

In all stacked correlations, a significant result in excess of the 95% confidence limit band is found. All stacks show a highest-correlation time lag around six months. We also see a

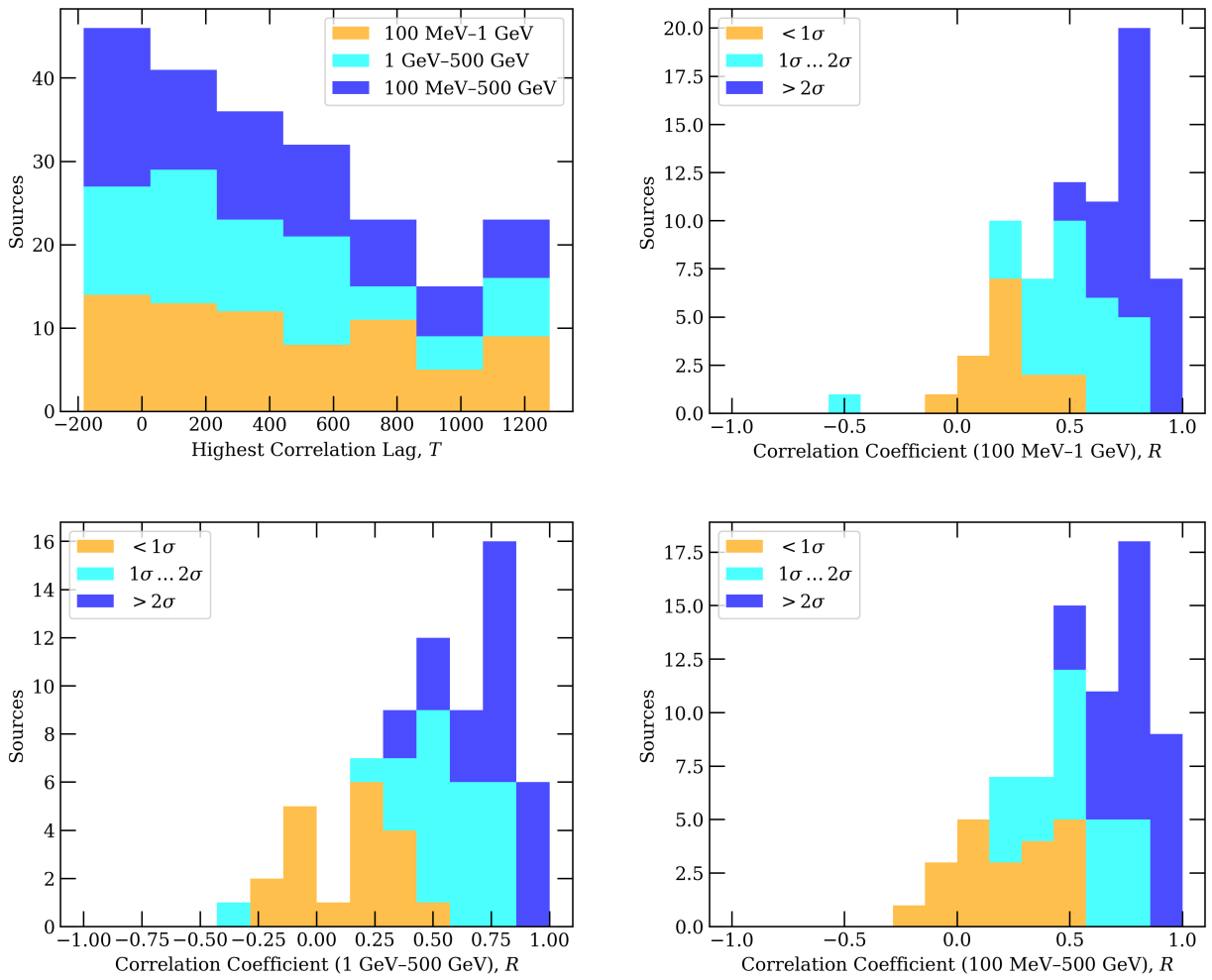

Figure 14.2 Best-fit time lags and estimated significances for a delayed gamma-ray-radio flare. We find that only a small selection of sources shows some evidence for temporal correlation on this delayed timescale of 0.5–3.5 years. We plot these highest-correlation lags, T_{delay}, in the top left panel. Results for all gamma-ray energy bands are provided. We also provide distributions of estimated significances for each gamma-ray energy band. Here, significance is relative to the central 68% and 95% confidence containment regions constructed from randomized trials.

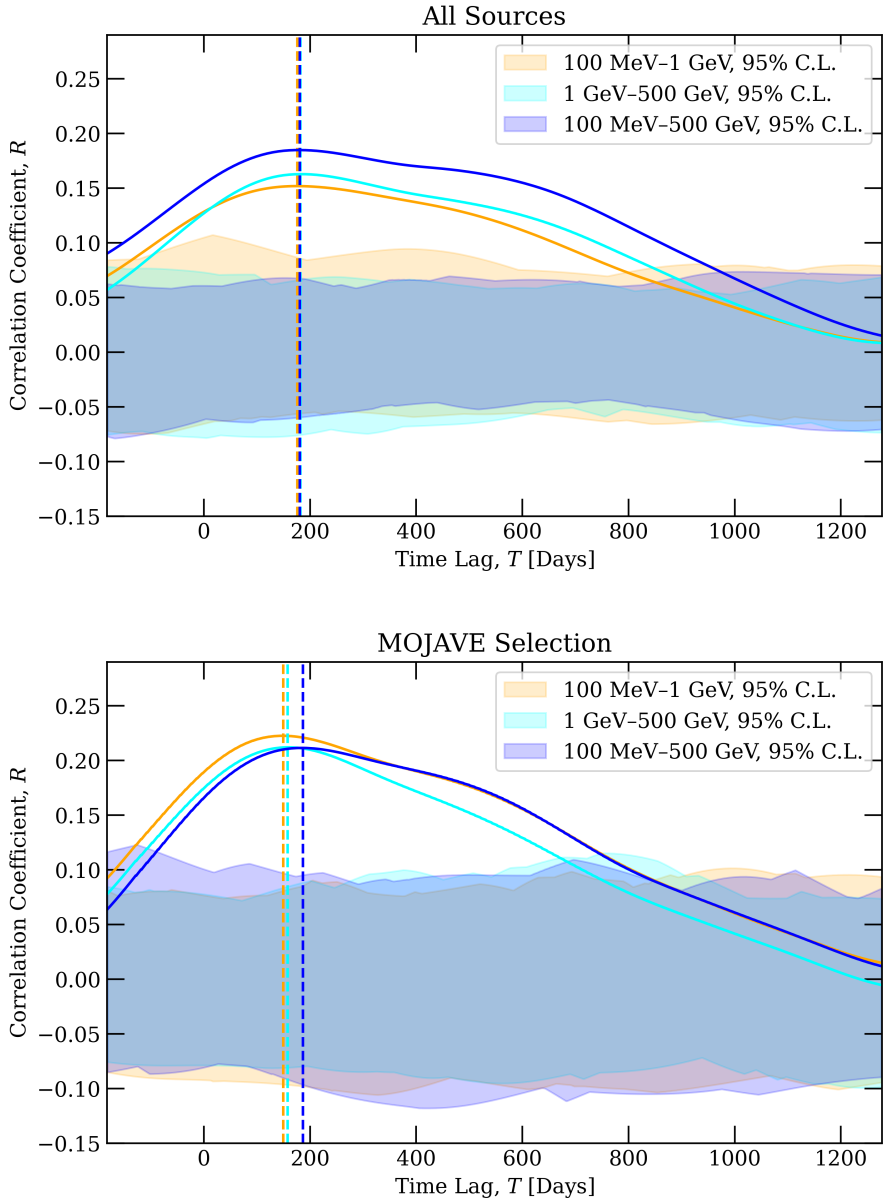

Figure 14.3 Correlation coefficient as a function of time lag. Here we plot the correlation coefficient for the three gamma-ray energy ranges considered in this work. At the top, the correlation result for the set of all sources is shown. At the bottom, the result from the MOJAVE selection is plotted. The shaded bands indicate the 95% confidence regions determined for each light curve selection. The highest correlation time delays for all selections are indicated by dashed, vertical lines. These lines slightly overlap around the six month time. In all cases, a maximal correlation with significance beyond the 95% confidence level band is found.

Selection	Gamma–Ray Energy Band	T_{stack} [Days]	ΔT_{stack} [Days]	R_{stack}	σ_{stack}
All Sources	100 MeV–1 GeV	175.75	24.71	0.15	$> 2\sigma$
	1 GeV–500 GeV	181.75	22.1	0.16	$> 2\sigma$
	100 MeV–500 GeV	180.75	26.84	0.18	$> 2\sigma$
MOJAVE Selection	100 MeV–1 GeV	149.73	17.4	0.22	$> 2\sigma$
	1 GeV–500 GeV	157.73	14.41	0.21	$> 2\sigma$
	100 MeV–500 GeV	186.75	18.44	0.21	$> 2\sigma$

Table 14.2 Correlation results for our selection of stacked correlations. Here, we provide the highest correlation time lag and uncertainty, T_{stack} and ΔT_{stack}, as well as the corresponding correlation coefficient, R_{stack}. The significance, σ_{stack}, is also provided for either result.

slight change in inflection of the correlation curve. This may suggest a population of sources with larger best-fit time lags or radio activity over an extended time period. The MOJAVE selection shows a slightly stronger correlation, potentially reflecting the more refined selection of jet core activity.

14.4 Conclusions

In this work, we have searched for a correlation between RATAN-600 blazar radio data and Fermi-LAT light curves constructed for several energy bands. We examined both ∼80 individual sources as well as stacked populations. While previous studies have indicated a general delay between gamma-ray and radio data on the scale of a few months, we have considered a larger relative search window. This was partially motivated by the flaring phenomenology of likely neutrino-bright blazar sources, as well as the general dynamics and structure of the gamma-ray-radio jet.

While a number of sources exhibit evidence for a highest-correlation lag within -0.5 to 0.5 years, more than half of our tested population was associated with time delays between 0.5 to 3.5 years. This may be due to the longer duration of the period, however we also found that the best-fit time delay for all stacked searches was on the order of six months. These stacked results were significant beyond a 2σ significance. As our background trials were constructed from mismatched light curves, it appears that there is a substantial, significant correlation at these higher time delay values. While sources with best-fit time lags closer to zero contribute, it's likely that a significant signal is also driven by radio flaring at later times. The radio

activity of a selection of blazars follows or continues after gamma-ray activity, potentially related to either slow jet expansion and propagation or to a more complex jet structure.

We considered three gamma-ray energy bands in our analysis, 100 MeV–1 GeV, 1 GeV–500 GeV, and the integral band between 100 MeV and 500 GeV. We have found the highest significance stacked result using this integral band, and comparing the maximal correlation coefficient, R, and the 95% confidence region. This may be due to the higher statistical significance of this gamma-ray data used for light curve construction. The two distinct energy bands were constructed to test for potential lag differences owing to preferential gamma-ray absorption by the broad line region. We did not find any statistically significant difference between these two energy bands in our stacked analyses.

While we have demonstrated some evidence for a potential population of blazars with longer gamma-ray-radio delays or extended periods of radio emission, further work may focus on isolating and explaining these sources. In particular, more refined models of the central jet structure and evolution may help to explain the relation between multimessenger observations.

CHAPTER 15

CONCLUSIONS

15.1 Overview

We have explored high-energy emission from jetted, astrophysical sources through a variety of studies. In particular, we have focused on radio-bright, active galactic nuclei, as well as X-ray binaries. We first considered both source classes as potential sites of hadronic cosmic-ray acceleration, and used multiwavelength data to test for potential neutrino excesses modulated by jet or accretion activity. We placed upper limits on a potential signal in both cases.

Further, we considered the radio jet evolution of the likely candidate neutrino source, TXS 0506+056, and its potential causal relationship with earlier periods of high-energy activity. We found a plausible model connecting a gamma-ray flare with a few-year-delayed radio flare. The gamma-ray activity may originate from a region near the jet base. As the jet propagates and expands, it could later interact with gaseous electron populations in its path, causing a delayed radio flare. A similar interpretation may apply to the multiwavelength activity of PKS 1424+240. Such a physical model could indicate that jetted systems with sporadic or messy histories play a role as hadronic acceleration sites.

Last, we presented an additional correlation study between radio light-curves and multiband gamma-ray emission from a population of roughly 100 blazars. Further, morphological radio data was analyzed for each source, where available. We considered the strength of correlation between light curves, dependent on the gamma-ray energy band, and the localization of radio variability to the core. We did not find evidence of a correlation dependence on the gamma-ray energy band. We found notable evidence of an overall correlation with a preferred time lag on the order of 0.75 to 2 years, approximately. This could suggest a population of additional blazars with delayed radio flares, but may also represent a general extended period of radio emission relative to gamma rays.

15.2 Open Questions

This past decade has initiated modern high-energy astrophysics. For the first time, resolved, TeV-PeV energy astronomy has become available. The environments of the most extreme leptonic and hadronic acceleration sites can be probed. In particular, jetted or actively accreting active galactic nuclei provide opportunities for energy dissipation and acceleration. Study of their associated neutrino production and radiative emission may provide insight into the accretion and jet physics ultimately impacting galactic-scale feedback.

Future work will continue to characterize high-energy particle production in blazar AGN. In particular, the exact site and mechanism of hadronic acceleration remains to be established. Additionally, it seems possible that exceptional conditions may allow for efficient neutrino production in only a small set of blazars. General-relativistic magneto-hydrodynamic and kinetic-scale simulation may provide the necessary disk-jet context for sufficient particle acceleration. Next-generation analyses and simulation may begin to explore these extreme scenarios of hadronic particle acceleration and loading.

APPENDIX

ADDITIONAL SOURCE INFORMATION AND RESULTS FROM THE MILLIMETER-WAVELENGTH ANALYSIS

In this appendix we provide measurements of source spectral indices compared synchronously between two frequency bands. We also provide complete tables of the ACT sources used for individual searches (Table .1), as well as the list of sources selected for each of the linearly-interpolated, baseline-subtracted and index-filtered individual searches (Tables .2, .3 and .4, respectively).

Table .1 ACT sources unblinded in individual IceCube searches. Here, we provide information on the combined set of blazars analyzed as individual sources. The BZCAT name, classification, average 147 GHz flux density, and equatorial coordinates are provided. Here, 'BCU' (blazar class unknown) is taken to represent those sources classified with 'blazar uncertain type'. Source coordinates are adopted from either the VizieR database, the NVSS databases, or the AT20G Australia Telescope 20 GHz survey catalog through a cross-match process with ACT localizations. We note that the source, TXS 0506+056, is listed as 5BZB J0509+0541 in this table and Tables .2, .3 and .4. Each source is tested under at least one temporal assumption – linear-interpolation, baseline-subtraction or index-filtering.

Source Name	Blazar Class	Average 147 GHz Flux Density [Jy]	R.A. [deg.]	Dec. [deg.]
5BZQ J1229+0203	FSRQ	7.67	187.28	2.05
5BZQ J2232+1143	FSRQ	3.63	338.15	11.73
5BZB J0854+2006	BL Lac	3.60	133.70	20.11
5BZU J1058+0133	BCU	3.41	164.62	1.57
5BZQ J1833-2103	FSRQ	3.14	278.42	-21.06
5BZQ J0423-0120	FSRQ	2.77	65.82	-1.34
5BZU J0433+0521	BCU	2.54	68.30	5.35
5BZB J0006-0623	BL Lac	2.44	1.56	-6.39

Source Name	Blazar Class	Average 147 GHz Flux Density [Jy]	R.A. [deg.]	Dec. [deg.]
5BZU J0725-0054	BCU	2.36	111.46	-0.92
5BZQ J1743-0350	FSRQ	2.18	266.00	-3.83
5BZB J1751+0939	BL Lac	2.01	267.89	9.65
5BZQ J1549+0237	FSRQ	1.94	237.37	2.62
5BZQ J0510+1800	FSRQ	1.93	77.51	18.01
5BZQ J0739+0137	FSRQ	1.67	114.83	1.62
5BZQ J2229-0832	FSRQ	1.64	337.42	-8.55
5BZQ J2148+0657	FSRQ	1.57	327.02	6.96
5BZQ J0501-0159	FSRQ	1.57	75.30	-1.99
5BZQ J1504+1029	FSRQ	1.54	226.10	10.49
5BZQ J0108+0135	FSRQ	1.46	17.16	1.58
5BZQ J0224+0659	FSRQ	1.23	36.12	6.99
5BZQ J2101+0341	FSRQ	1.16	315.41	3.69
5BZQ J2136+0041	FSRQ	1.15	324.16	0.70
5BZB J0831+0429	BL Lac	1.13	127.95	4.49
5BZQ J0339-0146	FSRQ	1.10	54.88	-1.78
5BZQ J2123+0535	FSRQ	1.08	320.94	5.59
5BZB J0238+1636	BL Lac	1.08	39.66	16.62
5BZB J2134-0153	BL Lac	1.06	323.54	-1.89
5BZQ J0532+0732	FSRQ	1.05	83.16	7.55
5BZQ J0750+1231	FSRQ	1.01	117.72	12.52
5BZB J0509+0541	BL Lac	0.99	77.36	5.69
5BZQ J2225-0457	FSRQ	0.91	336.45	-4.95
5BZQ J2218-0335	FSRQ	0.89	334.72	-3.59
5BZB J0825+0309	BL Lac	0.87	126.46	3.16
5BZQ J2301-0158	FSRQ	0.85	345.28	-1.97

Source Name	Blazar Class	Average 147 GHz Flux Density [Jy]	R.A. [deg.]	Dec. [deg.]
5BZB J0217+0837	BL Lac	0.83	34.32	8.62
5BZQ J2323-0317	FSRQ	0.77	350.88	-3.28
5BZQ J1224+2122	FSRQ	0.74	186.23	21.38
5BZQ J0217+0144	FSRQ	0.70	34.45	1.75
5BZQ J1224+0330	FSRQ	0.66	186.22	3.51
5BZQ J1222+0413	FSRQ	0.63	185.59	4.22
5BZU J1415+1320	BCU	0.58	214.00	13.34
5BZQ J2327+0940	FSRQ	0.56	351.89	9.67
5BZQ J1028-0236	FSRQ	0.52	157.14	-2.62
5BZB J0811+0146	BL Lac	0.48	122.86	1.78
5BZQ J0839+0104	FSRQ	0.46	129.96	1.07

Source Name	Model Rank	$-\log_{10}(p_{\rm local})$	$\hat{n}_s$	$\hat{\gamma}$	$\phi_{90\%,\gamma=2.0}$	$\phi_{90\%,\gamma=2.5}$
5BZQ J1229+0203	1.00	0.65	4.01	2.2	8.59	22.93
5BZU J1058+0133	0.47	0.00	0.00	4.00	5.05	11.99
5BZQ J0423-0120	0.43	0.21	2.81	4.00	4.8	11.61
5BZQ J2232+1143	0.38	0.53	1.04	1.48	9.61	24.66
5BZU J0725-0054	0.34	0.64	15.79	4.00	7.91	20.55
5BZQ J1743-0350	0.31	0.32	0.65	4.00	5.83	13.50
5BZB J0854+2006	0.30	0.35	3.36	2.63	9.90	20.30
5BZU J0433+0521	0.29	0.58	16.80	3.87	9.67	24.50
5BZQ J1549+0237	0.25	0.25	1.50	3.87	5.71	14.25
5BZQ J0501-0159	0.23	0.49	12.96	4.00	6.75	17.55
5BZB J0006-0623	**0.23**	**1.74**	**11.29**	**4.00**	**21.84**	**44.72**
5BZB J1751+0939	0.23	0.33	3.08	2.68	7.61	17.07
5BZQ J0739+0137	0.21	0.51	2.73	2.09	8.02	18.83
5BZQ J0108+0135	0.20	0.20	0.75	3.06	5.23	12.45
5BZQ J2148+0657	0.19	0.00	0.00	4.00	5.53	16.42
5BZQ J0510+1800	0.17	0.00	0.00	3.25	6.93	18.33
5BZQ J1504+1029	0.17	0.61	8.88	2.52	10.16	24.77
5BZB J2134-0153	0.16	0.44	10.78	2.95	6.39	16.25
5BZQ J0339-0146	0.15	0.52	10.48	4.00	7.62	18.57
5BZQ J2136+0041	0.15	0.80	18.36	3.75	9.52	22.88
5BZQ J2101+0341	0.15	0.00	0.00	4.00	5.37	13.14
5BZQJ0224+0659	0.14	0.00	0.00	3.00	7.16	15.93
5BZB J0831+0429	0.14	0.58	13.25	2.80	8.74	21.60
5BZQ J2123+0535	0.13	0.00	0.00	4.00	6.03	13.24
5BZQ J2301-0158	0.13	0.00	0.00	3.00	4.97	12.42
5BZQ J0532+0732	0.12	0.00	0.00	4.00	6.83	17.87
5BZQ J2229-0832	0.12	0.00	0.00	3.00	11.08	17.90
5BZQ J2218-0335	0.12	0.37	2.27	4.00	6.54	13.92
5BZB J0509+0541	**0.12**	**2.42**	**9.94**	**2.06**	**20.08**	**50.13**
5BZB J0825+0309	0.12	0.79	20.31	3.25	9.72	24.28
5BZQ J2225-0457	0.11	0.00	0.0	2.25	5.47	14.27
5BZQ J2323-0317	0.11	0.30	3.31	3.31	5.44	13.67
5BZQ J0750+1231	0.10	0.86	21.47	3.22	13.19	34.06

Table .2 ACT sources selected for linearly-interpolated individual searches. In this table we report best-fit results and 90% upper limits for sources tested with the linearly-interpolated temporal model. This model reflects the assumption that neutrino flux increases proportional to its mm flux density. The two sources in excess of 2σ are bolded within the table. Sources are listed in order of their model rank. The effective source weight statistic is determined from the model-dependent average flux and search sensitivity. This model rank is reported as a relative fraction of the maximum source statistic for this set. The negative logarithm of the local p-value of the search and best-fit signal parameters, $\hat{n}_s$ and $\hat{\gamma}$ are reported. Lastly, upper limits are provided for an assumed neutrino spectrum of index 2.0 and 2.5. Here, upper limits are presented in the form, $dN_\nu/dE_\nu(100\,\mathrm{TeV}) = \phi_{90\%} \times 10^{-12}\,\mathrm{GeV}^{-1}\,\mathrm{cm}^{-2}$, and represent the rate of neutrinos and antineutrinos of a single flavor.

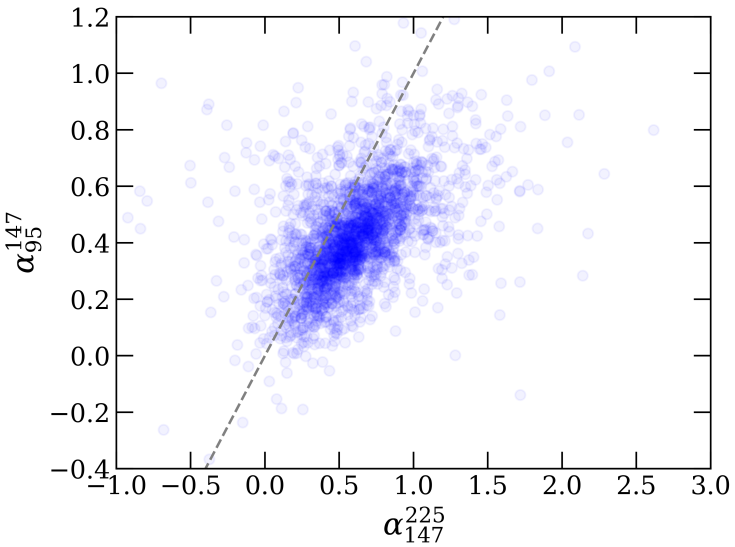

Figure .1 A comparison of synchronous spectral index measurements between the 95 and 147 GHz and the 147 and 225 GHz frequency bands. In this comparison, we have constructed 84-day binned light curves for each of the 95, 147 and 225 GHz frequency bands. At each time period where an index comparison between the indices of both the 95–147 GHz and the 147–225 GHz frequency bands was possible, we have plotted the corresponding value as a function of index, α, again following the $S_\nu \propto \nu^{-\alpha}$ convention. The gray, dashed line represents an equivalent index between the two frequency bands. We find that the distribution of spectral indices does not lie along the diagonal. Instead, a softer (more likely unabsorbed) 147–225 GHz spectral index corresponds to a slightly harder (more likely to be absorbed) 95–147 GHz spectral index.

Source Name	Model Rank	$-\log_{10}(p_{\text{local}})$	$\hat{n}_s$	$\hat{\gamma}$	$\phi_{90\%,\gamma=2.0}$	$\phi_{90\%,\gamma=2.5}$

Table .3 ACT sources selected for baseline-subtracted individual searches. In this table we report best-fit results and 90% upper limits for sources tested with the baseline-subtracted temporal model. This model reflects the assumption that a source's neutrino flux increases in proportion with variability of the source beyond its quiescent state. Emission from extended regions beyond the blazar core are expected to contribute a steady-state mm flux. To correlate only with activity or particle injection at the variable jet base, the observed flux density minimum is taken to reflect this steady-state emission and subtracted. The two sources in excess of 2σ are bolded within the table. As described in Table .2, the source name, ranking, local p-value, best fit signal parameters and upper limits are provided. Upper limits are provided in the form, $dN_\nu/dE_\nu(100\,\text{TeV}) = \phi_{90\%} \times 10^{-12}\,\text{GeV}^{-1}\,\text{cm}^{-2}$, and represent the rate of neutrinos and antineutrinos of a single flavor.

Source Name	Model Rank	$-\log_{10}(p_{\text{local}})$	$\hat{n}_s$	$\hat{\gamma}$	$\phi_{90\%,\gamma=2.0}$	$\phi_{90\%,\gamma=2.5}$
5BZQ J1229+0203	1.00	0.71	3.62	2.14	8.78	21.27
5BZQ J0423-0120	0.83	0.22	3.26	4.00	4.76	11.30
5BZQ J2232+1143	0.69	0.48	0.96	1.49	8.72	22.91
5BZU J1058+0133	0.56	0.24	1.99	4.00	4.97	12.11
5BZU J0433+0521	0.43	0.61	16.77	3.89	9.69	24.48
5BZB J0854+2006	0.42	0.40	5.46	2.77	10.59	21.93
5BZQ J1743-0350	0.42	0.00	0.00	4.00	5.22	12.79
5BZQ J0739+0137	0.38	0.48	2.44	2.08	7.52	16.76
5BZB J0006-0623	0.32	1.22	8.27	4.00	17.24	34.04
5BZQ J1504+1029	0.31	0.66	9.44	2.52	10.36	25.24
5BZU J0725-0054	0.31	0.62	14.03	4.00	7.78	19.74
5BZQ J0108+0135	0.29	0.34	4.68	3.09	5.51	12.87
5BZQ J1549+0237	0.28	0.26	1.23	4.00	5.59	13.04

Source Name	Model Rank	$-\log_{10}(p_{\rm local})$	$\hat{n}_s$	$\hat{\gamma}$	$\phi_{90\%,\gamma=2.0}$	$\phi_{90\%,\gamma=2.5}$
5BZQ J0501-0159	0.27	0.46	11.49	4.00	6.36	16.75
5BZB J0831+0429	0.27	0.62	13.77	2.78	9.02	22.26
5BZQ J0339-0146	0.26	0.60	11.39	4.00	8.24	19.69
5BZB J1751+0939	0.23	0.33	2.74	2.65	7.35	16.65
5BZQ J2301-0158	0.20	0.00	0.00	3.00	4.98	12.14
5BZQ J0510+1800	0.20	0.00	0.00	3.25	6.69	18.84
5BZB J0825+0309	0.19	0.78	19.82	3.30	9.61	23.76
5BZB J0509+0541	**0.19**	**2.21**	**9.35**	**2.04**	**18.85**	**46.56**
5BZQ J0224+0659	0.18	0.21	0.32	3.25	6.82	15.07
5BZQ J2148+0657	0.17	0.00	0.00	4.00	6.02	16.17
5BZB J0238+1636	0.16	0.25	3.17	3.97	8.96	17.63
5BZQ J2218-0335	0.15	0.47	3.56	4.00	7.12	15.26
5BZQ J1224+0330	0.15	0.00	0.00	3.00	6.41	14.82
5BZQ J2101+0341	0.14	0.00	0.00	4.00	5.42	12.92
5BZQ J2229-0832	0.14	0.00	0.00	3.00	11.03	16.77
5BZQ J1028-0236	0.14	0.00	0.00	4.00	5.10	11.40
5BZQJ0217+0144	0.13	0.00	0.00	4.00	5.93	14.07
5BZQ J2323-0317	0.13	0.00	0.00	3.25	5.43	12.51
5BZB J2134-0153	0.12	0.42	8.55	2.78	6.11	15.08
5BZQ J0532+0732	0.12	0.00	0.00	4.00	6.58	16.38
5BZU J1415+1320	**0.12**	**2.00**	**20.76**	**2.44**	**20.64**	**50.60**
5BZQ J1224+2122	0.12	0.00	0.00	4.00	7.52	18.94
5BZQ J2327+0940	0.12	0.00	0.00	4.00	7.03	16.79
5BZB J0811+0146	0.12	1.48	31.86	3.97	13.39	33.64
5BZB J0217+0837	0.11	0.00	0.00	4.00	6.68	15.91
5BZQ J1222+0413	0.11	0.00	0.00	2.75	6.59	12.31

Source Name	Model Rank	$-\log_{10}(p_{\rm local})$	$\hat{n}_s$	$\hat{\gamma}$	$\phi_{90\%,\gamma=2.0}$	$\phi_{90\%,\gamma=2.5}$
5BZQ J0839+0104	0.11	0.00	0.00	3.75	5.36	13.57
5BZQ J1833-2103	0.10	0.29	0.72	1.97	34.52	53.07
5BZQ J0750+1231	0.10	0.68	15.23	3.05	11.68	28.64

Source Name	Model Rank	$-\log_{10}(p_{\rm local})$	$\hat{n}_s$	$\hat{\gamma}$	$\phi_{90\%,\gamma=2.0}$	$\phi_{90\%,\gamma=2.5}$
5BZQ J1229+0203	1.00	0.98	1.63	1.93	6.84	14.42
5BZU J1058+0133	0.48	0.00	0.00	4.00	2.72	6.76
5BZQ J2232+1143	0.43	0.00	0.00	2.25	3.93	8.44
5BZB J0006-0623	0.32	0.43	1.65	2.42	5.18	10.48
5BZU J0725-0054	0.31	0.95	8.07	4.00	5.00	11.76
5BZQ J1549+0237	0.29	0.00	0.00	4.00	3.09	6.36
5BZQ J1743-0350	0.26	0.00	0.00	4.00	2.52	5.35
5BZB J0854+2006	0.26	1.48	15.75	4.00	11.54	23.65
5BZU J0433+0521	0.21	1.18	10.82	4.00	6.43	13.94
5BZQ J0108+0135	0.20	0.00	0.00	3.25	2.90	6.48
5BZQ J0501-0159	0.20	0.00	0.00	4.00	2.86	5.98
5BZQ J1504+1029	0.20	0.47	2.40	3.49	4.95	10.33
5BZQ J0423-0120	0.17	0.71	3.88	4.00	3.88	8.17
5BZQ J0739+0137	0.16	0.00	0.00	4.00	2.73	6.33
5BZB J1751+0939	0.16	1.29	6.55	2.63	8.39	19.42
5BZQ J2301-0158	0.13	0.27	0.98	3.50	2.39	5.30
5BZQ J0339-0146	0.13	0.76	4.36	4.00	4.52	9.22
5BZQ J2148+0657	0.13	1.00	0.00	4.00	3.34	6.68
5BZQ J2323-0317	0.12	0.00	0.00	2.50	2.79	6.29
5BZQ J2136+0041	0.12	0.58	4.41	3.34	4.01	9.38
5BZQ J2101+0341	0.12	1.18	11.74	4.00	6.82	16.51
5BZQ J0224+0659	0.12	0.46	3.64	4.00	3.37	8.08
5BZB J0831+0429	0.11	0.39	3.19	4.00	3.81	9.10
5BZB J2134-0153	0.11	0.33	2.22	4.00	2.70	4.88
5BZQ J0510+1800	0.11	0.65	4.92	2.99	6.03	11.63
5BZQ J2218-0335	0.11	0.51	1.82	4.00	3.60	7.88
5BZB J0825+0309	0.10	1.06	11.14	4.00	6.12	14.93

Table .4 ACT sources selected for index-filtered individual searches. Here, results for sources analyzed with the index-filtered temporal model are reported. Best-fit results and 90% upper limits are provided. As TXS 0506+056 shows mm-spectral hardening during the period of the IC-170922A alert event, we consider hardened states for other sources within the catalog. Specifically, we choose to correlate with the top 32% of hardened activity. Emission following the 147 GHz flux density is assumed only during this period, while no neutrino emission is assumed during other periods. As described for Table .2, the source name, ranking, local p-value, best fit signal parameters and upper limits are provided. Upper limit fluxes are presented in the form, $dN_\nu/dE_\nu(100\,\mathrm{TeV}) = \phi_{90\%} \times 10^{-12}\,\mathrm{GeV}^{-1}\ \mathrm{cm}^{-2}$, and represent the rate of neutrinos and antineutrinos of a single flavor.

APPENDIX

ADDITIONAL SOURCE INFORMATION AND RESULTS FOR THE ANALYSIS OF X-RAY BINARIES

Here, we provide several plots and tables to further illustrate the searches performed in this work. Additionally, we provide summary plots of the best-fit results of each search.

Source Name	Instrument	Energy Band	Range [days]	Threshold [photon flux]
MWC 656	Fermi (Low)	100–800 MeV	-50, +50	20.0
	Fermi (High)	0.8–10 GeV	-50, +50	2.0
Cygnus X-3	MAXI	2–20 keV	-150, +150	0.65
	Swift	15–50 keV	-150, +150	0.0375
	Fermi	0.1–100 GeV	-50, +50	4.0×10^{-7}
Cygnus X-1	MAXI	2–20 keV	-150, +150	2.0
	Swift	15–50 keV	-150, +150	0.1
	Fermi (Low)	100–800 MeV	-50, +50	30.0
	Fermi (High)	0.8–10 GeV	-50, +50	4.0
MAXI J1836-194	MAXI	2–20 keV	-150, +150	0.03
	Swift	15–50 keV	-150, +150	2.5×10^{-3}
	Fermi (Low)	100–800 MeV	-50, +50	50.0
	Fermi (High)	0.8–10 GeV	-50, +50	3.0
V4641 Sagittarii	MAXI	2–20 keV	-200, +200	0.05
	Swift	15–50 keV	-200, +200	2.5×10^{-3}
	Fermi (Low)	100–800 MeV	-50, +50	40.0
	Fermi (High)	0.8–10 GeV	-50, +50	3.0

Table .1 Parameters Relevant to All Analyses of the Model-Motivated Search. Here, we provide the source, instrument used for multi-wavelength data and energy band, as well as the chosen lag range and selected flux threshold relevant to the model-motivated source analyses. In the case of X-ray data, the selected lag range was roughly based on the scale of variability seen in X-ray data, assumed to be associated with a varying accretion state. In the case of each gamma-ray light curve, we assume a smaller lag between gamma-ray variability and neutrino variability, potentially associated with the opacity of the jet. We provide the selected threshold in units of photon flux, photons/cm^2/s.

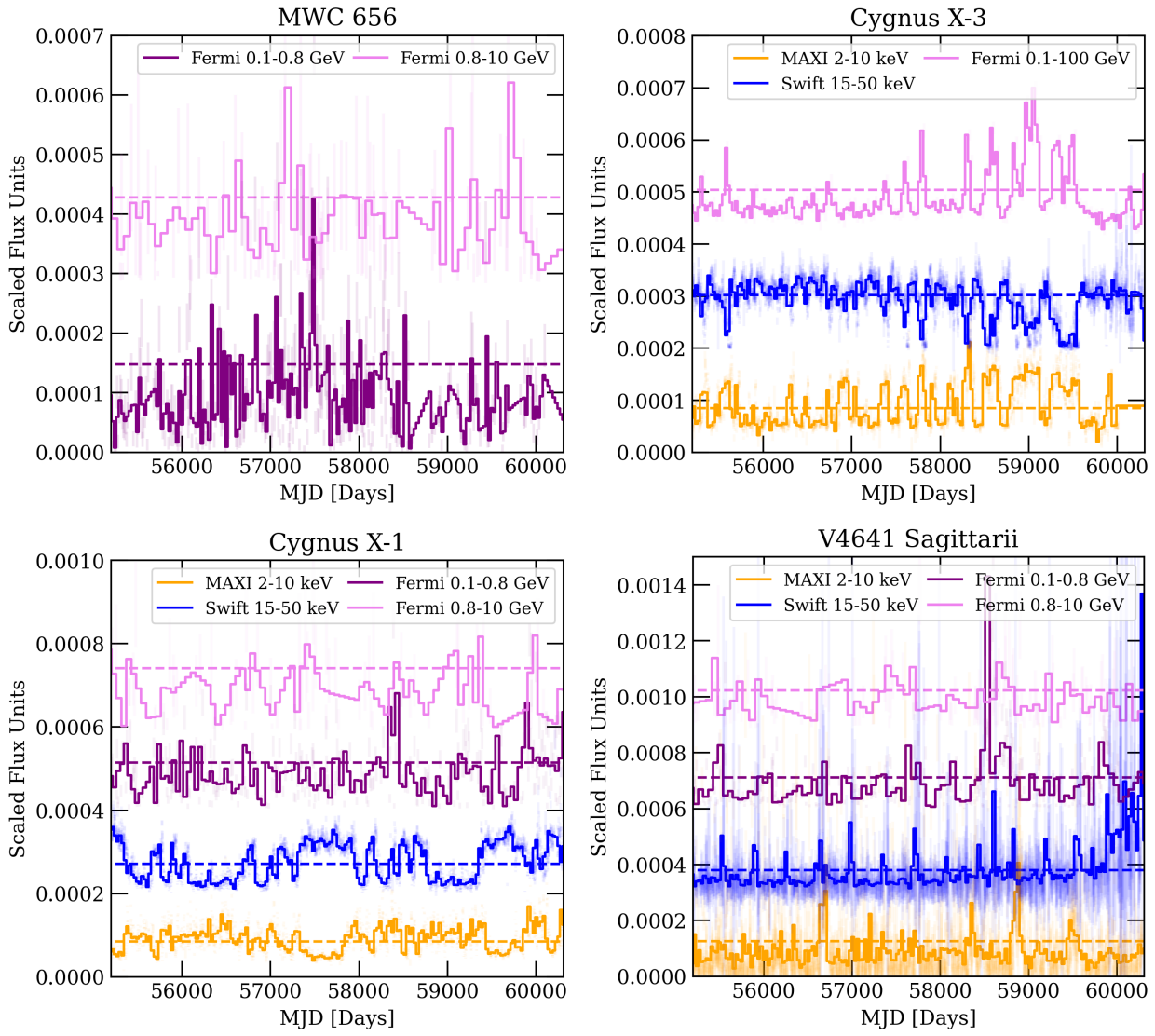

Figure .1 Scaled temporal PDFs for additional sources considered in the model-motivated search. In this plot, we provide normalized temporal PDFs constructed from MAXI, Swift and Fermi-LAT public light curves for MWC 656, Cygnus X-3. Cygnus X-1 and V4641 Sagitarii. We acknowledge that MWC 656 may be a relatively dim, soft gamma-ray source. It is likely that signal contamination from the 72-day precession of the International Space Station (ISS) may be present in the MAXI data, so the corresponding light curve is not considered in this analysis [Mihara et al., 2022]. The original instrument data is scaled by the normalization constant and plotted with flux uncertainties in the same color with a higher transparency as each PDF. We plot a line indicating the relative threshold value assumed in construction of each baseline-shifted temporal PDF. To allow for comparison, each subsequent PDF, data set and threshold is offset in a given plot by a constant amount.

Source Name	TS	n_s	γ	$T_{\rm lag}$	p-value	U.L.$^{90\%}_{E^{-2}}$	U.L.$^{90\%}_{E^{-3}}$
MWC 656	0.0	0.0	3.25	-15.09	1.0	0.01	0.23
Cygnus X-3	1.45	15.47	2.5	-0.05	0.34	0.02	0.36
Cygnus X-1	0.37	7.66	4.0	-0.78	0.59	0.01	0.25
MAXI J1836-194	9.09	92.23	2.78	-0.14	0.2	0.07	6.65
V4641 Sagittarii	8.24	50.56	2.56	-0.7	0.3	0.07	6.14

Table .2 Best-Fit Results and Upper Limits for the Periodic Analyses of the Model-Motivated Search. Here, we list the best-fit n_s, γ and $T_{\rm lag}$ for each fit, as well as the TS and local p-value. Upper limits are presented for two neutrino energy flux assumptions of $\gamma = 2$ and $\gamma = 3$ in units of TeV/cm^2 at 1 TeV. The listed upper limits are scaled up by a factor of 100 for presentation.

Model	Source	Instrument	TS	n_s	γ	$T_{\rm lag}$	p-value	U.L.$^{90\%}_{E^{-2}}$	U.L.$^{90\%}_{E^{-3}}$
Linear Interpolation	MWC 656	Fermi (Low)	0.0	0.0	3.5	-50.0	1.0	0.03	0.48
		Fermi (High)	0.0	0.0	3.0	30.0	1.0	0.03	0.45
	Cygnus X-3	MAXI	1.06	11.58	2.46	-149.96	0.5	0.03	0.65
		Swift	1.37	19.64	4.0	50.02	0.41	0.04	0.71
		Fermi	0.83	4.59	2.02	30.0	0.47	0.03	0.63
	Cygnus X-1	MAXI	0.7	11.77	4.0	99.99	0.49	0.03	0.61
		Swift	0.32	6.42	4.0	132.45	0.67	0.03	0.67
		Fermi (Low)	0.23	5.92	3.32	-20.01	0.69	0.03	0.63
		Fermi (High)	0.03	2.16	4.0	-49.98	0.74	0.03	0.54
	MAXI J1836-194	MAXI	10.36	40.51	2.3	-80.01	0.23	0.16	13.97
		Swift	12.91	29.98	2.19	-29.04	0.1	0.18	8.64
		Fermi (Low)	8.72	43.56	2.94	30.0	0.11	0.08	6.27
		Fermi (High)	6.79	98.17	3.06	-50.0	0.29	0.14	13.31
	V4641 Sagittarii	MAXI	11.7	83.51	2.75	-140.54	0.24	0.17	14.50
		Swift	12.04	46.55	2.53	-120.0	0.19	0.20	14.78
		Fermi (Low)	8.1	55.97	2.77	20.49	0.27	0.14	11.10
		Fermi (High)	11.78	66.25	2.65	-40.01	0.11	0.20	15.74
Baseline-Shifted	MWC 656	Fermi (Low)	0.05	1.3	4.0	-20.42	0.95	0.01	0.11
		Fermi (High)	0.0	0.1	4.0	20.0	0.89	0.01	0.09
	Cygnus X-3	MAXI	1.66	9.01	2.38	-149.96	0.63	0.01	0.25
		Swift	4.07	23.08	4.0	20.0	0.34	0.02	0.41
		Fermi	1.61	2.14	1.64	30.0	0.48	0.01	0.16
	Cygnus X-1	MAXI	4.48	24.13	4.0	99.98	0.24	0.02	0.41
		Swift	0.26	3.93	4.0	130.72	0.83	0.02	0.44
		Fermi (Low)	2.23	6.39	2.52	-20.0	0.41	0.01	0.21
		Fermi (High)	0.22	2.55	4.0	0.0	0.82	0.01	0.18
	MAXI J1836-194	MAXI	13.33	9.81	2.03	-80.0	0.04	0.04	2.28
		Swift	12.2	12.68	1.96	-27.77	0.08	0.10	3.11
		Fermi (Low)	8.12	30.58	2.96	10.0	0.1	0.03	2.22
		Fermi (High)	5.35	28.54	3.06	30.0	0.25	0.03	2.35
	V4641 Sagittarii	MAXI	8.68	40.03	3.19	-159.7	0.38	0.03	2.23
		Swift	11.45	25.53	2.46	-120.0	0.16	0.12	6.61
		Fermi (Low)	4.54	17.13	2.89	20.4	0.39	0.03	1.55
		Fermi (High)	10.4	29.1	2.47	-40.0	0.08	0.06	4.0

Table .3 Best-Fit Results and Upper Limits for the Multi-Wavelength Analyses of the Model-Motivated Search. Here, we provide the best-fit n_s, γ and $T_{\rm lag}$ for each analysis. The resulting TS and local p-value is provided in each case. Upper limits are determined for two neutrino energy flux assumptions of $\gamma = 2$ and $\gamma = 3$ in units of TeV/cm^2 at 1 TeV. The listed upper limits are scaled up by a factor of 100 for presentation.

APPENDIX

ADDITIONAL RESULTS AND INFORMATION FOR A RADIATIVE MODEL OF DELAYED RADIO FLARES

.1 Jet Stream Composition in Simulation

In this section, we describe simulation of the jet stream with time-varying injected electron luminosity. The jet is composed of a series of spherical zones. To reduce computation time, we simulate a smaller number of uniquely evolving particle populations, and use a linear combination of these sampled portions of the jet stream to compose the expected, observed emission.

The period associated with an observed gamma-ray flare is split into several sub-periods. The center time of each sub-period will be used to evolve a blob of initial injected luminosity $L_{\rm e}(t)$. Injection will continue for a period, $\tau_{\rm steady} = 3 \times r_0$, as the spectrum from the blob reaches a steady state subject to other losses. After a time $\tau_{\rm SS}$, injection ends, and radius is allowed to evolve.

For the remaining time within the sub-period, copies of this blob evolution are placed every $2 \times r_0$ in light time in the jet frame. As blobs are separated by their diameter, this approximates a near-continuous stream in the relativistic jet. In the special case of the first blob which acts as the jet front, an additional blob simulation is performed to fill out the remaining time of that sub-period. This evolution will not include additional injected electrons from the distant, cooled blob.

.2 Evaluation of Radio Zones

As we explained in the main text, our model describes the radio flare by the interaction of the parsec-scale jet with clumps of higher particle density, which we refer to in a generic manner as "clouds", leading to a temporary enhancement in the luminosity of the accelerated particles. For the sake of simplicity, we consider only particle emission from one jet blob as it crosses these clouds.

In order to reproduce the complex features of the multi-frequency radio light curves,

we found empirically that reproducing the complex structure of the multi-frequency radio light curves requires a minimum of three clouds. This can be represented by three spatially-overlapping particle populations or clouds, with separate temporal peaks (reflecting distance along the jet), luminosity normalizations, and densities. Specifically, given the jet front radius, $r(t)$, we treat this by introducing two inner regions of radii $\xi_0 r(t)$ and $\xi_1 r(t)$. These are the three concentric spatial sizes of our modeled clouds, $\xi_1 r(t) < \xi_0 r(t) < r(t)$. As there is overlap between the volumes of these particle populations, assuming spherical geometry, we determine the corresponding regions of uniform particle densities associated with these superpositions. The innermost volume has contributions from all three particle populations, the second surrounding volume has contributions from only the two outermost populations, and the third has only a single contribution. The corresponding volumes are,

$$V_a(t) = \frac{3}{4}\pi\, r(t)^3 (1-\xi_0)^3, \tag{.1}$$

$$V_b(t) = \frac{3}{4}\pi\, r(t)^3 (\xi_0-\xi_1)^3, \tag{.2}$$

$$V_c(t) = \frac{3}{4}\pi\, r(t)^3 \xi_1^3. \tag{.3}$$

Each zone can be evaluated as a spherical blob of equivalent volume. Denser initial regions lead to self-absorption, while larger, later regions are unabsorbed. The luminosity of each evaluated volume is given below,

$$L_a(t) = L_{e,\mathrm{cloud},0}(t)\,(1-\xi_0^3), \tag{.4}$$

$$\begin{aligned} L_b(t) = {} & L_{e,\mathrm{cloud},0}(t)\,(\xi_0^3-\xi_1^3) \\ & + L_{e,\mathrm{cloud},1}(t)\,(\xi_0^3-\xi_1^3)/\xi_0^3, \end{aligned} \tag{.5}$$

$$\begin{aligned} L_c(t) = {} & L_{e,\mathrm{cloud},0}(t)\,\xi_1^3 + L_{e,\mathrm{cloud},1}(t)\,\xi_1^3/\xi_0^3 \\ & + L_{e,\mathrm{cloud},2}(t). \end{aligned} \tag{.6}$$

We note that this assumption of concentric spherical symmetry and extension differs slightly in expectation from the conical description given in the text, though we expect

sufficient agreement between this tractable model and an ideal model of conical regions. Given the same luminosity and particle populations, this difference in geometry would likely account for a sub-order-of-magnitude difference, and still provides a useful model of extended particle populations.

.3 Parameterization of Steady-State Emission

In this section, we provide a comparison of the spectral parameterization used in this work, along with archival data for TXS 0506+056. This is presented in Figure .1.

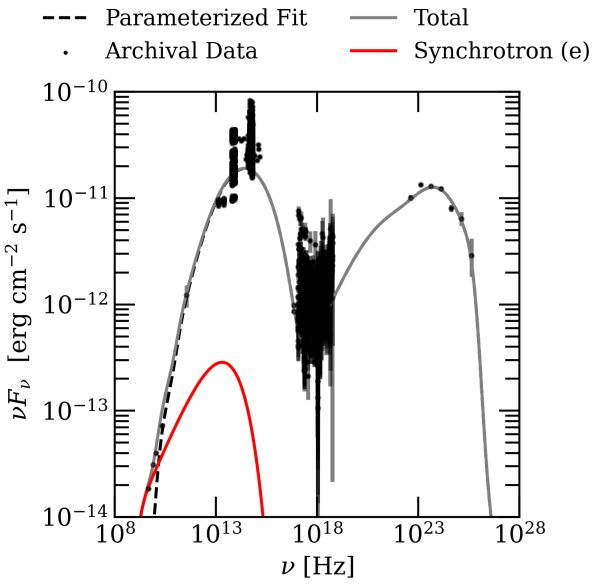

Figure .1 The steady-state spectral model underlying our analysis of evolving emission from TXS 0506+056. We present the steady-state fit used in our evolving radiative model. A fit to archival data, plotted as black data points, is repurposed from a previous analysis [Rodrigues et al., 2026] To improve upon this baseline prediction for the source radio intensity, we have added an additional electron population and synchrotron component. This added component, previous fit, and total, are plotted with red, dashed black, and gray lines respectively.

.4 Sampled Parameters Relevant to the Radio Cloud

In Figure .2, we provide sampled distributions of several parameters in our model of electron populations contributing to the delayed radio flare. We also include comparison with several key parameters relevant to the jet stream environment, Γ, η and B.

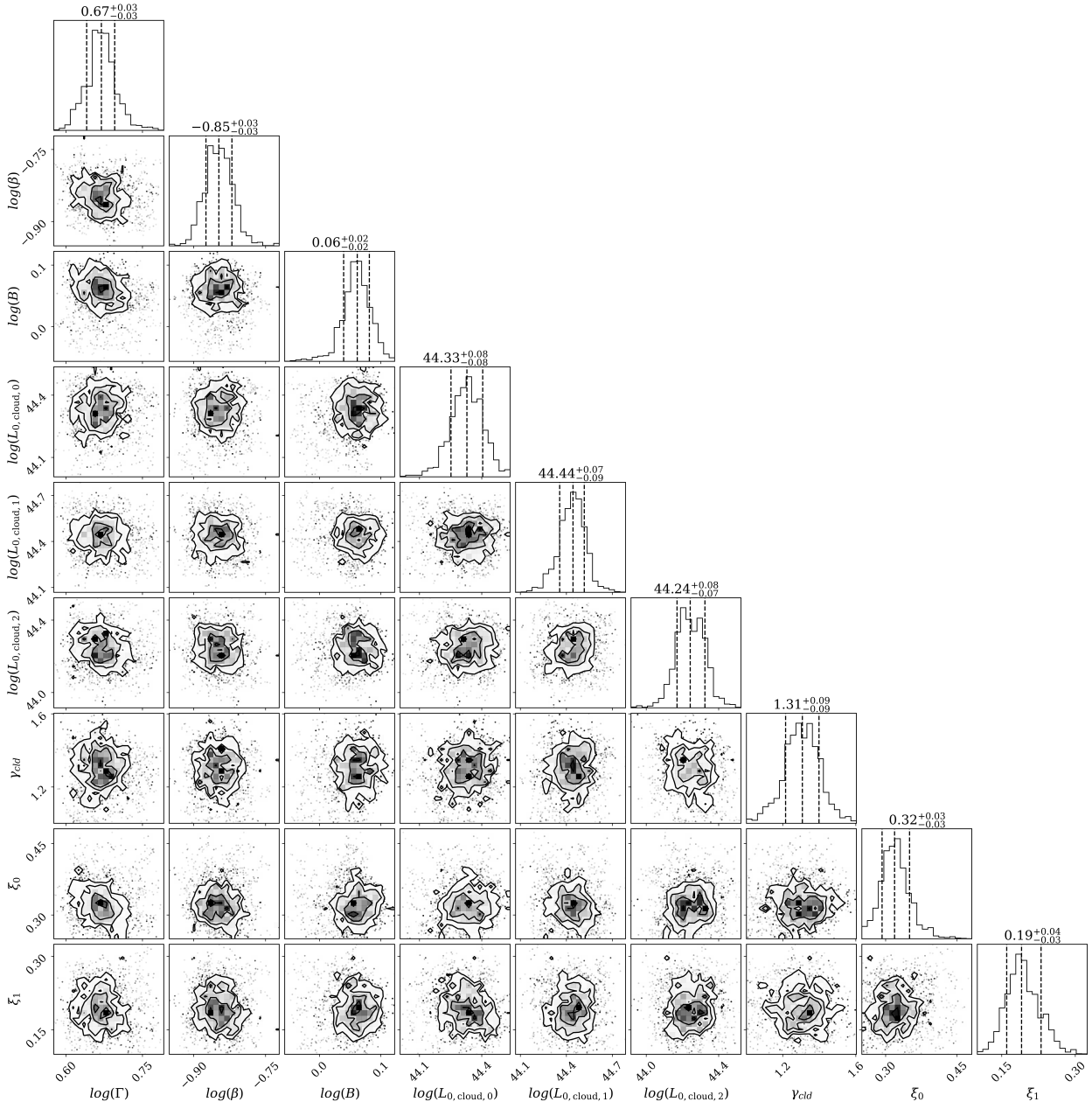

Figure .2 Parameter values relevant to the radio clouds explored through MCMC sampling. We plot the distributions of parameter values sampled through our MCMC study, reflecting ∼24,000 realizations. The represents exploration of the parameter space near a local, high-likelihood solution.

.5 Best-Fit Cloud Luminosity Profiles

In Figure .3, we provide a plot of the highest-likelihood parameterizations of the cloud luminosity profiles, determined from our MCMC sampling.

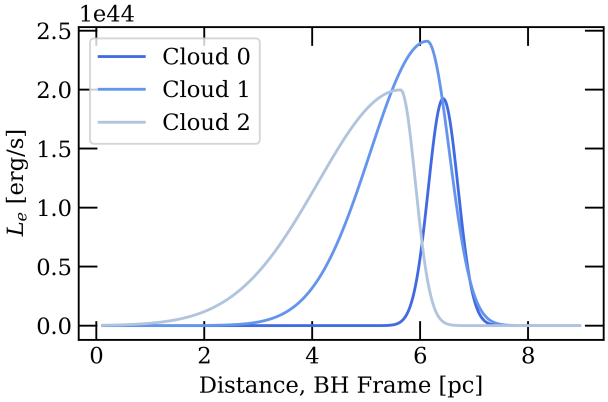

Figure .3 The highest-likelihood luminosity profiles for the electron clouds driving the radio flare. Specifically, these profiles reflect the free parameters, $L_{0,\text{cloud},0}, L_{0,\text{cloud},1}, L_{0,\text{cloud},2}$, as well as ϵ, ρ, ξ_0 and ξ_1.

APPENDIX

ADDITIONAL RESULTS FOR A GAMMA-RADIO CORRELATION

Table .1 Correlation results for a radio-delayed flare. Given our search window of -0.5 to 3.5 years, we provide the tested lag and uncertainty in days, $T_{\rm delay}$ and $\Delta T_{\rm delay}$, corresponding to the highest correlation coefficient $R_{\rm delay}$. Results for the integral gamma-ray energy band are provided.

Source Name	R.A. [°]	Dec. [°]	$T_{\rm delay,\ integral}$	$\Delta T_{\rm delay,\ integral}$	$R_{\rm delay,\ integral}$
J0013.6-0424	3.48	-4.4	1277.5	571.94	-0.14
J0018.8+2611	4.91	26.05	665.08	228.0	0.93
J0112.8+3208	18.21	32.14	620.05	165.14	0.18
J0118.9-2141	19.74	-21.69	599.04	13.92	0.72
J0132.7-1654	23.18	-16.91	534.99	15.49	0.77
J0144.6+2705	26.14	27.08	217.77	37.58	0.46
J0152.2+2206	28.07	22.12	-182.5	43.96	0.41
J0238.6+1637	39.66	16.62	-0.38	9.03	0.78
J0239.7+0415	39.96	4.27	712.11	236.63	0.8
J0312.8+0134	48.18	1.55	24.64	400.08	0.8
J0343.4+3621	55.87	36.37	1272.5	195.9	0.79
J0348.6-2749	57.16	-27.82	578.02	26.56	0.95
J0405.6-1308	61.39	-13.14	180.75	39.69	0.75
J0416.5-1852	64.15	-18.85	1.63	546.22	0.78
J0423.3-0120	65.81	-1.34	248.8	217.02	0.76
J0423.9+4150	65.98	41.83	1047.34	534.18	0.57
J0434.1-2014	68.53	-20.25	-182.5	532.5	0.46
J0442.6-0017	70.66	-0.3	-182.5	369.28	0.46
J0449.1+1121	72.28	11.36	30.65	17.61	0.89

Source Name	R.A. [°]	Dec. [°]	$T_{\text{delay, integral}}$	$\Delta T_{\text{delay, integral}}$	$R_{\text{delay, integral}}$
J0453.1-2806	73.31	-28.13	183.75	314.99	0.32
J0457.0-2324	74.26	-23.41	104.7	18.46	0.65
J0502.4+0609	75.56	6.15	741.13	9.37	0.66
J0510.0+1800	77.51	18.01	-62.42	8.9	0.56
J0532.6+0732	83.16	7.55	1149.41	489.88	0.56
J0533.3+4823	83.31	48.38	380.89	26.54	0.88
J0539.9-2839	84.97	-28.67	293.83	29.32	0.44
J0654.4+4514	103.6	45.24	-33.4	351.45	0.6
J0656.3-0322	104.05	-3.38	-158.48	455.78	0.24
J0659.6-2742	104.95	-27.75	297.83	172.81	0.63
J0718.0+4536	109.46	45.63	749.14	86.81	0.06
J0725.2+1425	111.32	14.42	645.07	51.53	0.29
J0748.6+2400	117.15	24.01	432.92	115.11	0.44
J0754.4-1148	118.61	-11.79	-43.4	158.05	0.39
J0808.2-0751	122.06	-7.85	78.68	29.87	0.85
J0809.3+4053	122.23	40.88	504.97	312.2	-0.16
J0829.0+1755	127.27	17.9	245.79	371.1	0.14
J0830.8+2410	127.72	24.18	274.81	80.87	0.56
J0850.0+5108	132.49	51.14	-53.41	191.74	0.04
J0920.9+4441	140.24	44.7	18.64	34.25	0.83
J0921.6+6216	140.4	62.26	18.64	141.05	0.63
J0923.5+4125	140.88	41.42	102.7	28.23	-0.14
J1006.7-2159	151.69	-21.99	584.03	254.32	0.26
J1114.5-0819	168.63	-8.28	-182.5	512.73	0.48
J1118.6-1235	169.57	-12.55	801.17	131.47	0.91
J1127.0-1857	171.77	-18.95	1029.33	10.24	0.93

Source Name	R.A. [°]	Dec. [°]	$T_{\text{delay, integral}}$	$\Delta T_{\text{delay, integral}}$	$R_{\text{delay, integral}}$
J1129.8-1447	172.53	-14.82	939.27	108.72	0.79
J1135.7-0427	173.99	-4.47	-41.4	289.08	0.26
J1345.8+0706	206.45	7.11	978.3	394.12	0.28
J1357.1+1921	209.27	19.32	669.08	459.14	0.5
J1613.6+3411	243.42	34.21	702.11	71.3	0.88
J1616.7+4107	244.27	41.11	99.69	450.66	0.88
J1631.2+4926	247.82	49.46	1008.32	402.92	0.8
J1635.2+3808	248.81	38.13	86.68	6.95	0.73
J1642.9+3948	250.74	39.81	-96.44	30.09	0.7
J1728.4+0427	262.1	4.45	-80.43	577.86	0.71
J1733.0-1305	263.26	-13.08	1277.5	0.0	0.42
J1734.3+3858	263.58	38.96	669.08	180.87	0.42
J1740.5+5211	265.15	52.2	266.81	16.96	0.69
J1753.7+2847	268.42	28.8	871.22	47.97	0.96
J2136.2+0032	324.16	0.7	1277.5	84.67	0.48
J2146.4-1528	326.59	-15.43	1179.43	155.69	0.72
J2147.1+0931	326.79	9.5	101.69	416.27	0.2
J2158.1-1501	329.52	-15.02	371.88	255.48	0.11
J2219.2-0342	334.72	-3.59	389.89	100.52	0.59
J2219.2+1806	334.81	18.11	-19.39	133.58	0.56
J2225.6+2120	336.41	21.3	333.85	384.26	0.13
J2229.7-0832	337.42	-8.55	-2.38	13.34	0.82
J2232.6+1143	338.15	11.73	37.65	103.38	-0.09
J2236.3+2828	339.09	28.48	71.67	17.01	0.55
J2243.9+2021	340.97	20.35	511.98	218.81	0.59
J2253.9+1609	343.49	16.15	478.95	19.97	0.84

Source Name	R.A. [°]	Dec. [°]	$T_{\text{delay, integral}}$	$\Delta T_{\text{delay, integral}}$	$R_{\text{delay, integral}}$
J2311.0+3425	347.77	34.42	451.93	93.66	0.16
J2321.9+3204	350.47	32.07	523.98	164.7	0.36
J2321.9+2734	350.5	27.55	302.83	430.68	0.74
J2338.0-0230	354.49	-2.52	242.79	65.06	0.61
J2348.0-1630	357.01	-16.52	1277.5	0.0	0.44

BIBLIOGRAPHY

M. Grudzinska and et al. On the formation and evolution of the first be star in a black hole binary: Mwc 656. *Monthly Notices of the Royal Astronomical Society*, 452(3):2773–2780, September 2015. doi: 10.1093/mnras/stv1419. URL https://doi.org/10.1093/mnras/stv1419.

Timothy Kallman and et al. Photoionization emission models for the cyg x-3 x-ray spectrum. *The Astrophysical Journal*, 874(1):51, March 2019. doi: 10.3847/1538-4357/ab09f8. URL https://doi.org/10.3847/1538-4357/ab09f8.

A. A. Stepanian. On a possible model of the object cyg x-3. *Astrophysics and Space Science*, 84:347–361, June 1982. doi: 10.1007/BF00651316. URL https://doi.org/10.1007/BF00651316.

Jiachen Jiang. Fifty years after the discovery of the first stellar-mass black hole: A review of cyg x-1. *Galaxies*, 12(6):80, June 2024. doi: 10.3390/galaxies12060080. URL https://doi.org/10.3390/galaxies12060080.

Juri Poutanen and et al. Superorbital variability of x-ray and radio emission of cyg x-1 – ii. dependence of the orbital modulation and spectral hardness on the superorbital phase. *Monthly Notices of the Royal Astronomical Society*, 389(3):1427–1438, September 2008. doi: 10.1111/j.1365-2966.2008.13666.x. URL https://doi.org/10.1111/j.1365-2966.2008.13666.x.

Arghajit Jana and et al. Accretion flow dynamics of maxi j1836-194 during its 2011 outburst from tcaf solution. *The Astrophysical Journal*, 819(2):107, March 2016. doi: 10.3847/0004-637X/819/2/107. URL https://iopscience.iop.org/article/10.3847/0004-637X/819/2/107/meta.

Jerome A. Orosz and et al. A black hole in the superluminal source sax j1819.3–2525 (v4641 sgr). *The Astrophysical Journal*, 555(1):489–503, July 2001. doi: 10.1086/321442. URL https://iopscience.iop.org/article/10.1086/321442/fulltext/.

Simona Paiano, Renato Falomo, Aldo Treves, and Riccardo Scarpa. The redshift of the bl lac object txs 0506+056. *The Astrophysical Journal Letters*, 854(2):L32, February 2018. ISSN 2041-8213. doi: 10.3847/2041-8213/aaad5e. URL http://dx.doi.org/10.3847/2041-8213/aaad5e.

Sarira Sahu, D I Páez-Sánchez, B Medina-Carrillo, R de J Pacheco-Aké, G Sánchez-Colón, and Subhash Rajpoot. Redshift constrain of bl lac pks 1424+240. *Monthly Notices of the Royal Astronomical Society*, 533(2):2156–2161, July 2024. ISSN 1365-2966. doi: 10.1093/mnras/stae1847. URL http://dx.doi.org/10.1093/mnras/stae1847.

P Padovani, B Boccardi, R Falomo, and P Giommi. Pks1424+240: yet another mas-

querading bl lac object as a possible icecube neutrino source. *Monthly Notices of the Royal Astronomical Society*, 511(4):4697–4701, February 2022. ISSN 1365-2966. doi: 10.1093/mnras/stac376. URL http://dx.doi.org/10.1093/mnras/stac376.

P Padovani, F Oikonomou, M Petropoulou, P Giommi, and E Resconi. Txs0506+056, the first cosmic neutrino source, is not a bl lac. *Monthly Notices of the Royal Astronomical Society: Letters*, 484(1):L104–L108, January 2019. ISSN 1745-3933. doi: 10.1093/mnrasl/slz011. URL http://dx.doi.org/10.1093/mnrasl/slz011.

Christian Grefe. Detector optimization studies and light higgs decay into muons at clic. 02 2014.

Roger Blandford, David Meier, and Anthony Readhead. Relativistic jets from active galactic nuclei. *Annual Review of Astronomy and Astrophysics*, 57(1):467–509, August 2019. ISSN 1545-4282. doi: 10.1146/annurev-astro-081817-051948. URL http://dx.doi.org/10.1146/annurev-astro-081817-051948.

Alejandro Cruz-Osorio et al. State-of-the-art energetic and morphological modelling of the launching site of the m87 jet. *Nature Astronomy*, 6(1):103–108, November 2021. ISSN 2397-3366. doi: 10.1038/s41550-021-01506-w. URL http://dx.doi.org/10.1038/s41550-021-01506-w.

C. Megan Urry and Paolo Padovani. Unified Schemes for Radio-Loud Active Galactic Nuclei. , 107:803, September 1995. doi: 10.1086/133630.

Mitchell C. Begelman and Philip J. Armitage. A mechanism for hysteresis in black hole binary state transitions. *Astrophys. J. Lett.*, 782(2):L18, 2014. doi: 10.1088/2041-8205/782/2/L18.

Anatoli Fedynitch, Ralph Engel, Thomas K. Gaisser, Felix Riehn, and Todor Stanev. Calculation of conventional and prompt lepton fluxes at very high energy, 2015. URL https://arxiv.org/abs/1503.00544.

Markus Ahlers, Klaus Helbing, and Carlos Pérez de los Heros. Probing particle physics with icecube. *The European Physical Journal C*, 78(11), November 2018. ISSN 1434-6052. doi: 10.1140/epjc/s10052-018-6369-9. URL http://dx.doi.org/10.1140/epjc/s10052-018-6369-9.

Yasuyuki T. Tanaka, Sara Buson, and Daniel Kocevski. Fermi-LAT detection of increased gamma-ray activity of TXS 0506+056, located inside the IceCube-170922A error region. *The Astronomer's Telegram*, 10791:1, September 2017.

IceCube Collaboration. Characteristics of the diffuse astrophysical electron and tau neutrino flux with six years of icecube high energy cascade data. *Phys. Rev. Lett.*, 125:121104, Sep 2020. doi: 10.1103/PhysRevLett.125.121104. URL https://link.aps.org/doi/10.

1103/PhysRevLett.125.121104.

IceCube Collaboration. Improved Characterization of the Astrophysical Muon-neutrino Flux with 9.5 Years of IceCube Data. , 928(1):50, March 2022a. doi: 10.3847/1538-4357/ac4d29.

Yu. V. Sotnikova et al. The ratan-600 multi-frequency catalogue of blazars—blcat. *Astrophysical Bulletin*, 77(4):361–371, December 2022. ISSN 1990-3421. doi: 10.1134/s1990341322040149. URL http://dx.doi.org/10.1134/S1990341322040149.

Fermi-LAT Collaboration. The fermi-lat lightcurve repository*. *The Astrophysical Journal Supplement Series*, 265(2):31, March 2023. ISSN 1538-4365. doi: 10.3847/1538-4365/acbb6a. URL http://dx.doi.org/10.3847/1538-4365/acbb6a.

M. L. Lister, M. F. Aller, H. D. Aller, M. A. Hodge, D. C. Homan, Y. Y. Kovalev, A. B. Pushkarev, and T. Savolainen. MOJAVE. XV. VLBA 15 GHz Total Intensity and Polarization Maps of 437 Parsec-scale AGN Jets from 1996 to 2017. , 234(1):12, January 2018. doi: 10.3847/1538-4365/aa9c44.

Tatehiro Mihara, Hiroshi Tsunemi, and Hitoshi Negoro. MAXI: Monitor of All-Sky X-Ray Image. In Cosimo Bambi and Andrea Sangangelo, editors, *Handbook of X-ray and Gamma-ray Astrophysics*, page 47. 2022. doi: 10.1007/978-981-16-4544-0_38-1.

Xavier Rodrigues, Frank Rieger, Artem Bohdan, and Paolo Padovani. Hillas meets Eddington: The case for blazars as ultra-high-energy neutrino sources. *Astron. Astrophys.*, 706: A351, 2026. doi: 10.1051/0004-6361/202556986.

Dragan Huterer. *A course in cosmology: from theory to practice*. 2023.

Edwin Hubble. A Relation between Distance and Radial Velocity among Extra-Galactic Nebulae. *Proceedings of the National Academy of Science*, 15(3):168–173, March 1929. doi: 10.1073/pnas.15.3.168.

Planck Collaboration. ¡i¿planck¡/i¿2018 results: Vi. cosmological parameters. *Astronomy amp; Astrophysics*, 641:A6, 2020. ISSN 1432-0746. doi: 10.1051/0004-6361/201833910. URL http://dx.doi.org/10.1051/0004-6361/201833910.

Michael E. Peskin and Daniel V. Schroeder. *An Introduction to quantum field theory*. Addison-Wesley, Reading, USA, 1995. ISBN 978-0-201-50397-5, 978-0-429-50355-9, 978-0-429-49417-8. doi: 10.1201/9780429503559.

Peter W. Higgs. Broken symmetries, massless particles and gauge fields. *Phys. Lett.*, 12: 132–133, 1964. doi: 10.1016/0031-9163(64)91136-9.

F. Englert and R. Brout. Broken symmetry and the mass of gauge vector mesons. *Phys. Rev. Lett.*, 13:321–323, Aug 1964. doi: 10.1103/PhysRevLett.13.321. URL https://link.aps.

org/doi/10.1103/PhysRevLett.13.321.

G. S. Guralnik, C. R. Hagen, and T. W. Kibble. Global Conservation Laws and Massless Particles. , 13(20):585–587, November 1964. doi: 10.1103/PhysRevLett.13.585.

A. C. Fabian. Observational Evidence of Active Galactic Nuclei Feedback. , 50:455–489, September 2012. doi: 10.1146/annurev-astro-081811-125521.

M.J. Hardcastle and J.H. Croston. Radio galaxies and feedback from agn jets. *New Astronomy Reviews*, 88:101539, June 2020. ISSN 1387-6473. doi: 10.1016/j.newar.2020.101539. URL http://dx.doi.org/10.1016/j.newar.2020.101539.

Steven A. Balbus and John F. Hawley. A Powerful Local Shear Instability in Weakly Magnetized Disks. I. Linear Analysis. , 376:214, July 1991. doi: 10.1086/170270.

Steven A. Balbus and John F. Hawley. Instability, turbulence, and enhanced transport in accretion disks. *Reviews of Modern Physics*, 70(1):1–53, January 1998. doi: 10.1103/RevModPhys.70.1.

J. M. Miller et al. On the Role of the Accretion Disk in Black Hole Disk-Jet Connections. , 757(1):11, September 2012. doi: 10.1088/0004-637X/757/1/11.

N. I. Shakura and R. A. Sunyaev. Black holes in binary systems. Observational appearance. , 24:337–355, January 1973.

Alexander Tchekhovskoy, Jonathan C McKinney, and Ramesh Narayan. General relativistic modeling of magnetized jets from accreting black holes. *Journal of Physics: Conference Series*, 372:012040, 2012. ISSN 1742-6596. doi: 10.1088/1742-6596/372/1/012040. URL http://dx.doi.org/10.1088/1742-6596/372/1/012040.

R. D. Blandford and R. L. Znajek. Electromagnetic extraction of energy from Kerr black holes. , 179:433–456, May 1977. doi: 10.1093/mnras/179.3.433.

R. D. Blandford and D. G. Payne. Hydromagnetic flows from accretion disks and the production of radio jets. , 199:883–903, June 1982. doi: 10.1093/mnras/199.4.883.

Y. E. Lyubarsky. On the relativistic magnetic reconnection. *Monthly Notices of the Royal Astronomical Society*, 358(1):113–119, March 2005. ISSN 1365-2966. doi: 10.1111/j.1365-2966.2005.08767.x. URL http://dx.doi.org/10.1111/j.1365-2966.2005.08767.x.

Lorenzo Sironi and Anatoly Spitkovsky. Relativistic reconnection: An efficient source of nonthermal particles. *The Astrophysical Journal*, 783(1):L21, February 2014. ISSN 2041-8213. doi: 10.1088/2041-8205/783/1/l21. URL http://dx.doi.org/10.1088/2041-8205/783/1/L21.

Enrico Fermi. On the Origin of the Cosmic Radiation. *Phys. Rev.*, 75:1169–1174, 1949. doi: 10.1103/PhysRev.75.1169.

R. D. Blandford and J. P. Ostriker. Particle acceleration by astrophysical shocks. , 221: L29–L32, April 1978. doi: 10.1086/182658.

George B. Rybicki and Alan P. Lightman. *Radiative Processes in Astrophysics*. 1986.

George R. Blumenthal and Robert J. Gould. Bremsstrahlung, Synchrotron Radiation, and Compton Scattering of High-Energy Electrons Traversing Dilute Gases. *Reviews of Modern Physics*, 42(2):237–271, January 1970. doi: 10.1103/RevModPhys.42.237.

Robert J. Gould and Gérard P. Schréder. Pair production in photon-photon collisions. *Phys. Rev.*, 155:1404–1407, Mar 1967. doi: 10.1103/PhysRev.155.1404. URL `https://link.aps.org/doi/10.1103/PhysRev.155.1404`.

Kohta Murase and Floyd W. Stecker. *High-Energy Neutrinos from Active Galactic Nuclei*, page 483–540. WORLD SCIENTIFIC, October 2023. ISBN 9789811282645. doi: 10.1142/9789811282645_0010. URL `http://dx.doi.org/10.1142/9789811282645_0010`.

Armen Atoyan and Charles D. Dermer. High-energy neutrinos from photomeson processes in blazars. *Physical Review Letters*, 87(22), November 2001. ISSN 1079-7114. doi: 10.1103/physrevlett.87.221102. URL `http://dx.doi.org/10.1103/PhysRevLett.87.221102`.

Charles D. Dermer and Govind Menon. *High Energy Radiation from Black Holes: Gamma Rays, Cosmic Rays, and Neutrinos*. 2009.

Carl . Seyfert. *108. Nuclear Emission in Spiral Nebulae*, pages 738–743. Harvard University Press, Cambridge, MA and London, England, 1979. ISBN 9780674366688. doi: doi:10.4159/harvard.9780674366688.c116. URL `https://doi.org/10.4159/harvard.9780674366688.c116`.

Clive Tadhunter. An introduction to active galactic nuclei: Classification and unification. *New Astronomy Reviews*, 52(6):227–239, 2008. ISSN 1387-6473. doi: https://doi.org/10.1016/j.newar.2008.06.004. URL `https://www.sciencedirect.com/science/article/pii/S1387647308001012`. Active Galactic Nuclei at the Highest Angular Resolution: Theory and Observations.

Ronald A. Remillard and Jeffrey E. McClintock. X-ray properties of black-hole binaries. *Annual Review of Astronomy and Astrophysics*, 44(1):49–92, September 2006. ISSN 1545-4282. doi: 10.1146/annurev.astro.44.051905.092532. URL `http://dx.doi.org/10.1146/annurev.astro.44.051905.092532`.

Pierre-Olivier Petrucci and et al. The role of the disc magnetization on the hysteresis behaviour of x-ray binaries. *Monthly Notices of the Royal Astronomical Society: Letters*, 385

(1):L88–L92, March 2008. ISSN 1745-3933. doi: 10.1111/j.1745-3933.2008.00439.x. URL http://dx.doi.org/10.1111/j.1745-3933.2008.00439.x.

Steven A. Balbus and John F. Hawley. Instability, turbulence, and enhanced transport in accretion disks. *Rev. Mod. Phys.*, 70:1–53, Jan 1998. doi: 10.1103/RevModPhys.70.1. URL https://link.aps.org/doi/10.1103/RevModPhys.70.1.

Chris Nixon and Greg Salvesen. A physical model for state transitions in black hole X-ray binaries. *Mon. Not. Roy. Astron. Soc.*, 437(4):3994–3999, 2014. doi: 10.1093/mnras/stt2215.

Nicolas Scepi et al. Thermal solutions of strongly magnetized disks and the hysteresis in x-ray binaries. *Astronomy amp; Astrophysics*, 692:A153, December 2024. ISSN 1432-0746. doi: 10.1051/0004-6361/202451568. URL http://dx.doi.org/10.1051/0004-6361/202451568.

Jiahui Huang, Hua Feng, and Lian Tao. Magnetic accretion flow explains the hysteresis q-diagram seen in outbursts of black hole low-mass x-ray binaries, 2025. URL https://arxiv.org/abs/2410.22661.

Rohan Raha, Banibrata Mukhopadhyay, and Koushik Chatterjee. Grmhd simulations of black hole accretion variabilities: implications to hard state x-ray binary transients. *Monthly Notices of the Royal Astronomical Society*, 546(4), January 2026. ISSN 1365-2966. doi: 10.1093/mnras/stag148. URL http://dx.doi.org/10.1093/mnras/stag148.

Ramesh Narayan, Igor V. Igumenshchev, and Marek A. Abramowicz. Magnetically arrested disk: an energetically efficient accretion flow. *Publications of the Astronomical Society of Japan*, 55(6):L69–L72, December 2003. ISSN 2053-051X. doi: 10.1093/pasj/55.6.l69. URL http://dx.doi.org/10.1093/pasj/55.6.L69.

Francis Halzen and Spencer R. Klein. Invited review article: Icecube: An instrument for neutrino astronomy. *Review of Scientific Instruments*, 81(8), August 2010. ISSN 1089-7623. doi: 10.1063/1.3480478. URL http://dx.doi.org/10.1063/1.3480478.

Péter Mészáros, Derek B. Fox, Chad Hanna, and Kohta Murase. Multi-messenger astrophysics. *Nature Reviews Physics*, 1(10):585–599, October 2019. ISSN 2522-5820. doi: 10.1038/s42254-019-0101-z. URL http://dx.doi.org/10.1038/s42254-019-0101-z.

J A Van Allen et al. Observation of high intensity radiation by satellites 1958 alpha and gamma. *Jet Propulsion*, Vol: 28, 09 1958. doi: 10.2514/8.7396. URL https://www.osti.gov/biblio/4300875.

W. Kraushaar, G. W. Clark, G. Garmire, H. Helmken, P. Higbie, and M. Agogino. Explorer XI Experiment on Cosmic Gamma Rays. , 141:845, April 1965. doi: 10.1086/148179.

John Linsley. Evidence for a Primary Cosmic-Ray Particle with Energy 10^{20} eV. , 10(4): 146–148, February 1963. doi: 10.1103/PhysRevLett.10.146.

M. Nagano and A. A. Watson. Observations and implications of the ultrahigh-energy cosmic rays. *Reviews of Modern Physics*, 72(3):689–732, July 2000. doi: 10.1103/RevModPhys.72.689.

Raymond Davis. A review of the homestake solar neutrino experiment. *Progress in Particle and Nuclear Physics*, 32:13–32, January 1994. doi: 10.1016/0146-6410(94)90004-3.

D. H. Perkins. Proton decay experiments. *Annual Review of Nuclear and Particle Science*, 34:1–50, 1984. doi: 10.1146/annurev.ns.34.120184.000245.

R. C. Lamb, C. P. Godfrey, W. A. Wheaton, and T. Tümer. Cygnus x-3 observed at photon energies above 500 gev. *Nature*, 296(5858):543–544, April 1982. doi: 10.1038/296543a0.

M. Samorski and W. Stamm. Detection of 2 x 10**15-eV to 2 x 10**16-eV gamma Rays from Cygnus X-3. *Astrophys. J. Lett.*, 268:L17–L21, 1983. doi: 10.1086/184021.

J. A. Kochocki et al. Study of muons from the direction of cygnus x-3 using an underground proportional-tube array. *Phys. Rev. D*, 42:2967–2973, Nov 1990. doi: 10.1103/PhysRevD.42.2967. URL `https://link.aps.org/doi/10.1103/PhysRevD.42.2967`.

K. Hirata et al. Observation of a neutrino burst from the supernova sn1987a. *Phys. Rev. Lett.*, 58:1490–1493, Apr 1987. doi: 10.1103/PhysRevLett.58.1490. URL `https://link.aps.org/doi/10.1103/PhysRevLett.58.1490`.

Todd Haines et al. Neutrinos from SN1987a in the IMB detector. *Nuclear Instruments and Methods in Physics Research A*, 264(1):28–31, February 1988. doi: 10.1016/0168-9002(88)91097-2.

E. N. Alekseev, L. N. Alekseeva, I. V. Krivosheina, and V. I. Volchenko. Detection of the Neutrino Signal from Supernova 1987A Using the INR Baksan Underground Scintillation Telescope. In I. J. Danziger, editor, *European Southern Observatory Conference and Workshop Proceedings*, volume 26 of *European Southern Observatory Conference and Workshop Proceedings*, page 237, January 1987.

T. C. Weekes et al. Observation of TeV Gamma Rays from the Crab Nebula Using the Atmospheric Cerenkov Imaging Technique. , 342:379, July 1989. doi: 10.1086/167599.

AMS Collaboration. First result from the alpha magnetic spectrometer on the international space station: Precision measurement of the positron fraction in primary cosmic rays of 0.5–350 gev. *Phys. Rev. Lett.*, 110:141102, Apr 2013. doi: 10.1103/PhysRevLett.110.141102. URL `https://link.aps.org/doi/10.1103/PhysRevLett.110.141102`.

Pierre Auger Collaboration. The Pierre Auger Cosmic Ray Observatory. *Nuclear Instruments and Methods in Physics Research A*, 798:172–213, October 2015. doi: 10.1016/j.nima.2015.06.058.

IceCube Collaboration. The surface detector array of the telescope array experiment. *Nuclear Instruments and Methods in Physics Research Section A: Accelerators, Spectrometers, Detectors and Associated Equipment*, 689:87–97, October 2012. ISSN 0168-9002. doi: 10.1016/j.nima.2012.05.079. URL http://dx.doi.org/10.1016/j.nima.2012.05.079.

W. B. Atwood et al. The Large Area Telescope on the Fermi Gamma-Ray Space Telescope Mission. , 697(2):1071–1102, June 2009. doi: 10.1088/0004-637X/697/2/1071.

J.A Hinton. The status of the hess project. *New Astronomy Reviews*, 48(5-6):331–337, April 2004. ISSN 1387-6473. doi: 10.1016/j.newar.2003.12.004. URL http://dx.doi.org/10.1016/j.newar.2003.12.004.

MAGIC Collaboration. The major upgrade of the MAGIC telescopes, Part II: A performance study using observations of the Crab Nebula. *Astroparticle Physics*, 72:76–94, January 2016. doi: 10.1016/j.astropartphys.2015.02.005.

VERITAS Collaboration. The first veritas telescope. *Astroparticle Physics*, 25(6):391–401, 2006. ISSN 0927-6505. doi: 10.1016/j.astropartphys.2006.04.002. URL http://dx.doi.org/10.1016/j.astropartphys.2006.04.002.

HAWC Collaboration. Observation of the Crab Nebula with the HAWC Gamma-Ray Observatory. , 843(1):39, July 2017. doi: 10.3847/1538-4357/aa7555.

LHAASO Collaboration. Ultrahigh-energy photons up to 1.4 petaelectronvolts from 12 γ-ray Galactic sources. , 594(7861):33–36, June 2021. doi: 10.1038/s41586-021-03498-z.

Eduardo C. Andrés and et al. The amanda neutrino telescope: Principle of operation and first results. *Astroparticle Physics*, 13:1–20, 1999. URL https://api.semanticscholar.org/CorpusID:19684076.

IceCube Collaboration. The icecube neutrino observatory: instrumentation and online systems. *Journal of Instrumentation*, 12(03):P03012–P03012, March 2017. ISSN 1748-0221. doi: 10.1088/1748-0221/12/03/p03012. URL http://dx.doi.org/10.1088/1748-0221/12/03/P03012.

M.G. Aartsen, M. Ackermann, J. Adams, J.A. Aguilar, M. Ahlers, M. Ahrens, C. Alispach, K. Andeen, T. Anderson, I. Ansseau, and et al. Evidence for High-Energy Extraterrestrial Neutrinos at the IceCube Detector. *Science*, 342(6161):1242856–1242856, Nov 2013. ISSN 1095-9203. doi: 10.1126/science.1242856. URL http://dx.doi.org/10.1126/science.1242856.

IceCube Collaboration. Neutrino Emission from the Direction of the Blazar TXS 0506+056 Prior to the IceCube-170922A Alert. *Science*, 361(6398):147–151, 2018a. ISSN 0036-8075. doi: 10.1126/science.aat2890. URL https://science.sciencemag.org/content/361/6398/147.

IceCube Collaboration. Evidence for neutrino emission from the nearby active galaxy ngc 1068. *Science*, 378(6619):538–543, November 2022b. ISSN 1095-9203. doi: 10.1126/science.abg3395. URL http://dx.doi.org/10.1126/science.abg3395.

IceCube Collaboration. Search for extended sources of neutrino emission in the galactic plane with icecube. *The Astrophysical Journal*, 956(1):20, October 2023. ISSN 1538-4357. doi: 10.3847/1538-4357/acf713. URL http://dx.doi.org/10.3847/1538-4357/acf713.

IceCube Collaboration. Icetop: The surface component of icecube. *Nuclear Instruments and Methods in Physics Research Section A: Accelerators, Spectrometers, Detectors and Associated Equipment*, 700:188–220, February 2013a. ISSN 0168-9002. doi: 10.1016/j.nima.2012.10.067. URL http://dx.doi.org/10.1016/j.nima.2012.10.067.

Jean Pierre Twagirayezu, Hans Niederhausen, Nathan Whitehorn, Mehr Nisa, Tyce Deyoung, Chris Weaver, and P-ONE Collaboration. Performance Studies for the Pacific Ocean Neutrino Experiment (P-ONE). In *APS April Meeting Abstracts*, volume 2024 of *APS Meeting Abstracts*, page C14.002, April 2024.

S Adrián-Martínez et al. Letter of intent for km3net 2.0. *Journal of Physics G: Nuclear and Particle Physics*, 43(8):084001, jun 2016. doi: 10.1088/0954-3899/43/8/084001. URL https://doi.org/10.1088/0954-3899/43/8/084001.

Kumiko Kotera and Angela V. Olinto. The astrophysics of ultrahigh-energy cosmic rays. *Annual Review of Astronomy and Astrophysics*, 49(1):119–153, 2011. ISSN 1545-4282. doi: 10.1146/annurev-astro-081710-102620. URL http://dx.doi.org/10.1146/annurev-astro-081710-102620.

Eli Dwek and Frank Krennrich. The extragalactic background light and the gamma-ray opacity of the universe. *Astroparticle Physics*, 43:112–133, March 2013. ISSN 0927-6505. doi: 10.1016/j.astropartphys.2012.09.003. URL http://dx.doi.org/10.1016/j.astropartphys.2012.09.003.

Markus Ahlers and Francis Halzen. Opening a new window onto the universe with icecube. *Progress in Particle and Nuclear Physics*, 102:73–88, 2018. ISSN 0146-6410. doi: 10.1016/j.ppnp.2018.05.001. URL http://dx.doi.org/10.1016/j.ppnp.2018.05.001.

Ralph Engel, Dieter Heck, and Tanguy Pierog. Extensive air showers and hadronic interactions at high energy. *Ann. Rev. Nucl. Part. Sci.*, 61:467–489, 2011. doi: 10.1146/annurev.nucl.012809.104544.

Felix Riehn, Ralph Engel, Anatoli Fedynitch, Thomas K. Gaisser, and Todor Stanev. Hadronic interaction model Sibyll 2.3d and extensive air showers. *Phys. Rev. D*, 102 (6):063002, 2020. doi: 10.1103/PhysRevD.102.063002.

Tim Huege. Corsika 8 – the next-generation air shower simulation framework, 2022. URL `https://arxiv.org/abs/2208.14240`.

Anatoli Fedynitch. *Cascade equations and hadronic interactions at very high energies*. PhD thesis, KIT, Karlsruhe, Dept. Phys., 11 2015.

Paolo Lipari and Todor Stanev. Propagation of multi-tev muons. *Phys. Rev. D*, 44:3543–3554, Dec 1991. doi: 10.1103/PhysRevD.44.3543. URL `https://link.aps.org/doi/10.1103/PhysRevD.44.3543`.

Donald E. Groom, Nikolai V. Mokhov, and Sergei I. Striganov. Muon Stopping Power and Range Tables 10 MeV-100 TeV. *Atomic Data and Nuclear Data Tables*, 78(2):183–356, July 2001. doi: 10.1006/adnd.2001.0861.

Z. Maki, M. Nakagawa, and S. Sakata. Remarks on the Unified Model of Elementary Particles. *Progress of Theoretical Physics*, 28(5):870–880, November 1962. doi: 10.1143/PTP.28.870.

M.C. Gonzalez-Garcia and Michele Maltoni. Phenomenology with massive neutrinos. *Physics Reports*, 460(1-3):1–129, April 2008. ISSN 0370-1573. doi: 10.1016/j.physrep.2007.12.004. URL `http://dx.doi.org/10.1016/j.physrep.2007.12.004`.

L. Wolfenstein. Neutrino oscillations in matter. , 17(9):2369–2374, May 1978. doi: 10.1103/PhysRevD.17.2369.

S. P. Mikheyev and A. Yu. Smirnov. Resonance enhancement of oscillations in matter and solar neutrino spectroscopy. *Yadernaya Fizika*, 42:1441–1448, January 1985.

F. Halzen and D. Saltzberg. Tau neutrino appearance with a 1000 megaparsec baseline. *Physical Review Letters*, 81(20):4305–4308, November 1998. ISSN 1079-7114. doi: 10.1103/physrevlett.81.4305. URL `http://dx.doi.org/10.1103/PhysRevLett.81.4305`.

Carlos A. Argüelles, Jordi Salvado, and Christopher N. Weaver. nusquids: A toolbox for neutrino propagation. *Computer Physics Communications*, 277:108346, August 2022. ISSN 0010-4655. doi: 10.1016/j.cpc.2022.108346. URL `http://dx.doi.org/10.1016/j.cpc.2022.108346`.

I. M. Frank and I. E. Tamm. Coherent visible radiation of fast electrons passing through matter. *Compt. Rend. Acad. Sci. URSS*, 14(3):109–114, 1937. doi: 10.3367/UFNr.0093.196710o.0388.

S. Navas et al. Review of particle physics. *Phys. Rev. D*, 110(3):030001, 2024. doi: 10.1103/PhysRevD.110.030001.

J. A. Formaggio and G. P. Zeller. From ev to eev: Neutrino cross sections across energy scales. *Reviews of Modern Physics*, 84(3):1307–1341, 2012. ISSN 1539-0756. doi: 10.1103/revmodphys.84.1307. URL http://dx.doi.org/10.1103/RevModPhys.84.1307.

IceCube Collaboration. Detection of astrophysical tau neutrino candidates in icecube. *The European Physical Journal C*, 82(11), November 2022c. ISSN 1434-6052. doi: 10.1140/epjc/s10052-022-10795-y. URL http://dx.doi.org/10.1140/epjc/s10052-022-10795-y.

IceCube Collaborarion. Observation of seven astrophysical tau neutrino candidates with icecube. *Physical Review Letters*, 132(15), April 2024. ISSN 1079-7114. doi: 10.1103/physrevlett.132.151001. URL http://dx.doi.org/10.1103/PhysRevLett.132.151001.

Thomas K. Gaisser, Ralph Engel, and Elisa Resconi. *Cosmic Rays and Particle Physics: 2nd Edition*. Cambridge University Press, 6 2016. ISBN 978-0-521-01646-9.

IceCube Collaboration. Measurement of south pole ice transparency with the icecube led calibration system. *Nuclear Instruments and Methods in Physics Research Section A: Accelerators, Spectrometers, Detectors and Associated Equipment*, 711:73–89, May 2013b. ISSN 0168-9002. doi: 10.1016/j.nima.2013.01.054. URL http://dx.doi.org/10.1016/j.nima.2013.01.054.

Dmitry Chirkin. Evidence of optical anisotropy of the South Pole ice. In *33rd International Cosmic Ray Conference*, page 0580, 2013.

Rasha Abbasi et al. In situ estimation of ice crystal properties at the South Pole using LED calibration data from the IceCube Neutrino Observatory. *The Cryosphere*, 18(1):75–102, 2024. doi: 10.5194/tc-18-75-2024.

IceCUbe Collaboration. Energy reconstruction methods in the icecube neutrino telescope. *Journal of Instrumentation*, 9(03):P03009–P03009, March 2014. ISSN 1748-0221. doi: 10.1088/1748-0221/9/03/p03009. URL http://dx.doi.org/10.1088/1748-0221/9/03/P03009.

Joeran Stettner. Measurement of the diffuse astrophysical muon-neutrino spectrum with ten years of icecube data, 2019. URL https://arxiv.org/abs/1908.09551.

IceCube Collaboration. Evidence for a spectral break or curvature in the spectrum of astrophysical neutrinos from 5 tev to 10 pev. *Physical Review Letters*, 136(12), March 2026a. ISSN 1079-7114. doi: 10.1103/2gh9-d4q7. URL http://dx.doi.org/10.1103/2gh9-d4q7.

IceCube Collaboration. Improved measurements of the tev-pev extragalactic neutrino spectrum from joint analyses of icecube tracks and cascades. *Physical Review D*, 113(6), March 2026b. ISSN 2470-0029. doi: 10.1103/4n6v-r7n4. URL http://dx.doi.org/10.1103/4n6v-r7n4.

Thomas K. Gaisser, Kyle Jero, Albrecht Karle, and Jakob van Santen. Generalized self-veto probability for atmospheric neutrinos. *Physical Review D*, 90(2), 2014. ISSN 1550-2368. doi: 10.1103/physrevd.90.023009. URL http://dx.doi.org/10.1103/PhysRevD.90.023009.

Carlos A. Argüelles, Sergio Palomares-Ruiz, Austin Schneider, Logan Wille, and Tianlu Yuan. Unified atmospheric neutrino passing fractions for large-scale neutrino telescopes. *Journal of Cosmology and Astroparticle Physics*, 2018(07):047–047, 2018. ISSN 1475-7516. doi: 10.1088/1475-7516/2018/07/047. URL http://dx.doi.org/10.1088/1475-7516/2018/07/047.

IceCube Collaboration. Icecube data for neutrino point-source searches years 2008-2018, 2021a. URL https://arxiv.org/abs/2101.09836.

IceCube Collaboration. A convolutional neural network based cascade reconstruction for the icecube neutrino observatory. *Journal of Instrumentation*, 16(07):P07041, 2021b. ISSN 1748-0221. doi: 10.1088/1748-0221/16/07/p07041. URL http://dx.doi.org/10.1088/1748-0221/16/07/P07041.

IceCube Collaboration. Multimessenger observations of a flaring blazar coincident with high-energy neutrino IceCube-170922A. *Science*, 361(6398):eaat1378, July 2018b. doi: 10.1126/science.aat1378.

IceCube Collaboration. Neutrino emission from the direction of the blazar txs 0506+056 prior to the icecube-170922a alert. *Science*, 361(6398):147–151, July 2018c. ISSN 1095-9203. doi: 10.1126/science.aat2890. URL http://dx.doi.org/10.1126/science.aat2890.

IceCube Collaboration. Time-Integrated Neutrino Source Searches with 10 Years of IceCube Data. *Physical Review Letters*, 124(5), Feb 2020a. ISSN 1079-7114. doi: 10.1103/physrevlett.124.051103. URL http://dx.doi.org/10.1103/PhysRevLett.124.051103.

M. Huber. Searches for steady neutrino emission from 3FHL blazars using eight years of IceCube data from the Northern hemisphere. In *36th International Cosmic Ray Conference (ICRC2019)*, volume 36 of *International Cosmic Ray Conference*, page 916, July 2019. doi: 10.22323/1.358.0916.

IceCube Collaboration. Search for astrophysical neutrinos from 1fle blazars with icecube. *The Astrophysical Journal*, 938(1):38, October 2022d. ISSN 1538-4357. doi: 10.3847/1538-4357/ac8de4. URL http://dx.doi.org/10.3847/1538-4357/ac8de4.

IceCube Collaboration. Evidence for neutrino emission from x-ray-bright active galactic nuclei with icecube. *The Astrophysical Journal Letters*, 1000(1):L26, March 2026c. ISSN 2041-8213. doi: 10.3847/2041-8213/ae4aad. URL http://dx.doi.org/10.3847/2041-8213/ae4aad.

Alexander Plavin, Yuri Y. Kovalev, Yuri A. Kovalev, and Sergey Troitsky. Observational Evidence for the Origin of High-energy Neutrinos in Parsec-scale Nuclei of Radio-bright Active Galaxies. , 894(2):101, May 2020. doi: 10.3847/1538-4357/ab86bd.

A. V. Plavin, Y. Y. Kovalev, Yu. A. Kovalev, and S. V. Troitsky. Directional association of tev to pev astrophysical neutrinos with radio blazars. *The Astrophysical Journal*, 908(2): 157, Feb 2021. ISSN 1538-4357. doi: 10.3847/1538-4357/abceb8. URL http://dx.doi.org/10.3847/1538-4357/abceb8.

T. Hovatta, Lindfors, et al. Association of IceCube neutrinos with radio sources observed a t Owens Valley and Metsähovi Radio Observatories. , 650:A83, June 2021. doi: 10.1051/0004-6361/202039481.

Julien Aublin and Alexander Plavin. Search for an association between neutrinos and radio-selected blazars with ANTARES. *PoS*, ICRC2021:1164, 2021. doi: 10.22323/1.395.1164.

Giulia Illuminati and Alexander Plavin. ANTARES search for neutrino flares from the direction of radio-bright blazars. *PoS*, ICRC2021:972, 2021. doi: 10.22323/1.395.0972.

A V Plavin et al. Growing evidence for high-energy neutrinos originating in radio blazars. *Monthly Notices of the Royal Astronomical Society*, 523(2):1799–1808, May 2023. ISSN 1365-2966. doi: 10.1093/mnras/stad1467. URL http://dx.doi.org/10.1093/mnras/stad1467.

IceCube Collaboration. Probing the Connection between IceCube Neutrinos and MOJAVE AGN. , 973(2):97, October 2024. doi: 10.3847/1538-4357/ad643d.

L. Fuhrmann et al. Detection of significant cm to sub-mm band radio and -ray correlated variability in fermi bright blazars. *Monthly Notices of the Royal Astronomical Society*, 441(3):1899–1909, May 2014. ISSN 1365-2966. doi: 10.1093/mnras/stu540. URL http://dx.doi.org/10.1093/mnras/stu540.

IceCube Collaboration and Atacama Cosmology Telescope Collaboration. A search for millimeter-bright blazars as astrophysical neutrino sources, 2025. URL https://arxiv.org/abs/2507.03989.

Atacama Cosmology Telescope Collaboration. Overview of the atacama cosmology telescope: Receiver, instrumentation, and telescope systems. *The Astrophysical Journal Supplement Series*, 194(2):41, June 2011. ISSN 1538-4365. doi: 10.1088/0067-0049/194/2/41. URL http://dx.doi.org/10.1088/0067-0049/194/2/41.

Atacama Cosmology Telescope Collaboration. The Atacama Cosmology Telescope: The Polarization-sensitive ACTPol Instrument. , 227(2):21, December 2016a. doi: 10.3847/1538-4365/227/2/21.

Atacama Cosmology Telescope Collaboration. Advanced ACTPol Cryogenic Detector Arrays and Readout. *Journal of Low Temperature Physics*, 184(3-4):772–779, August 2016b. doi: 10.1007/s10909-016-1575-z.

Atacama Cosmology Telescope Collaboration. The Atacama Cosmology Telescope: arcminute-resolution maps of 18 000 square degrees of the microwave sky from ACT 2008-2018 data combined with Planck. , 2020(12):046, December 2020a. doi: 10.1088/1475-7516/2020/12/046.

Atacama Cosmology Telescope Collaboration. Atacama Cosmology Telescope: Dusty Star-forming Galaxies and Active Galactic Nuclei in the Equatorial Survey. , 893(2):104, April 2020b. doi: 10.3847/1538-4357/ab7915.

F. Ochsenbein, P. Bauer, and J. Marcout. The VizieR database of astronomical catalogues , 2000.

Condon, J. J. and others. The NRAO VLA Sky Survey. , 115(5):1693–1716, May 1998. doi: 10.1086/300337.

Tara Murphy et al. The Australia Telescope 20 GHz Survey: the source catalogue. , 402(4):2403–2423, March 2010. doi: 10.1111/j.1365-2966.2009.15961.x.

Kevork N. Abazajian, Steve Blanchet, and J. Patrick Harding. Contribution of blazars to the extragalactic diffuse gamma-ray background and their future spatial resolution. *Phys. Rev. D*, 84:103007, Nov 2011. doi: 10.1103/PhysRevD.84.103007. URL `https://link.aps.org/doi/10.1103/PhysRevD.84.103007`.

J. Patrick Harding and Kevork N Abazajian. Models of the contribution of blazars to the anisotropy of the extragalactic diffuse gamma-ray background. *Journal of Cosmology and Astroparticle Physics*, 2012(11):026–026, November 2012. ISSN 1475-7516. doi: 10.1088/1475-7516/2012/11/026. URL `http://dx.doi.org/10.1088/1475-7516/2012/11/026`.

Chun Fai Tung, Theo Glauch, Michael Larson, Alex Pizzuto, Rene Reimann, and Ignacio Taboada. Firesong: A python package to simulate populations of extragalactic neutrino sources. *Journal of Open Source Software*, 6(61):3194, 2021. doi: 10.21105/joss.03194. URL `https://doi.org/10.21105/joss.03194`.

Baikal-GVD Collaboration. High-energy neutrino-induced cascade from the direction of the flaring radio blazar txs 0506 + 056 observed by baikal-gvd in 2021. *Monthly Notices of the Royal Astronomical Society*, 527(3). ISSN 1365-2966. doi: 10.1093/mnras/stad3653. URL `http://dx.doi.org/10.1093/mnras/stad3653`.

IceCube Collaboration. *arXiv e-prints*, art. arXiv:2101.09836, January 2021c. doi: 10.48550/arXiv.2101.09836.

Jim Braun et al. Methods for point source analysis in high energy neutrino telescopes. *Astroparticle Physics*, 29(4):299–305, May 2008. ISSN 0927-6505. doi: 10.1016/j.astropartphys.2008.02.007. URL http://dx.doi.org/10.1016/j.astropartphys.2008.02.007.

Richard H. Byrd, Peihuang Lu, Jorge Nocedal, and Ciyou Zhu. A limited memory algorithm for bound constrained optimization. *SIAM Journal on Scientific Computing*, 16(5):1190–1208, 1995. doi: 10.1137/0916069. URL https://doi.org/10.1137/0916069.

Ciyou Zhu et al. Algorithm 778: L-bfgs-b: Fortran subroutines for large-scale bound-constrained optimization. *ACM Trans. Math. Softw.*, 23(4):550–560, December 1997. ISSN 0098-3500. doi: 10.1145/279232.279236. URL https://doi.org/10.1145/279232.279236.

José Morales and Jorge Nocedal. Remark on "algorithm 778: L-bfgs-b: Fortran subroutines for large-scale bound constrained optimization". *ACM Trans. Math. Softw.*, 38:7, 11 2011. doi: 10.1145/2049662.2049669.

S. S. Wilks. The Large-Sample Distribution of the Likelihood Ratio for Testing Composite Hypotheses. *The Annals of Mathematical Statistics*, 9(1):60 – 62, 1938. doi: 10.1214/aoms/1177732360. URL https://doi.org/10.1214/aoms/1177732360.

H. K. Vedantham et al. The Peculiar Light Curve of J1415+1320: A Case Study in Extreme Scattering Events. , 845(2):90, August 2017a. doi: 10.3847/1538-4357/aa7741.

H. K. Vedantham et al. Symmetric achromatic variability in active galaxies: A powerful new gravitational lensing probe? *The Astrophysical Journal*, 845(2):89, August 2017b. ISSN 1538-4357. doi: 10.3847/1538-4357/aa745c. URL http://dx.doi.org/10.3847/1538-4357/aa745c.

Bidzina Kapanadze, Stefano Vercellone, and Patrizia Romano. Stochastic acceleration in the relativistic jets of BL Lacertae objects. , 79:101393, August 2020. doi: 10.1016/j.newast.2020.101393.

Simons Observatory Collaboration. The Simons Observatory: science goals and forecasts. , 2019(2):056, February 2019. doi: 10.1088/1475-7516/2019/02/056.

Simons Observatory Collaboration. , 2025(8):034, August 2025. doi: 10.1088/1475-7516/2025/08/034.

Talvikki Hovatta and Elina Lindfors. Relativistic Jets of Blazars. , 87:101541, December 2019. doi: 10.1016/j.newar.2020.101541.

Oliver de Bruijn, Imre Bartos, Peter L. Biermann, and J. Becker Tjus. Recurrent neutrino emission from supermassive black hole mergers. *The Astrophysical Journal Letters*, 905 (1):L13, December 2020. ISSN 2041-8213. doi: 10.3847/2041-8213/abc950. URL http://dx.doi.org/10.3847/2041-8213/abc950.

Julia Becker Tjus et al. Neutrino cadence of txs 0506+056 consistent with supermassive binary origin. *The Astrophysical Journal Letters*, 941(2):L25, December 2022. ISSN 2041-8213. doi: 10.3847/2041-8213/aca65d. URL http://dx.doi.org/10.3847/2041-8213/aca65d.

D Kantzas and et al. A new lepto-hadronic model applied to the first simultaneous multi-wavelength data set for cygnus x–1. *Monthly Notices of the Royal Astronomical Society*, 500(2):2112–2126, October 2020. ISSN 1365-2966. doi: 10.1093/mnras/staa3349. URL http://dx.doi.org/10.1093/mnras/staa3349.

D Kantzas and et al. Possible contribution of x-ray binary jets to the galactic cosmic ray and neutrino flux. *Monthly Notices of the Royal Astronomical Society*, 524(1):1326–1342, June 2023. ISSN 1365-2966. doi: 10.1093/mnras/stad1909. URL http://dx.doi.org/10.1093/mnras/stad1909.

Sera Markoff, Michael Nowak, and Jörn Wilms. Going with the flow: Can the base of jets subsume the role of compact accretion disk coronae? *The Astrophysical Journal*, 635: 1203, 12 2005. doi: 10.1086/497628.

Tatehiro Mihara and et al. *MAXI: Monitor of All-Sky X-Ray Image*, page 1–25. Springer Nature Singapore, 2022. ISBN 9789811645440. doi: 10.1007/978-981-16-4544-0_38-1. URL http://dx.doi.org/10.1007/978-981-16-4544-0_38-1.

H. A. Krimm et al. The swift-bat hard x-ray transient monitor. *The Astrophysical Journal Supplement Series*, 209(1):14, October 2013. ISSN 1538-4365. doi: 10.1088/0067-0049/209/1/14. URL http://dx.doi.org/10.1088/0067-0049/209/1/14.

S. Abdollahi and et al. The fermi-lat lightcurve repository*. *The Astrophysical Journal Supplement Series*, 265(2):31, March 2023. ISSN 1538-4365. doi: 10.3847/1538-4365/acbb6a. URL http://dx.doi.org/10.3847/1538-4365/acbb6a.

IceCube Collaboration. Neutrino emission from the direction of the blazar txs 0506+056 prior to the icecube-170922a alert. *Science*, 361(6398):147–151, July 2018d. ISSN 1095-9203. doi: 10.1126/science.aat2890. URL http://dx.doi.org/10.1126/science.aat2890.

M.G. Aartsen, M. Ackermann, J. Adams, Juan Antonio Aguilar Sánchez, M. Ahlers, M. Ahrens, Imen Al Samarai, David Altmann, Karen Andeen, Travi Anderson, I. Ansseau, G. Anton, Carlos Arguelles Delgado, J. Auffenberg, Spencer Axani, H. Bagherpour, Xiaoqiong Bai, J.P. Barron, S.W. Barwick, and G.R. Sivakoff. Multimessenger observations of a flaring blazar coincident with high-energy neutrino icecube-170922a. 01 2018.

V. A. Acciari et al. Investigating the blazar txs 0506+056 through sharp multiwavelength eyes during 2017–2019. *The Astrophysical Journal*, 927(2):197, March 2022. ISSN 1538-4357. doi: 10.3847/1538-4357/ac531d. URL http://dx.doi.org/10.3847/1538-4357/ac531d.

Yu-Ling Chang, Bruno Arsioli, Wenlian Li, Donglian Xu, and Liang Chen. Hunting for neutrino emission from multifrequency variable sources. *The Astrophysical Journal*, 939 (2):123, November 2022. ISSN 1538-4357. doi: 10.3847/1538-4357/ac8c32. URL http://dx.doi.org/10.3847/1538-4357/ac8c32.

IceCube Collaboration and Atacama Cosmology Telescope Collaboration. A search for millimeter-bright blazars as astrophysical neutrino sources. *The Astrophysical Journal*, 999(1):98, feb 2026. doi: 10.3847/1538-4357/ae31e2. URL https://doi.org/10.3847/1538-4357/ae31e2.

E Kun, P L Biermann, and L Á Gergely. Very long baseline interferometry radio structure and radio brightening of the high-energy neutrino emitting blazar txs 0506+056. *Monthly Notices of the Royal Astronomical Society: Letters*, 483(1):L42–L46, November 2018. ISSN 1745-3933. doi: 10.1093/mnrasl/sly216. URL http://dx.doi.org/10.1093/mnrasl/sly216.

Emma Kun and Attila Medveczky. Multiwavelength Analysis of the IceCube Neutrino Source Candidate Blazar PKS 1424+240. *Symmetry*, 15(2):270, January 2023. doi: 10.3390/sym15020270.

Alina Kochocki, Emma Kun, and Sam Hori. Characterizing gamma-radio delayed flaring activity from blazars, 2026. URL https://arxiv.org/abs/2604.03847.

M. Boettcher et al. Leptonic and Hadronic Modeling of Fermi-Detected Blazars. *Astrophys. J.*, 768:54, 2013. doi: 10.1088/0004-637X/768/1/54.

S. Britzen et al. A cosmic collider: Was the IceCube neutrino generated in a precessing jet-jet interaction in TXS 0506+056? , 630:A103, October 2019. doi: 10.1051/0004-6361/201935422.

William J. Potter. Modelling blazar flaring using a time-dependent fluid jet emission model – an explanation for orphan flares and radio lags. *Monthly Notices of the Royal Astronomical Society*, 473(3):4107–4121, September 2017. ISSN 1365-2966. doi: 10.1093/mnras/stx2371. URL http://dx.doi.org/10.1093/mnras/stx2371.

Stella Boula, Maria Petropoulou, and Apostolos Mastichiadis. On the connection of radio and -ray emission in blazars. *Galaxies*, 7(1):3, December 2018. ISSN 2075-4434. doi: 10.3390/galaxies7010003. URL http://dx.doi.org/10.3390/galaxies7010003.

A. Keivani et al. A Multimessenger Picture of the Flaring Blazar TXS 0506+056: implications for High-Energy Neutrino Emission and Cosmic Ray Acceleration. *Astrophys. J.*,

864(1):84, 2018. doi: 10.3847/1538-4357/aad59a.

Shan Gao, Anatoli Fedynitch, Walter Winter, and Martin Pohl. Modelling the coincident observation of a high-energy neutrino and a bright blazar flare. *Nature Astron.*, 3(1): 88–92, 2019. doi: 10.1038/s41550-018-0610-1.

M. Cerruti, A. Zech, C. Boisson, G. Emery, S. Inoue, and J. P. Lenain. Leptohadronic single-zone models for the electromagnetic and neutrino emission of TXS 0506+056. *Mon. Not. Roy. Astron. Soc.*, 483(1):L12–L16, 2019. doi: 10.1093/mnrasl/sly210. [Erratum: Mon.Not.Roy.Astron.Soc. 502, L21–L22 (2021)].

Maria Petropoulou, Kohta Murase, Marcos Santander, Sara Buson, Aaron Tohuvavohu, Taiki Kawamuro, Georgios Vasilopoulos, Hiroshi Negoro, Yoshihiro Ueda, Michael H. Siegel, Azadeh Keivani, Nobuyuki Kawai, Apostolos Mastichiadis, and Stavros Dimitrakoudis. Multi-epoch modeling of txs 0506+056 and implications for long-term high-energy neutrino emission. *The Astrophysical Journal*, 891(2):115, March 2020. ISSN 1538-4357. doi: 10.3847/1538-4357/ab76d0. URL `http://dx.doi.org/10.3847/1538-4357/ab76d0`.

M. Cerruti, A. Zech, C. Boisson, and S. Inoue. A hadronic origin for ultra-high-frequency-peaked BL Lac objects. *Mon. Not. Roy. Astron. Soc.*, 448(1):910–927, 2015. doi: 10.1093/mnras/stu2691.

William Atwood. Pass 8: A Comprehensive Revision Of The Fermi Lat Event-level Analysis. In *American Astronomical Society Meeting Abstracts #219*, volume 219 of *American Astronomical Society Meeting Abstracts*, page 145.18, January 2012.

P Padovani, P Giommi, E Resconi, T Glauch, B Arsioli, N Sahakyan, and M Huber. Dissecting the region around icecube-170922a: the blazar txs0506+056 as the first cosmic neutrino source. *Monthly Notices of the Royal Astronomical Society*, 480(1):192–203, July 2018. ISSN 1365-2966. doi: 10.1093/mnras/sty1852. URL `http://dx.doi.org/10.1093/mnras/sty1852`.

G. Ghisellini, F. Tavecchio, L. Foschini, G. Ghirlanda, L. Maraschi, and A. Celotti. General physical properties of bright fermi blazars: Properties of bright fermi blazars. *Monthly Notices of the Royal Astronomical Society*, 402(1):497–518, November 2009. ISSN 0035-8711. doi: 10.1111/j.1365-2966.2009.15898.x. URL `http://dx.doi.org/10.1111/j.1365-2966.2009.15898.x`.

Moshe Elitzur and Isaac Shlosman. The agn-obscuring torus: The end of the "doughnut" paradigm? *The Astrophysical Journal*, 648(2):L101–L104, September 2006. ISSN 1538-4357. doi: 10.1086/508158. URL `http://dx.doi.org/10.1086/508158`.

M. Klinger, A. Rudolph, X. Rodrigues, C. Yuan , G. Fichet de Clairfontaine, A. Fedynitch, W. Winter, M. Pohl, and S. Gao. Am3: An open-source tool for time-dependent lepto-hadronic modeling of astrophysical sources. *The Astrophysical Journal Supplement Series*,

275(1):4, October 2024a. ISSN 1538-4365. doi: 10.3847/1538-4365/ad725c. URL http://dx.doi.org/10.3847/1538-4365/ad725c.

Svetlana G. Jorstad et al. Multi-epoch VLBA observations of EGRET-detected quasars and BL Lac objects: Superluminal motion of gamma-ray bright blazars. *Astrophys. J. Suppl.*, 134:181–240, 2001. doi: 10.1086/320858.

Y. Y. Kovalev et al. Early Fermi gamma-ray detections of AGN: a strong connection with parsec-scale VLBA jet properties. *Astrophys. J. Lett.*, 696:L17, 2009. doi: 10.1088/0004-637X/696/1/L17.

M. L. Lister et al. MOJAVE XIII. Parsec-Scale AGN Jet Kinematics Analysis Based on 19 years of VLBA Observations at 15 GHz. *Astron. J.*, 152:12, 2016. doi: 10.3847/0004-6256/152/1/12.

Marc Klinger, Annika Rudolph, Xavier Rodrigues, Chengchao Yuan , Gaëtan Fichet de Clairfontaine, Anatoli Fedynitch, Walter Winter, Martin Pohl, and Shan Gao. Am3: An open-source tool for time-dependent lepto-hadronic modeling of astrophysical sources. *The Astrophysical Journal Supplement Series*, 275(1):4, October 2024b. ISSN 1538-4365. doi: 10.3847/1538-4365/ad725c. URL http://dx.doi.org/10.3847/1538-4365/ad725c.

Xavier Rodrigues, Vaidehi S. Paliya, Simone Garrappa, Anastasiia Omeliukh, Anna Franckowiak, and Walter Winter. Leptohadronic multi-messenger modeling of 324 gamma-ray blazars. *Astron. Astrophys.*, 681:A119, 2024. doi: 10.1051/0004-6361/202347540.

J. C. McKinney. General relativistic magnetohydrodynamic simulations of the jet formation and large-scale propagation from black hole accretion systems. *Monthly Notices of the Royal Astronomical Society*, 368(4):1561–1582, June 2006. ISSN 1365-2966. doi: 10.1111/j.1365-2966.2006.10256.x. URL http://dx.doi.org/10.1111/j.1365-2966.2006.10256.x.

Xiaofeng Li, Tao An, Prashanth Mohan, and Marcello Giroletti. The parsec-scale jet of the neutrino-emitting blazar txs 0506+056. *The Astrophysical Journal*, 896(1):63, June 2020. ISSN 1538-4357. doi: 10.3847/1538-4357/ab8f9f. URL http://dx.doi.org/10.3847/1538-4357/ab8f9f.

S. I. Stathopoulos et al. Delayed radio flares in neutrino-associated blazars: The case of txs 0506+056, 2026. URL https://arxiv.org/abs/2604.01196.

R. D. Blandford and R. L. Znajek. Electromagnetic extractions of energy from Kerr black holes. *Mon. Not. Roy. Astron. Soc.*, 179:433–456, 1977. doi: 10.1093/mnras/179.3.433.

George R. Blumenthal and Robert J. Gould. Bremsstrahlung, synchrotron radiation, and compton scattering of high-energy electrons traversing dilute gases. *Rev. Mod. Phys.*, 42:237–270, Apr 1970. doi: 10.1103/RevModPhys.42.237. URL https://link.aps.org/

doi/10.1103/RevModPhys.42.237.

Matteo Cerruti. Leptonic and hadronic radiative processes in supermassive-black-hole jets. *Galaxies*, 8(4):72, October 2020. ISSN 2075-4434. doi: 10.3390/galaxies8040072. URL http://dx.doi.org/10.3390/galaxies8040072.

M. Petropoulou and A. Mastichiadis. Bethe–heitler emission in bl lacs: filling the gap between x-rays and -rays. *Monthly Notices of the Royal Astronomical Society*, 447(1): 36–48, December 2014. ISSN 0035-8711. doi: 10.1093/mnras/stu2364. URL http://dx.doi.org/10.1093/mnras/stu2364.

William J. Potter and Garret Cotter. Synchrotron and inverse-compton emission from blazar jets - i. a uniform conical jet model: A uniform conical jet model. *Monthly Notices of the Royal Astronomical Society*, 423(1):756–765, April 2012. ISSN 0035-8711. doi: 10.1111/j.1365-2966.2012.20918.x. URL http://dx.doi.org/10.1111/j.1365-2966.2012.20918.x.

William J. Potter and Garret Cotter. Synchrotron and inverse-compton emission from blazar jets – iii. compton-dominant blazars. *Monthly Notices of the Royal Astronomical Society*, 431(2):1840–1852, March 2013. ISSN 0035-8711. doi: 10.1093/mnras/stt300. URL http://dx.doi.org/10.1093/mnras/stt300.

William J. Potter and Garret Cotter. New constraints on the structure and dynamics of black hole jets. *Monthly Notices of the Royal Astronomical Society*, 453(4):4071–4089, September 2015. ISSN 1365-2966. doi: 10.1093/mnras/stv1657. URL http://dx.doi.org/10.1093/mnras/stv1657.

A. T. Araudo, V. Bosch-Ramon, and G. E. Romero. Gamma rays from cloud penetration at the base of agn jets. *Astronomy amp; Astrophysics*, 522:A97, November 2010. ISSN 1432-0746. doi: 10.1051/0004-6361/201014660. URL http://dx.doi.org/10.1051/0004-6361/201014660.

H. T. Liu and J. M. Bai. Absorption of 10-200 GeV Gamma Rays by Radiation from Broad-Line Regions in Blazars. , 653(2):1089–1097, December 2006. doi: 10.1086/509097.

Ze-Rui Wang, Ruo-Yu Liu, Maria Petropoulou, Foteini Oikonomou, Rui Xue, and Xiang-Yu Wang. Unified model for orphan and multiwavelength blazar flares. *Physical Review D*, 105(2), January 2022. ISSN 2470-0029. doi: 10.1103/physrevd.105.023005. URL http://dx.doi.org/10.1103/PhysRevD.105.023005.

I G Kramarenko, A B Pushkarev, Y Y Kovalev, M L Lister, T Hovatta, and T Savolainen. A decade of joint mojave–fermi agn monitoring: localization of the gamma-ray emission region. *Monthly Notices of the Royal Astronomical Society*, 510(1):469–480, November 2021. ISSN 1365-2966. doi: 10.1093/mnras/stab3358. URL http://dx.doi.org/10.1093/mnras/stab3358.

E. Kun, K. É. Gabányi, M. Karouzos, S. Britzen, and L. Á. Gergely. A spinning supermassive black hole binary model consistent with VLBI observations of the S5 1928+738 jet. , 445 (2):1370–1382, December 2014. doi: 10.1093/mnras/stu1813.

E. Kun, S. Frey, K. É. Gabányi, S. Britzen, D. Cseh, and L. Á. Gergely. Constraining the parameters of the putative supermassive binary black hole in PG 1302-102 from its radio structure. , 454(2):1290–1296, December 2015. doi: 10.1093/mnras/stv2049.

M. C. Shepherd. Difmap: an Interactive Program for Synthesis Imaging. In Gareth Hunt and Harry Payne, editors, *Astronomical Data Analysis Software and Systems VI*, volume 125 of *Astronomical Society of the Pacific Conference Series*, page 77, January 1997.

D. Foreman-Mackey. Scalable Backpropagation for Gaussian Processes using Celerite. *Research Notes of the American Astronomical Society*, 2(1):31, February 2018. doi: 10.3847/2515-5172/aaaf6c.